Inflow measurements from blade-mounted flow sensors: Flow analysis, application and aeroelastic response

Pedersen, Mads Mølgaard

Link to article, DOI:
10.11581/DTU:00000030

Publication date:
2018

Document Version
Publisher's PDF, also known as Version of record

DTU Wind Energy
Department of Wind Energy

Ph.D. Thesis

Inflow measurements from blade-mounted flow sensors

- Flow analysis, application and aeroelastic response

Mads M. Pedersen

Risø campus, Roskilde, 2018

DTU

Technical University of Denmark
DTU Wind Energy
Department of Wind Energy

DTU Risø Campus
Frederiksborgvej 399 4000 Roskilde, Denmark
mmpe@dtu.dk
www.vindenergi.dtu.dk

Summary (English)

The power and load performance of wind turbines are both crucial for the development and expansion of wind energy. The power and loads are highly dependent on the inflow conditions, which can be measured using different types of sensors mounted on nearby met masts, on the nacelle, at the spinner or at the blade. Each combination of sensor type and mounting position has advantages and shortcomings.

To characterise the inflow that results in high and low fatigue loads, information about the temporal and spatial variations within the rotor area is required. This information can be obtained from a blade-mounted flow sensor, BMFS, e.g. a five-hole pitot tube, which has been used in several research experiments over the last 30 years. The BMFS measured flow velocity is, however, located inside the induction zone and thereby influenced by the aerodynamic properties, the control strategy and the operational status of the turbine.

In this project, a method to estimate the free-inflow velocity from the BMFS measured flow velocity has been developed and implemented. The method is based on the aerodynamic engineering models that are used in well-established aeroelastic codes to describe the relation between the free-inflow and the velocity at the blades.

Before these models can be applied, the measured local flow must be compensated for flow deflection and change of flow speed near the airfoil. Furthermore, the sensor velocity must be subtracted and the resulting absolute flow must be mapped into fixed ground coordinates. In these steps, uncertainty is introduced because the actual velocity and orientation of the BMFS are unknown due to the deflection and torsion of the blade. The introduced uncertainties have been investigated using HAWC2 simulations and simulations performed by Flex5 coupled with the LES flow solver, EllipSys3D.

The uncertainties should, however, be considered in relation to the advantages of measuring the flow at the blade: a BMFS yaws with the turbine, measures the inflow at the rotor plane and sweeps different parts of the rotor. It is thereby exposed to exactly the same inflow conditions as the turbine (including wake effects from upstream turbines) and able to provide valuable information about the instant inflow velocity as well as variations within the rotor plane, and that goes for all wind directions.

From the BMFS measurements, estimates of the local aerodynamic forces, the angle-of-attack and relative flow speed, the rotor-plane velocity and the free-inflow velocity can be obtained. Applications of these measures have been investigated. It is concluded that a BMFS provides valuable information about the inflow, which can be used for the control of load alleviating concepts like individual pitch and trailing edge flaps, to investigate the complex relation between the inflow and the power and loads, to characterise the inflow conditions that yield high loads, and as input for aeroelastic simulations to improve the

correlation between the measured and simulated loads.

Summary (Danish)

Energiproduktion og holdbarhed er afgørende parametre for udviklingen af vindmøller og deres udbredelse. Disse parametre afhænger af vindforholdene, som kan måles med forskellige typer af instrumenter, der hver især kan placeres forskellige steder, f.eks. på en målemast, på nacellen, i spinneren eller på en vinge. Hver kombination af instrumenttype og placering har fordele og ulemper.

For at karakterisere de vindforhold, som giver store og små belastninger på vindmøller, er det nødvendigt at kende de tidslige og rummelige variationer af vinden over rotorskiven. Denne information kan måles med en vingemonteret vindmåler, f.eks. et fem-huls pitotrør, som har været anvendt i adskillige forskningsprojekter gennem de seneste 30 år. På vingen er vindmåleren dog påvirket af møllens induktion og dermed af møllens aerodynamiske egenskaber, kontrolmekanisme og operationelle status.

I dette projekt har vi udviklet og implementeret en metode til at kompensere for møllens påvirkning, så de frie indstrømningsforhold kan estimeres. Metoden er baseret på de aerodynamiske ingeniørmodeller, som anvendes i veletablerede aeroelastiske simuleringsværktøjer til at beskrive forholdet mellem de frie indstrømningsforhold og vinden på vingerne. Inden disse modeller kan anvendes, skal de målte lokale flow hastigheder kompenseres for de afbøjninger og hastighedsændringer, der sker tæt på vingeprofilet. Derudover skal de målte hastigheder konverteres til et fast globalt koordinatsystem, og vindmålerens egenhastighed skal fratrækkes. Dermed fås et estimat af vindens hastighed og retning i forhold til et fast punkt på jorden. Da vindmåleren sidder på vingen, der bøjer og vrider sig pga. vindens påvirkning, kendes vindmålerens nøjagtige orientering og egenhastighed ikke helt præcist, og dermed bliver den estimerede vindhastighed i forhold til jorden heller ikke helt præcist. Vi har undersøgt de usikkerheder, som bliver indført i hvert af disse trin ved hjælp af HAWC2 simuleringer og simuleringer udført med Flex5 koblet med LES flow løseren, EllipSys3D.

Usikkerhederne skal dog ses i forhold til fordelene ved at måle vinden på vingen: En vingemonteret vindmåler følger møllen, når den krøjer, den måler i rotor planet, og den måler forskellige steder på rotorskiven. Den måler derfor nøjagtigt de vindhold, som møllen er udsat for inklusiv skyggevirkninger fra foranstående møller, og kan give værdifuld information om øjeblikkelige vindforhold såvel som variationer hen over rotoren – og det gælder for alle vindretninger.

Ud fra den vind, der måles på vingen, er det muligt at estimere de lokale aerodynamiske kræfter, angrebsvinklen og den relative flow hastighed, samt vindens hastighed i rotor planet med og uden møllens påvirkning. Vi har undersøgt forskellige anvendelsesmuligheder for disse estimater og konkluderer, at en vingemonteret vindmåler giver værdifuld

information. Denne information kan anvendes til at kontrollere lastreducerende foranstaltninger, f.eks. individuel pitchregulering og flaps, til at undersøge den komplekse relation mellem vindforhold og møllens reaktion i form af energiproduktion og belastninger, til at karakterisere de vindforhold som giver store belastninger og endelig som input til aeroelastiske simuleringer, så sammenhængen mellem målte og simulerede belastninger forbedres.

Preface and acknowledgement

This Ph.D. thesis has been prepared at the Department of Wind Energy at the Technical University of Denmark during the period from 2015 to 2018, in partial fulfillment of the requirements for acquiring a Ph.D. degree.

The present work consists of four scientific papers and a summary report. The summary report gives an introduction to the topic and links the work and results presented in the papers together with additional background material and results. Hence, the four publications are considered as a central part of the thesis.

The work has been supervised by Senior Scientist Torben J. Larsen and co-supervised by Professor Helge Aagaard Madsen, Senior Scientist Gunner Chr. Larsen and Senior Scientist Uwe Schmidt Paulsen. I would like to thank my supervisors for invaluable discussions, explanations and support.

Furthermore, I am grateful to all my colleagues for always having time to help me and answer questions. In particular, I would like to thank Søren Juhl Andersen and Niels Troldborg for setting up and performing CFD simulations for this project, and Mac Gaunaa for theoretical discussions, paper notes and scripts on aerodynamic theory and vortex methods.

I also wish to thank Siemens Wind Power for their interest in the project and for providing information and measurement data for the applied simulation models as well as the permission to publish the simulation and measurement results of their turbines.

The project has been funded by DTU Wind Energy which is gratefully acknowledged.

Risø campus, Roskilde, April 17, 2018

Mads M. Pedersen

Papers included in this thesis

A Pedersen, Mads M., Torben J. Larsen, Gunner C. Larsen, Helge A. Madsen, and Niels Troldborg (Jan. 2015). "Turbulent wind field characterization and regeneration based on pitot tube measurements mounted on a wind turbine". In: *33rd Wind Energy Symposium*. AIAA SciTech. Kissimmee, Florida: American Institute of Aeronautics and Astronautics. ISBN: 978-1-62410-344-5. DOI: 10.2514/6.2015-1467. URL: http://arc.aiaa.org/doi/10.2514/6.2015-1467

B Pedersen, Mads M., Torben J. Larsen, Helge Aa. Madsen, and Gunner Chr. Larsen (Nov. 2017). "Using wind speed from a blade-mounted flow sensor for power and load assessment on modern wind turbines". In: *Wind Energy Science* 2.2, pp. 547–567. ISSN: 2366-7451. DOI: 10.5194/wes-2-547-2017. URL: https://www.wind-energ-sci.net/2/547/2017/

C Pedersen, Mads Mølgaard, Torben Juul Larsen, Helge Aagaard Madsen, and Søren Juhl Andersen (2018a). "Free-flow wind speed from a blade-mounted flow sensor". In: *Wind Energy Science* 3.1, pp. 121–138. ISSN: 2366-7451. DOI: 10.5194/wes-3-121-2018. URL: https://www.wind-energ-sci.net/3/121/2018/

D Pedersen, Mads Mølgaard, Torben Juul Larsen, Helge Aagaard Madsen, and Gunner Christian Larsen (Apr. 2018b). "More accurate aeroelastic wind-turbine load simulations using detailed inflow information". In: *Wind Energy Science Discussions*, pp. 1–33. ISSN: 2366-7621. DOI: 10.5194/wes-2018-4. URL: https://www.wind-energ-sci-discuss.net/wes-2018-4/

Contributions

Contributions directly or indirectly related to the current work:

- Postprocessing of data from the inflow experiments conducted on the Tellus turbine at Risø (1989), the NM80 turbine at Tjæreborg (2003) and the SWT3.6-107 turbine at Høvsøre (2009)
- Investigation of the application of the rotor-plane velocity (without induction compensation) for fast power and load assessment, presented in Paper B
- Development and implementation of the Reversed-BEM induction compensation method, presented in Paper C and applied in Paper A (preliminary implementation) and Paper D
- Demonstration of the Reversed-BEM induction compensation method with focus on shear profiles in free flow, half- and full-wake situations, presented in Paper A
- Implementation of the setup used in Paper D to extract inflow characteristics from selected measurement files and generate input to HAWC2
- Demonstration of the potential of using BMFS measurements for accurate aeroelastic simulations, presented in Paper D
- Improvements related to the application, usability and efficiency of the constraint turbulence simulator used to obtain results for Paper A and D
- Implementation (one of two main contributors) of the Wind Energy Toolbox (https://gitlab.windenergy.dtu.dk/toolbox/WindEnergyToolbox) - an open source toolbox of python scripts to e.g.:
  - Facilitate tasks related to the application of HAWC2 (generate input, execute simulations, analyse output etc.)
  - Work with measurement data (read, analyse, filter, fix, etc)
  - Apply and fit parameters for different wind and turbulence models
- Development/improvement of three software tools (http://tools.windenergy.dtu.dk):
  - Pdap: A graphical application for the post processing, analysis, visualisation and presentation of data, e.g. simulation results and measurements

  - HAWC2Launcher: A graphical program to handle the execution of HAWC2 simulations, suitable for the parallel execution of multiple simulations on, e.g., clusters
  - HAWC2Visualization: A graphical 3D visualisation tool to visualise HAWC2 structural models and simulations

Other contributions:

- Postprocessing of data measured at the Nysted2 wind farm and extraction of data for Larsen et al. (2017)

Abbreviations and definitions

Angle of attack	AOA	Angle between the chord line of an airfoil and the undisturbed 2D streamlines far upstream. This angle is related to the geometric angle of an airfoil in a wind tunnel experiment
Blade element momentum	BEM	
Blade-mounted flow sensor	BMFS	
Computational fluid dynamics	CFD	
Free inflow velocity		Inflow velocity without influence of the wind turbine; i.e. the velocity that would exists at the same time and location if the turbine was not present to influence the inflow
Large Eddie Simulation	LES	
Local flow angle	LFA	Angle between the chord line of an airfoil and the streamline local to an airfoil
Relative flow velocity/speed		Velocity/speed of the flow far upstream relative to an airfoil
Relative local flow velocity/speed		Velocity/speed of the flow relative to a point local to an airfoil
Root mean square	RMS	
Rotor plane velocity		Velocity at the rotor plane, influenced by the wind turbine induction, but corrected for flow deflection and change of speed local to the airfoil; i.e. it is the relative flow velocity in a global frame of reference

Contents

CHAPTER 1

Inflow measurement

1.1 Introduction

For wind turbines, the levelised cost of energy, LCOE, is a crucial parameter for the development and expansion of wind energy. The LCOE can be reduced, e.g. by increasing the power production, minimising the materials used to build the turbine, extending the life-time or by lowering the costs for maintenance. These options are closely related to the inflow-dependent power and load performance.

Information about the inflow is therefore essential, as well as an understanding of the relation between the inflow and the power and loads. This knowledge can be used to predict the life-time energy production and life-time fatigue and extreme loads for a potential wind turbine or site, and is furthermore an important factor in the development of power-optimising and load-alleviating concepts.

The aerodynamic forces that drive a wind turbine and cause the major part of the structural loads are closely related to the flow relative to the blades. These forces depend on the angle of attack (AOA), i.e. the angle between the flow and the blades, and are proportional to the square of the relative flow speed. The relative flow velocity is, furthermore, related to the free-inflow velocity via the rotor speed, the pitch angle and the wind turbine induction; see Fig. 1.1.

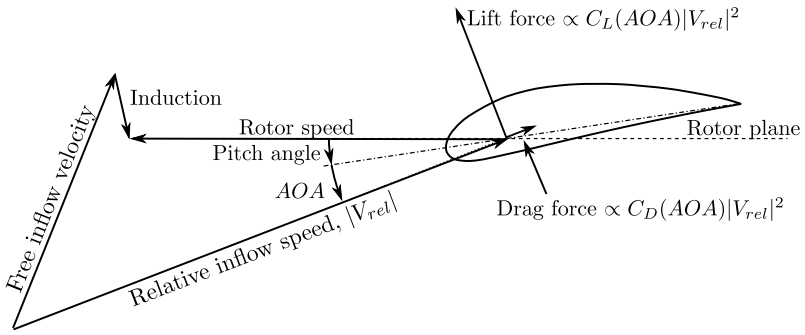

Figure 1.1: The flow relative to the blade, in terms of AOA and relative flow speed, is linked to the free inflow velocity as well as the aerodynamic lift and drag forces.

The relative flow velocity, which is very interesting in relation to wind turbine operation and control, can thereby be considered as a intermediate measure between the inflow conditions and the power and loads (see Fig. 1.2).

Consequently, the free-inflow velocity throughout the rotor, the relative velocity at the

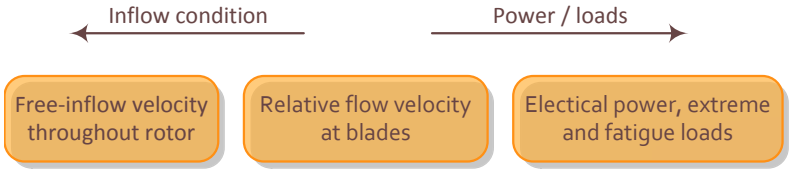

Figure 1.2: Essential measures with respect to the research, design and operation of wind turbines.

blades, and the power and loads are all crucial measures with respect to the research, design and operation of wind turbines.

1.2 Free inflow velocity

The free-inflow velocity is a very important measure because it is independent of the wind turbine, including its aerodynamic properties, control strategy and operational state, and reflects the inflow that the turbine is exposed to. The free-inflow wind speed is typically used as a reference for power and loads, as input for numerical simulations, and as a link between the turbine performance and the wind resources that enables the prediction of the life-time energy production and the life-time fatigue and extreme loads.

The free-inflow velocity is in this work defined as the flow velocity at the rotor plane that would exist at the same time and location if the turbine was not present to obstruct the inflow. The free-inflow velocity is impossible to measure exactly (see Fig. 1.3): some distance up stream, the flow (red in Fig. 1.3) is unaffected by the turbine, but different from the free inflow at the rotor (blue in Fig. 1.3) due to the spatial separation; and at the rotor plane, the flow is disturbed by the velocity induced by the rotor (black in Fig. 1.3).

The only options are thereby to measure some distance upstream (outside the induction zone) and average in time or space to cancel out the differences due to spatial distance, or to measure closer to the rotor and compensate for the presence of the turbine.

According to IEC 61400-12-2 (2013), a reasonably good estimate of the 10-minute mean free-inflow wind speed can be obtained from an anemometer on a met mast 2-4 diameters away if the terrain is flat and the anemometer is not in wake of the turbine or exposed to mast or boom effects. While suitable as a reference for power observations, Fig. 1.4 (left), the 10-minute mean met-mast wind speed is inappropriate for characterising the inflow with respect to fatigue loads; see Fig. 1.4 (right). The observations in Fig. 1.4 are measurements from the DAN-AERO database (see Section 2.1.7). The maximum fatigue load observed at 8 m/s is seen to be 2.5 times higher than the minimum load observed at the same wind speed, and predicting the life-time of a wind turbine to be between e.g. 10 and 25 years will probably not satisfy an investor. Consequently, a more detailed free-inflow estimate that characterises the temporal and spatial variations throughout the rotor is required.

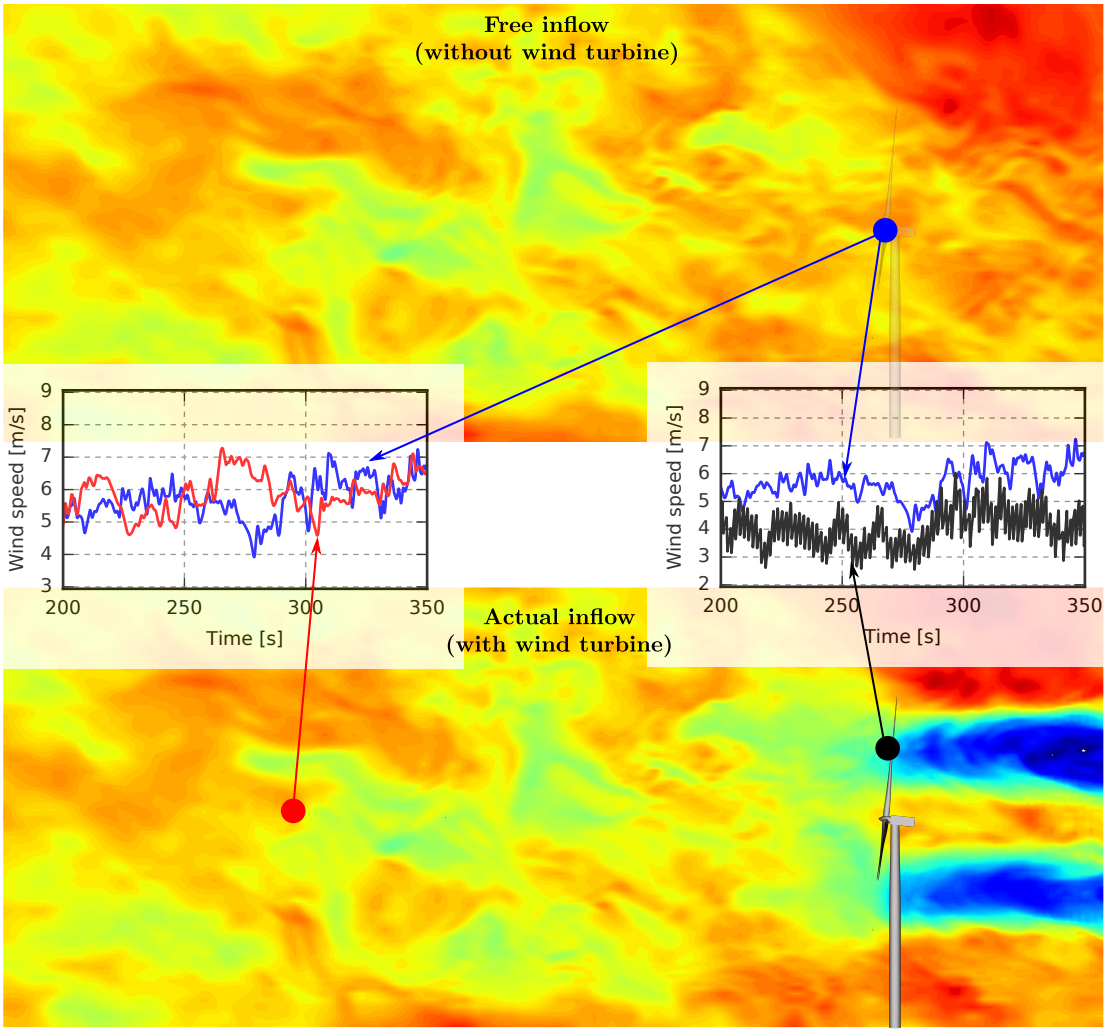

Figure 1.3: 2.5 diameters upstream, the flow (red) is different from the free inflow (blue) due to spatial distance; and at the rotor, the flow is disturbed by the turbine induction (black).

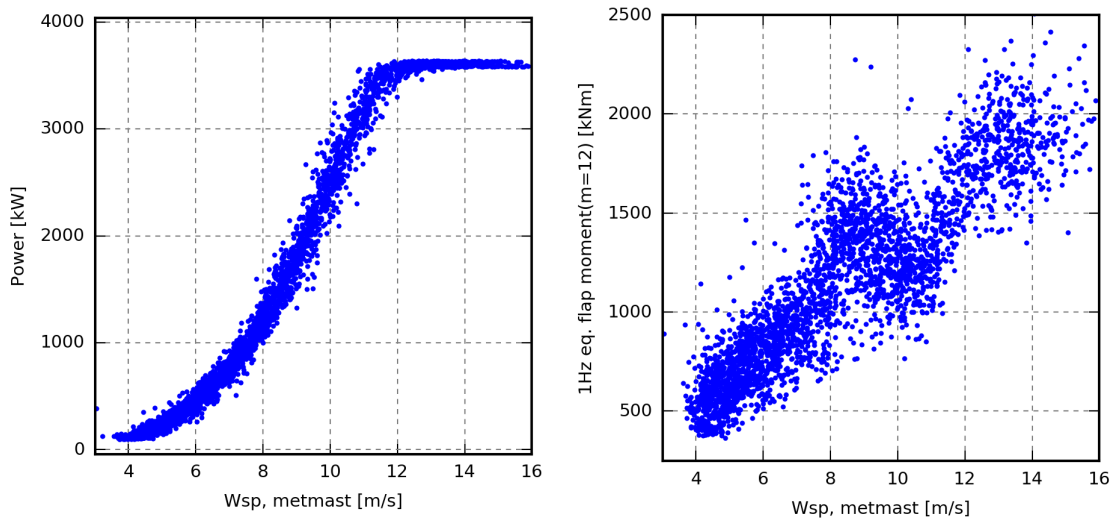

Figure 1.4: 10-minute observation of power (left) and flap-moment fatigue loads (right) plotted as a function of met-mast wind speed.

1.3 Inflow characteristics

Ideally, the instant free-inflow velocity is obtainable at all positions throughout the rotor simultaneously. This is, however, not possible using the current measurement techniques. Different models are therefore typically used to provide realistic values of the velocities that are not measured. Often, the inflow model is a combination of models describing the steady and the fluctuating conditions, and the purpose of the inflow measurements is thereby to provide input for these models. The models range from simple models, which are based on several assumptions and standard parameters and therefore only need the 10-minute horizontal wind speed statistics from a single nearby sensor, to more advanced models that provide much more detail about the inflow, but require the instant 3D inflow velocity at multiple positions throughout the rotor area.

1.3.1 Steady inflow characteristics

In the simplest case, the steady axial 10-minute-mean wind speed can be characterised by a single cup anemometer measuring the horizontal wind speed. The instant wind speed at a single fixed point is different from the instant rotor-average wind speed, but the 10-minute average represents the rotor average quite well, if the distance is not too big. In case of yaw misalignment, however, the wind direction (lateral component) should also be included, while the flow-tilt angle (vertical component) may be important in complex terrain and wake situations.

Furthermore, the mean wind speed typically varies with the height. To describe this variation, different shear-profile models exist. The logarithmic shear profile describes the long-term-average shear profile in the surface layer (approximately the lowest 100 m of the atmosphere) over flat homogeneous terrain during stationary and neutral atmospheric conditions (Counihan, 1975). This profile can be estimated from a single wind speed sensor using a parameter related to the roughness of the terrain or based on wind-speed measurements from at least two different heights. The logarithmic shear profile can be extended with a stability term to be valid in stable and unstable conditions as well. In this case, however, information about the current atmospheric stability conditions must be available.

Similarly, the power-law shear profile can be applied using a standard parameter and the wind speed measured at one height, or it can be fitted to wind speed measurements from two or more heights.

The assumptions behind the logarithmic shear profile are, however, not always satisfied; modern turbines are higher than 100 m and in some cases the terrain is not flat or changes in front of the turbine e.g. from land to sea. In such cases, a better solution may be to measure the mean wind speed at several heights, interpolate between the measurements and use the profile directly. This approach will also produce the current shear profile instead of a long-term average, but, obviously, it requires several sensors at different heights, a moving sensor or remote sensing technology.

The wind direction (lateral component) may change slightly with the height. To

characterise this variation, 2D sensors, e.g. cup-anemometers in combination with wind vanes, are required, while 3D sensors are needed to characterise variations in the flow-tilt angle (vertical component) that may occur at complex sites and in wake situations.

Finally, the mean wind speed may be horizontally inhomogeneous, e.g. in half-wake situations, where one side of the rotor is in the wake of an upstream turbine. To characterise this variation, a grid of sensors located in front of the rotor, blade-mounted sensors or remote sensing technology is required.

1.3.2 Turbulence

In the simplest case, turbulence can be characterised by a single cup-anemometer in terms of the turbulence intensity; i.e. the standard deviation of the wind speed divided by the mean wind speed.

The turbulence intensity does, however, not characterise the frequency of the turbulence energy or the relation between the longitudinal, lateral and vertical components, which is important with respect to loads. These properties can be described using e.g. the Mann turbulence model (Mann, 1998, 1994), which is recommended by IEC 61400-1 (2005) and used in this study.

The Mann model can be applied using standard parameters and the turbulence intensity, or the parameters can be fitted if long-term 3D measurements are available.

Furthermore, the instant wind speed measurement (1, 2 or 3D) can be used to constrain the turbulence, e.g. using the a constraint turbulence simulation method from Nielsen et al. (2003). In this way, stochastic turbulence field realisations can be modified to reproduce the specified wind speeds at the corresponding positions while preserving the turbulence statistics.

1.3.3 Wind speed trend

The split between steady mean wind speed and fluctuating turbulence is only appropriate in stationary conditions where the mean wind is constant. If this is not the case, a linear wind speed trend or moving average can be used to characterise the mean wind speed. The wind speed trend should be derived from the instant rotor-averaged wind speed, which, depending on the required uncertainty level, can be estimated from one or more spatial separated sensors.

1.4 Flow sensors

The inflow characteristics can be obtained using different flow sensors. Commonly used flow sensors for wind energy research applications comprise cup and sonic anemometers, lidars and five-hole pitot tubes.

Cup anemometers measure the horizontal wind speed (1D), but may be used in combination with wind vanes to include the wind direction. A cup anemometer is very

accurate and the mean wind speed can be determined within around 1 % (Kristensen, 1999). The sensor behaves as a low pass filter to the wind where the cut-off frequency, which is related to the size of the smallest turbulence structures that can be measured (typically 1-2 m), depends on the inertia of the cups (Berg et al., 2013).

A **sonic anemometer** measures the 3D flow speed as well as the temperature with high temporal and spatial resolution, typically 10-20 Hz (Mortensen, 1994; Berg et al., 2013).

Lidars measure the flow in a probe volume some distance away. They can be divided into continuous wave and pulsed lidars. Continuous wave lidars measure the flow speed at one distance while pulsed lidars measure the flow speed at multiple distances simultaneously. Both types of lidars measure the 1D average flow speed in the line-of-sight direction of the probe volume. For continuous wave lidars, the length of the probe volume increases with the distance while it is constant for pulsed lidars (Berg et al., 2013). In some setups, lidars are able to measure the flow speed in 2D under the assumption of horizontal homogeneity, while the Wind Scanner system uses three synchronised scanning lidars to measure the 3D flow velocity (Mikkelsen et al., 2008; Harris et al., 2006).

The **five-hole pitot tube** measures the flow speed as well as the angle of the flow at two perpendicular angles; i.e. it measures the 3D flow with high temporal and spatial resolution if the flow incidence angle is below 55-70° (Telionis et al., 2009; Moscardi and Johnson, 2016).

Comparing the typical spatial and temporal resolution and accuracy of these four types of sensors is inappropriate in this context, because their capabilities are highly dependent on the particular instrument, the setup, application and specific evaluation parameters.

1.5 Measurement position

Flow sensors can be mounted at different positions, e.g. at a met-mast, on the nacelle, in the spinner, at the blade or at the ground; see Fig. 1.5.

Met masts are typically placed outside the induction zone, and met-mast-based flow sensors, e.g. a cup or sonic anemometers, are thereby measuring the the free wind speed when not in the wake of the turbine or exposed to mast or boom effects. The measured wind speed is, nevertheless, different from the free-inflow at the turbine due to the spatial separation.

Nacelle-mounted flow sensors follow the yaw direction and are thereby able to measure in all wind directions. They are, however, inside the induction zone, and therefore a proper transfer function must be applied to obtain the free-inflow mean wind speed. St. Martin et al. (2017) derived the nacelle transfer function for a nacelle-mounted anemometer and found the estimated annual energy production (AEP) to match the estimate obtained using a met-mast-based anemometer within 1 %, but concluded that the transfer function depended on atmospheric stability and turbulence. Furthermore, shadow effects from the blade passing make it very challenging to estimate the free-inflow

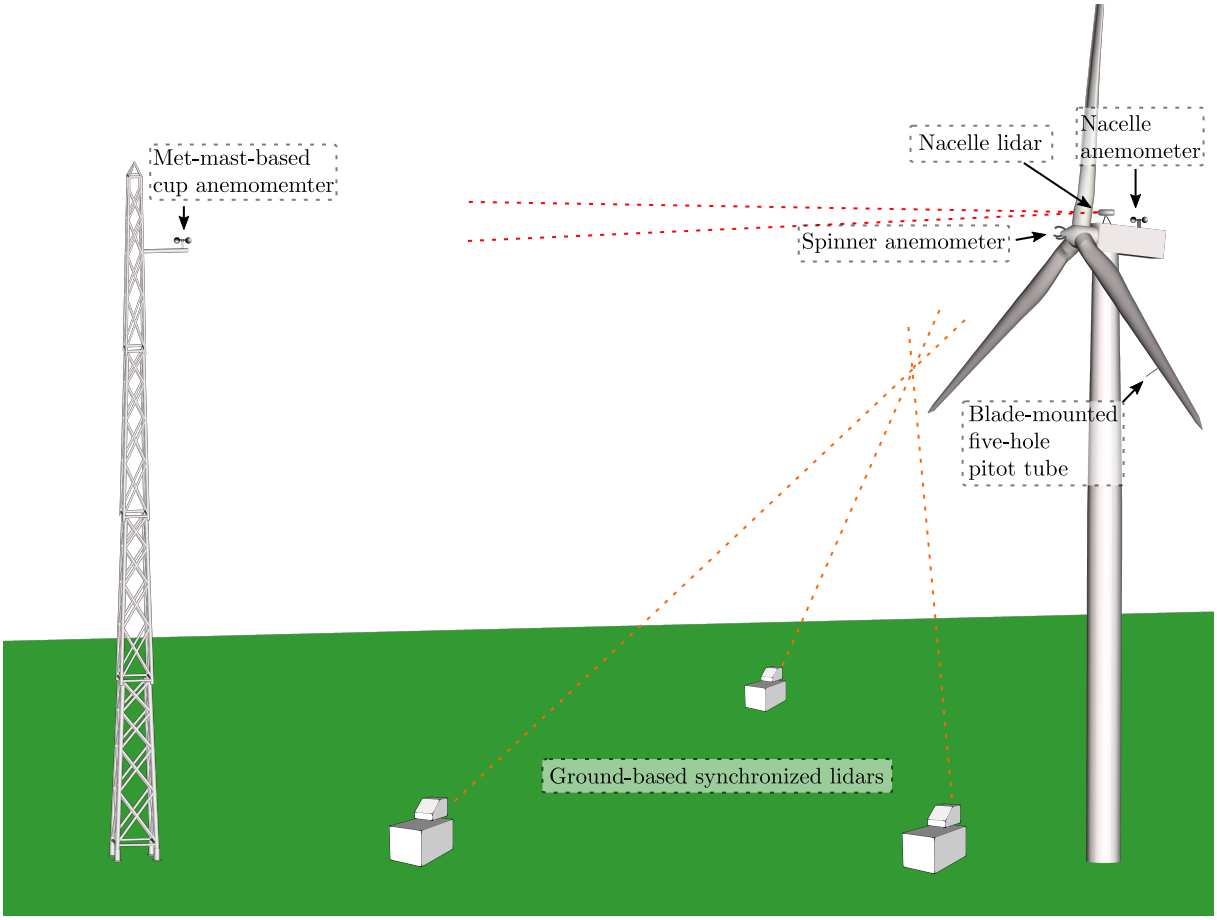

Figure 1.5: Different flow sensors and positions.

turbulence.

Spinner-mounted flow sensors are located in front of the turbine and are thereby exposed to less flow disturbance. At this position, the 3D mean flow speed as well as the turbulence intensity can be measured (Pedersen et al., 2014). Dynamic effects are, however, not considered by typical transfer functions, and consequently deviations in the high-frequency part of the instant wind speed may occur.

A **blade**-mounted flow sensor, BMFS, sweeps different parts of the rotor while it moves with the blade. It is thereby able to measure vertical and horizontal variations on its rotating path. In contrast to met-mast-, nacelle- and spinner-mounted flow sensors, a BMFS measures the local flow velocity relative to the blade (local measure of the intermediate step in Fig. 1.2); i.e. it is more related to the power and loads and less to the free-inflow velocity than the flow measured at the other positions. It is, however, possible to derive the absolute flow velocity, even though uncertainty is introduced due to static and dynamic blade deflection and torsion. The flow at the blade is obviously also influenced by the turbine inductions, but in this case, the well-established aerodynamic engineering models that are used in aeroelastic codes like Fast, Flex5, Bladed and HAWC2

can be used to compensate for the induction; see Chapter 3 and Paper C.

Finally, it should be mentioned that lidars have been mounted on the nacelle, in the spinner, at the blade and on the ground to measure the 1D, 2D or 3D flow speed, in one or multiple positions upstream, downstream, near the rotor or in front of the blade. (Mikkelsen et al., 2008; Mikkelsen et al., 2010; Medina et al., 2012; Pedersen et al., 2013; Fleming et al., 2014; Wagner et al., 2015; Simley et al., 2016; Meyer Forsting et al., 2017; Herges et al., 2017). A review of these combinations is, however, out of the scope of this work.

An overview of the information that can be extracted from inflow velocities from the different positions is given in Table 1.1.

Table 1.1: Overview of the information that can be extracted from flow velocities obtained at different positions.

	Upstream[1]	Nacelle[2]	Spinner[2]	Blade[3]
Free inflow mean wind speed	x	x	x	x
Turbulence intensity	x	-	x	x
Flow direction	x	(x)[4]	x	x
Flow inclination	x	-	x	x
Instant free-inflow velocity at the rotor	(x)[5]	-	(x)[6]	x
Vertical variations within the rotor	x[7]	-	-	x[8]
Horizontal variations within the rotor	x[9]	-	-	x[8]

[1] Assumed to be out the induction zone and in similar wake conditions

[2] With transfer function

[3] With aerodynamic model

[4] Considerable deviation may occur

[5] Different due to distance

[6] Dynamic effects not considered by typical transfer function

[7] Requires inflow information from multiple heights, e.g. using multiple sensors or remote sensing technology

[8] Depending on the radial position

[9] Requires inflow information from multiple horizontal positions, e.g. using multiple sensors or remote sensing technology

The current work focuses on BMFSs and investigates if their ability to measure the instant free-inflow veloicty at the rotor as well as vertical and horizontal variations with in the rotor make up for the shortcomings and associated uncertainties.

CHAPTER 2
Blade-mounted flow sensors

Blade-mounted flow sensors have been used in many research experiments over the last 30 years. The most frequently used BMFS instrument is the five-hole pitot tube, but other types of sensors have been considered as well, for example, lidars telescopes (see Section 2.1.9), flush-mounted pressure sensors and sonic anemometers; see Fig. 2.1. The sensor must be very robust as the environment at the blade is harsh with high flow speeds, large centrifugal force, rain, snow, ice and lightning. Furthermore, the sensor must be very sensitive to distinguish the small angle and speed variations due to variations in the inflow from the huge velocity due to rotational speed.

Figure 2.1: Different sensors that have been considered as a BMFS. Left: Aeroprobe five-hole pitot tube (www.aeroprobe.com). Centre: Kulite FAP-250 flush-mounted flow angle probe (www.kulite.com). Right: CSAT3A 3-D Sonic anemometer (www.campbellsci.com).

2.1 Field-test experiments using BMFSs

In this section, an overview of the field test experiments where blade-mounted flow sensors have been used is presented, as well as examples of what the measurements have been used for. The list is not complete, but contains the most well-documented experiments that are known to the authors.

2.1.1 The Tellus experiment, 1989

In 1989, an experiment was performed on a three-bladed 95 kW stall regulated Tellus turbine at Risø. One of the 8.2 m blades was replaced with a test blade, where the shield was removed at three 0.5 m segments to ease the measurement of the normal

and tangential force and the pitching moment (Madsen and Markkilde Petersen, 1990; Madsen, 1991a). Around 100 data files were obtained in three measurement periods. Most data files contain 10 min of measurements. A sonic anemometer was available in measurement period 1 and 2 and a cup anemometer in period 1 and 3. In addition, a five-hole Rosemount M858 pitot tube (Schmidt Paulsen, 1990) was inserted into prefabricated mounting holes at the leading edge at two radial positions (Madsen, 1991c).

The purpose of the experiment was to perform a detailed investigation of 3D flow effects, unsteady effects and rotary wing effects. This requires a high correlation between the instantaneous measured power and blade bending moments and the measured inflow conditions that can be achieved with a BMFS (Madsen, 1991a). Details about the measurement setup and the measured data were presented by Madsen (1991b).

The experiment revealed that the 30 s mean statistics of the measured power and flap-wise bending moments are much more correlated with the inflow angle measured by the pitot tube than with the met-mast wind speed measured 50 m upstream; see Figure 2.2.

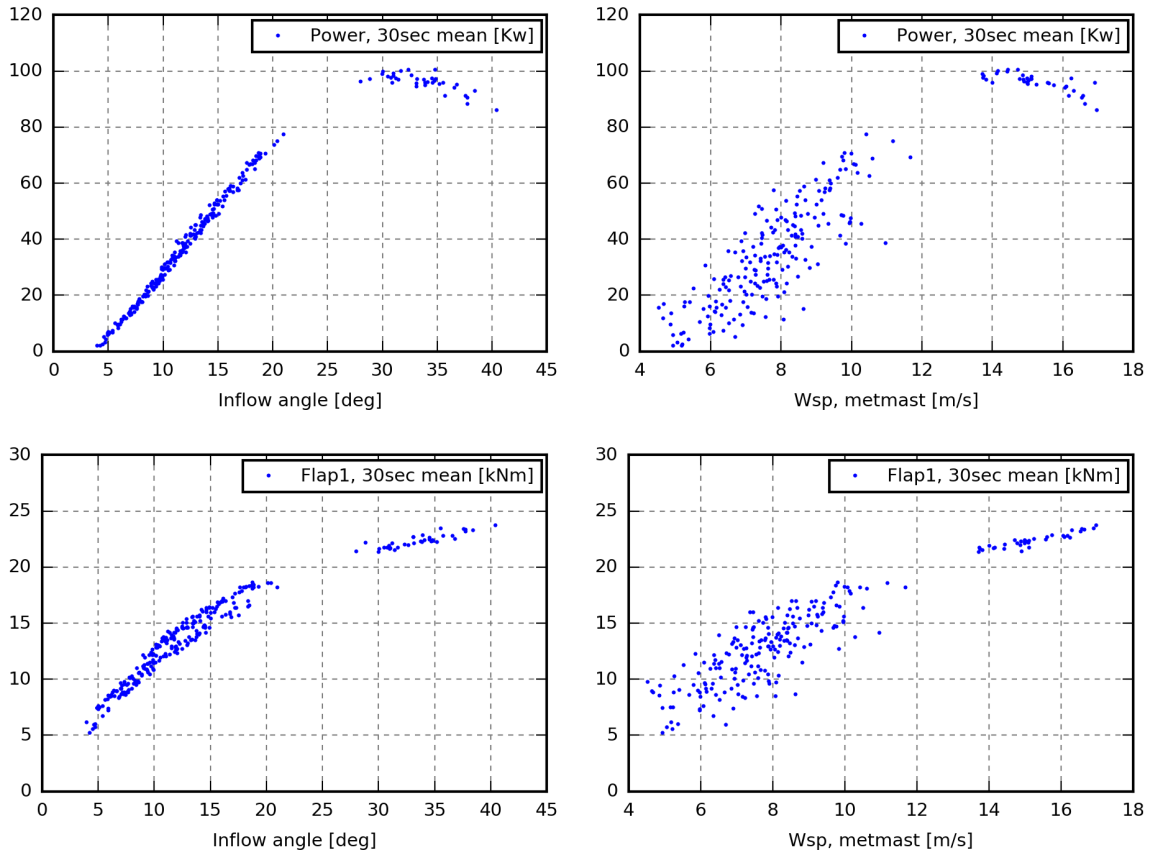

Figure 2.2: 30 s mean statistics of electrical power (top) and flap-wise bending moment (bottom) as a function of the local inflow angle (left) and met-mast wind speed (right). Data obtained from the restored Tellus database.

The data was used to compare measured and simulated turbulence with a focus on fatigue loads (Kretz et al., 1994) and investigating dynamic stall effects (Christensen and Sørensen, 1995). Later, the experiment setup was used to compare the performance of different tip shapes; see Section 4.1. In this study, the use of the pitot tube reduced the amount of data needed to obtain reliable results (Antoniou et al., 1995).
Part of this dataset was restored and used for Fig. 2.2 and as a starting point in Paper B.

2.1.2 Unsteady Aerodynamics Experiment, NREL, 1987-1996

During the Unsteady Aerodynamics Experiment, UAE, performed by the National Renewable Energy Laboratory, NREL, a three-bladed downwind horizontal-axis free-yawing turbine with a 10 m rotor was extensively instrumented and field tested for more than 10 years (Phase 1 - 5) as well as in the the 80 x 120 ft wind tunnel at NASA's Ames Research Center (Phase 6) (Simms et al., 1999; Hand et al., 2001a,b).

In Phases 2 - 6, the turbine was equipped with five-hole pitot tubes at five radial positions.

The database has been used to investigate, for example, dynamic stall and rotational effects (Laino et al., 2002; Schreck and Robinson, 2005).

2.1.3 NTK500, Risø, 1996

In 1996-1997, the Rosemount pitot tube from the Tellus experiment (see Section 2.1.1) was mounted on a 500 kW stall-regulated Nordtank turbine at Risø. Petersen and Madsen (1997) describe the setup and calibration, present the measurements and compare the results with simulations performed by the aeroelastic code HAWC (Petersen, 1996). Figs. 2.3 and 2.4 show examples of the comparison where a very close correlation was found between the spectra of the measured and simulated AOA and relative velocity.

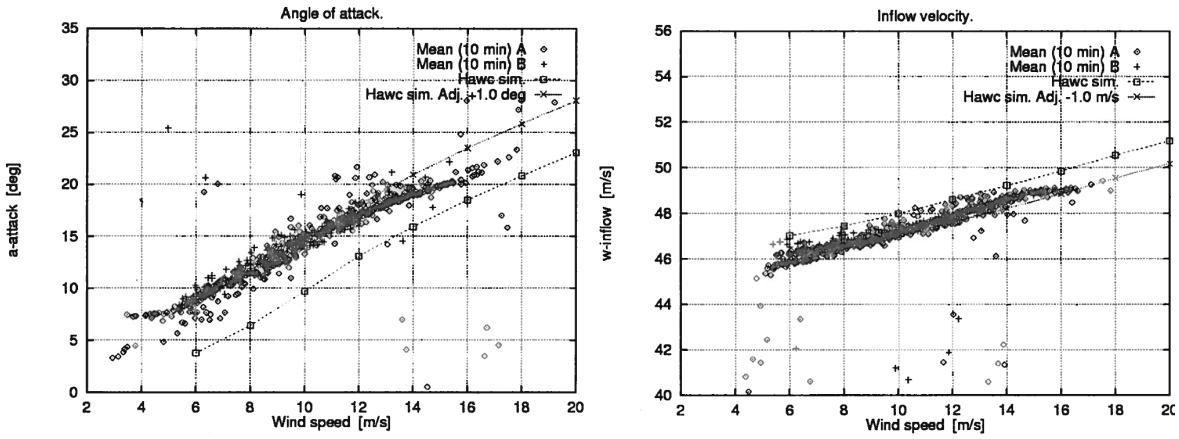

Figure 2.3: Comparison of the measured and simulated angle of attack (left) and relative velocity (right). Figures 20 and 21 from Petersen and Madsen (1997).

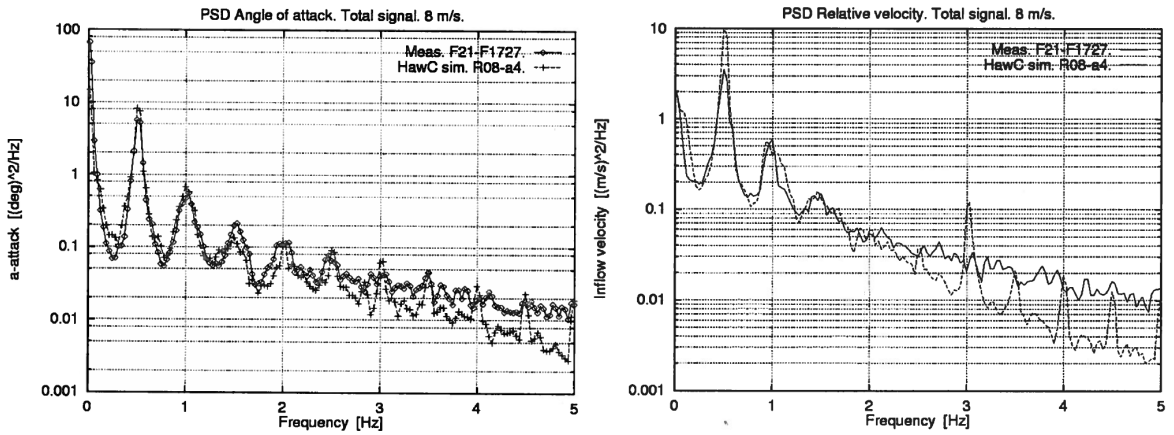

Figure 2.4: Comparison of the power spectral density of the measured and simulated angle of attack (left) and relative velocity (right). Figures 49 and 50 from Petersen and Madsen (1997).

2.1.4 IEA Tasks XIV and XVIII experiments

The IEA Tasks XIV and XVIII (Schepers et al., 1997, 2002) describe six field test experiments where the local forces, inflow velocities and flow angles are measured at several radial positions along the blades using five-hole pitot tubes, pressure tabs etc. The six experiments were carried out by:

- Delft University of Technology, DUT Netherlands
- Imperial College, IC and Rutherford Appleton Laboratory, RAL, United Kingdom
- Netherlands Energy Research Foundation, ECN, Netherlands (Brand et al., 1996)
- National Renewable Energy Laboratory, NREL, USA; see Section 2.1.2
- RISØ National Laboratory, Denmark; see Section 2.1.1
- Mie University, Japan

The outcome of the collaboration was a unique database with a huge amount of local aerodynamic measurement from six different turbines with rotor sizes from 10 to 27 m (Schepers et al., 2002).

2.1.5 NM80, Tjæreborg 2003

In 2003, the Rosemount pitot tube from the Tellus and NTK500 experiements was mounted on a 2 MW NM80 turbine at Tjæreborg wind farm. The NM80 has a 80m rotor and the pitot tube was glued/plugged onto the blade at 26.2 m corresponding to 66 % radius; see Fig. 2.5. The attachment housing of the NTK500 experiment was used, and

therefore the angle of the pitot tube was 31° even though 10-15° had been more optimal. Power and structural sensors were available from a previous experiment, but two nacelle-mounted wind vanes and anemometers were the only available met data sources. During the three-week measurement campaign, 1809 data files of 10-minutes measurements were obtained. The purpose of the experiment was to obtain detailed information about the wake flow characteristics under full scale conditions. The measured data was used for the validation of a new aeroelastic wake simulation model (Madsen et al., 2003) and later the dynamic wake meandering model (Madsen et al., 2008). Furthermore, the dataset was used to obtain statistical information about the angle of attack for a study on noise caused by transient trailing edge stall (Madsen, 2014).

This dataset has been examined during the current project and routines were set up to estimate the free velocities from the pitot-tube measurements. The idea was to use the data for Paper D because of the high quality pitot-tube and structural load measurements. The idea was, however, abandoned because no met-mast wind sensors were available.

Figure 2.5: Rosemount pitot tube mounted on the NM80 turbine at Tjæreborg in 2003. Photo by Risø National Laboratory.

2.1.6 SWT-2.1-101, Colorado, 2009

In 2009, a Siemens 2.1 MW turbine with a 101 m rotor was installed on the National Wind Technology Center (NWTC), grounds in Colorado in a collaboration between Siemens Wind Power and the National Renewable Energy Laboratory (NREL). The turbine was equipped with four five-hole pitot tubes as well as pressure tabs at nine radial positions along the blade (Medina et al., 2011). Based on measurements from the experiment, Medina et al. (2012) compare the shear profile derived from the pitot-tube measurements with the profile obtained from a met mast and a lidar, and conclude that the pitot-tube profile has acceptable accuracy; see Fig. 2.6. Furthermore, the measurements were used to investigate dynamic stall behaviour.

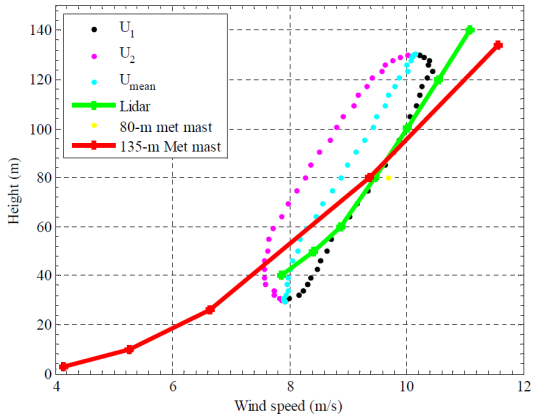

Figure 2.6: Estimation of inflow profile using the five-hole pitot tube mounted at 43 m radius. U_1 represents the measurements during the downstroke and U_2 the during upstroke. U_{mean} is the mean of U_1 and U_2. This is Fig. 12 from Medina et al. (2012).

2.1.7 SWT3.6-107, Høvsøre 2009

During the DAN-AERO project (Madsen et al., 2010), a Siemens 3.6 MW turbine at Høvsøre Test Site for Large Wind Turbines was equipped with blade-root load sensors and a five-hole pitot tube. The turbine has a 107 m rotor and the pitot tube was mounted at radius 36 m; i.e. around one third from the tip. The dataset includes wind speed and wind direction sensors from from several met masts as well as measurements of temperature, pressure, humidity etc.

During three months of operation, 9600 data files of 10-minute measurements were recorded. Most of the time the turbine was operated at variable speeds, but for a few days the turbine was operated as a stall-regulated constant-speed turbine.

Based on this dataset and an optimisation routine coupled with HAWC2 (see Section 3.3.3), Madsen and Fischer (2009) derived shear and turbulence characteristics from the pitot-tube measurements that were in agreement with the met-mast recordings.

This dataset forms the basis for Papers A, B and D. Several issues were, however, detected, e.g. a mismatch between rotor speed and rotor position, temperature-dependent load signals, periods of malfunctioning sensors, etc. Moreover, the pitot tube was found to be very sensitive to rain, as reported in Paper B.

2.1.8 NM80, Tjæreborg 2009

During the DAN-AERO project (Madsen et al., 2010), the NM80 turbine at Tjæreborg was equipped with four five-hole pitot tubes, 10 strain gauges, 4x64 pressure taps and 56 microphones. Over two months, 350 data files of 10-min measurements were obtained from the turbine as well as the nearby met mast. Troldborg et al. (2013a) present the dataset and results achieved during the project.

Fischer and Madsen (2013, 2014) investigate the load alleviation potential of trailing-edge flaps controlled by inflow data and compare numerical results with measurements from the pitot tubes in this dataset.

Furthermore, the dataset was used by Madsen (2014) to show that low frequency noise (amplitude modulation) is strongly increased for high angles of attack where transient stall is initiated.

2.1.9 Dual-Telescope lidar on NM80, Tjæreborg, 2012

In 2012, a dual-telescope lidar was tested on the NM80 turbine at Tjæreborg. The lidar was mounted in the hub and connected to telescopes mounted on both sides of the blade at radius 16.2 m; see Fig. 2.7. The telescopes were focused on a point 5 m in front of the blade. From the measurements, it was possible to determine the angle of attack and relative 2D velocity (Pedersen et al., 2013).

Figure 2.7: Lidar telescope mounted on the blade of the NM80 turbine at Tjæreborg. this is Fig. from Pedersen et al. (2013).

2.2 Optimal position of the BMFS

The optimal position and alignment of the BMFS relative to the airfoil is closely related to the local circulation compensation (see Section 3.1), which estimates the AOA and relative flow speed from the BMFS measured LFA and relative local flow speed.

In this work, the AOA and relative flow speed denote the angle and speed of the flow far upstream relative to a 2D airfoil, while the LFA and relative local flow speed reflect the angle and speed of the flow at a point, e.g. the sensor position, local to the airfoil.

Near the airfoil, the local flow field is deflected and the speed is also influenced by the bound circulation on the surface of the airfoil. The BMFS-measured LFA is therefore different from the AOA. The following results are based on velocities extracted from 2D CFD computations of an airfoil in steady uniform inflow and AOA ranging from -4 to 20°; see Section 3.1 for details about the CFD setup.

Figure 2.8 shows the relation between the AOA and the LFA (centre) and between the AOA and the normalised local flow speed (right) at the positions illustrated in Fig. 2.8 (left). It is seen that the range and linearity of the LFA and the normalised local flow speed are highly dependent on the position. This means that the optimal position depends on the measurable range and the uncertainty specification of the sensor.

Near the leading edge of the airfoil (blue point), the LFA varies from -52 to 88° with high sensitivity for LFA above 80°, and the normalised local flow speed varies from 0.35 to 1.85. A BMFS at this position should therefore be able to measure a huge range of LFAs with very high accuracy in the range from 0 to 90°. Moreover, the sensor must be able to measure 185 % of the maximum occurring relative flow speed due to the speed-up of the local flow speed at high AOA. In addition, its resolution must be high to maintain the accuracy at low AOA, where the measured local flow speed is only 35 % of the relative flow speed.

At the green point, on the other hand, the amplification of the AOA is almost linear, but very low. A sensor at this position must therefore be able to measure LFAs from -3 to 3° with very high accuracy.

Figure 2.9 shows the uncertainty of the derived wind speed in a simplified example with fixed pitch (-6°) and fixed rotational speed (50 m/s). In this example, the uncertainty of the measured LFA is set to 1 % of the required range and similarly the uncertainty of the local flow speed is set to 1 % of of the maximum occurring local flow speed.

In this case, the red position, 1/4 chord length in front of the leading edge, seems to be best. It should, however, be noted that the result is highly dependent on the uncertainty of the sensor and the dynamics of the sensor boom structure. If, for instance, the uncertainty increases with the distance from the airfoil due to deflection and the vibration of the sensor structure, a position closer to the airfoil may be better.

Figure 2.10 shows the relation between the AOA and the LFA for different positions in front of the airfoil. At the four positions, the shape of the relation is approximately similar, but the offset is very different. It is therefore important to choose an appropriate

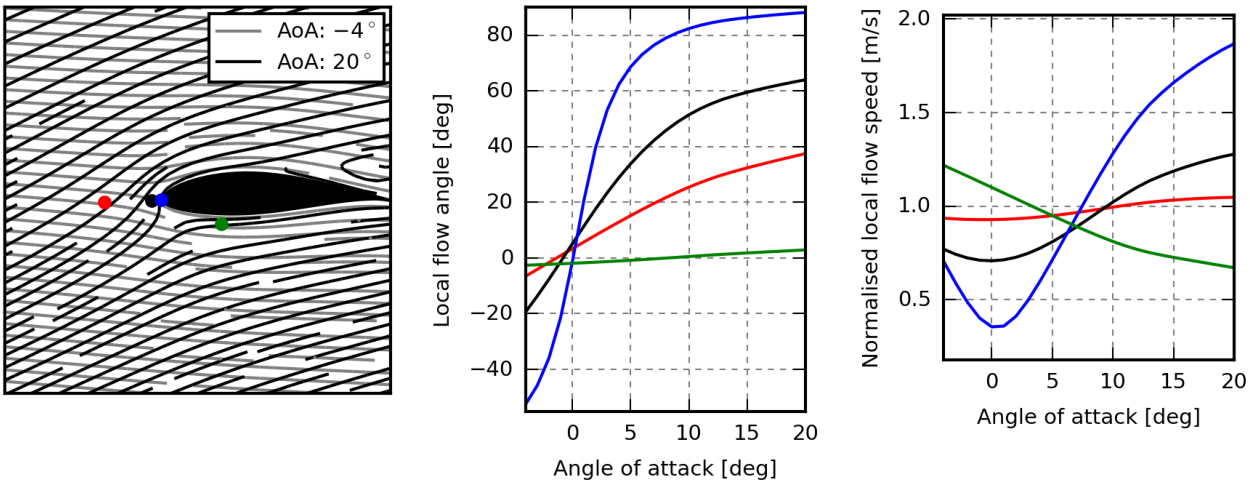

Figure 2.8: Relation between the AOA and the LFA (centre) and between the AOA and the normalised local flow speed (right) at different locations around the airfoil.

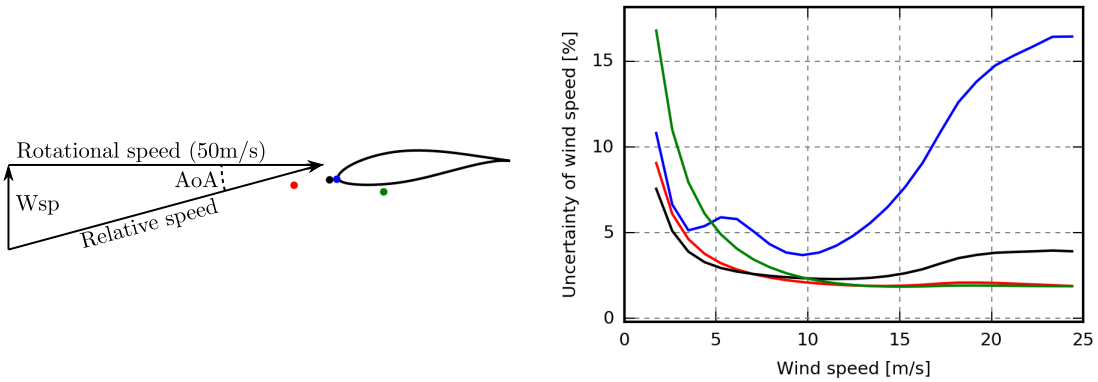

Figure 2.9: Uncertainty of the wind speed derived from the LFA and local flow speed at different sensor positions. This example is based on fixed pitch and rotational speed and the uncertainty of the measured LFA and local flow speed is set to 1 %.

position if the sensor has a limited flow-angle range and the tip cannot be bent.

The optimal radial position depends on the rotor design and the objective. Near the tip, a BMFS sweeps a large area and it is exposed to the full vertical and horizontal shear profiles. It may, however, be difficult to obtain usable information from this position due to the increased deflection and rotation of the sensor, which introduces uncertainty in the mapping from the deflected blade-section to the fixed ground coordinates, plus unknown movement of the sensor that cannot be subtracted from the measured relative velocity; see Paper C. Furthermore, higher uncertainty of the estimated free wind speed must be expected due to increased tip loss effects and additional expansion of the flow.

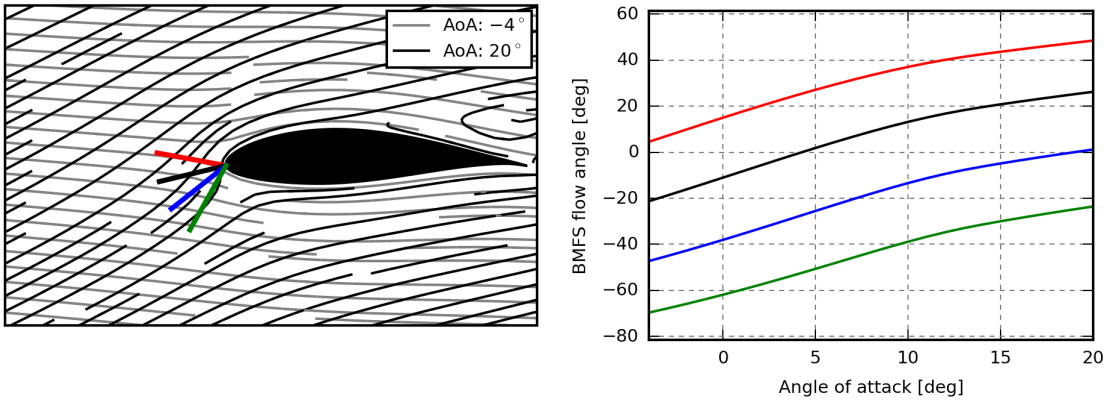

Figure 2.10: Relation between the angle of attack and the flow angle at different locations around the airfoil.

Paper B investigates the quality of the power and mean flap-load curves based on the BMFS measurements. In the analysis, 16 sets of HAWC2 (Larsen and Hansen, 2007) simulations were used to generate 16 power and flap-load curves based on the wind speed from BMFSs at different radial positions. It was found that the most similar power curves were obtained when using wind speed from a BMFS at 70 % radial position while the most similar flap-load curves were obtained when using a BMFS at 50 % radial position.

In both cases, slightly better results were obtained when using the average wind speed of sensors at 20, 50 and 80 %.

CHAPTER 3
BMFS measurement refinement

In this context, a BMFS is assumed to provide the instant 3D local flow velocity measured relative to the sensor. From this velocity, the LFA and local flow speed can be derived. For wind turbines with a fixed pitch, constant rotor speed and stiff blades, the axial wind speed can be considered as a monotonic function of the LFA when averaging over one or more revolutions, as described in Paper B. The raw BMFS measurements are thereby usable for this kind of turbine; see Section 4.1. For modern wind turbines with variable pitch and rotor speed, however, the local flow speed and pitch angle must also be taken into account. Near the airfoil, the LFA and local flow speed change due to local bound circulation, and therefore some refinement is required before measurements from a flow sensor mounted on the blade of a modern wind turbine are usable.

In the current presentation, the refinement is split into three steps; see Fig. 3.1. The first step compensates the BMFS measured LFA and local flow speed for local circulation, i.e. the flow deflection and change of speed local to the airfoil, and provides the AOA and relative flow speed that can be used to calculate the local aerodynamic forces. The second step calculates the rotor-plane velocity, by mapping the relative velocity into a global frame of reference; i.e. the velocity due to sensor movement is subtracted and the resulting flow velocity is mapped to fixed ground coordinates. The final step compensates for the induction and calculates the free inflow velocity.

The difference between the velocity measured near the blade of an operating wind turbine and the free inflow velocity that would have been present at the same time and location if the wind turbine was absent is caused by the wind turbine induction. The split between local circulation and induction is therefore tricky, because both effects are induced by the same event; namely, the interaction between the airfoils and the flow.

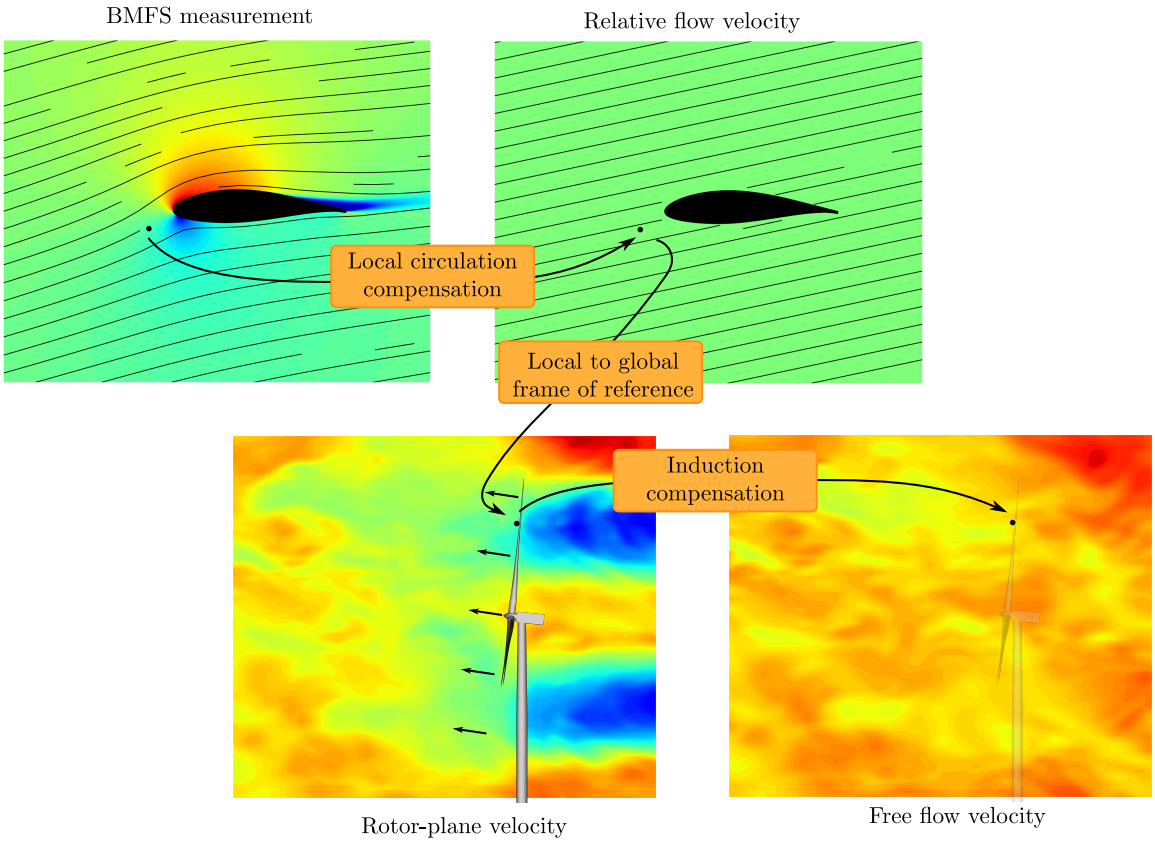

Figure 3.1: The induction compensation is split into three steps. The first step compensates the local flow velocity for the flow deflection and speed change local to the airfoil and returns the relative flow velocity. The second step maps onto a global frame of reference and provides the rotor-plane velocity. The last step estimates the free inflow velocity by compensating for the turbine induction.

3.1 Local circulation compensation

The interaction between the airfoil and the flow (see Fig. 3.2) can be modelled using full blade-resolving 3D CFD, but this is very computationally demanding. In aeroelastic codes like HAWC2, and in the Reversed-BEM induction compensation method presented in Paper C (see Section 3.3.4), the interaction is therefore not modelled directly. Instead, engineering models are used to calculate the aerodynamic forces, and the axial, tangential and radial induction. The engineering models are simple models, often derived for 1D or 2D, based on a several simplifications and assumptions of the describing flow equations, and extended with additional correction models addressing e.g. tip loss, dynamic effects and skew inflow, etc.

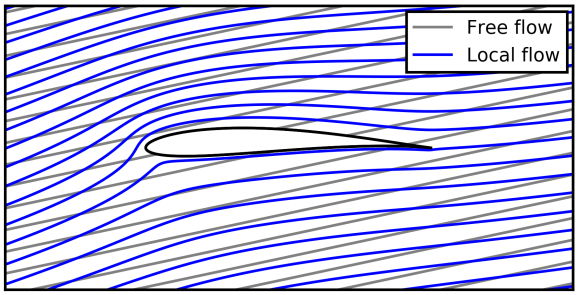

Figure 3.2: The interaction between the airfoil and the flow results in the aerodynamic forces on the blade and influences the flow. Streamlines are obtained from the potential flow around a Joukowski airfoil (Currie, 2012).

The axial and tangential induction models are typically based on blade element momentum (BEM) theory - first presented by Glauert (1935). In these models, the induced velocities are calculated from the relative flow speed and the AOA-dependent lift and drag coefficients. The required flow speed and AOA are, however, the angle and speed of the BEM flow (i.e. the sum of the free inflow and the induced velocities considered in the BEM-based induction models; see Fig. 3.3. Hence, the flow speed and AOA are different from the BMFS measured LFA and local flow speed, as the BEM models do not include deflection and change of speed local to the airfoil. Instead, the AOA corresponds to the geometrical angle of an airfoil in wind tunnel experiments or the flow angle far upstream in 2D CFD computations.

The purpose of this initial step is therefore to compensate for the deflection and speed of change local to the airfoil to obtain the BEM-flow-equivalent relative flow velocity, which can be used to calculate the aerodynamic forces and as input for the BEM-based induction models in Section 3.3.4. As mentioned above, this step is tricky because it implies that the influence of the wake (axial and tangential induction) must be distinguished from the influence of the airfoil which in fact generates the wake. In other words, the AOA is a 2D concept that is difficult to relate to the 3D flow near an operating wind turbine,

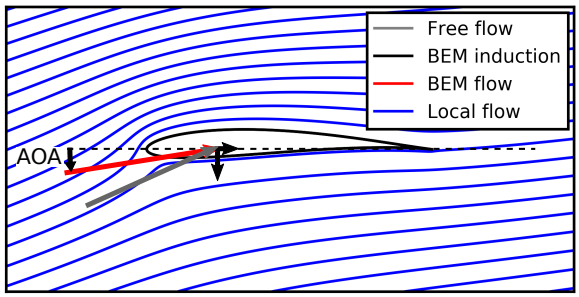

Figure 3.3: BEM-based approach. The axial and tangential induction are calculated directly from the AOA-dependent lift and drag coefficient, where the AOA is the angle of the BEM flow; i.e. the sum of the free flow and the induced velocities considered in the BEM-based induction models. Streamlines obtained from potential flow around a Joukowski airfoil, see Currie (2012).

as it is the angle of the flow that is both far upstream to disregard deflections near the airfoil and at the rotor plane to retain the induction conditions.

Shen et al. (2006) presented a method to extract the AOA based on vortex theory. In this method, the velocity induced on a control point (e.g. the position of a BMFS) by the bound vortex on the blades is subtracted from the flow at the control point. In this way, the remaining flow at the control point is influenced by the free flow and the wake vorticity only. The flow angle at the control point is thereby equivalent to the AOA; see Fig. 3.4. This method, however, requires information about the lift distribution along the blades to determine the strength of the bound vortices.

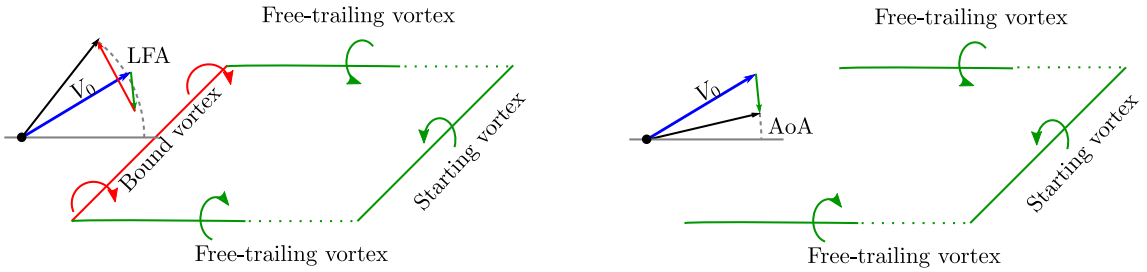

Figure 3.4: Left: Classic lifting line model. The flow at the control point is influenced by the free inflow (blue), the bound circulation (red) and the wake vorticity (green). Right: Subtracting the velocity induced by the bound circulation, results in a system where the flow at the control point is influenced by the free inflow (blue) and the wake vorticity (green) only, and the flow angle is thereby equivalent to the AOA.

Furthermore, the bound circulation is modelled using a point vortex. Hence, the control point should not be too close to the airfoil (Shen et al., 2006). This is clearly seen in Fig. 3.5, where the streamlines around the airfoil differ considerably from the streamlines of the point vortex in the regions near the airfoil.

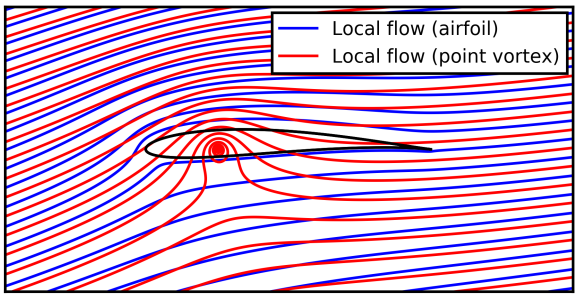

Figure 3.5: Near the airfoil, the flow around an airfoil differs considerably from the flow around a point vortex. Streamlines are obtained from potential flow around a cylinder with cirulation and a Joukowski airfoil (Currie, 2012).

Madsen and Fischer (2009) used measurements of a blade-mounted five-hole pitot tube for inflow characterisation. In the upwash-correction model they used, the influence (upwash) of the bound circulation on the blade was reduced to a linear function of the lift coefficient and the flow velocity only. The model was calibrated using full 3D CFD computations to provide the right upwash rather than ensuring the right circulation of the bound vortex. In this way, the deviation seen in Fig. 3.5 was reduced.

Another effect near the airfoil is that the local flow speed is affected. This is also the case in the flow around a point vortex, but the location of the speed-up and slow-down regions differ; see Fig. 3.6.

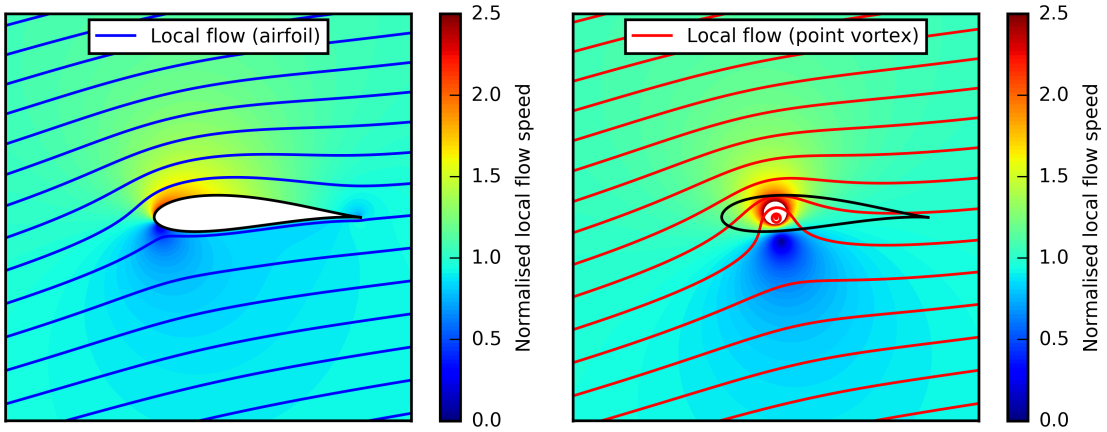

Figure 3.6: Near the airfoil the flow speed is affected and the locations of the speed-up and slow-down regions in the flow around an airfoil (left) differ from the locations in the flow around a point vortex (right). Streamlines and flow speeds are obtained from the potential flow around a cylinder with circulation and a Joukowski airfoil (Currie, 2012).

Shen et al. (2009) proposed a more advanced vortex method to obtain the AOA at a point close to the airfoil. In this method, the local distribution of circulation along the

surface contour of the blade is modelled based on the full pressure distribution on the blade, which must be known.

Guntur and Sørensen (2014) and Rahimi et al. (2018) presented several other methods to calculate the AOA, but the methods require information that cannot be obtained directly from a BMFS, e.g. the Inverse-BEM method that requires the local forces to calculate the induction; the Average Azimuthal Technique (AAT) which needs data from several up- and downstream positions; and methods that compare the pressure distribution around the airfoil with 2D distributions for known AOA.

The local circulation compensation model, which is applied in Paper A, B and D, is based on velocities around an airfoil extracted from 2D CFD simulations. The Reynolds-Averaged Navier-Stokes (RANS) simulations are performed using the flow solver, EllipSys2D/3D (Michelsen, 1992; Sørensen, 1995) for AOA ranging from -4 to 20°. Further details about the simulation setup can be found in (Troldborg et al., 2013b). The resulting velocities at the position of the BMFS are used to determine the relation between the LFA and AOA and between the relative local flow speed and relative flow speed; see Fig. 3.7. This approach is convenient because, when the relations are established, it only requires input that can be extracted from the BMFS measurements. It does, however, not take dynamic effects, or 3D effects due to tip vortices and non-constant lift distribution, into account.

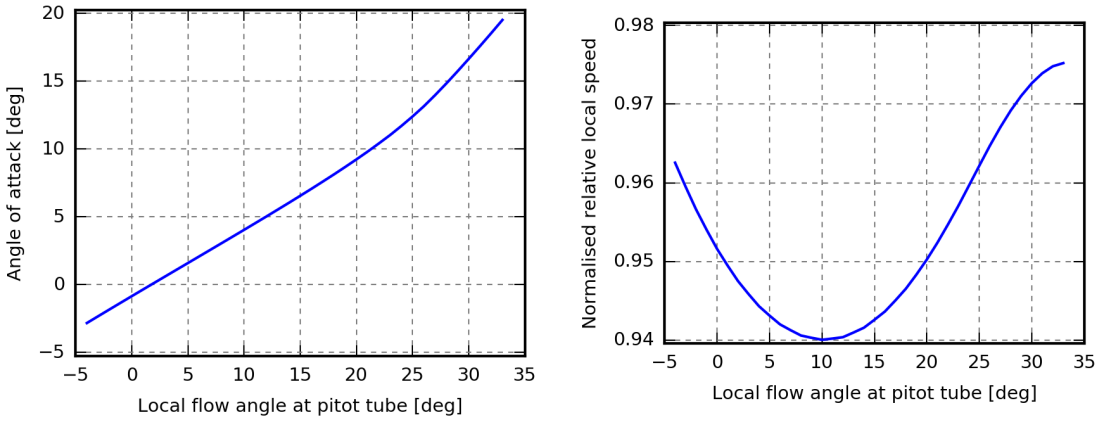

Figure 3.7: Relation between the LFA at the BMFS and the AOA (left) and between the LFA and the normalised relative local flow speed (right).

The AOA and relative flow speed can be used to obtain the rotor-plane velocity as described in the next section, or to calculate the local normal and tangential blade forces.

$$f_n = \frac{1}{2}\rho \left(C_l(AOA)\cos\phi + C_d(AOA)\sin\phi\right) c \left|V_{rel}\right|^2 \tag{3.1}$$

$$f_t = \frac{1}{2}\rho \left(C_l(AOA)\sin\phi - C_d(AOA)\cos\phi\right) c \left|V_{rel}\right|^2 \tag{3.2}$$

where f_n and f_t are the local normal and tangential forces, ρ is the air density, C_l and C_d is the local lift and drag coefficients, $|V_{rel}|$ is the relative flow speed, and ϕ is the angle between the $|V_{rel}|$ and the rotor plane; see Fig. 3.8.

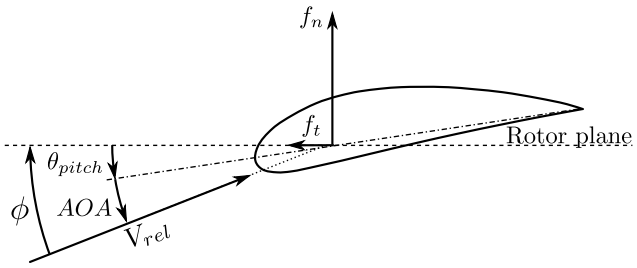

Figure 3.8: Local normal and tangential force of a blade section.

3.2 Local to global frame of reference

In this step, the relative flow velocity is mapped onto a global frame of reference by subtracting the velocity due to sensor movement and mapping the resulting absolute flow velocity to fixed global coordinates. The uncertainty introduced in this step is summarised below based on simulation and measurement results regarding the SWT3.6-107 turbine at Høvsøre (see Section 2.1.7). A detailed analysis and explanation is included in Paper C.

The current sensor-velocity-calculation implementation includes the velocity due to rotor rotation and pitch motion as briefly described in Paper B. The speed due to rotor rotation is absolutely dominant, with tangential speeds up to 53 m/s at the position of the BMFS while the speed (mainly axial) due to pitch motion is less than 0.2 m/s.

The calculated sensor velocity does, however, not include velocity due to the dynamic deflection and rotation of the structure and is therefore different from the real sensor velocity. The simulation example in Fig. 3.9 compares the 'real' sensor velocity simulated by HAWC2 with the estimated sensor velocity and gives an indication of the deviation. It is seen that the instant discrepancy in the axial direction may be more than 1 m/s. Averaging over a few seconds, however, reduces the deviation considerably.

The calculated sensor velocity is obtained in the rotor coordinate system while the flow velocity is measured relative to the sensor orientation and is assumed to be provided in the blade section coordinate system; see Fig. 3.10.

The flow velocity must therefore be mapped into rotor coordinates (Step 2a) using rotation for the orientation of the blade section, the instant pitch angle and the blade-cone angle, before the sensor velocity can be subtracted in Step 2b. Finally, the resulting absolute flow is mapped to fixed ground coordinates (Step 2c) using rotation from the rotor position, tilt and yaw angle.

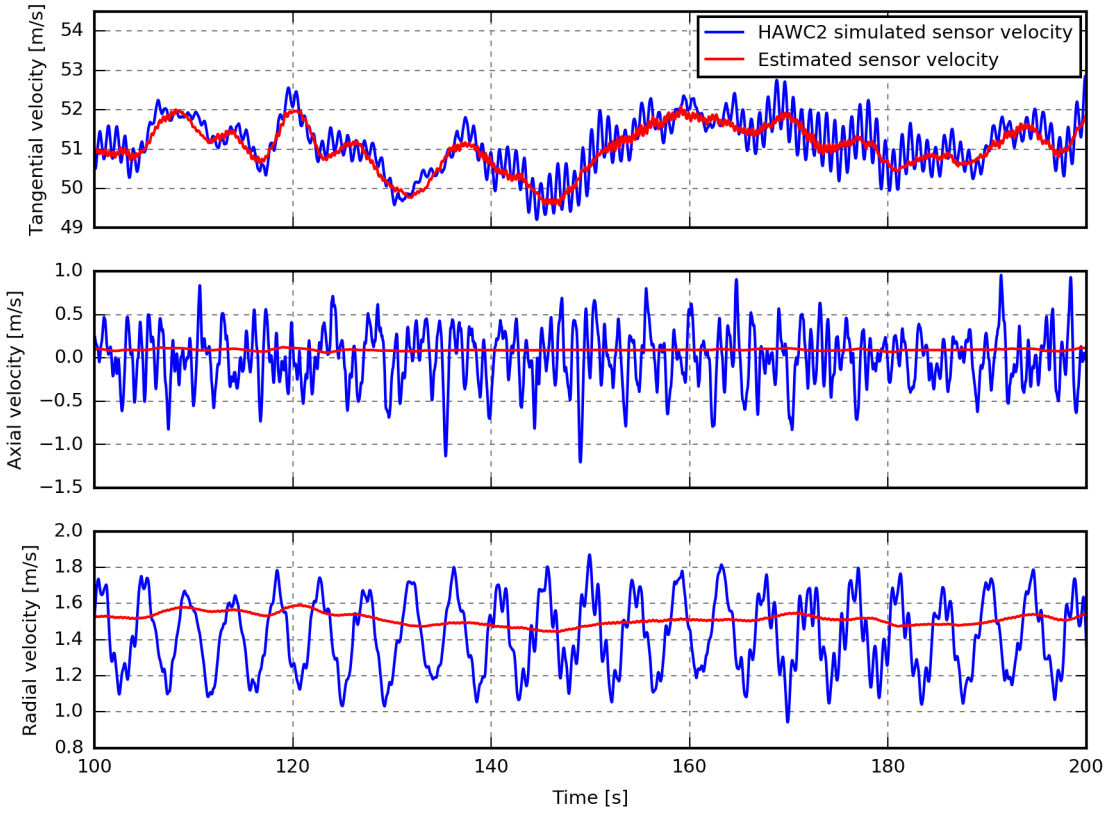

Figure 3.9: HAWC2 simulated and estimated sensor velocity at 11 m/s.

In the HAWC2-based verification part of Paper C, the deviation of the estimated free inflow velocity is investigated. It is concluded that the current step introduces more uncertainty than the succeeding induction compensation.

The root-mean-square (RMS) errors seen in Fig. 3.11 are obtained from the simulation with a flexible structure and turbulent inflow used for Case 5 in Paper C. In Fig. 3.11, however, the RMS-errors reflect the uncertainties of the rotor-plane velocity in contrast to the RMS-errors of the estimated free-inflow velocity that are presented in Paper C.

From the HAWC2 simulation, the AOA, side-slip angle and relative flow speed of the BMFS are obtained and used to derive the relative velocity in the blade-section coordinates. This velocity is, as expected, almost equal to the HAWC2 reference, and the RMS-errors in Fig. 3.11 (A) are therefore very close to zero.

In Step 2a, the relative velocity is mapped to the rotor coordinate system. The uncertainties introduced due to unknown orientation of the blade section are seen in Fig. 3.11 (B). Due to torsion of the blade section, the tangential sensor speed, which is typically 3 - 6 times larger than the absolute flow speed, unintentionally contributes to the axial wind speed estimation that, furthermore, is influenced by flap-wise deflection. These effects result in the error of the axial (y) component in Fig. 3.11 (B).

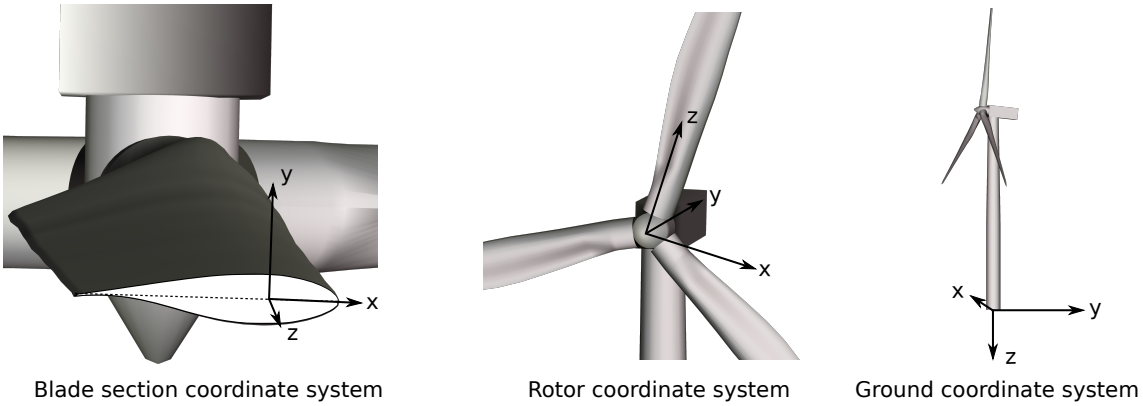

Figure 3.10: Overview of coordinate systems.

The error in the radial (z) component, see Fig. 3.11 (B), is introduced by the axial wind speed due to flap-wise blade deflection and by the rotational speed due to the torque- and gravity-induced edge-wise rotation of the blade section.

In Step 2b, the sensor velocity is subtracted. This step increases the error of the tangential (x) and axial (y) components, see Fig. 3.11 (C) as the assumed sensor velocity is different from the 'real' velocity: the 'real' velocity varies in the tangential direction due to the gravity-induced edge-wise deflection of the blade and in the axial direction due to turbulence-induced dynamic flap-wise deflections while the assumed sensor velocity does not include these effects. The error in the radial (z) component, on the other hand, is reduced, as the tangential-speed variations partly counterbalance the mapping-error due to the edge-wise deflection of the blade section.

Finally, Step 2c, maps the absolute velocity from rotor to ground coordinates. In this step, an offset may be introduced in the final vertical (z) wind-speed component due to tower deflection. At 7 m/s, however, this offset is very small and the RMS error is therefore similar, but redistributed due to the coordinate transformation; see Fig. 3.11 (D).

At high wind speeds, the deviation due to tower-deflection is more distinct. It can, however, be compensated for by including the tower-top deflection angle measured by e.g. an inclinometer. Similarly, the blade deflection and torsion angles can be included in the coordinate transformation. These angles are, however, more challenging to measure due to the high speed of the blade section and the resulting large centrifugal force. Another possibility is to use a model, e.g. HAWC2, to estimate the average deflection and rotation angles. This idea has, however, not been tested.

3.3 Induction compensation

In this section, three different induction compensation methods are presented before the Reversed-BEM compensation method, which is used in this study, is introduced in

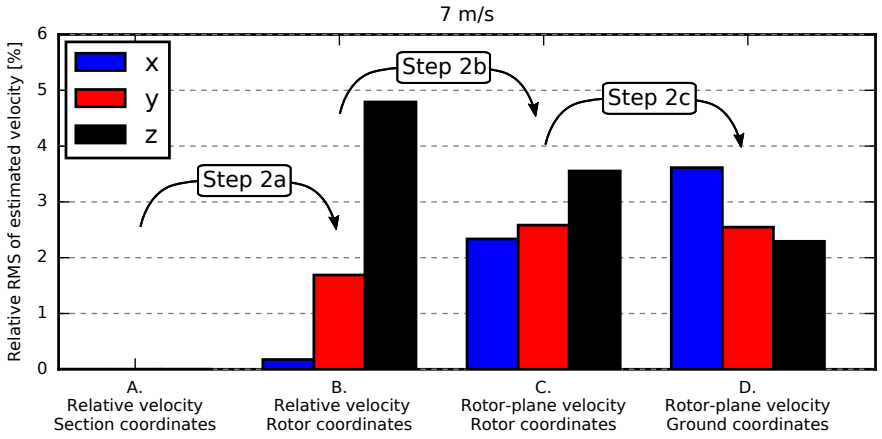

Figure 3.11: RMS error introduced in this step.

Section 3.3.4.

3.3.1 Turbine-independent compensation

The average upstream induction can in the simplest approach be calculated from an analytical model that only depends on the free flow velocity, the thrust coefficient, and the radial and axial upstream position. This model can be applied to lidar measurements to estimate the free wind speed suitable for power curves, for any rotor down to one rotor radius upstream (Troldborg et al., 2017). The method is e.g. used by Borraccino et al. (2016) to compensate nacelle-lidar measurements for the effects of the induction. Closer to the turbine, however, more information about the rotor is required.

3.3.2 Average free-to-BMFS wind speed compensation

Medina et al. (2012) used an aeroelastic code to obtain the relation between the free-inflow wind speed and the flow speed at the pitot-tube tip; see an example of this relation generated by the authors using HAWC2 in Fig. 3.12.

This approach can be used to estimate the average free wind speed in the axial direction as long as the turbine is operated under similar conditions. The method will, however, be subject to some of the issues that were revealed in Paper B: small uncertainties in the BMFS measurement are amplified due to the high slope of the relation curve around 5 m/s, and different inflow conditions or change of control strategy will change the relation and thereby introduce inaccuracy.

Finally, only the low frequency part of the estimated free wind speed will be correct, as the high frequency part is less affected by the induction. Figure 3.13 shows an example where we have applied the method to the instant wind speed of a HAWC2 simulation. The low-frequency part of the estimated free wind speeds is very similar to the free wind speed, while deviations are seen in the high-frequency part.

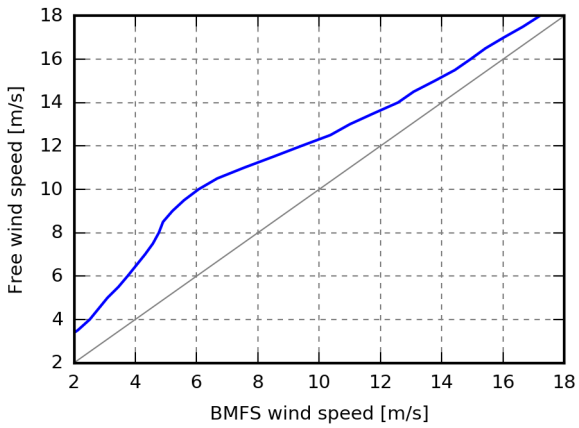

Figure 3.12: Relation between the average free wind speed and the simulated BMFS wind speed. This example is based on 10-min mean values simulated by HAWC2.

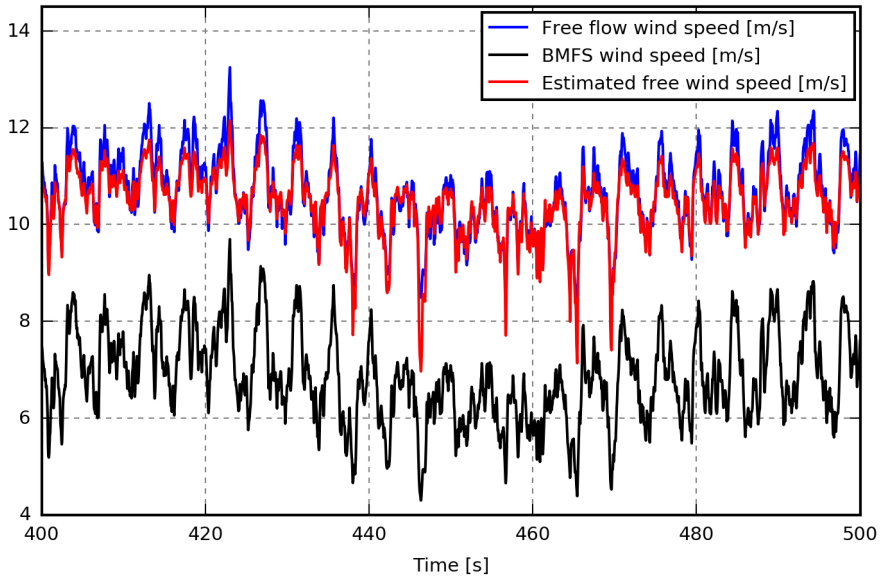

Figure 3.13: HAWC2 example where the average free-to-BMFS wind-speed relation (see Fig. 3.12) is used to compensate the BMFS wind speed for induction.

3.3.3 HAWC2-based compensation

Madsen and Fischer (2009) used measurements from the five-hole pitot-tube mounted on the SWT3.6-107 turbine at Høvsøre in 2009 (see Section 2.1.7) to obtain the free flow mean wind speed, the vertical U and V shear profiles and the turbulence level at different heights. To compensate for the induction, they used an optimisation routine coupled with HAWC2; see Fig. 3.14.

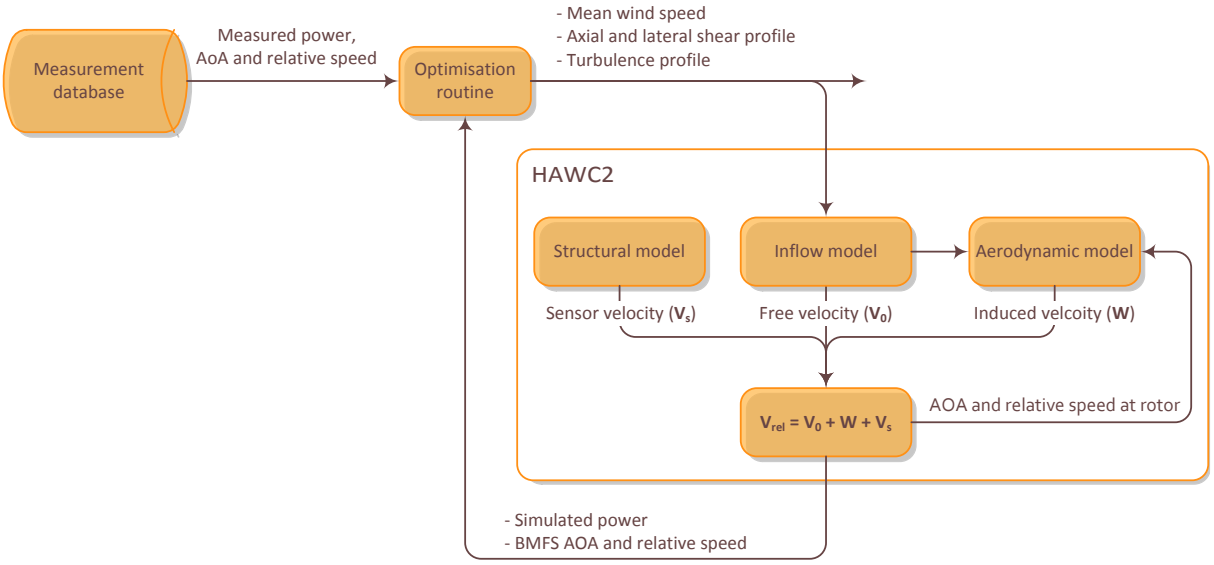

Figure 3.14: Induction compensation procedure used by Madsen and Fischer (2009).

First, the optimisation routine varied the mean wind speed until the HAWC2-simulated power level matched the measured power. Then the wind speed was varied at several different heights to find the shear profile. The result was evaluated by comparing the measured and simulated azimuthally binned AOA, which is affected by the axial wind speed profile; see an example of how the AOA is affected by shear in Fig. 3.15 (left).

In the next step, the side-wind profile caused by yaw misalignment and veer was varied and evaluated by comparing the measured and simulated mean relative velocity when the blade was in the top or bottom position; see examples of the mean relative velocity for 0, 10 and 20° of yaw misalignment in Fig. 3.15 (middle). Finally, the turbulence level was changed at different heights until the standard deviation of the azimuthally binned AOA coincided with the measurements; see an example of how the standard deviation of the azimuthally binned AOA is affected by turbulence in Fig. 3.15 (right).

The method was verified using measurements from 10-minutes periods and the obtained inflow characteristics were found to agree with observations from the met masts; see Fig. 3.16.

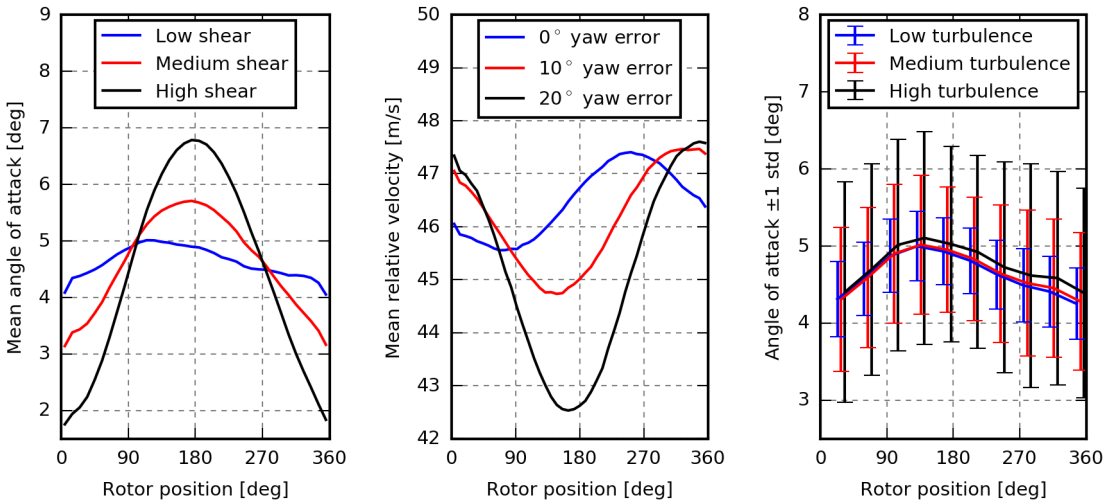

Figure 3.15: HAWC2 results showing the angle-of-attack variation due to shear (left), the mean relative velocity variation due to yaw misalignment (centre) and the variation of the standard deviation of the angle of attack due to turbulence (right).

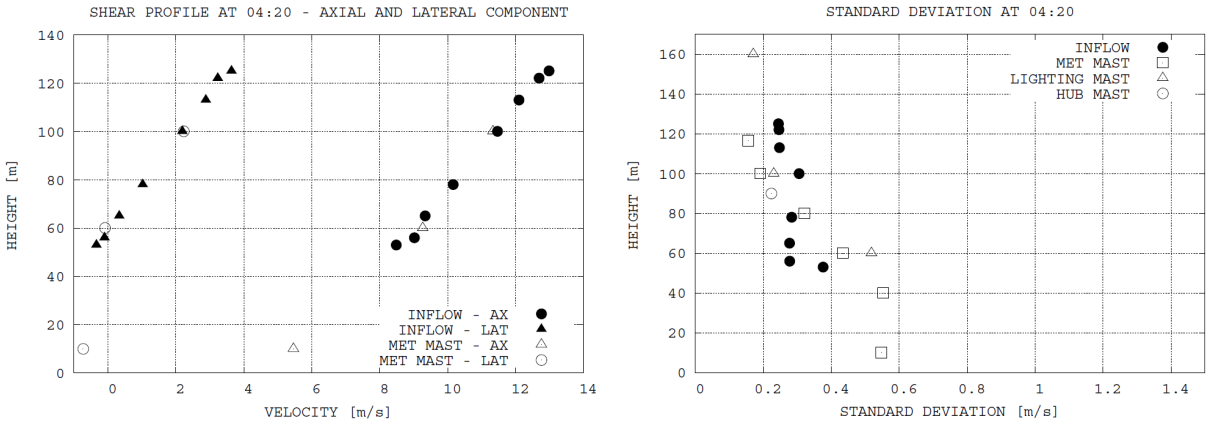

Figure 3.16: The axial and lateral shear profile (left) and turbulence level profile (right) obtained using the method of Madsen and Fischer (2009) are very similar to the met mast observations. This is Figs. 14 and 19 from Madsen and Fischer (2009).

3.3.4 Reversed-BEM induction compensation

The Reversed-BEM induction-compensation method, developed and implemented within this project, is presented briefly in Paper A and thoroughly in Paper C. The method was used to obtain the results presented in Paper D, while a preliminary implementation was used for the results in Paper A.

The aerodynamic models used to calculate the induction are similar to the aerodynamic models in HAWC2. The method differs, however, from the HAWC2-based compensation method (Section 3.3.3) as the models are integrated in the method which is thereby independent of HAWC2. Furthermore, the trial-and-error steps are partly bypassed by reversing the process, such that the induced velocity and sensor velocity are subtracted from the BMFS measured relative velocity to obtain the free inflow velocity; see Fig. 3.17. Another advantage of the current method is that it estimates the instantaneous free inflow velocity, whereas the inflow characteristics obtained from the HAWC2-based compensation method (Section 3.3.3) are averaged over several rotor revolutions.

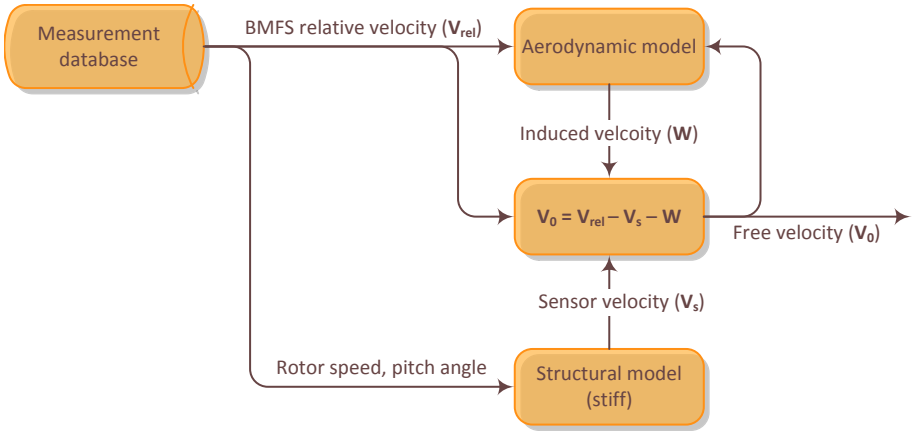

Figure 3.17: Induction compensation procedure used in the current study.

The aerodynamic models comprise BEM-based models for axial and tangential induction, a radial induction model and tip loss correction, as well as models for skew and dynamic inflow. Some of these models require information that cannot be obtained from a BMFS, e.g. the rotor-average instant thrust coefficient and axial induction. An advantage of the HAWC2-based compensation method (Section 3.3.3) is therefore that the inflow model provides realistic information about the inflow throughout the rotor. This means that the required rotor-average quantities can be extracted, and, furthermore, deflections and torsion can be predicted.

In the current method, the relative velocity, induced velocity and estimated free inflow are only obtainable at the position of the BMFS. The revolution-averaged local thrust coefficient and axial induction are therefore used as approximations of the rotor-average instant quantities, and deflection and rotation of the blade are disregarded, as described in Section 3.2.

The axial and tangential induction models as well as the skew inflow model require the free inflow wind speed, i.e. the final output of the method, as input. A trial-and-error loop is therefore still present in the current method (see Fig. 3.17). It is, however, reduced to a rather fast Newton-Raphson-based iterative approach.

In Paper C, the two latter refinement steps, i.e. local to global frame of reference and induction compensation (see Fig. 3.1), are tested using HAWC2 simulations and simulations performed by the structural model of Flex5 (Øye, 1996) coupled with the large eddy simulation (LES) flow solver, EllipSys3D (Michelsen, 1992; Sørensen, 1995).

Figure 3.18 shows the RMS error of the estimated free inflow velocity at 7 m/s; see Paper C for details about the simulation setup, and note that the SWT3.6-107 turbine model is used for the HAWC2 simulations while the EllipSys3D/Flex5 simulations are performed using the smaller SWT2.3-93 turbine model. Furthermore, step number two (local to global frame of reference) is only partly tested using the EllipSys3D/Flex5 simulations, as the BMFS velocities are extracted in undeflected coordinates; i.e. the uncertainty introduced in step two only comprises deviation of the assumed sensor velocity.

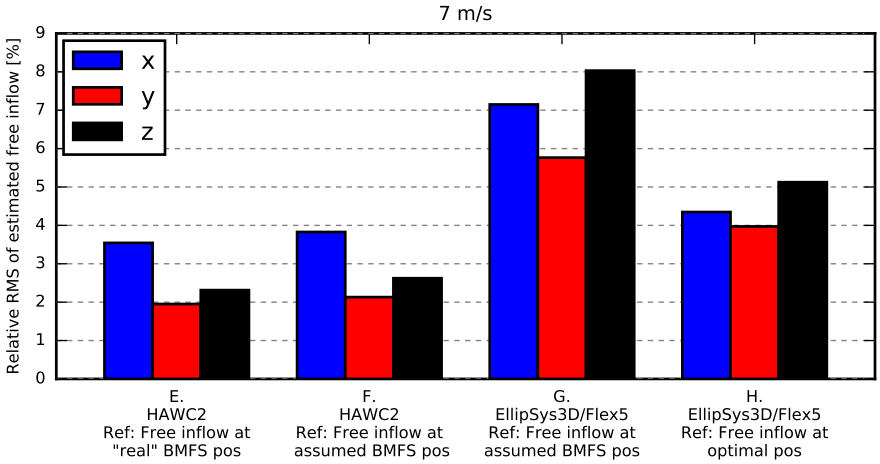

Figure 3.18: RMS error of the estimate free inflow velocity in ground coordinates (see orientation of the coordinates in Fig. 3.10).

The RMS error of the estimated free inflow velocities obtained from the HAWC2 simulation (E in Fig. 3.18) is similar to the RMS error of the estimated rotor-plane velocity without induction compensation in Fig. 3.11 (D). It is therefore concluded that only minor uncertainties are introduced by the Reversed-BEM induction-compensation method.

The error in Fig. 3.18 (E) reflects the deviation between the estimated and the 'real' free inflow at the same position; i.e. the 'real' position of the sensor (black dot in Fig. 3.19). This position is, however, different from the assumed (undeflected) position (blue dot in Fig. 3.19). For some applications, the position is irrelevant, while for others,

e.g. the constraint turbulence simulation applied in Papers A and D, the velocity and position are equally important. In such cases, the RMS errors in Fig. 3.18 (F) are more appropriate as they reflect the deviation between the estimated free inflow obtained at the deflected (black) position and the free inflow at the assumed (blue) position. The difference is, however, very limited in this case.

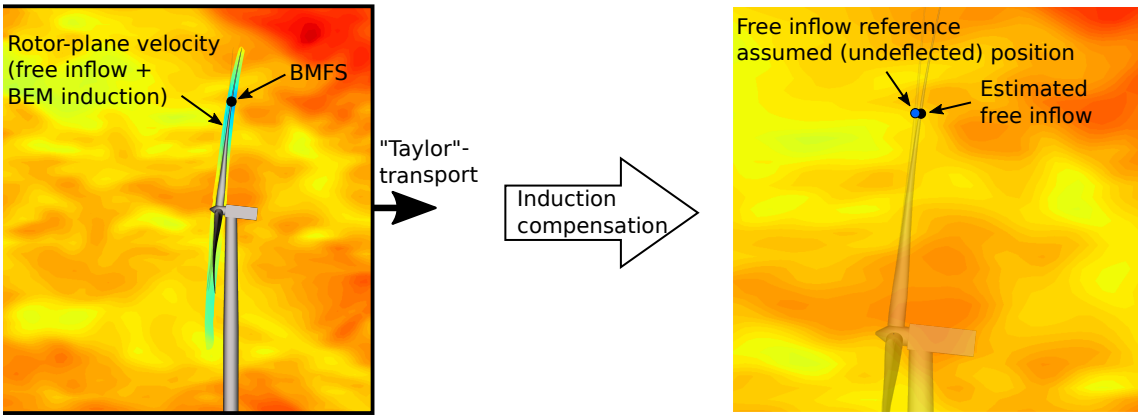

Figure 3.19: HAWC2 case: the induction-compensated BMFS inflow velocity is compared to the free flow velocity of the undeflected position. The free inflow reference velocity is independent of turbine operation as the turbulence is transported with the mean wind in agreement with Taylor's frozen turbulence hypothesis.

Several effects of real flow are, however, disregarded in HAWC2 due to the application of Taylor's frozen turbulence hypothesis, e.g. the evolvement of the turbulence as well as the expansion and delay of the flow when approaching the rotor. These effects are modelled in the EllipSys3D/Flex5 simulations where they alter the flow such that an air parcel that hits the BMFS of an operating turbine at a certain time, see Fig. 3.20 (left), would be somewhere else if the turbine was absent. The black dot in Fig. 3.20 (right) indicates the position of the parcel if it flows with the mean wind, while the grey dots show some possible positions of the parcel if it moves with the instant local wind.

This means that deviation must be expected (even if the induction compensation was absolutely perfect), because comparing the estimated free inflow velocity to the free inflow velocity without the turbine[1] corresponds to comparing the free flow turbulence at two different positions, in this case the velocity at the blue and black/grey dots in Fig. 3.20 (right). It is therefore expected that the RMS error of the EllipSys3D/Flex5 simulations (G in Fig. 3.18) will be higher than the HAWC2 cases.

In Fig. 3.18 (H), the estimated free inflow velocity is compared to the free inflow velocity that hits the rotor-plane 2.2 s before and 4.2 m closer to the rotor centre, corresponding to the black dot in Fig. 3.18 (right). In this case, the RMS errors are significantly lower,

[1]In practice, a separate simulation is performed where the effects of the aerodynamic forces on the flow are disabled

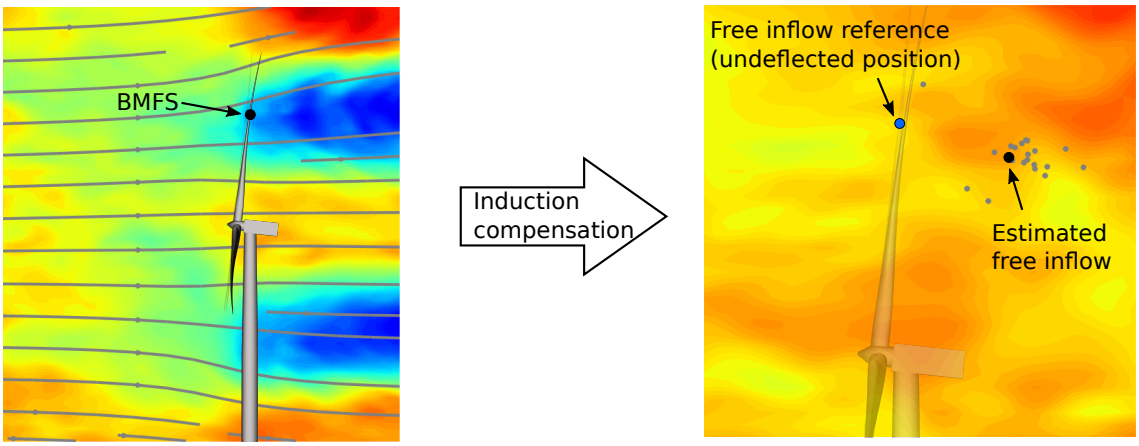

Figure 3.20: Ellipsys3D/Flex5 case: when the turbine is operating, the flow is delayed and deflected. To test the current method, the induction-compensated BMFS inflow velocity is compared to the free inflow velocity obtained at the same time and location in an equivalent simulation without the turbine. In this simulation, however, the air parcel that hits the BMFS in the simulation with the turbine is at the point of the black dots (right) if it flows with the mean wind, while the grey dots show the possible positions if it moves with the instant local wind.

and Paper C concludes therefore that the relatively high RMS errors of Fig. 3.18 (G) are more related to the difference between the turbulence at the sensor position and the reference position than to deviations introduced in the induction-compensation method itself.

It should be noted that the estimated free-inflow velocity is the induction-compensated velocity of the air parcel that hits the blade. If the turbine was absent, this parcel would be somewhere else (at the black/grey dots), and another parcel would have hit the position of the sensor. Which of the velocities that are more interesting depends on the application. In Papers A and D, for instance, the instant estimated free-inflow velocities are used as input for a constraint turbulence simulator that modifies existing turbulence fields to reproduce the specified wind speeds at the corresponding positions while preserving the statistics of the turbulence. The generated turbulence fields are used as input for aeroelastic simulations. For this purpose, the induction-compensated velocity of the flow that hits the sensor is more appropriate as the delay and expansion of the turbulence is not modelled in the succeeding aeroelastic simulation.

The actual uncertainty of the estimated free inflow velocity is highly dependent on the application as some of the uncertainty, e.g. the uncertainty related to sensor velocity and different turbulence at the BMFS and reference position, will cancel out when averaging in time (or space). Figure 3.21 shows the wind speed profiles obtained from 200 s of HAWC2 (left) and EllipSys3D/Flex5 (right) simulations. The x, y and z components refer to the ground coordinate system; see Fig. 3.10. The mean wind speed and shear profiles are seen to be well captured in the longitudinal (y) direction while small deviations

are seen in the lateral (x) and vertical (z) components. In the lateral (x) and vertical (z) components of the EllipSys3D/Flex5 rotor-plane velocity profiles, the effect of flow expansion is clearly seen, but the effects are relatively well compensated for by the radial induction model.

Similarly, Fig. 3.22 shows the standard deviation of the wind speed. Also, in this case, only small deviations are seen.

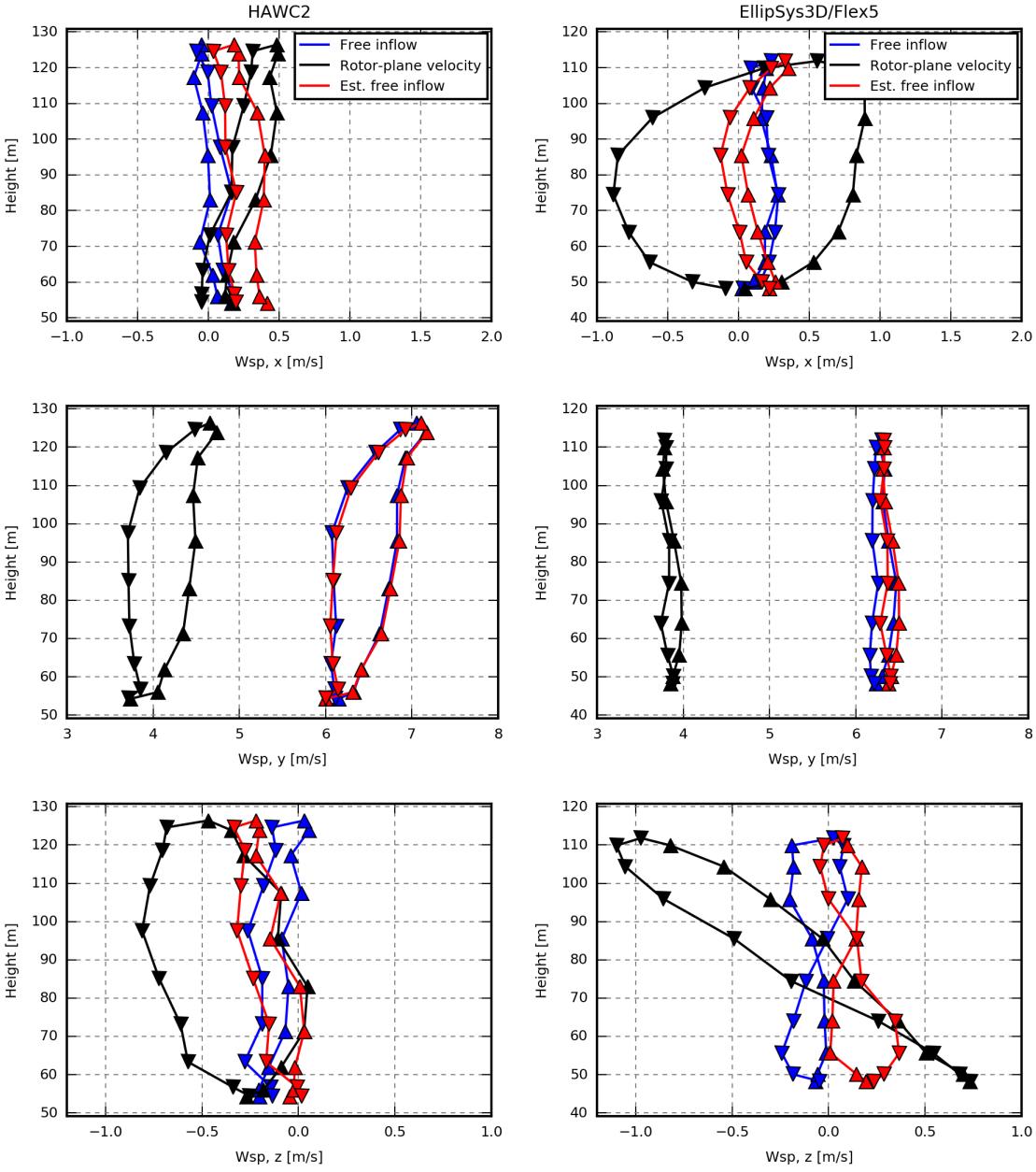

Figure 3.21: Mean wind speed and wind speed profiles obtained from 200 s of HAWC2 (left) and EllipSys3D/Flex5 (right) simulations. The markers indicate the up- and downstroke, and the x, y, and z components refer to the ground coordinate system; see Fig. 3.10.

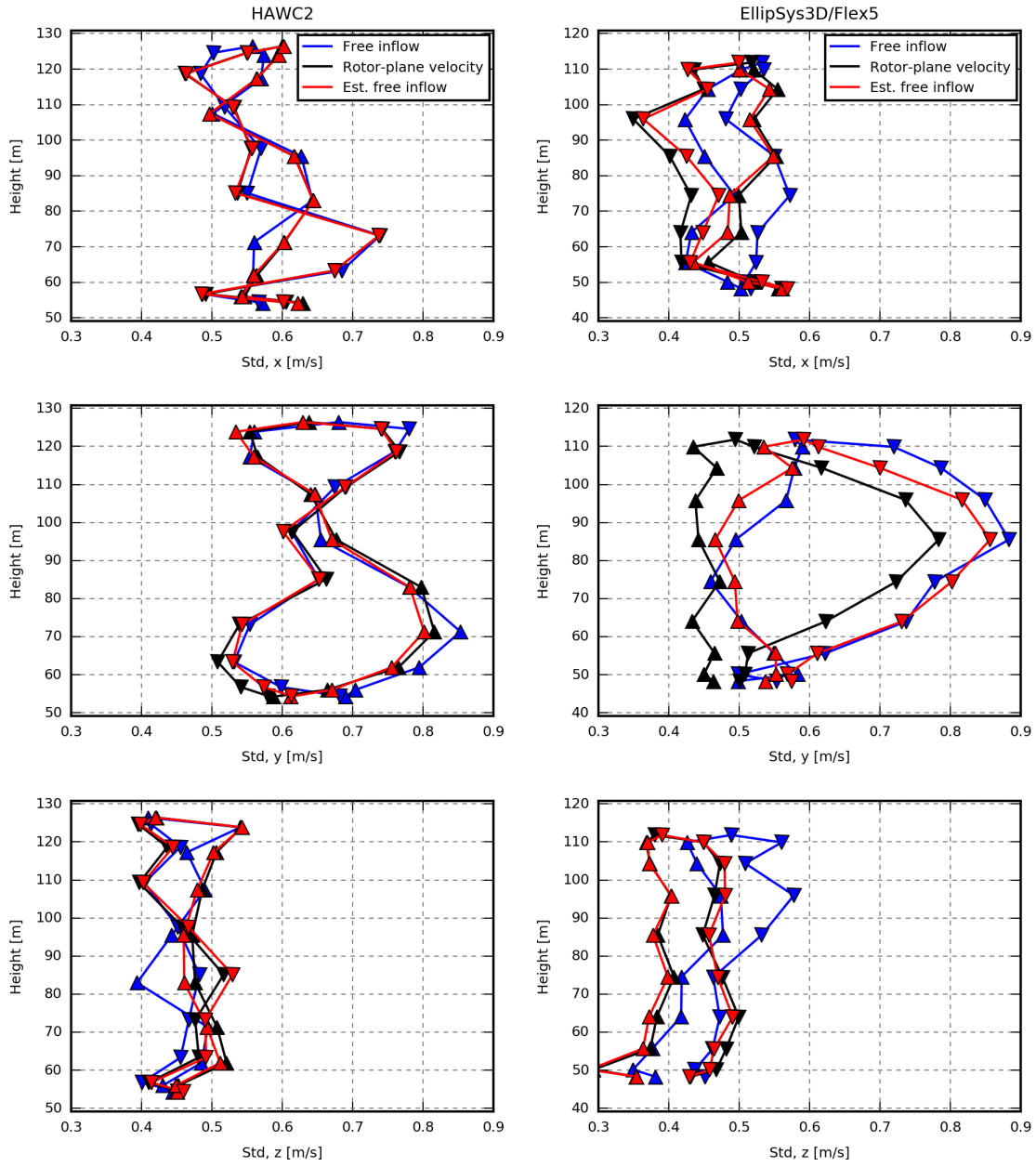

Figure 3.22: Standard deviation of the wind speed (mean value and profile) obtained from 200 s of HAWC2 (left) and EllipSys3D/Flex5 (right) simulations. The markers indicate the up- and downstroke, and the x, y, and z components refer to the ground coordinate system; see Fig. 3.10.

CHAPTER 4
Application of BMFS measurements

In Chapter 3, the refinement of BMFS measurements from relative local flow velocity over AOA and relative flow speed to rotor-plane velocity, and finally free-inflow velocity, was described. In addition, the step from AOA and relative flow speed to local normal and tangential force was shown. The local normal and tangential forces are correlated with the thrust, torque and blade-root bending moments and, using a proper calibration, estimates of these measures may be obtained as well. This means that estimates of different measures are obtainable from BMFS measurements. The measures range from the estimated free-inflow velocity, which reflects the inflow conditions, to the thrust, torque and bending moment estimates, which are closely related to the power and actual loads; see Fig. 4.1. Inevitably, uncertainty is introduced in each step; i.e. the estimated free-inflow velocity is subject to more uncertainty than the rotor-plane velocity and so on. The different measures, however, make it possible to divide the complex process from inflow to power and loads into smaller steps that can be investigated individually. Some of the estimates can be compared to measurements, e.g. lidar or met-mast wind speed, electrical power output or strain gauge measurements, while all estimates can be analysed and compared to numerical simulations.

This opens up the field for a wide range of applications. An example is the study of the correlation between noise (amplitude modulation) and inflow characteristics by Madsen (2014) that first reveals a relation between transient stall (AOA) and noise, and then investigates in which inflow conditions transient stall occurs.

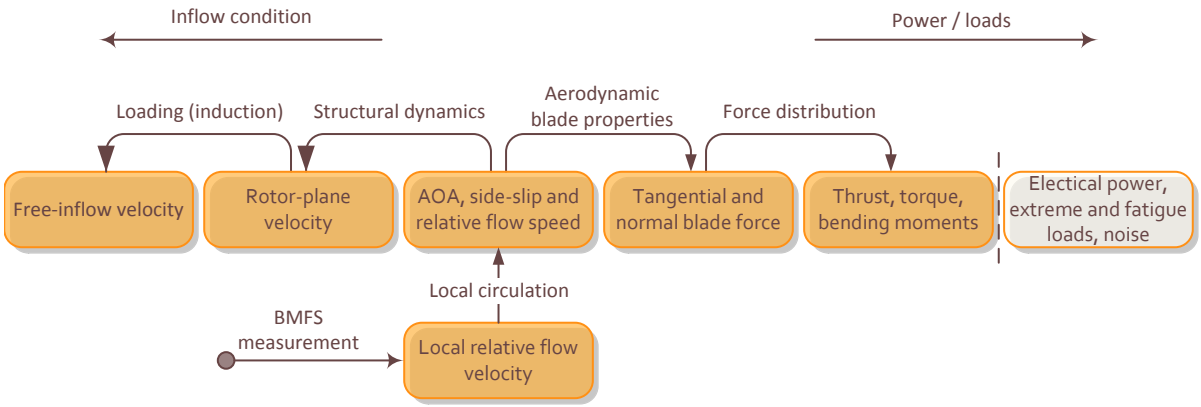

Figure 4.1: Estimates obtainable from BMFS measurements.

Another example is illustrated in Fig. 4.2. In this case, the revolution-averaged blade-root flap-wise bending moment of two 5-hour periods is plotted as a function of

the estimated free wind speed (left), the rotor-plane velocity (middle) and the local blade normal force (right). In the first period (19 May), the turbine is operated as a stall-regulated turbine with a fairly constant rotor speed, while it is operated as a modern pitch-regulated variable-speed turbine in the second period (25 May). It can be clearly seen that the different control strategies make the turbine respond differently to similar inflow conditions, while the relation between the local normal force and the flap-wise bending moment is seen to be independent of the control strategy. In this way, the influence of the control strategy can be investigated at different stages.

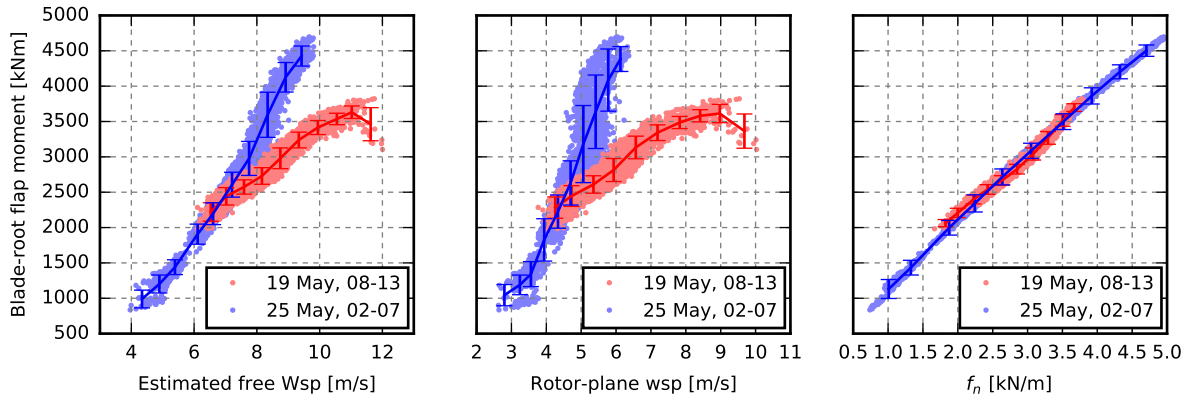

Figure 4.2: Revolution-average blade-root flap moment obtained from two different 5-hour periods where the turbine was operated with different control strategies.

In this chapter, examples of the applications of the different measures that can be extracted from BMFS measurements will be described.

4.1 BMFS measured flow angle

In Paper B, it is shown that for wind turbines with fixed pitch, constant rotor speed and stiff blades (e.g. the Tellus turbine, see Section 2.1.1), the axial rotor-plane wind speed can be considered as a monotonic function of the BMFS measured LFA when averaging over one or more revolutions. This means that the LFA can be used as a reference for power and flap-load curves. These curves are obviously different from the typical wind-speed-based curves, but due to the high correlation between the LFA and the power and flap-wise bending moment, e.g. reported by Madsen (1991b), the turbine performance can be compared between relatively short periods. Antoniou et al. (1995), for example, were able to evaluate and compare the performance of five different tip shapes based on the revolution-averaged LFA and the power and flap-wise bending moment observed during 30-40 minutes of measurements; see Fig. 4.3.

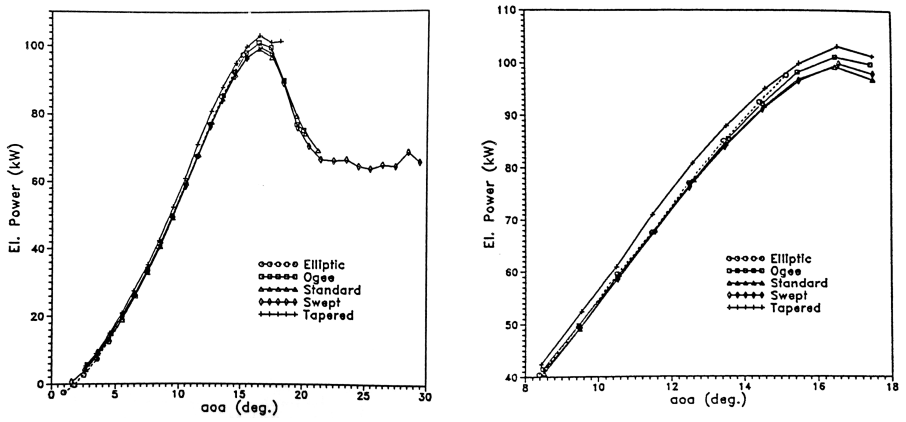

Figure 4.3: Performance of the Tellus turbine (see Section 2.1.1) with different tip shapes evaluated from 30-40 minutes of measurement. This is Figures 5 and 6 from Antoniou et al. (1995).

4.2 Angle of attack and relative flow speed

The AOA and relative flow speed measures are only one step from the BMFS measured local relative flow velocity in Fig. 4.1 and therefore subject to less uncertainty than the succeeding measures. Furthermore, the AOA is closely related to the pitch angle and aerodynamic forces and thereby suitable for pitch and flap control.

Larsen et al. (2005) developed a control method to reduce loads using individual pitch based on the AOA and relative flow speed measured by a BMFS. The method was implemented in the aeroelastic code, HAWC (Petersen, 1996), and compared to a cyclic and a standard collective pitch control method. The individual pitch control method was able to reduce the life-time fatigue loads significantly while retaining the power production. Larsen et al. (2005) stated that an advantage of an inflow-based individual pitch controller was that it was very fast compared to a blade-load-based controller, as the blade behaves as a filter with time delay.

Incorporation of the AOA and relative flow speed measured by a BMFS in the control algorithm for the control of trailing edge flaps has been suggested and investigated in several studies; e.g. Andersen (2008, 2010), Barlas et al. (2012), and Fischer and Madsen (2013, 2014, 2016).

Andersen (2010) used the AOA and relative flow speed from a BMFS alone and in combination with the rotor-speed, the AOA derived from pressure tabs and blade-load sensors to control trailing edge flaps in aeroelastic simulations and wind tunnel experiments.

Fischer and Madsen (2014, 2016) investigated the theoretical load alleviation potential of an ideal flap control. The control aimed at minimising the variation of the local blade normal force based on the AOA and relative flow speed obtained from a BMFS. The performance of the control was tested in different inflow conditions; i.e. shear, turbulence

and wake situations.

Finally, Madsen (2014) and Madsen et al. (2016) used the BMFS measured LFA and AOA to investigate different aspects of aero-acoustics.

4.3 Rotor-plane velocity

In some cases, the AOA and relative flow speed are challenging to use because they are not one, but two measures that increase alternately; see the HAWC2 simulation example in Fig. 4.4. The relative flow speed increases in the variable speed region (4-9 m/s in Fig. 4.4), while the AOA is nearly constant. In the constant-speed region (9-18 m/s in Fig. 4.4), the flow speed is almost constant, while the AOA increases up to the rated power (11 m/s in Fig. 4.4) and then decreases. This means that the AOA and relative flow speed are difficult to use as reference for the full range of power and loads. Instead, it is convenient to derive the rotor-plane velocity and use the axial component; i.e. one measure that increases monotonically with the free axial wind speed; see Fig. 4.4.

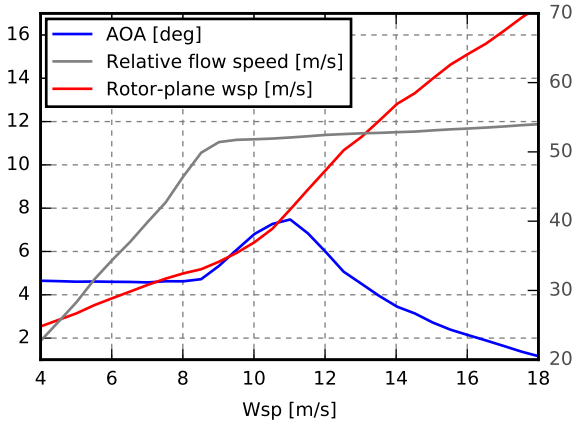

Figure 4.4: AOA, relative flow speed and rotor-plane wind speed as a function of free flow wind speed (example obtained from HAWC2 simulations).

In the study of Antoniou et al. (1995) - see Section 4.1 - the use of pitot-tube measurements made it possible to evaluate the performance of different tip shapes based on 30-40 minutes of revolution-averaged observations. In contrast, the IEC 61400-12-2 (2013) standard requires at least 180 hours of 10-minute observations to produce a power curve based on e.g. met-mast wind speed. In Paper B, it was therefore investigated whether reliable power curves for a modern wind turbine could be generated from shorter periods (e.g. a few hours or days) if they were based on the BMFS measured axial rotor-plane wind speed. The study in Paper B is based on measurements from the DAN-AERO database; see Section 2.1.7 and HAWC2 simulations using a corresponding SWT3.6-107 turbine model.

These power curves are not comparable to standard met-mast-based power curves as the rotor-plane wind speed is influenced by the induction. They can, however, be used to investigate aerodynamic modifications or detect performance issues by comparing the relative power and load curves between different periods or turbines.

The numerical part of the study concludes, based on HAWC2 simulations, that lowering the observation average time from 10 minutes to 5-30 s improves the reliability of the rotor-plane-velocity-based power and flap-load curves. In this context, the reliability is evaluated in terms of the variability of the generated curves; i.e. if 16 simulations, performed using different turbulence realisations (seeds), produce the same power curves, then the reliability is considered to be good, while larger variability between the power curves is interpreted as lower reproducibility and reliability.

Furthermore, it was found that met-mast-based power and flap-load curves required around seven times more data to achieve the same reliability level as the BMFS-based curves, assuming that the observed wind speeds were uniformly distributed in the range of interest.

The promising potential assessment-time reduction could, however, not be confirmed in the measurement part of the study due to a number of different practical reasons: several sensors were temporarily error-prone and the pitot tube was found to be malfunctioning up to 12 hours after each rainfall. The amount of observations that were usable for the BMFS-based power and flap-load curves was thereby considerably reduced. Moreover, the relation between the rotor-plane wind speed and the power and flap loads seemed to shift from time to time, even though a very fine correlation was found during short periods, as seen in Fig. 4.5. In addition, a pitch motion procedure that changes the pitch angle 1° every minute results in a severe scatter of observations averaged over less than 120 s. The potential improvement related to shorter average times, which was seen in the numerical study, was thereby only partly achievable. Finally, the rotor-plane velocity is highly sensitive to changes in the induction, e.g. due to change of the control strategy, yaw misalignment or the pitch-motion procedure described above.

It is concluded that in the setup of Paper C, the power and flap-load curves based on the BMFS measured axial rotor-plane wind speed, are similar to the met-mast-based counterparts with respect to assessment time. The technique can, however, be used offshore, in wind farms and in complex terrains where it may not be possible to install a met mast, and the sensor will never be in the wake of the turbine as it follows the yaw direction.

4.4 Free-inflow velocity

The free-inflow velocity is independent of the wind turbine, including its aerodynamic properties, control strategy and operational state, and reflects the inflow that the turbine is exposed to. The free-inflow wind speed is therefore typically used as reference for power and loads and as the input to numerical simulations.

The free-inflow wind speed that can be extracted from BMFS measurements is probably

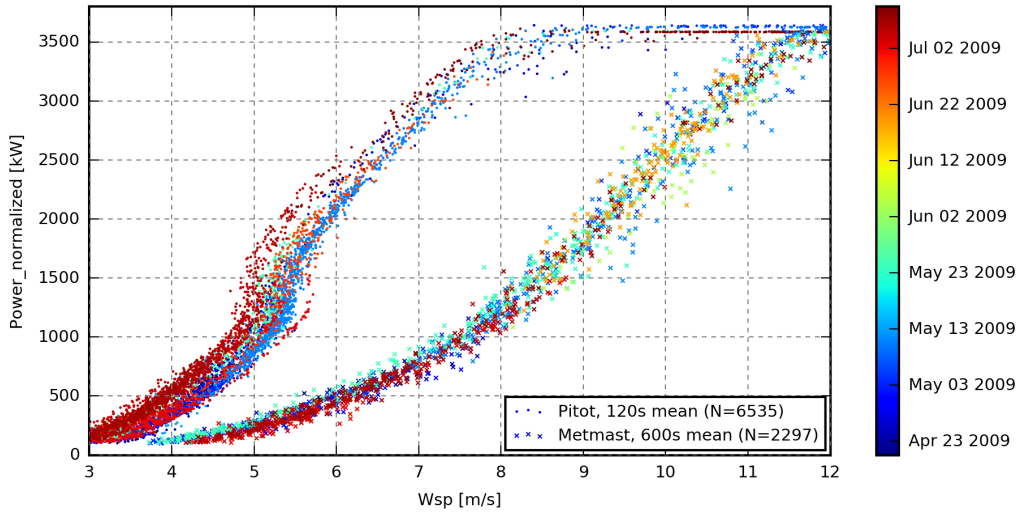

Figure 4.5: Measured power (normalised with respect to rotor-speed variations) plotted as a function of BMFS (120 s mean) and met-mast (600 s mean) wind speed. A very fine correlation is seen between the BMFS-measured axial rotor-plane wind speed and the power during short periods, but the relation seems to shift from time to time. This is Fig. 23 from Paper B.

not suitable for the power curves that are used to predict the life-time power production due to uncertainty and bias introduced in the refinement steps. It has, however, advantages over the free-inflow velocity estimates that can be derived from nacelle-, hub- or met-mast-mounted flow sensors, as it estimates the instant 3D flow velocity at its rotating path on the rotor and sweeps a wide range of the rotor plane.

This information represents the actual inflow conditions and does not rely on assumptions of stationary conditions, horizontal homogeneity, negligible vertical wind speed, etc. Fig. 4.6 shows a non-stationary example from the DAN-AERO database (see Section 2.1.7) where the wind over one minute increases from 3-4 m/s to 8-9 m/s after a steady period. The blade-root flap moment increases too and peaks at the same time as the BMFS wind speed while the met-mast wind speed, measured 250 m upstream, peaks around one minute earlier. Furthermore, the azimuthal variation of the BMFS wind speed is seen to correlate with the flap-moment variation. In Fig. 4.6 (right), the instant flap moment is plotted as a function of the met-mast and BMFS wind speed. A clear relation is seen between the BMFS wind speed and the flap moment while the full range of flap moments are observed at met-mast wind speeds around 8 m/s.

Figure 4.7 shows a half-wake situation from the DAN-AERO database. In this case, the estimated free-inflow wind speed, extracted from the BMFS, is considerably lower on the left-hand side of the rotor than on the right-hand side. This variation is obviously not captured by the fixed-point measurement at the met mast. Adding the shear profile to the met-mast wind speed results in variation, but the amplitude is too low and the

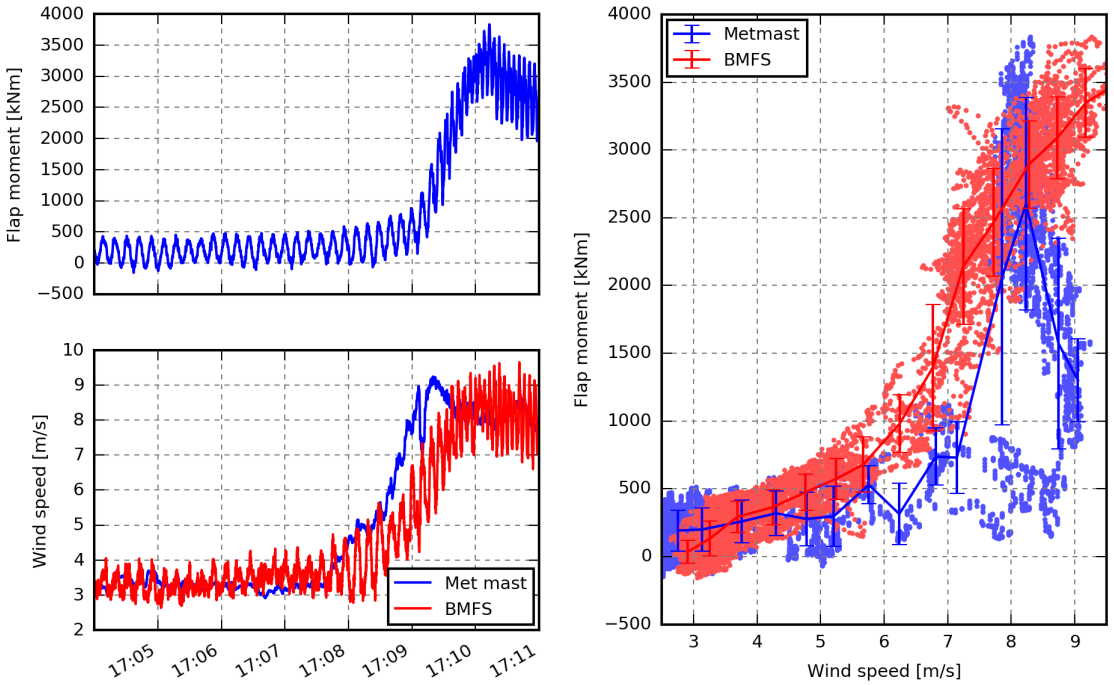

Figure 4.6: A non-stationary example from the DAN-AERO database (see Section 2.1.7). The instant flap moment is much more correlated with the BMFS wind speed than the met-mast wind speed.

peak is at the top instead of the right-hand side. The pattern of the BMFS wind speed, on the other hand, is seen to be very similar to the flap-moment pattern when plotted as a function of rotor position. The BMFS measured wind speed is thereby also in this case much more suitable to characterise the inflow conditions that actually cause the observed loads.

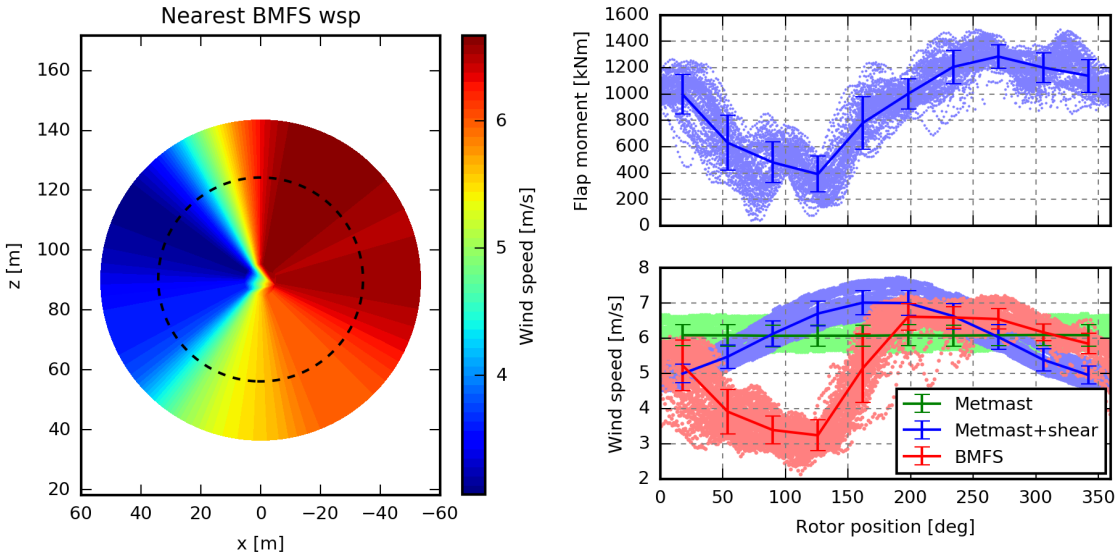

Figure 4.7: A half-wake example from the DAN-AERO database (see Section 2.1.7). The flap moment is much more correlated with the BMFS wind speed than the met-mast wind speed.

In Paper A, BMFS measurements from the DAN-AERO database (See Section 2.1.7) were used to characterise the 10-minute shear profiles. Figure 4.8 (left), outlines a half-wake situation by showing the five turbines, the nearby met masts and the estimated wake sectors. In this case, the right-hand side of the SWT3.6-107 turbine (red) is in the wake of turbine four (light blue) while turbine five (green) is presumably not operating. The 10-minute mean winds measured by the met masts are plotted as a function height in Fig. 4.8 (right). Furthermore, the estimated free inflow wind speed obtained from the pitot-tube mounted on the SWT3.6-107 turbine is shown in red. The markers indicate the up- and downstroke. During the upstroke (with the BMFS on the left-hand side of the rotor), the estimated free BMFS wind speed is similar to the wind speed measured by the met masts. During the downstroke, on the other hand, the BMFS wind speed is considerably lower, as the right-hand side of the rotor is in the wake of turbine four. Examples of free-flow and full-wake situations are presented in Paper A.

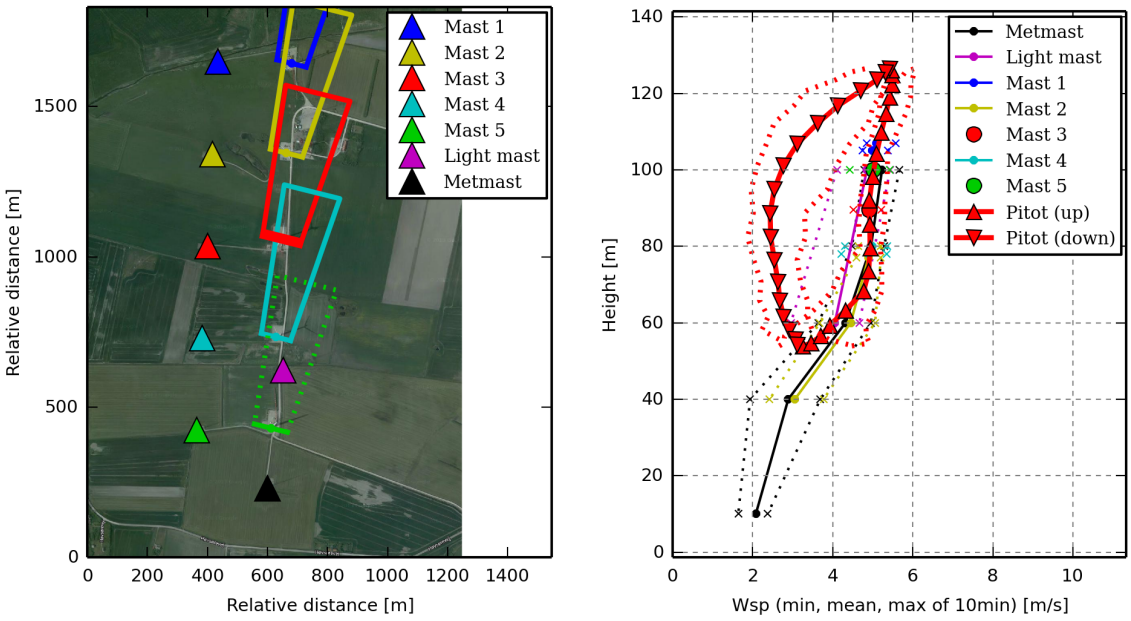

Figure 4.8: A half-wake situation from the DAN-AERO database (see Section 2.1.7). During the upstroke, the estimated free wind speed obtained from the pitot tube on the SWT3.6-107 turbine (red) is similar to the free-inflow wind speed measured by the nearby masts, while a considerably lower wind speed is measured during the downstroke where the blade is in the wake of turbine four. This is Fig. 13 from Paper A.

In Paper D, inflow information has been extracted from the pitot-tube mounted on the SWT3.6-107 turbine during the DAN-AERO experiment (see Section 2.1.7). Inflow characteristics extracted from the BMFS are used as the input for the aeroelastic HAWC2 simulations to investigate if more detailed inflow information improves the correlation between the simulated and measured loads. Twenty 10-minute periods representing a wide range of loads at 8 and 14 m/s were selected. From these periods, inflow information was extracted for 12 different cases, where Cases 8-12 were based on BMFS measurements.

A BMFS provides information from its current position only, and therefore an inflow model is required to estimate the inflow in the other parts of the domain. Typically, the inflow model combines the mean wind speed with a shear profile and a turbulence model, but in this case the measured wind speed trend, mean-wind-speed variations inside the rotor plane, and the instantly measured axial wind-speed were also included.

The mean wind speed was extracted at hub height ± 5 m to avoid the influence of non-linear shear. The wind speed trend was characterised using a linear fit. For most periods, this is sufficient, but for cases like the period shown in Fig. 4.6, a moving average should be considered to avoid the large deviations from a linear fit being interpreted as turbulence. The shear profile was obtained by fitting a power-shear profile to one hour of BMFS measurements. This model was extended to include the 10-minute mean variations within the rotor; i.e. a grid, covering the rotor, was used to specify the mean wind speed using a combination of the 10-minute azimuthal-dependent mean wind speeds and the one-hour shear profile.

The Mann model (Mann, 1994, 1998) was used to generate the turbulence. The model requires three parameters: a length scale of the spectral velocity tensor, L, a shear distortion parameter, Γ, and an energy dissipation factor, $\alpha\epsilon$. L and Γ cannot be determined from 10 minutes of measurements, and therefore standard values or the atmospheric-stability-dependent site-average values were used. The $\alpha\epsilon$, which is closely related to the turbulence intensity, was fitted based on the rotating BMFS-measured turbulence. Furthermore, a constraint turbulence simulation method (Nielsen et al., 2003) was used to modify the generated turbulence fields to reproduce the BMFS-measured instant wind speeds at the corresponding positions while preserving the turbulence statistics.

Figure 4.9 shows the best result, which includes all the inflow characteristics described above. The dots at 8 and 14 m/s show the measured 1 Hz equivalent fatigue loads while the connected error bars reflect the associated simulation results.

Note that the derived tower-bottom fore-aft as well as the tower-top yaw and tilt bending moment sensors in this study are derived from the blade-root flap- and edge-wise bending moments, as no tower-load sensors were available in the measurement database. therefore, they do not reflect actual measurements, but well-matching estimates.

In Paper D, the accuracy of the BMFS-wind-speed-based simulations was found to be significantly better than the accuracy of the met-mast-based simulations with respect to all the considered loads except the tilt moment at 8 m/s, which was only slightly worse. The mean error of the simulated 1 Hz equivalent loads, shown in Fig. 4.9, is below 10 %, except the tower-bottom fore-aft moment at 8 m/s, which is 13 %. Furthermore, the range of the simulated loads reflects the range of the measured loads, and at 8 m/s the sequence of the simulated and measured flap and tower-bottom loads is almost similar, meaning that the inflow conditions that result in high load levels in the measurements also result in high load levels in the simulations. The same tendency is seen for the tilt and yaw moment at 14 m/s.

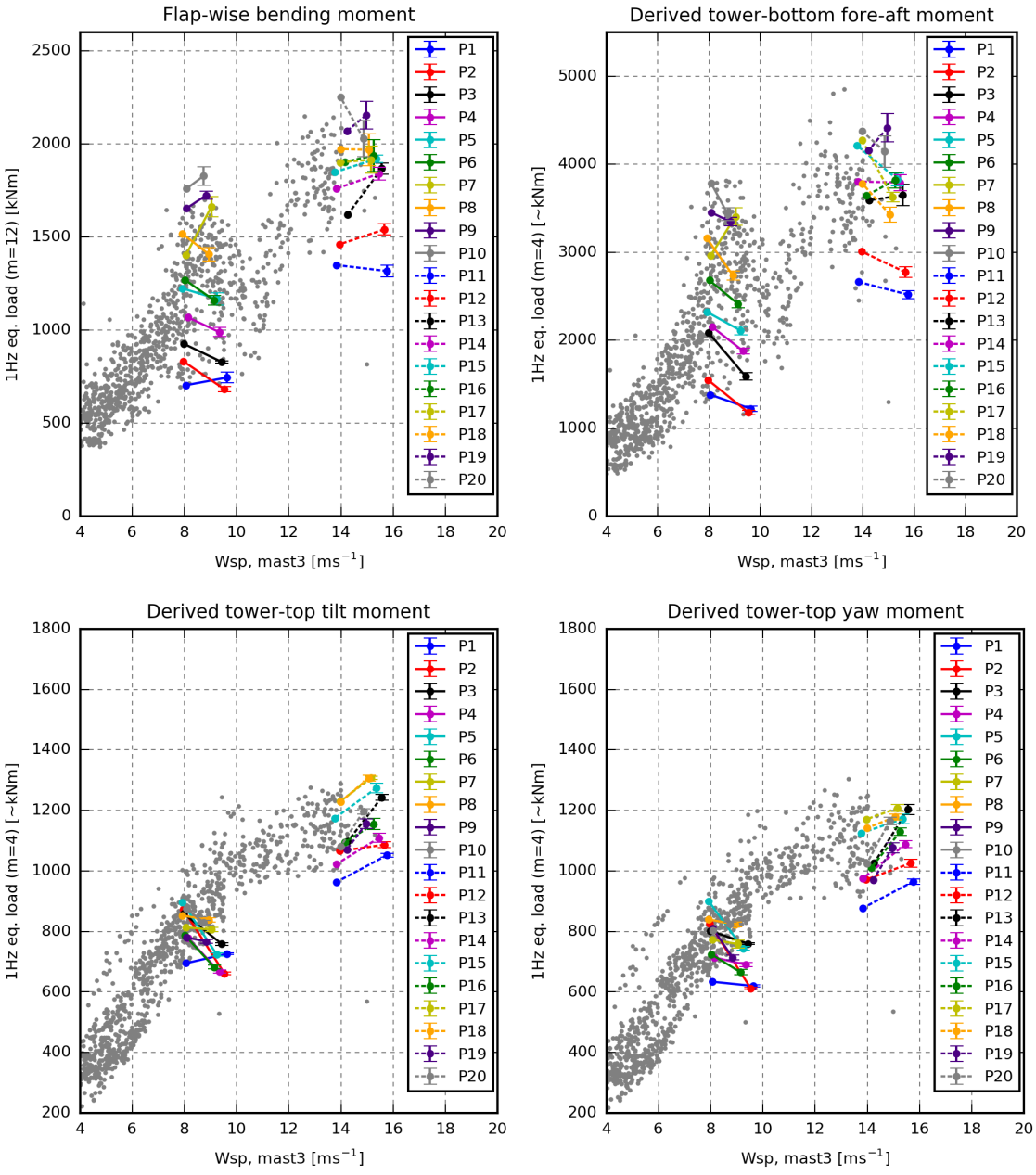

Figure 4.9: Best case based on BMFS measured inflow information. For interpretation, see Fig. A6 in Paper D. This is Fig. A10 from Paper D.

The most important inflow characteristics with respect to accuracy were found to be the mean wind speed and turbulence level. Utilising the instantly measured mean wind speed via the constraint turbulence simulator was found to improve the precision of the simulated loads such that the need for multiple simulations with different turbulence realisations (seeds) was reduced.

Including information about the wind speed trend, the shear profile and mean-wind-speed variations within the rotor plane were found to have a significant influence in a few of the selected periods, while the overall result was hardly affected. In other situations, however, e.g. half-wake situations and periods with high shear, this information may be more important to include.

Finally, two simulation sets were performed. Both sets comprise 970 simulations representing all suitable periods in the measurement database (one seed per period). In the first set, inflow information was extracted from the met masts (similar to the best met-mast-based case) while the second set was based on information from the BMFS (similar to the best BMFS-based case). The error of the simulations is shown in Fig. 4.10. In this case, the BMFS-based simulations are also more accurate than the met-mast-based simulations with respect to the considered fatigue loads, especially for the flap and tower-bottom fore-aft bending moments where the absolute mean errors are 45 and 43 % lower, respectively.

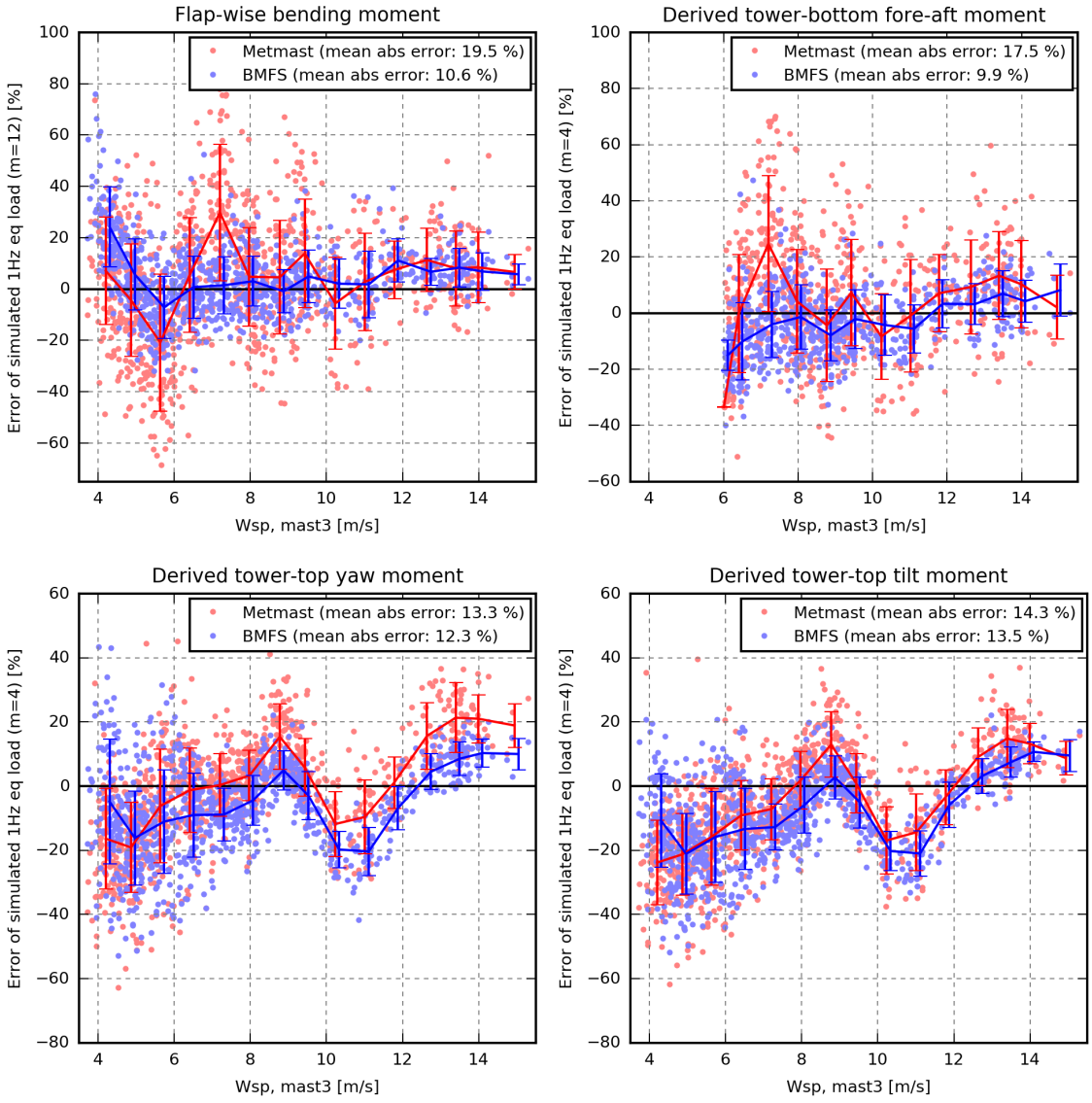

Figure 4.10: Error of the simulations based on inflow information from the met masts and the BMFS.

Major deviations are, however, still seen in some periods. The split between the mean wind and turbulence in periods with non-linear wind-speed trend was suspected to introduce deviation. The constraint turbulence simulator handles the problem quite well with respect to the wind speed at the position of the BMFS, while the inflow at other positions has much more low-frequent variation in the simulations compared to the measurements. This variation mostly affects the tilt and yaw moments while the flap and tower-bottom moments seem to be unaffected.

Plotting the revolution-averaged flap moment from a subset of the periods as a function of the local normal force derived from the BMFS, reveals a mismatch between the measurements and simulations, and moreover the measured flap moment seems to drift slightly; see Fig. 4.11. The deviation can be explained by uncertainties in the structural and aerodynamic models or, more likely, by uncertainties related to the calibration procedure; see Paper D for details about the procedure. Recalibrating the measurements will, however, only offset the flap-moment errors in Fig. 4.10, and further investigation is required to explain the deviation of the simulated loads.

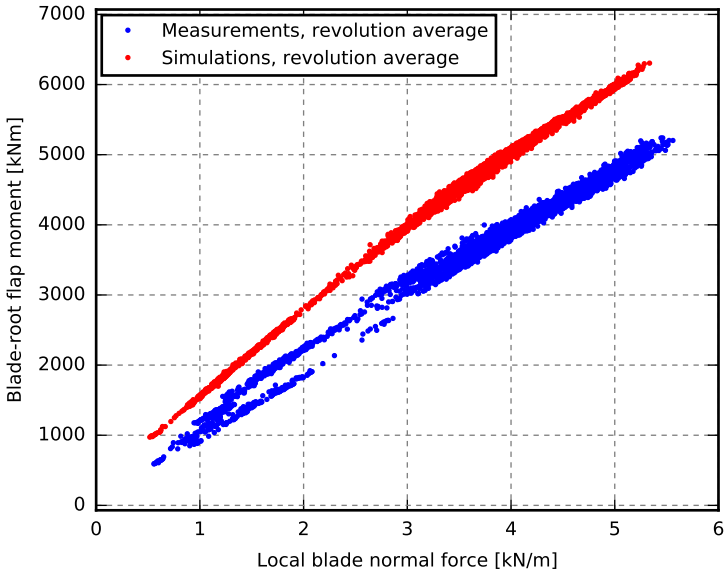

Figure 4.11: Measured and simulated revolution-averaged flap moment plotted as a function of the local blade force derived from the BMFS.

Considerable wind-speed-dependent bias is seen in the tilt- and yaw-moment fatigue loads in Fig. 4.10. At some wind speeds the loads are overestimated, while they are underestimated at other wind speeds. The reason for these deviations may be related to the calibration of the flap-moment sensor, uncertainties in the measured pitch angle offsets, or to different control behaviour as a result of the differences between the Siemens controller, which was used for the real turbine, and the Basic DTU controller (Hansen and Henriksen, 2013), which was used for the simulations.

Figure 1.4 revealed a huge amount of scatter in the 1 Hz equivalent flap-moment fatigue loads that could not be explained by the 10-minute-mean met-mast wind speed. It was consequently stated that a more detailed free-inflow estimate that characterises the temporal and spatial variations throughout the rotor was required. Some of the scatter can be explained by different levels of turbulence, as seen in 4.12 (left), where the observations are coloured by turbulence intensity. Still, however, a wide range of fatigue loads are observed under the same wind speed and turbulence conditions. In Fig. 4.12 (centre and right), the observations are coloured according to the simulated loads of the 970 met-mast-based and 970 BMFS-based simulations, respectively. It is seen that most of the loads of the BMFS-based simulations are correlated with the measured loads as most of the red, green and blue observations are in the top, middle and bottom, respectively, while the colours in the met-mast-based plot are more mixed. It is therefore concluded that the BMFS-measured inflow characteristics are able to explain most of the measured flap-moment fatigue load scatter.

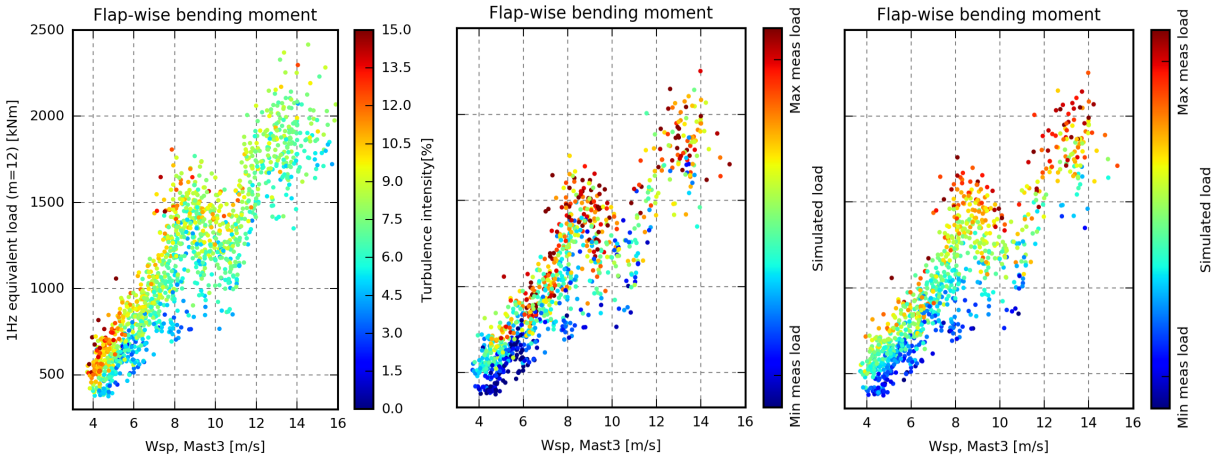

Figure 4.12: 1 Hz equivalent flap-moment fatigue loads plotted as a function of wind speed and coloured by turbulence intensity (left), relative load of the met-mast-based simulations (centre) and relative load of the BMFS-based simulations (right).

CHAPTER 5

Conclusion

The power and load performances of wind turbines are essential for the development and expansion of wind energy. The power and loads are highly dependent on the inflow conditions, which can be measured using different sensors. Cup and sonic anemometers, lidars and five-hole pitot tubes are frequently used for wind energy research applications. Furthermore, these sensors can be mounted on nearby met masts, on the nacelle, in the spinner or at the blade. Each combination of sensor and mounting position has advantages and shortcomings.

For power performance, the 10-minute mean wind speed measured at a nearby met mast is typically appropriate for characterising the inflow, while major variation in the fatigue load scatter is seen when plotting against the 10-minute-mean wind speed. Consequently, information about the temporal and spatial variations within the rotor area is required to characterise the inflow with respect to loads.

This information can be obtained from a blade-mounted flow sensor, BMFS. Five-hole pitot tubes have been used as BMFS in several research experiments over the last 30 years. A BMFS is, however, located inside the induction zone, and the measured flow velocity is thereby different from the free-inflow velocity; i.e. the inflow velocity that would have been observed at the same time and location if the turbine was not present to obstruct the flow. This is problematic because the measured flow is thereby dependent on the aerodynamic properties, the control strategy and the operational state of the turbine.

Aerodynamic engineering models that describe the relation between the free-inflow and the velocity at the blades have, however, been used in well-established aeroelastic codes for many years, and these models can be used for the reversed process too; i.e. to estimate the free-inflow velocity from the flow velocity at the blade.

Before these models can be applied, flow deflection and change of flow speed due to local circulation on the airfoil must be compensated for in the BMFS-measured local velocity. In this work, a model based on the velocities around an airfoil extracted from 2D CFD computations has been used.

Furthermore, the relative flow velocity must be mapped onto absolute flow in fixed global coordinates. In this step, uncertainty is introduced, because the actual velocity and orientation of the BMFS are unknown due to the static and dynamic deflection and torsion of the blade.

Finally, the induced velocities can be estimated using a combination of aerodynamic models and an iterative procedure. This method has been developed, implemented, verified and applied in this project. The aerodynamic models included in the current

implementation comprise blade-element-moment(BEM)-based models for axial and tangential induction, a radial-induction model and tip-loss correction as well as models for skew and dynamic inflow.

The method has been verified using HAWC2 simulations and simulations performed by Flex5 coupled with the LES flow solver, EllipSys3D. It is concluded that the method works and is able to compensate for most of the rotor-induced flow disturbance.

Furthermore, the uncertainty introduced in each step of the method has been investigated. The major part of the uncertainty introduced in the method is due to the mapping from the relative flow velocity to the absolute flow velocity in fixed global coordinates due to unknown deflection and rotation of the blade section. This part of the uncertainty can be reduced by including the actual orientation and velocity of the sensor in the transformation. This information may, however, be challenging to measure due to the high rotational speed of the blade section and the resulting large centrifugal force.

Another part of the uncertainty was found to be related to the choice of reference free-inflow velocity. In the HAWC2 simulations, the uncertainty was introduced because the reference free-inflow velocity was extracted at the assumed (undeflected) sensor position. In the Flex5/EllipSys3D simulations the turbulence moves differently in simulations with and without the turbine, and additional deviation is therefore to be expected when the instant inflow velocities estimated from a simulation with a turbine are compared to the free inflow velocity in an equivalent simulation without a turbine. Hence, the method will not provide exactly the instant free-inflow velocity that would have been at the same time and location without the presence of the turbine. It is, however, concluded that for some applications, the current free-inflow estimate is more appropriate.

The accuracy of the estimated free-inflow velocity is highly dependent on the sensor, the actual position, and the aerodynamic and structural properties of the turbine. The accuracy should, however, be considered in relation to the advantages of measuring the flow at the blade:

A BMFS yaws with the turbine. It is thereby exposed to exactly the same inflow conditions as the turbine including the wake from upstream turbines. Consequently, BMFS measurements from all wind directions are usable and provide important information e.g. about wake flow.

A BMFS measures at the rotor. This means that the instantly measured inflow velocities can be used without the need for temporal averaging to compensate for the delay, expansion and evolvement of the flow on its way from the sensor to the rotor.

A BMFS sweeps different parts of the rotor while it moves with the blade. Hence, it is able to measure vertical and horizontal variations on its rotating path due to, for example, shear, half wake and large scale turbulence.

Finally, a BMFS measures the local flow velocity relative to the blade, which is closely related to the local aerodynamic forces. The BMFS measurements can therefore be considered as an intermediate measure between the free inflow and the power and loads, that can be used to split the complex process from inflow to power and loads into smaller

steps, which can be investigated individually.

Applications of the different BMFS measure estimates, i.e. the local aerodynamic forces, the AOA and and relative flow speed, the rotor-plane velocity and the free-inflow velocity, have been examined:

An excellent control-strategy-independent correlation between the revolution-averaged local normal force extracted from a BMFS and the measured flap-wise bending moment was shown based on two 5-hour periods where the turbine was operated with variable and a quite constant rotor speed, respectively. For the same periods, considerable difference is seen in the relation between the measured flap-wise bending moment and the estimated free axial inflow. It is thereby confirmed that BMFS measurements can be used to split the complex process from inflow to power and loads into smaller steps that can be investigated individually - in this case a control-dependent and a control-independent step.

Several studies have used the BMFS-measured AOA and relative flow speed for control of load alleviating concepts, e.g. individual pitch and trailing edge flaps, and for the investigation of aero-acoustics.

Application of the rotor-plane velocity as a reference for short-term power and load assessment has been investigated. Numerical simulations revealed high potential; around seven times speed up compared to a met-mast-based assessment, but the promising improvement could not be confirmed using measurements due to practical issues and circumstances.

The free-inflow velocity estimates have been used to characterise the shear profile in free-flow, half- and full-wake situations. The derived profiles were found to be similar to observations from the nearby met masts. It is consequently concluded that the method is suitable to characterise vertical and horizontal mean wind speed variations within the rotor.

Finally, detailed inflow characteristics have been derived from different periods and used as the input for aeroelastic simulations. The inflow characteristics comprised mean wind speed and trend, turbulence intensity, horizontal and vertical variations inside the rotor as well as the instantly measured wind speed, which was used to constrain the turbulence models. The simulations based on the BMFS-measured inflow characteristics were concluded to be significantly more accurate than the simulations based on the met-mast-measured free-inflow characteristics with respect to the correlation between the measured and simulated fatigue loads.

The most important inflow characteristics with respect to accuracy were found to be the mean wind speed and turbulence level. Furthermore, the application of constraint turbulence simulation was found to improve the precision of the simulated loads such that the need for multiple simulations was reduced.

Information about the wind-speed trend, the shear profile and the 10-minute-mean wind-speed variations within the rotor plane influenced a few of the selected periods

significantly, while the overall result was hardly affected. It is therefore concluded that if the periods of interest comprise many situations with, e.g. half-wake or high shear, then it is important to include this information.

Furthermore, inflow characteristics were extracted from 970 periods and used for aeroelastic simulations. Based on these simulations, it is concluded that the BMFS-measured inflow characteristics are able to explain most of the measured flap-moment fatigue load scatter and thereby to characterise the inflow conditions that cause high loads.

The overall conclusion is therefore that the free-inflow velocity can be estimated from BMFS measurements using the presented method. The estimated free-inflow velocity is subject to uncertainty that is mainly introduced because the exact orientation and velocity of the sensor is unknown due to deflection and rotation of the blade. Despite this uncertainty, a BMFS is able to provide valuable information about the inflow. This information can be used for wind turbine control, to investigate the complex relation between the inflow and the power and loads, to characterise the inflow conditions that cause high loads, and as input to aeroelastic simulations to improve the correlation between measured and simulated loads.

Bibliography

Andersen, Peter Bjørn (2008). "Integrating deformable trailing edge geometry in modern Mega-Watt wind turbine controllers". In: *Scientific Proceedings*, pp. 15–21.

Andersen, Peter Bjørn (2010). *Advanced Load Alleviation for Wind Turbines using Adaptive Trailing Edge Flaps: Sensoring and Control*. Ed. by Mac Gaunaa, Christian Bak, Thomas Buhl, and Niels Kjølstad Poulsen. Risø National Laboratory for Sustainable Energy. ISBN: 978-87-550-3824-0 BT - Advanced Load Alleviation for Wind Turbines using Adaptive Trailing Edge Flaps: Sensoring and Control.

Antoniou, Ioannis, Helge Aagaard Madsen, and Uwe Schmidt Paulsen (1995). "Experimental and numerical results for a series of tip shapes". In: *Contributions from the Department of Meteorology and Wind Energy to the EWEC'94 Conference in Thessaloniki, Greece*. Ed. by Gunner Chr. Larsen. RisøNational Laboratory, Roskilde, Denmark, pp. 79–85.

Barlas, T.K., G.J. van der Veen, and G.A.M. van Kuik (2012). "Model predictive control for wind turbines with distributed active flaps: incorporating inflow signals and actuator constraints". In: *Wind Energy* 15.5, pp. 757–771. ISSN: 10954244. DOI: 10.1002/we.503. URL: http://doi.wiley.com/10.1002/we.503.

Berg, Jacob, Jakob Mann, and Morten Nielsen (2013). *Notes for DTU course 46100: Introduction to micro meteorology for wind energy*. Tech. rep.

Borraccino, Antoine, Michael Courtney, and Rozenn Wagner (Nov. 2016). "Generic Methodology for Field Calibration of Nacelle-Based Wind Lidars". In: *Remote Sensing* 8.11, p. 907. ISSN: 2072-4292. DOI: 10.3390/rs8110907. URL: http://www.mdpi.com/2072-4292/8/11/907.

Brand, A.J., J.W.M. Dekker, C.M. de Groot, and M. Späth (1996). *Overview of aerodynamic measurements on an Aerpac 25 WPX wind turbine blade at the HAT 25 experimental wind turbie*. ECN-DE-Memo-96-014, ECN.

Christensen, H. F. and Niels N. Sørensen (1995). "A comparative study between a dynamic stall model and experiments on a HAWT". In: *Contributions from the Department of Meteorology and Wind Energy to the EWEC'94 Conference in Thessaloniki, Greece*. Ed. by Gunner Chr. Larsen. Risø National Laboratory, Roskilde, Denmark, pp. 66–71.

Counihan, J. (Oct. 1975). "Adiabatic atmospheric boundary layers: A review and analysis of data from the period 1880–1972". In: *Atmospheric Environment (1967)* 9.10, pp. 871–905. ISSN: 0004-6981. DOI: 10.1016/0004-6981(75)90088-8. URL: https://www.sciencedirect.com/science/article/pii/0004698175900888.

Currie, Iain G (2012). "Two-Dimensional potential flows". In: *Fundamental mechanics of fluids*. CRC Press, pp. 63–115. ISBN: 1439874603.

Fischer, Andreas and Helge Aagaard Madsen (2013). "Load alleviation potential with trailing edge flaps for turbines in wake operation". In: *Proceedings of the 2013*

International Conference on Aerodynamics of Offshore Wind Energy Systems and Wakes (icowes2013). Technical University of Denmark (DTU).

Fischer, Andreas and Helge Aagaard Madsen (2014). "Investigation of the maximum load alleviation potential using trailing edge flaps controlled by inflow data". In: *Journal of Physics: Conference Series (Online)*. Vol. 555. DOI: 10.1088/1742-6596/555/1/012037.

Fischer, Andreas and Helge Aagaard Madsen (2016). "Investigation of the theoretical load alleviation potential using trailing edge flaps controlled by inflow data". In: *Wind Energy* 19.9, pp. 1567–1583. ISSN: 10954244. DOI: 10.1002/we.1937. URL: http://doi.wiley.com/10.1002/we.1937.

Fleming, P. A., A. K. Scholbrock, A. Jehu, S. Davoust, E. Osler, A. D. Wright, and A. Clifton (2014). "Field-test results using a nacelle-mounted lidar for improving wind turbine power capture by reducing yaw misalignment". In: *Journal of Physics: Conference Series* 524.1, p. 12002. ISSN: 1742-6596. URL: http://stacks.iop.org/1742-6596/524/i=1/a=012002.

Glauert, H (1935). "Airplane Propellers". In: *Aerodynamic Theory: A General Review of Progress Under a Grant of the Guggenheim Fund for the Promotion of Aeronautics*. Berlin, Heidelberg: Springer Berlin Heidelberg, pp. 169–360. ISBN: 978-3-642-91487-4. DOI: 10.1007/978-3-642-91487-4_3.

Guntur, S and N N Sørensen (2014). "An evaluation of several methods of determining the local angle of attack on wind turbine blades". In: *Journal of Physics: Conference Series* 555.1, p. 12045. ISSN: 1742-6596. URL: http://stacks.iop.org/1742-6596/555/i=1/a=012045.

Hand, M. M., D A Simms, L J Fingersh, D W Jager, and J R Cotrell (2001a). *Unsteady aerodynamics experiment phase V: test configuration and available data campaigns*. Tech. rep. URL: https://www.nrel.gov/docs/fy01osti/29491.pdf.

Hand, M. M., D. A. Simms, L. J. Fingersh, D. W. Jager, J. R. Cotrell, S. Schreck, and S. M. Larwood (2001b). *Unsteady aerodynamics experiment phase VI: wind tunnel test configurations and available data campaigns*. Tech. rep. URL: https://www.nrel.gov/docs/fy02osti/29955.pdf.

Hansen, Morten Hartvig and Lars Christian Henriksen (2013). *Basic DTU Wind Energy controller*. Tech. rep. DTU Wind Energy. URL: www.orbit.dtu.dk.

Harris, Michael, Maureen Hand, and A Wright (2006). *Lidar for Turbine Control*. Tech. rep. URL: http://stacks.iop.org/1742-6596/524/i=1/a=012002?key=crossref.efcc12681c6b46c26d377e1e2f7672c7.

Herges, T G, D C Maniaci, B T Naughton, T Mikkelsen, and M Sjöholm (2017). "High resolution wind turbine wake measurements with a scanning lidar". In: *Journal of Physics: Conference Series* 854, p. 012021. ISSN: 1742-6588. DOI: 10.1088/1742-6596/854/1/012021. URL: http://stacks.iop.org/1742-6596/854/i=1/a=012021?key=crossref.d626eb4dd9c5817e479b5af8e02e43e7.

IEC 61400-1 (2005). *Wind turbines - Part 1: Design requirements*. Tech. rep. International Electrotechnical Commission, Geneva, Switzerland, www.iec.ch.

IEC 61400-12-2 (2013). "IEC 61400-12-2: Power performance of electricity-producing wind turbines based on nacelle". In:

Kretz, A, Helge Aagaard Madsen, and J Thirstrup Petersen (1994). *Risø-R-671: Measured and simulated turbulence - compared at a section of a rotating wind turbine blade*. Tech. rep. Technical Report Risø-R-671, Risø National Laboratory, Roskilde, Denmark.

Kristensen, L (1999). "The perennial cup anemometer". In: *Wind Energy* 2, pp. 59–75. ISSN: 1095-4244.

Laino, David J, A Craig Hansen, and Jeff E Minnema (2002). "Validation of the AeroDyn subroutines using NREL unsteady aerodynamics experiment data". In: *Wind Energy* 5.2-3, pp. 227–244. ISSN: 1099-1824. DOI: 10.1002/we.69. URL: http://dx.doi.org/10.1002/we.69.

Larsen, T. J., G. C. Larsen, M. M. Pedersen, Enevoldsen K., and H. A. Madsen (2017). "Validation of the Dynamic Wake Meander model with focus on tower loads". In: *Journal of Physics: Conference Series* 854.1, p. 12027. ISSN: 1742-6596. URL: http://stacks.iop.org/1742-6596/854/i=1/a=012027.

Larsen, Torben Juul, Helge Aagaard Madsen, and Kenneth Thomsen (2005). "Active load reduction using individual pitch, based on local blade flow measurements". In: *Wind Energy* 8.1, pp. 67–80. ISSN: 1095-4244. DOI: 10.1002/we.141.

Larsen, Torben Juul and Anders Melchior Hansen (2007). *How 2 HAWC2, the user's manual*. Denmark. Forskningscenter Risoe. Risoe-R December. Technical Report, Risø National Laboratory, Roskilde, Denmark. ISBN: 978-87-550-3583-6. URL: www.orbit.dtu.dk.

Madsen, Helge Aagaard (1991a). *Risø-M-2887: Structural Dynamics of a 100kW HAWT*. Tech. rep. Technical Report Risø-M-2887, Risø National Laboratory, Roskilde, Denmark.

Madsen, Helge Aagaard (1991b). *Risø-M-2902: Aerodynamics and Structural Dynamics of a Horizontal Axis WindTurbine - Raw Data Overview*. Technical Report Risø-M-2902, Risø National Laboratory, Roskilde, Denmark. ISBN: 87-550-1687-1.

Madsen, Helge Aagaard (1991c). *Risø-M-2903: Aerodynamics of a horizontal-axis wind turbine in natural conditions*. Risø National Laboratory, Roskilde, Denmark. ISBN: 87-550-1689-8.

Madsen, Helge Aagaard (2014). "Correlation of amplitude modulation to inflow characteristics". In: *Proceedings of 43rd International Congress on Noise Control Engineering*. URL: http://www.acoustics.asn.au/conference_proceedings/INTERNOISE2014/papers/p171.pdf.

Madsen, Helge Aagaard, Christian Bak, Uwe Schmidt Paulsen, Mac Gaunaa, Peter Fuglsang, Jonas Romblad, Niels A Olesen, Peder Enevoldsen, Jesper Laursen, and Leo Jensen (2010). *The DAN-AERO MW Experiments: Final report*. Denmark. Forskningscenter Risoe. Risoe-R. Danmarks Tekniske Universitet, Risø Nationallaboratoriet for Bæredygtig Energi. ISBN: 978-87-550-3809-7. URL: www.orbit.dtu.dk.

Madsen, Helge Aagaard, Franck Bertagnolio, Andreas Fischer, Christian Bak, and Uwe Schmidt Paulsen (2016). *A novel full scale experimental characterization of wind turbine aero-acoustic noise sources - preliminary results*. URL: c:/mmpe/Library/Noise/A_novel_full_scale.pdf.

Madsen, Helge Aagaard and Andreas Fischer (2009). "Wind shear and turbulence characteristics from inflow measurements on the rotating blade of a wind turbine rotor". In: *EWEC 2009 Scientific proceedings*. EWEC, pp. 53–58.

Madsen, Helge Aagaard, Gunner Chr. Larsen, Torben J Larsen, R Mikkelsen, and Niels Troldborg (2008). *Wake deficit-and turbulence simulated with two models compared with inflow measurements on a 2MW turbine in wake conditions*.

Madsen, Helge Aagaard and Søren Markkilde Petersen (1990). *Risø-M-2761: Wind turbine test Tellus T-1995, 95 kW*. Risø National Laboratory, Roskilde, Denmark. ISBN: 87-550-1485-2.

Madsen, Helge Aagaard, Kenneth Thomsen, and Søren Markilde Petersen (2003). *Risø-I-210: Wind Turbine Wake Data from Inflow Measurements using a Five hole Pitot Tube on a NM80 Wind Turbine Rotor in the Tjæreborg Wind Farm*. Tech. rep. December. be.

Mann, Jakob (1994). "The spatial structure of neutral atmospheric surface-layer turbulence". In: *Journal of Fluid Mechanics* 273.-1, p. 141. ISSN: 0022-1120. DOI: 10.1017/S0022112094001886.

Mann, Jakob (1998). "Wind field simulation". In: *Probabilistic Engineering Mechanics* 13.4, pp. 269–282. ISSN: 02668920. DOI: 10.1016/S0266-8920(97)00036-2. URL: http://www.sciencedirect.com/science/article/pii/S0266892097000362%20http://linkinghub.elsevier.com/retrieve/pii/S0266892097000362.

Medina, P, M Singh, J Johansen, A Rivera Jove, E Machefaux, L J Fingersh, and S Schreck (2011). *Aerodynamic and performance measurements on a SWT-2.3-101 wind turbine*. Tech. rep. National Renewable Energy Laboratory (NREL), Golden, CO.

Medina, Paul, Manjinder Singh, Jeppe Johansen, Anna Jove, Lee Fingersh, and Scott Schreck (2012). "Inflow characterization and aerodynamics measurements on a SWT-2.3-101 wind turbine". In: *50th AIAA Aerospace Sciences Meeting, Nashville, TN, USA*, pp. 230–2012.

Meyer Forsting, Alexander Raul, Niels Troldborg, Juan Pablo Murcia Leon, Ameya Sathe, Nikolas Angelou, and Andrea Vignaroli (2017). "Validation of a CFD model with a synchronized triple-lidar system in the wind turbine induction zone". In: *Wind Energy* 20, pp. 1481–1498. ISSN: 1095-4244. DOI: 10.1002/we.2103.

Michelsen, J A (1992). *Basis3D – a Platform for Development of Multiblock PDE Solvers*. Tech. rep. Danmarks Tekniske Universitet.

Mikkelsen, T, J Mann, M Courtney, and M Sjöholm (2008). "Windscanner: 3-D wind and turbulence measurements from three steerable doppler lidars". In: *IOP Conference Series: Earth and Environmental Science* 1.1, p. 012018. ISSN: 1755-1315. DOI: 10.1088/1755-1315/1/1/012018.

Mikkelsen, Torben, Kasper Hjorth Hansen, Nikolas Angelou, Mikael Sjöholm, Michael Harris, Paul Hadley, Richard Scullion, Gary Ellis, and G Vives (2010). "Lidar wind speed measurements from a rotating spinner". In: *European Wind Energy Conference and Exhibition*. URL: www.orbit.dtu.dk.

Mortensen, N G (1994). *Wind measurements for wind energy applications. A review*. URL: http://orbit.dtu.dk/en/publications/wind-measurements-for-wind-

energy-applications-a-review(7de20235-23d5-47fb-9d02-757ec1dbb925).html.

Moscardi, Andrea and David A Johnson (2016). "A compact in-blade five hole pressure probe for local inflow study on a horizontal axis wind turbine". In: *Wind Engineering* 40.4, pp. 360–378. ISSN: 0309-524X. DOI: 10.1177/0309524X16650766. URL: https://doi.org/10.1177/0309524X16650766.

Nielsen, Morten, Gunner Chr Larsen, Jakob Mann, Søren Ott, Kurt S Hansen, and Bo Juul Pedersen (2003). "Wind simulation for extreme and fatigue loads". In: *Technical report, Risø-R-1437 (EN)* 104. URL: www.orbit.dtu.dk.

Øye, S (1996). "FLEX4 simulation of wind turbine dynamics". In: *Proceedings of 28th IEA Meeting of Experts Concerning State of the Art of Aeroelastic Codes for Wind Turbine Calculations. Available through International Energy Agency.* Lyngby, Denmark: Danmarks Tekniske Universitet, pp. 71–76.

Pedersen, Anders Tegtmeier, Mikael Sjöholm, Nikolas Angelou, Torben Mikkelsen, Belen Fernández Montes, Jens Engholm Pedersen, Chris Slinger, and Michael Harris (2013). *Full-Scale Field Test of a Blade-Integrated Dual-Telescope Wind Lidar*. Vienna, Austria. URL: http://orbit.dtu.dk/files/52390492/Full_Scale_Field_Test_poster.pdf.

Pedersen, Mads M., Torben J. Larsen, Gunner C. Larsen, Helge A. Madsen, and Niels Troldborg (Jan. 2015). "Turbulent wind field characterization and re-generation based on pitot tube measurements mounted on a wind turbine". In: *33rd Wind Energy Symposium*. AIAA SciTech. Kissimmee, Florida: American Institute of Aeronautics and Astronautics. ISBN: 978-1-62410-344-5. DOI: 10.2514/6.2015-1467. URL: http://arc.aiaa.org/doi/10.2514/6.2015-1467.

Pedersen, Mads M., Torben J. Larsen, Helge Aa. Madsen, and Gunner Chr. Larsen (Nov. 2017). "Using wind speed from a blade-mounted flow sensor for power and load assessment on modern wind turbines". In: *Wind Energy Science* 2.2, pp. 547–567. ISSN: 2366-7451. DOI: 10.5194/wes-2-547-2017. URL: https://www.wind-energ-sci.net/2/547/2017/.

Pedersen, Mads Mølgaard, Torben Juul Larsen, Helge Aagaard Madsen, and Søren Juhl Andersen (2018a). "Free-flow wind speed from a blade-mounted flow sensor". In: *Wind Energy Science* 3.1, pp. 121–138. ISSN: 2366-7451. DOI: 10.5194/wes-3-121-2018. URL: https://www.wind-energ-sci.net/3/121/2018/.

Pedersen, Mads Mølgaard, Torben Juul Larsen, Helge Aagaard Madsen, and Gunner Christian Larsen (Apr. 2018b). "More accurate aeroelastic wind-turbine load simulations using detailed inflow information". In: *Wind Energy Science Discussions*, pp. 1–33. ISSN: 2366-7621. DOI: 10.5194/wes-2018-4. URL: https://www.wind-energ-sci-discuss.net/wes-2018-4/.

Pedersen, Troels Friis, G Demurtas, A Sommer, and J. Højstrup (2014). "Measurement of rotor centre flow direction and turbulence in wind farm environment". In: *Journal of Physics: Conference Series* 524.1, p. 12167. ISSN: 1742-6596. URL: http://stacks.iop.org/1742-6596/524/i=1/a=012167.

Petersen, Jørgen Thirstrup (1996). "The aeroelastic code HawC - model and comparisons". In: *State of the art of aeroelastic codes for wind turbine calculations*. Technical

University of Denmark. Department of Fluid Mechanics, pp. 129–135. URL: http://orbit.dtu.dk/files/12777408/State_of_the_art_of_aeroelastic_codes.pdf.

Petersen, Jørgen Thirstrup and Helge Aagaard Madsen (1997). *Risø-R-993(EN): Local Inflow and Dynamics – Measured and Simulated on a Rotating Wind Turbine Blade*. Risø National Laboratory, Roskilde, Denmark.

Rahimi, Hamid, J.G. Schepers, W.Z. Shen, Néstor Ramos García, M.S. Schneider, Daniel Micallef, C.J. Simao Ferreira, Eva Jost, Levin Klein, and Iván Herráez (2018). "Evaluation of different methods for determining the angle of attack on wind turbine blades with CFD results under axial inflow conditions". In: *Renewable Energy*. ISSN: 09601481. DOI: 10.1016/j.renene.2018.03.018. arXiv: 1709.04298.

Schepers, J. G., A. J. Brand, A. Bruining, J. M. R. Graham, M. M. Hand, D. G. Infield, H. A. Madsen, J. Paynter, and D. A. Simms (1997). *Final report of IEA AnnexXIV : Field Rotor Aerodynamics*. Tech. rep.

Schepers, J. G., A. J. Brand, A. Bruining, M. Hand, D. Infield, H. Madsen, T. Maeda, J. Paynter, R. van Rooij, and Y. Shimizu (2002). "Final report of IEA Annex XVIII: enhanced field rotor aerodynamics database". In: *Energy Research Center of the Netherlands, ECN-C-02-016, February*. URL: ftp://ftp.ecn.nl/pub/www/library/report/2002/c02016.pdf.

Schmidt Paulsen, U (1990). *Risø-M-2878: Calibration of Rosemount M858 Pitot tube sensor*. Risø National Laboratory, Roskilde, Denmark. ISBN: 87-550-1656-1.

Schreck, S and M Robinson (2005). "Blade Three-Dimensional Dynamic Stall Response to Wind Turbine Operating Condition". In: *Journal of Solar Energy Engineering* 127.4, pp. 488–495. ISSN: 0199-6231. URL: http://dx.doi.org/10.1115/1.2035706.

Shen, Wen Zhong, Martin O L Hansen, and Jens Nørkær Sørensen (2009). "Determination of the angle of attack on rotor blades". In: *Wind Energy* 12.1, pp. 91–98. ISSN: 1099-1824. DOI: 10.1002/we.277.

Shen, Wen Zhong, Martin Otto Laver Hansen, and Jens Nørkær Sørensen (2006). *Determination of Angle of Attack (AOA) for Rotating Blades*. URL: www.orbit.dtu.dk.

Simley, Eric, Nikolas Angelou, Torben Mikkelsen, Mikael Sjöholm, Jakob Mann, and Lucy Y. Pao (2016). "Characterization of wind velocities in the upstream induction zone of a wind turbine using scanning continuous-wave lidars". In: *Journal of Renewable and Sustainable Energy* 8.1, p. 013301. ISSN: 1941-7012. DOI: 10.1063/1.4940025. URL: http://aip.scitation.org/doi/10.1063/1.4940025.

Simms, D. A., M. M. Hand, L. J. Fingersh, and D. W. Jager (1999). *Unsteady aerodynamics experiment phases II-IV test configurations and available data campaigns*. Tech. rep. National Renewable Energy Lab. URL: https://www.nrel.gov/docs/fy99osti/25950.pdf.

Sørensen, N N (1995). "General Purpose Flow Solver Applied to Flow over Hills". PhD thesis. Technical University of Denmark. URL: www.orbit.dtu.dk.

St. Martin, C M, J K Lundquist, A Clifton, G S Poulos, and S J Schreck (2017). "Atmospheric turbulence affects wind turbine nacelle transfer functions". In: *Wind Energ. Sci.* 2.1, pp. 295–306. ISSN: 2366-7451. DOI: 10.5194/wes-2-295-2017. URL: https://www.wind-energ-sci.net/2/295/2017/%20https://www.wind-energ-sci.net/2/295/2017/wes-2-295-2017.pdf.

Telionis, Demetri, Yihong Yang, and O Redinioti (2009). "Recent developments in multi-hole probe (mhp) technology". In: *20th International Congress of Mechanical Engineering*. Vol. 21.

Troldborg, Niels, Christian Bak, Helge Aagaard Madsen, and Witold Robert Skrzypinski (2013a). *DANAERO MW: Final Report*. Denmark: DTU Wind Energy.

Troldborg, Niels, Christian Bak, Niels N Sørensen, Helge Aagaard Madsen, Pierre-Elouan Réthoré, Frederik Zahle, and Srinivas Guntur (2013b). *Experimental and numerical investigation of 3D aerofoil characteristics on a MW wind turbine*. URL: www.orbit.dtu.dk.

Troldborg, Niels, Alexander Raul Meyer Forsting, and Alexander Raul Meyer Forsting (2017). "A simple model of the wind turbine induction zone derived from numerical simulations". In: *Wind Energy* 20.12, pp. 2011–2020. ISSN: 10954244. DOI: 10.1002/we.2137. URL: https://onlinelibrary.wiley.com/doi/abs/10.1002/we.2137%20http://doi.wiley.com/10.1002/we.2137.

Wagner, Rozenn, Andrea Vignaroli, Nikolas Angelou, Ameya Sathe, Alexander Raul Meyer Forsting, Mikael Sjöholm, and Torben Krogh Mikkelsen (2015). *Measurement of turbine inflow with a 3D windscanner system and a spinnerlidar*. URL: www.orbit.dtu.dk.

APPENDIX A

Turbulent wind field characterization and re-generation based on pitot tube measurements mounted on a wind turbine

Turbulent wind field characterization and re-generation based on pitot tube measurements mounted on a wind turbine

MM Petersen[*], TJ Larsen[†], HA Madsen[‡] and GC Larsen[§], N.Toldborg[**]
Department of Wind Energy, Technical University of Denmark,
Frederiksborgevej 299, Roskilde, 4000, Denmark

This paper describes a new method to estimate the undisturbed inflow field of a wind turbine based on measurements obtained from one or more five-hole pitot tubes mounted directly on the blades.
Based on the measurements, the disturbance caused by the wind turbine is estimated using aerodymanic models that compensate for axial and tangential induction, approximated by blade element momentum theory, radial expansion of the inflow, rotor tilt, dynamic and skew inflow, tip loss, as well as braking and circulation of the flow local to the airfoil.
The wind speeds measured on the rotating blades give a better estimate of the turbulence intensity over the rotor plane than can be measured at a single point, e.g. using a cup anemometer, and in addition the wind shear profile can be derived. In addition the measurements can be used to constrain a synthetic turbulence model to exactly produce the measured wind speeds at the recording position. In the theoretical part of this study a quite good agreement is seen between load sensors on a turbine model exposed to the reference and the re-generated turbulence field. Finally the method is applied to full scale measurements and reasonable wind shear profiles are derived.
It is expected that this method will lead to a new and effective experimental method to characterize the incoming flow field to a wind turbine and thus contribute to the understanding of wind turbine loads.

Nomenclature

a	=	Axial induction factor
a'	=	Tangential induction factor
c	=	Chord length
C_D	=	Drag coefficient
C_L	=	Lift coefficient
C_T	=	Thrust coefficient
C_y	=	Lift and drag coefficient projected to the axial direction
C_x	=	Lift and drag coefficient projected to the tangential direction
N_B	=	Number of blades
r	=	Radius of current blade section
u	=	Wind speed at the rotor plane in the direction of the mean wind
u_0	=	Free undisturbed wind speed in the direction of the mean wind
$Vrel$	=	Relative velocity measured by pitot tube
$Vrel_{xy}$	=	Relative wind speed ignoring the radial flow component
$V_{ind,tan}$	=	Tangential induced wind speed
α	=	Angle of attack measured by pitot tube

[**] Research assistant, DTU Wind Energy, 4000 Roskilde, Denmark
[†] Senior scientist, DTU Wind Energy, 4000 Roskilde, Denmark
[‡] Professor, DTU Wind Energy, 4000 Roskilde, Denmark
[§] Senior scientist, DTU Wind Energy, 4000 Roskilde, Denmark
[**] Senior scientist, DTU Wind Energy, 4000 Roskilde, Denmark

β = Side slip angle measured by pitot tube
ω = Angular velocity of rotor
ρ = Density of air
Θ = Angle between rotor plane and pitot tube, i.e. sum of twist and pitch
ϕ = Angle between rotor plane and relative wind, i.e. sum of α and Θ

I. Introduction

Detailed knowledge about the wind and its variation is essential in order to understand and analyze many aspects regarding wind turbines, e.g. power production and load conditions including derived component fatigue exposure. Normally the wind is measured at a few stationary points by cup or sonic anemometers. However, for current MW-sized turbines the variability of the wind field over the rotor area is significant and a more fine-gained depiction is desirable.

Recently lidars have been adapted as a sophisticated instrument for scanning an incoming flow field with high temporal and spatial resolution. Unfortunately lidars are normally an expensive and complex approach, especially as a setup of several simultaneous scanning lidars are required to measure also the lateral and vertical flow components[1,2].

In this paper a new approach that utilizes the potential of one or more five-hole pitot tubes mounted on the blades of a wind turbine is presented. It has previously been demonstrated that such measurements can be used to characterize shear and turbulence in the inflow[3], but much more information can be derived.

A pitot tube is an instrument used to measure flow velocity by measuring the pressure difference on a spherical sensor head. With five-hole pitot tubes also the flow direction, represented by two perpendicular angles, can be measured, and from this information the conventional cartesian longitudinal, lateral and vertical wind speed components can be derived at the paths swept by the pitot tubes. Figure 1 illustrates these paths through a turbulence field swept by five pitot tubes mounted on each blade of a wind turbine.

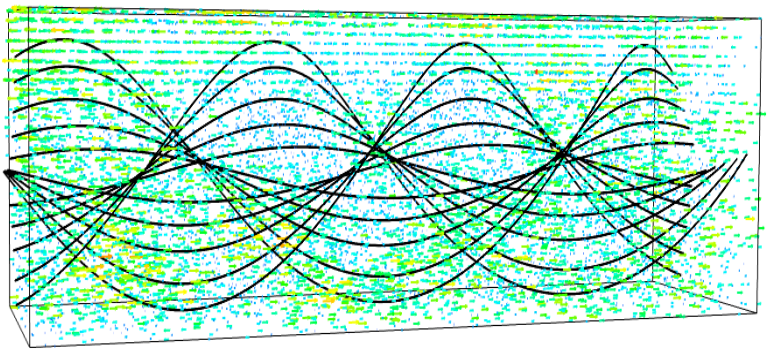

Figure 1. By mounting five pitot tubes on each blade of a wind turbine the wind speeds at the helices can be measured.

The advantages of this approach are obvious - with pitot tubes mounted on the rotating blades, the wind field can be measured where it has direct impact on the wind turbine, namely on the blades.

A challenging aspect is that the wind speed is disturbed by the presence of the turbine. For high wind speeds, i.e. above rated wind speed, only a part of the energy of the wind is extracted, hence the disturbance of the wind flow is limited, and the measured wind speed almost equal to the free wind speed. Uncertainties related to the model of the induction field is therefore small at high wind speeds – the region where the large turbine loads typically occurs. At low wind speeds a noticeable induction occurs which slowly adjust to the incoming windfield and turbine loading. This means that small high frequent turbulence eddies will pass unaffected through the rotor while the large low frequent eddies are directly affected by the induction field of the turbine. This modification can, however, be approximated by an extended blade element momentum (BEM) theory.

In contrast to existing aeroelatic codes that model the impact of a wind turbine on a turbulent wind field, the method presented in this paper reverses the process and estimates the free flow from the disturbed flow at the wind turbine rotor plane.

II. Method

The method consists of the following steps:

1) Measurement of relative velocity, *Vrel*, angle of attack, α, and side slip angle, β, by pitot tubes
2) Transformation into conventional cartesian wind speed components, *u*,*v*,*w*
3) Estimation of induced axial, tangential and radial velocity
4) Estimation of the free undisturbed wind speed at the location of measurement
5) Extract statistical information, e.g. mean wind speed, wind direction, turbulence intensity and shear profile
6) Modify a synthetic turbulence model to have the measured wind speeds at the corresponding positions while preserving the statistics

First the two angles and the relative velocity measured by the pitot tubes are mapped into three cartesian components. These wind speed components comprise the wind speed vector at the measurement location including a large contribution from the rotational speed, which must be subtracted.

The wind speed components are then mapped into a global coordinate system to eliminate rotations caused by the orientation of the pitot tube, the blade pitch, blade twist, blade coning and azimuthal position of the blade, as well as the tilt and yaw of the main shaft.

The wind vector component parallel to the main shaft is affected by the axial induction in the rotor plane, i.e. the rotor axial induction must be added to the measured wind speed to find the undisturbed wind speed.

The wind speed at the rotor plane in the direction of the mean wind, *u*, is in Ref. 4 calculated by subtracting the axial induction, au_0, from the free undisturbed wind speed, u_0. By reformulating an expression for u_0 is found:

$$u_0 = \frac{u}{(1-a)} \tag{1}$$

The axial induction factor a, is related to the thrust on rotor, expressed by the thrust coefficient of an infinite thin annular element of a blade, C_T. Using momentum theory the relation can be formulated as:

$$C_T = 4a(1-a) \tag{2}$$

This relation is invalid for induction factors above 0.4, and therefore Ref. 5 proposes the induction factor expressed in terms of a third order polynomial,

$$a = 0.0892C_T^3 + 0.0545\,C_T^2 + 0.2512C_T \tag{3}$$

which gives results similar to equation (2) for small induction factors and further has a smooth transition to empirical results for higher loadings in the invalid region of equation (2).

In Ref. 6 the thrust coefficient, C_T, is calculated from the relative velocity projected onto a section of the blade, $Vrel_{xy}$, the chord length, c, the lift and drag coefficients projected to the axial direction, C_y, the number of blades, N_B, the swept distance of the annular element, $2\pi r$, and the free undisturbed wind speed, u_0:

$$C_T = \frac{Vrel_{xy}^2\; c\; C_y N_B}{2\pi r u_0^2} \tag{4}$$

This is an iterative process as the undisturbed wind speed, u_0 is required to estimate the axial induction, which is subsequently used to calculate the undisturbed wind speed. In this study the measured wind speed was used as initial guess, and by utilizing the Newton-Raphson's method converged solutions were found within a few iterations.

The tangential induction describes the wake rotation, i.e. a reaction to the force that makes the turbine rotate and in turn affects the horizontal and vertical crosswind speeds measured at the rotor plane. In this study the model of Ref. 6,

$$V_{ind,tan} = \omega r \frac{Vrel_{xy}^2 c\; C_x N_B}{8\pi r^2(1-a)u_0\omega} \tag{5}$$

is used to find the tangential induced wind speed.

The induced velocities are parts of a flow field equilibrium which is gradually established between the load on the blades, the rotor wake and the induced flow field at the rotor plane[7]. To model this behavior a low pass filter is applied to the induced velocities.

Furthermore models that compensates for radial flow expansion, skew inflow and tip loss are included.

In the current paper the method is tested and validated based on simulations using the code, HAWC2aero, a rigid structure implementation of the nonlinear aeroelastic simulation code HAWC2[8].

Furthermore, the method has been applied to full scale pitot measurements performed on a Siemens 3.6MW wind turbine carried out within the DANAERO project[9].

The estimated free wind speed field can be used to generate a synthetic turbulence field which reproduces the estimated wind speeds identically at the corresponding positions while the statistics is preserved. The applied constrained turbulence simulation approach is described in Ref. 10 and 11. The method finds the most probable realization of a stationary Gaussian stochastic field, which meets some specified constraints, in this case the estimated wind speeds.

A. Full scale measurements

During the DANAERO project 2007-2009[9], a Siemens 3.6MW turbine at the Høvsøre test site in Denmark was instrumented with a five-hole pitot tube at radius 36.5 m of one of its 53.5 m blades.

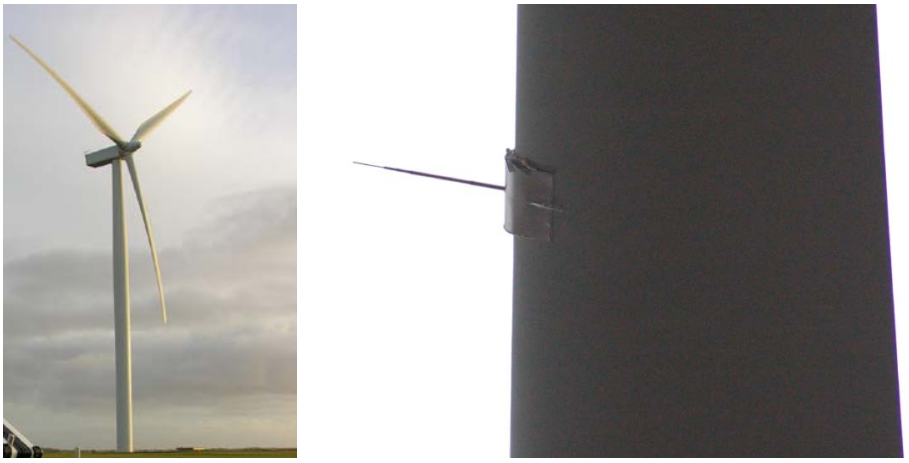

a) Turbine at Høvøre test site for large turbines in Denmark

b) Pitot tube mounted on the blade

Figure 2. Pitot tube mounted on Siemens 3.6MW turbine. Both images are from Ref. 3

Data from the turbine and nearby masts, see Figure 3, are available for around three month of operation.

Figure 3. Overview of the test site and available data

When applying the method to full scale measurements several issues appears e.g. the complexity in measuring the exact orientation and location of the pitot tube, the presence of corrupted sensors, outliers and missing data, measurement and calibration uncertainties, braking and diffraction of the flow caused by circulation local to the airfoil etc.

These problems have not been fully solved yet, but the orientation of the pitot tube has been derived by comparing statistics of measurements with simulations and in the present case a procedure to compensate for local circulation via a lookup table has been derived. The table, which has been generated using CFD, estimates the change in angle of attack and relative velocity caused by the current 2D airfoil at the location of the pitot tube, i.e. in the terminology of Figure 4, it maps (V_x, V_y) to ($V1_x$, $V1_y$).

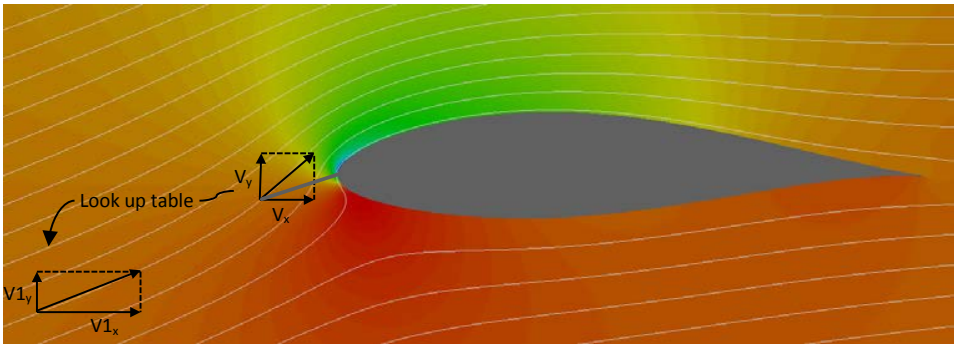

Figure 4. A look up table is used to compensate for circulation and brake up local to the airfoil

III. Results

The method has been applied to simulated pitot tube measurements from 5x3 pitot tubes, distributed as five tubes on each blade. The synthetic measurements were obtained from HAWC2aero simulations including a synthetic reference turbulence model. The resulting estimated free wind speeds estimated by the current method were used to constrain another synthetic turbulence model which was subsequently used as input for a new simulation. Finally the simulated loads and wind speeds at the blades of the two simulations were compared, see overview in Figure 5.

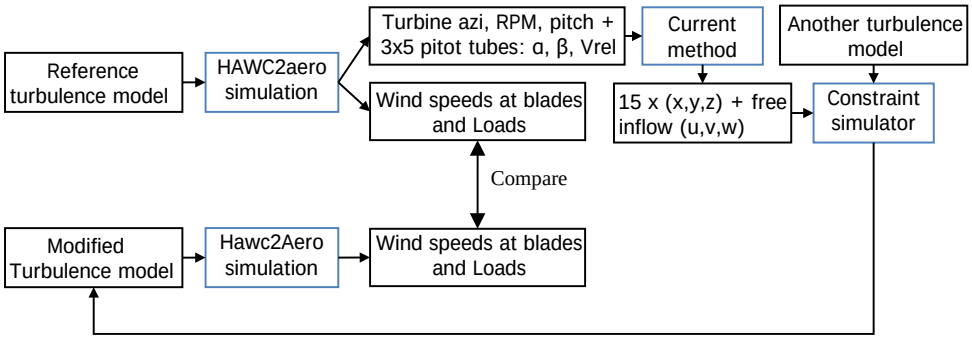

Figure 5. Overview of test process

The wind speeds measured on blade 1 at same radial position as the middle pitot tube is shown in Figure 6. A good agreement is seen, and the Root-Mean-Squared Error, RMSE, is only 0.1 m/s

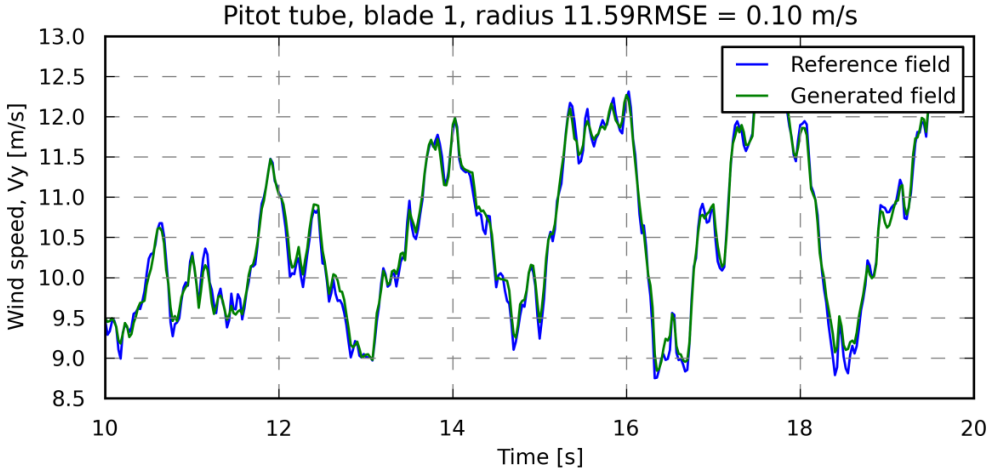

Figure 6. Comparison of wind speed measured at blade 1, at same radial position as the middle pitot tube in a field regenerated from measurements by 3x5 pitot tubes

The deviation between the target signal and the estimated signal increases with the distance from the points at which the constraints are imposed, i.e. in the middle between two pitot tubes, the deviation is more significant, see Figure 7 where the RMSE is 0.34m/s. However the large structures seems to be captured well.

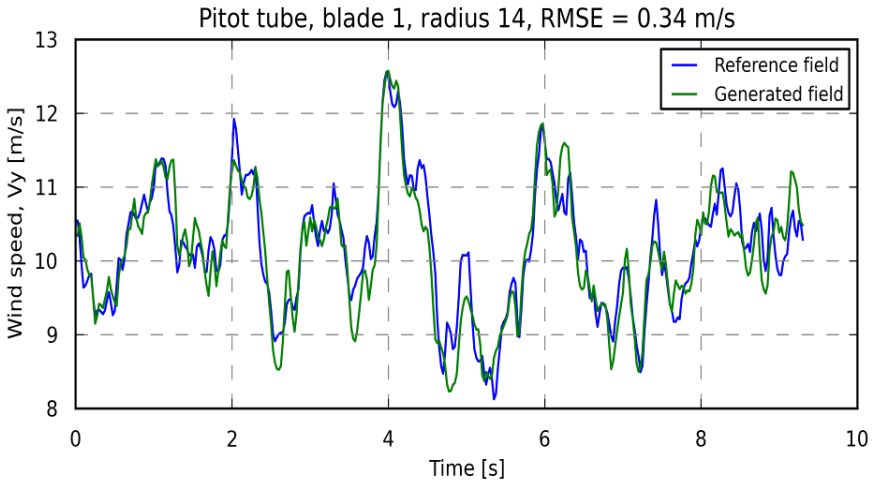

Figure 7. Comparison of wind speed measured at blade 1 in the middle between two pitot tubes. The deviation is more significant than in Figure 6

A comparison of the blade moment, the rotor thrust and the torque is shown in Figure 8. Again quite good agreement between target signals and estimated signals are seen.

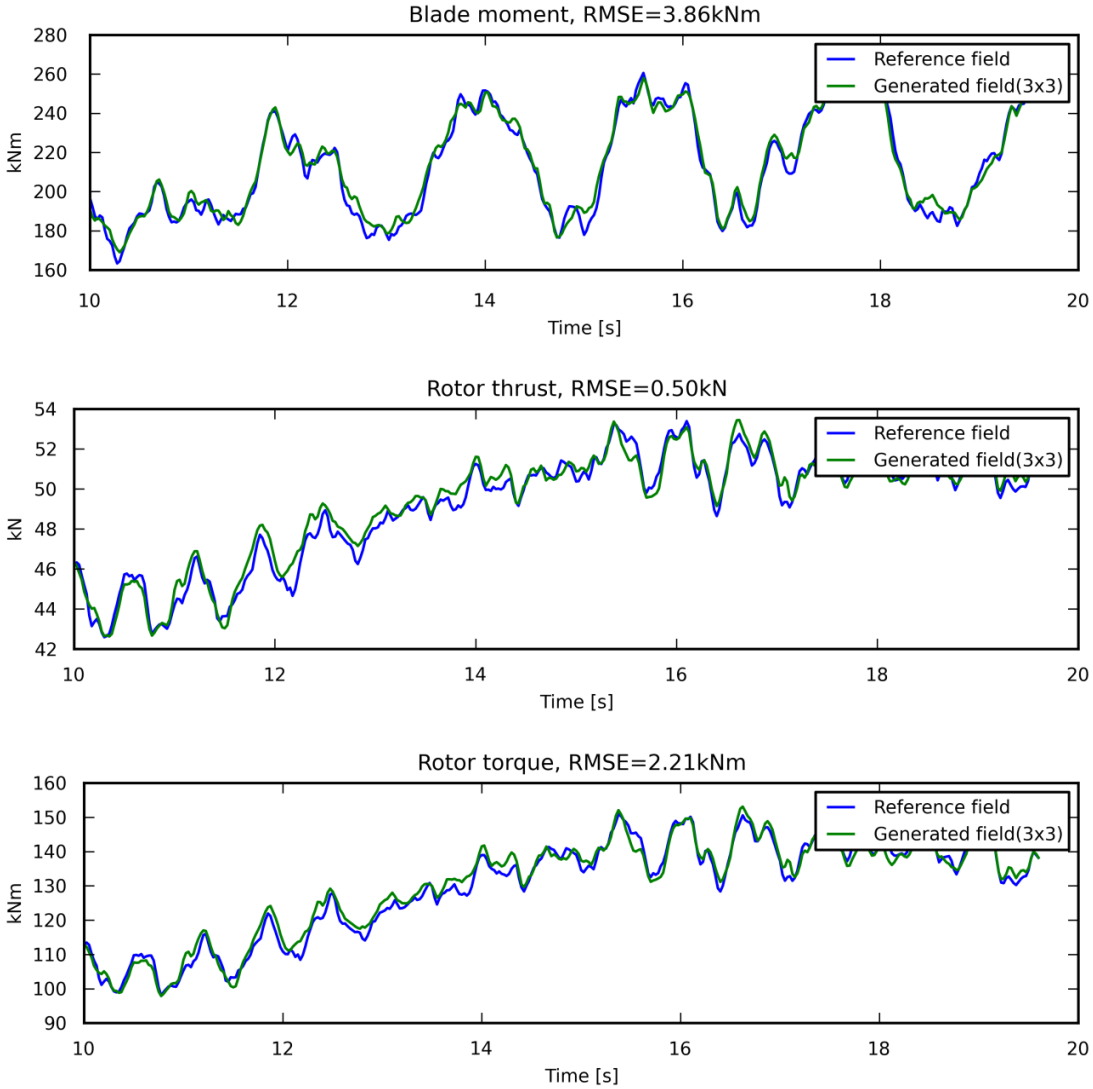

Figure 8. Time series of three load sensors in the reference field and a field generated from measurements of 3x3 pitot tubes. The correspondence is fairly good and the RMSE relatively low

B. Results using full scale measurements

To validate the results of applying the method to full scale measurements, the estimated free wind speed have been compared to the measured wind speeds on mast 3 in a situation where the wind direction is parallel to a straight line from mast 3 to the pitot tube when the blade is in azimuthal position 270, see Figure 9.

To compensate for the spatial distance between mast 3 and the turbine, a time offset is added to the measurements from mast 3 which corresponds to the time it takes an imaginary air parcel to travel the 240m at the current mean wind speed (i.e. Taylor advection is assumed).

Figure 9. The estimated free wind speed is compared to the measurements of mast 3 in a situation where the wind direction is 277, i.e. parallel to a straight line from mast 3 to the pitot tube when the blade is in azimuthal position 270

In the upper plot of Figure 10, the estimated free wind speeds for all azimuthal positions are seen, i.e. variations caused by shear and veer are included. The lower plot shows the estimated wind speeds of azimuthal position 270 only. In both plots a quite good correlation is seen, but the estimated free wind speed seems to be about 1.3 m/s lower in average. This is probably caused by an inaccurate estimation of the orientation of the pitot tube.

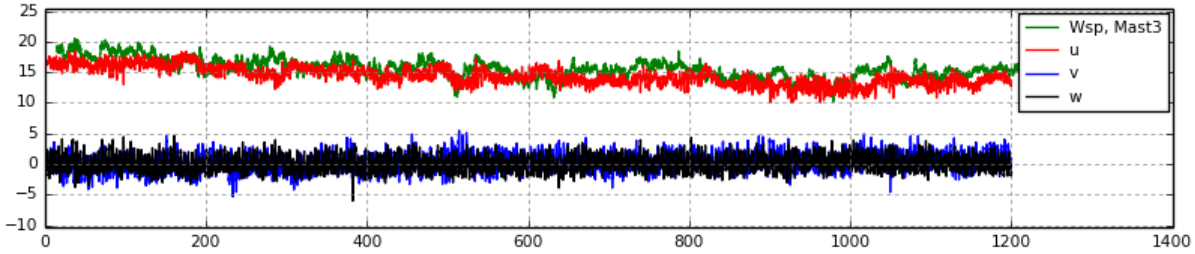

a) Comparison for all azimuthal positions

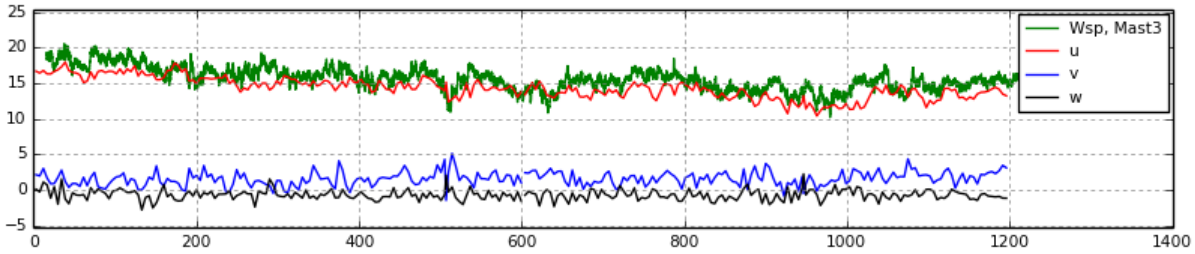

b) Comparison for azimuthal position 270 only

Figure 10. Comparison between estimated free wind speed and measured horizontal wind speed at mast 3. A quite good agreement is seen.

Furthermore the method has been applied to three sets of 10 minutes measurements and the resulting estimated free wind speeds as function of height have been compared to statistics, i.e. min, mean and max, of the the wind speeds measured by the nearby masts.

The situation at 2009-05-26 01:00 is seen in Figure 11. The wind is coming from East and the variation of the direction is fairly small - standard deviation is 0.9deg. The turbines, wake indicators and met masts are shown on the

map in Figure 11 a). The side length of the wake indicators are 500m long and follow the mean wind direction +/- 2 standard deviations. The average wind speed is around 8m/s and the current turbine (red) is generating 1.3MW.

In Figure 11 b), the min, mean and max statisticts of the wind speeds measured at the nearby masts are plotted as function of height.

As seen on the map, masts 1-5 are in wake of the turbines and the wind speeds measured by mast 1 and 3 are 2-3m/s lower than the wind speeds measured by the masts exposed to the free inflow. The reason why mast 2, 4 and 5 do not measure lower wind speeds is most likely that the corresponding turbines are not running, but unfortunately the status of these turbines are not available.

The result of applying the present method to the available pitot tube measurements is seen by the thick red line in Figure 11 b). The line shows the average of the estimated free wind speeds as function of azimuthal position mapped to height, i.e. two lines are seen, one for azimuthal position 0-180 deg, when the blade moves up, and one for azimuthal position 180-360 when the blade moves down. The little difference between the two sides of the rotor is probably due to skew inflow caused by a small yaw error.

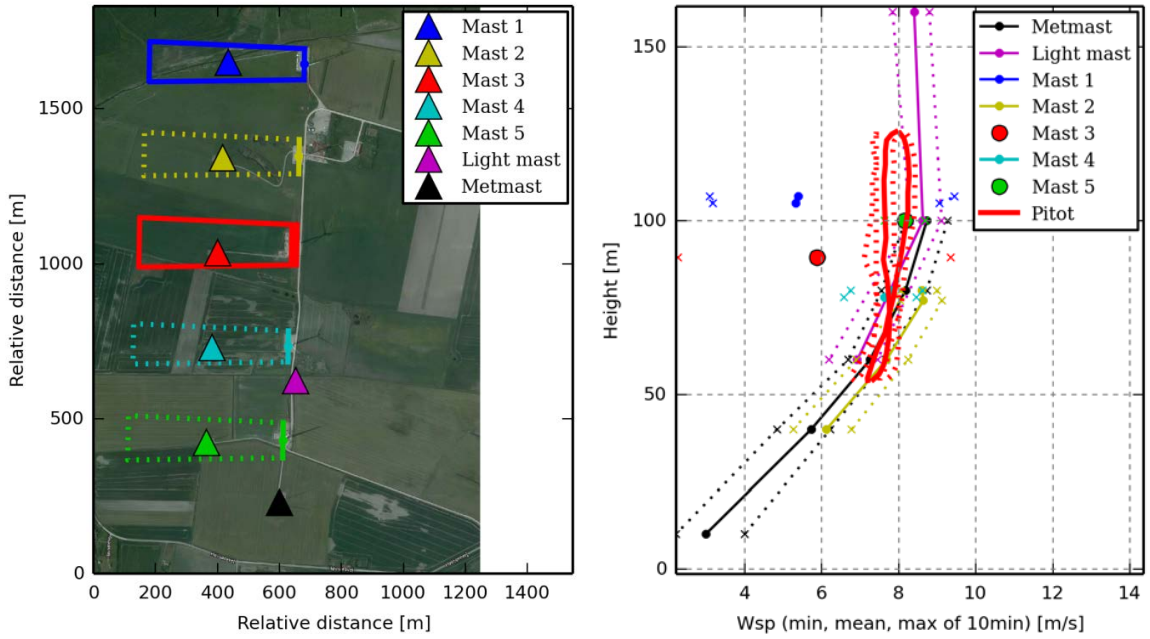

a) Turbines, wake indicators and masts

b) Measured and estimated wind speeds as function of height

Figure 11. Mast 3 in wake. Mean wind direction: 91.0 (std 0.9)

Another situation is shown in Figure 12. In this case, 2009-05-26 14:20, the wind comes from the South with larger turbulent fluctuations compared to the above case. The sensors at 60m and 100m of the light mast (purple triangle) are in wake, while the top sensor of the light mast, the Metmast and masts 1-5 are exposed to the free inflow.

The level of the estimated free wind speed is below wind speed of the free inflow as the turbine is in wake of turbine 5 and turbine 4 (which may not be operating), but above the wind speeds measured at the lower sensors of the light mast as the distance to the upstream blocking turbines are larger.

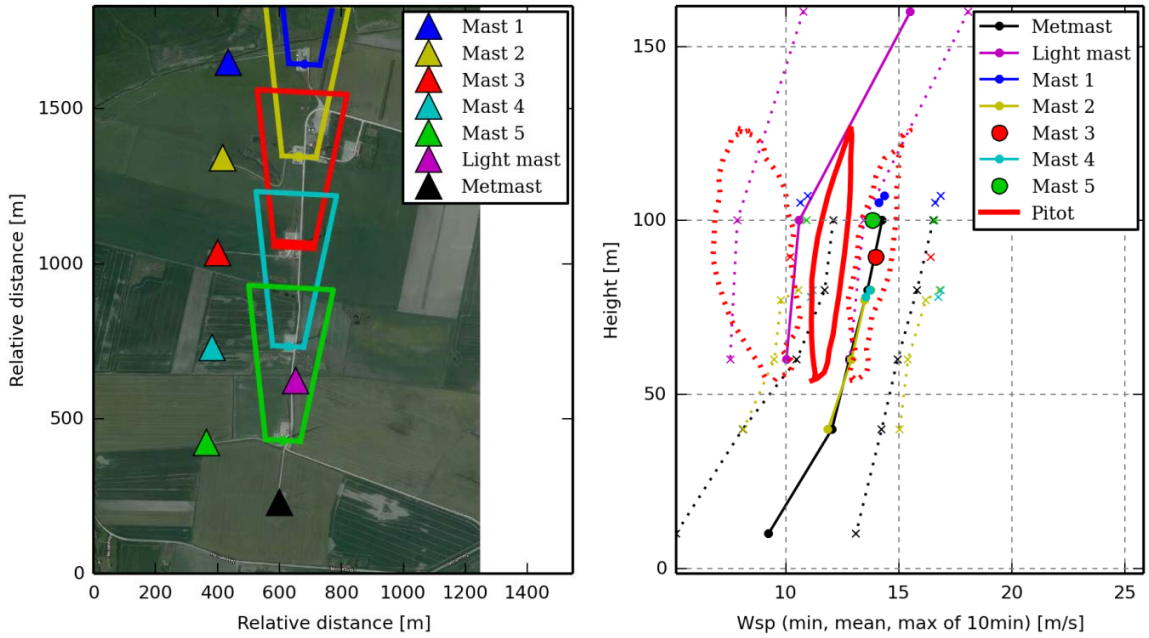

Figure 12.Light mast (60m and 100m) and turbine 3 in wake. Mean wind direction: 183.0 (std 4.6)

Finally Figure 13 illustrates a half wake situation occurring 2009-04-24 03:30 where only part of the rotor is exposed to the wake from the upstream positioned turbine 4 and 5, but as the light mast does not measure significant lower wind speeds, turbine 5 is probably not running. In this case markers have been attached to the estimated free inflow, and as expected the lowest wind speeds are measured when the blade moves down, i.e. in the right side of the rotor in Figure 13 which is covered by the wake indicator of turbine 4. In this case the difference in wind speed between the two sides of the rotor is about 2.5 m/s in average.

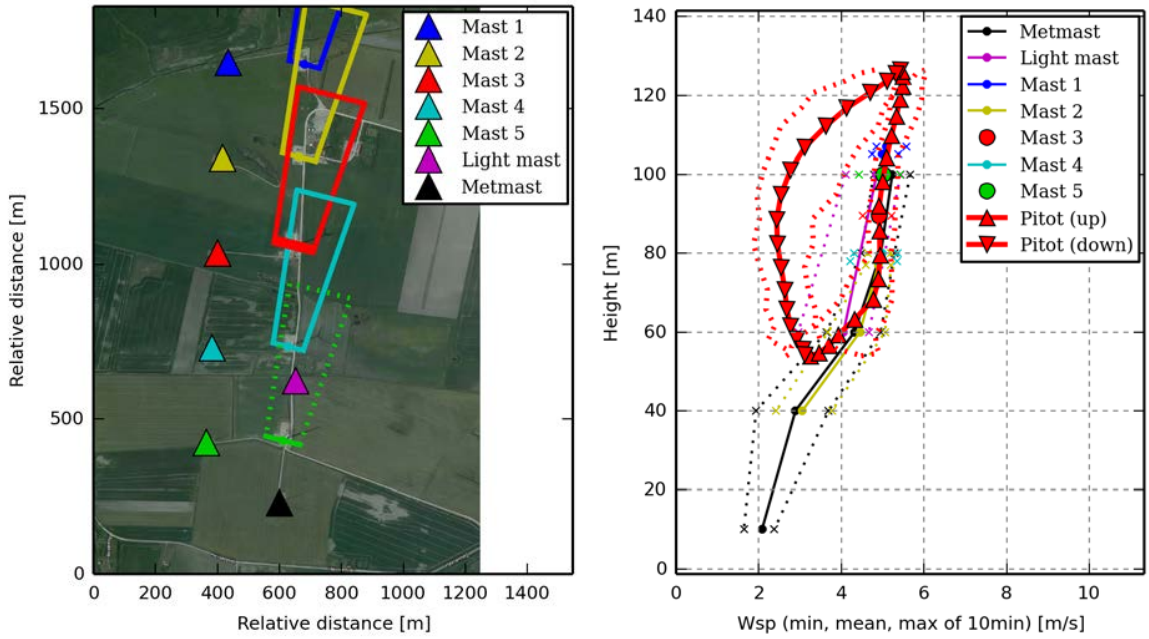

Figure 13.Turbine 3 in half wake. Mean wind direction: 194.0 (std: 2.6)

Conclusion

In this paper it is concluded that pitot tube measurements can be used to derive very detailed information of the incoming turbulent flow field.

For wind speeds above rated, the influence of turbine induction is very limited with very small blockage. At low wind speed the measured inflow is affected by the presence of the turbine. This blockage can, however, be compensated by well-established theory for induction of wind turbines using an extended blade element momentum theory.

The approach has been demonstrated in numerical studies and on full scale measurements.

It has also been shown numerically that the pitot tube measurements can be used as input for a constraint simulation turbulence model to re-generate the entire incoming turbulence field rather accurately. This can be used as input to aeroelastic simulations and hopefully contribute to the explanation of dynamic load issues observed occasionally.

Applied to full scale measurements, the method demonstrates capability to estimate the free inflow in different wake conditions, even though several issues regarding calibration, corrupted sensors, outliers etc. must be further addressed.

It is expected that pitot tubes can be used to complement lidar and cup anemometer measurements and thereby increase the available information regarding the incoming flow field.

Acknowledgments

The work has partly been carried out within the projects: “Aerodynamics and Optimization of Wind Power Systems in Complex Terrain” and “Research and development of optimal wind turbine rotors under offshore wind conditions in China (OffWindChina)” funded by The Sino-Danish Research Collaboration within Sustainable and Renewable Energy 2010 in corporation with the Chinese Ministry of Science and Technology and Danish Council for Strategic Research.

References

[1] Peña, A., Hasager, C. B., Lange, J., Anger, J., Badger, M., Bingöl, F., Bischoff, O., Cariou, J.-P., Dunne, F., Emeis, S., Harris, M., Hofsäss, M., Karagali, I., Laks, J., Larsen, S. E., Mann, J., Mikkelsen, T., Pao, L. Y., Pitter, M., Rettenmeier, A., Sathe, A., Scanzani, F., Schlipf, D., Simley, E., Slinger, C., Wagner, R., and Würth, I., *Remote Sensing for Wind Energy*, DTU Wind Energy, 2013.

[2] Mann, J., Cariou, J.-P., Courtney, M., Parmentier, R., Mikkelsen, T., Wagner, R., Lindelöw, P. J. P., Sjöholm, M., and Enevoldsen, K., “Comparison of 3D turbulence measurements using three staring wind lidars and a sonic anemometer,” *Meteorologische Zeitschrift*, vol. 18, 2009, pp. 135–140.

[3] Aagaard Madsen, H., and Fischer, A., “Wind shear and turbulence characteristics from inflow measurements on the rotating blade of a wind turbine rotor,” *EWEC 2009 Scientific proceedings*, EWEC, 2009, pp. 53–58.

[4] Andersen, P. S., Petersen, H., Krabbe, U., and Lundsager, P., *Basismateriale for beregning af propelvindmøller*, 1979.

[5] Madsen, H. A., Bak, C., Døssing, M., Mikkelsen, R., and Øye, S., “Validation and modifi cation of the Blade Element Momentum theory based on comparisons with actuator disc simulations,” 2010, pp. 373–389.

[6] “HAWC2 course apr 2013,” *Energi, Risø DTU Nationallaboratoriet for Bæredygtig* Available: http://www.hawc2.dk/HAWC2 Download/Presentations/HAWC2 course apr 2013.aspx.

[7] Sørensen, N. N., and Madsen, H. A., “Modelling of transient wind turbine loads during pitch motion,” *paper and poster). In: Proceedings (online). 2006 European Wind Energy Conference and Exhibition, Athens (GR)*, 2006.

[8] Larsen, T. J., and Hansen, A. M., *How 2 HAWC2, the user’s manual*, Risø National Laboratory, 2007.

[9] Aagaard Madsen, H., Bak, C., Schmidt Paulsen, U., Gaunaa, M., Fuglsang, P., Romblad, J., Olesen, N. A., Enevoldsen, P., Laursen, J., and Jensen, L., *The DAN-AERO MW Experiments: Final report*, Danmarks Tekniske Universitet, Risø Nationallaboratoriet for Bæredygtig Energi, 2010.

[10] Nielsen, M., Larsen, G. C., Mann, J., Ott, S., Hansen, K. S., and Pedersen, B. J., "Wind simulation for extreme and fatigue loads," *Technical report, Risø-R-1437 (EN)*, vol. 104, 2003.

[11] Mann, J., Larsen, G. C., and Larsen, T. J., "Towards more realistic extreme load predictions (paper and poster)," *European Wind Energy Association (EWEA), Proceedings (online)*, 2006.

APPENDIX B

Using wind speed from a blade-mounted flow sensor for power and load assessment on modern wind turbines

Wind Energ. Sci., 2, 547–567, 2017
https://doi.org/10.5194/wes-2-547-2017

eawe european academy of wind energy
Open Access
WIND ENERGY SCIENCE

Using wind speed from a blade-mounted flow sensor for power and load assessment on modern wind turbines

Mads M. Pedersen, Torben J. Larsen, Helge Aa. Madsen, and Gunner Chr. Larsen

Wind Energy Department, Technical University of Denmark,
Frederiksborgvej 399, 4000 Roskilde, Denmark

Correspondence to: Mads M. Pedersen (mmpe@dtu.dk)

Received: 19 May 2017 – Discussion started: 14 June 2017
Revised: 11 October 2017 – Accepted: 12 October 2017 – Published: 20 November 2017

Abstract. In this paper an alternative method to evaluate power performance and loads on wind turbines using a blade-mounted flow sensor is investigated. The hypothesis is that the wind speed measured at the blades has a high correlation with the power and loads such that a power or load assessment can be performed from a few hours or days of measurements.

In the present study a blade-mounted five-hole pitot tube is used as the flow sensor as an alternative to the conventional approach, where the reference wind speed is either measured at a nearby met mast or on the nacelle using lidar technology or cup anemometers. From the flow sensor measurements, an accurate estimate of the wind speed at the rotor plane can be obtained. This wind speed is disturbed by the presence of the wind turbine, and it is therefore different from the free-flow wind speed. However, the recorded wind speed has a high correlation with the actual power production as well as the flap-wise loads as it is measured close to the blade where the aerodynamic forces are acting.

Conventional power curves are based on at least 180 h of 10 min mean values, but using the blade-mounted flow sensor both the observation average time and the overall assessment time can potentially be shortened. The basis for this hypothesis is that the sensor is able to provide more observations with higher accuracy, as the sensor follows the rotation of the rotor and because of the high correlation between the flow at the blades and the power production. This is the research question addressed in this paper.

The method is first tested using aeroelastic simulations where the dependence of the radial position and effect of multiple blade-mounted flow sensors are also investigated. Next the method is evaluated on the basis of full-scale measurements on a pitch-regulated, variable-speed 3.6 MW wind turbine.

It is concluded that the wind speed derived from the blade-mounted flow sensor is highly correlated with the power and flap-wise bending moment and that the method has advantages over the traditional approach where the met-mast wind speed is used as reference, e.g. the capability of measuring the shear, veer and turbulence. The aeroelastic simulations show that the assessment time can be reduced, but this reduction cannot be confirmed from the current measurement database due to sensor problems and practical circumstances. Measuring the wind speed at the rotor plane comes with a price as the wind speed is affected by the induction which may be sensitive to the changes you want to evaluate, e.g. different vortex generator configurations. Furthermore it is concluded that a robust instrument and measurement system is required to obtain accurate and reliable wind speed recordings from pitot-tube measurements.

Published by Copernicus Publications on behalf of the European Academy of Wind Energy e.V.

1 Introduction

Detailed knowledge about the wind speed and its variations is essential when evaluating the power performance, load levels and noise migration of modern wind turbines as these properties are highly dependent on the incoming wind conditions (Elliott and Cadogan, 1990; Larsen et al., 2005; Barlas et al., 2012; Aagaard Madsen, 2014; St. Martin et al., 2016).

Measuring the correct wind speed is a challenge. Often the wind speed is measured by a cup or sonic anemometer at a met mast 2 to 3 rotor diameters away, but if the mean wind direction is not exactly towards the wind turbine, the measured wind will not hit the rotor. Even if the wind direction is exactly towards the turbine, the correlation between the measured wind and the wind at the rotor will decrease with the distance, as smaller turbulence structures will change on their way to the turbine. Using a proper average time, e.g. 10 min mean values, the temporal and spatial discrepancies are somewhat averaged out, and a good correlation between wind speed and power is achievable.

Another option is to measure the wind with an anemometer mounted on the spinner or the nacelle. In this case the spatial and temporal distance is not an issue, but the measured wind speed is distorted by the rotor. In addition the variation over the rotor plane is often significant due to shear, veer and turbulence – especially in complex terrain and wind farms – and this variation is not captured by an anemometer on the spinner or the nacelle.

Lidar technology is capable of measuring this variation, but in most setups the lidar is configured to scan the inflow at some distance upstream, where the temporal and spatial correlation is lower.

A fourth option is to measure the wind with a blade-mounted flow sensor. In this way the correlation between cause and effect is higher, as the wind is measured exactly where it affects the wind turbine and the effects of shear, veer and smaller turbulence structures are also captured.

Over the last 28 years, blade-mounted five-hole pitot tubes have been used in several research projects to characterize the inflow of wind turbines (Aagaard Madsen, 1991; Petersen and Aagaard Madsen, 1997; Aagaard Madsen et al., 2003, 2010b; Pedersen et al., 2015). Five-hole pitot tubes measure the relative flow velocity as well as the flow angle in two perpendicular planes, and from these quantities three-dimensional turbulent wind speeds can be derived.

In 1989, a pitot tube was mounted on a 95 kW Tellus turbine; see Fig. 1. The turbine was a fixed-pitch, constant-speed, stall-regulated turbine with rather stiff blades; i.e. the angle of attack, measured by the pitot tube, is highly correlated with the axial wind speed at the pitot tube.

A subset of the Tellus measurement dataset has been procured for this study. In Fig. 2, the 30 s mean power-production observations are plotted as a function of the angle of attack (a) and met-mast wind speed (b). The met mast is located 2.5 diameters from the turbine, and observations

Figure 1. Five-hole pitot tube mounted on the blade of a 95 kW Tellus turbine at Risø in 1995.

where the met mast is in the wake are excluded from Fig. 2b. It is seen that the power production correlates much more highly with the angle of attack than with the met-mast wind speed, especially below stall.

The quality of a power curve depends on the number of data points and the scatter of these points; furthermore, all regions of the curve must contain enough data points. The number of data points can be increased by extending the measurement period, but it can also be increased by reducing the averaging time. In Fig. 3 the averaging time of the pitot-tube-based plot is reduced to the time of one revolution (~ 1.25 s); i.e. around 24 times more data points are obtained from the same measurement period, and the scatter level is still lower than the met-mast-based 30 s mean observations in the region below stall.

This means that the assessment time can be significantly reduced, as many more data points with less scatter are obtained and in addition rarely occurring wind speeds are more likely to occur for a 1.25 s than for a 30 s averaging period.

Today, 28 years later, standard wind turbines are pitch regulated and operated with variable speed and have a 5–10 times larger rotor and very flexible blades. In this paper we will therefore investigate if a similar speed-up in power and flap load assessment time is achievable by using pitot-tube measurements as an inflow reference on modern megawatt wind turbines such that a power curve and load validation can be conducted from a few days of measurements.

The study is based on aeroelastic simulations using the code HAWC2 (Larsen and Hansen, 2007) and measurements on a Siemens 3.6 MW wind turbine.

2 Method

In this section the applied procedures for deriving wind speed from pitot-tube measurements are presented as well as the

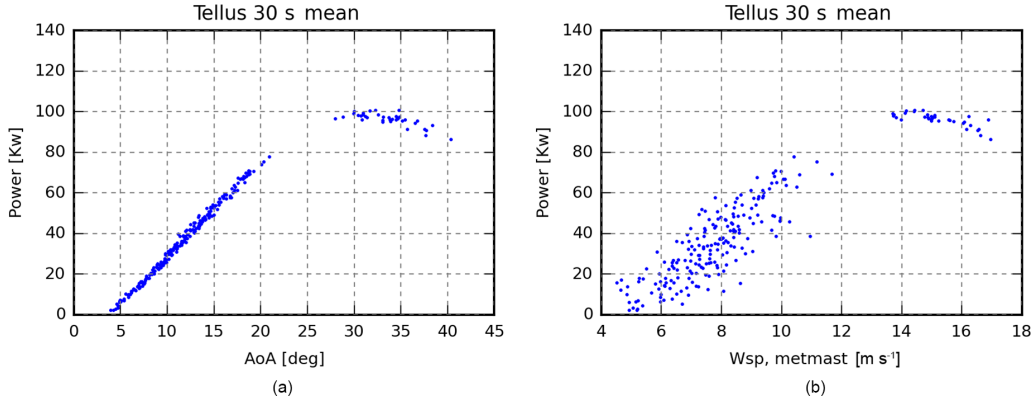

Figure 2. The 30 s mean electrical power of the Tellus turbine correlates much more highly with the angle of attack **(a)** than the met-mast wind speed **(b)**.

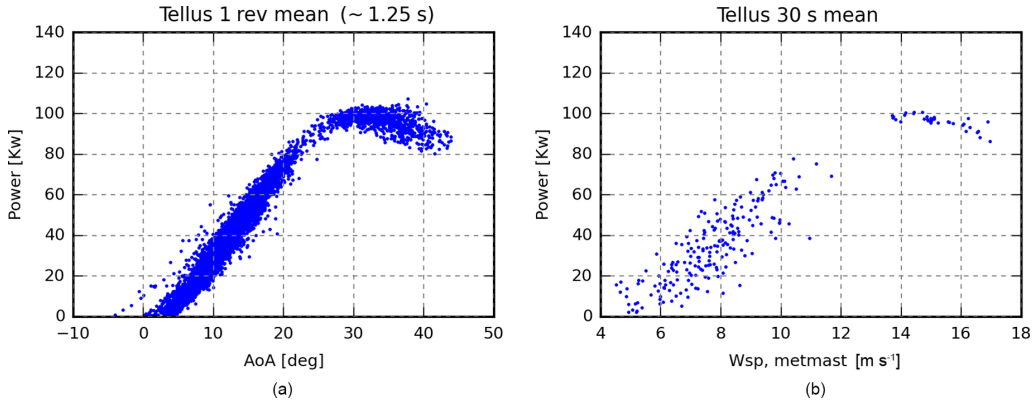

Figure 3. Despite the much lower average time – one revolution (∼ 1.25 s) instead of 30 s – the average scatter level of the pitot-tube-based observations **(a)** is still lower than the level of the met-mast-based observations in the region below stall **(b)**.

error measure that is used to evaluate the quality of power and flap load curves.

2.1 Deriving the wind speed from the angle of attack on the Tellus turbine

For the Tellus turbine which has a fixed pitch, constant rotor speed and rather stiff blades, the axial wind speed at the pitot tube, v_y, is a function of the rotor speed, v_{rot}, and the angle of attack, α (see Fig. 4):

$$v_y = \tan(\alpha)\, v_{\mathrm{rot}} \rightarrow \alpha \propto \operatorname{atan}\left(v_y\right). \tag{1}$$

The inflow angle measured by the pitot tube, α_{p}, obviously depends on the angle of the pitot tube but also on the position due to increased upwash near the airfoil; see Figure 5. In general the relation between the angle of attack and the flow angle at a point near the airfoil, F_α, is nonlinear but monotonically increasing in the region of interest if the effects of dynamic stall are neglected.

The Tellus turbine has 5° tilt (angle between shaft and horizontal); i.e. α_{p} is increased when the blade moves up and

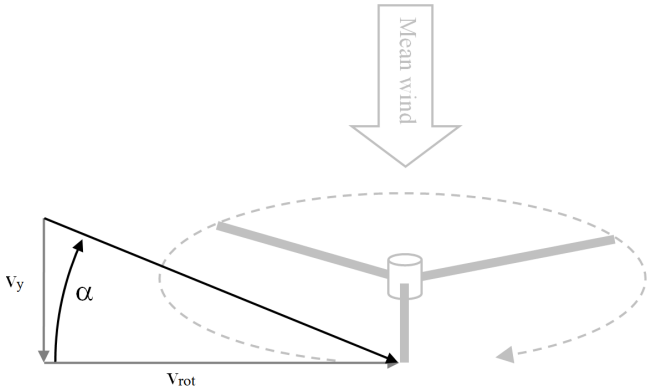

Figure 4. In the simple case, the axial wind speed, v_y, is a monotonic function of α.

vice versa, so that u_{p} becomes

$$v_y = \cos(\theta_{\mathrm{tilt}}) \tan\left(F_\alpha\left(\alpha_{\mathrm{p}}\right) + \theta_{\mathrm{pitot}} - \theta_{\mathrm{tilt}} \sin\left(\theta_{\mathrm{rotorposition}}\right)\right) v_{\mathrm{rot}}. \tag{2}$$

As the sinusoidal contribution from tilt is almost cancelled out when averaging over one revolution, the average axial

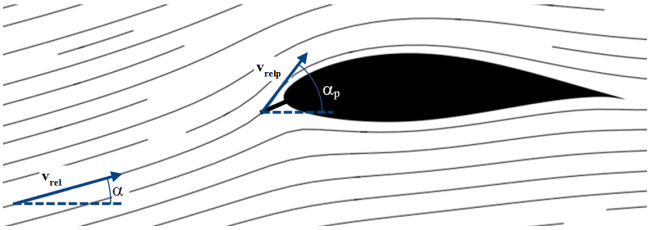

Figure 5. Map of flow velocities near the airfoil. The flow angle, α_p, and velocity, v_{relp}, are different due to local circulation and stagnation.

wind speed can be considered a monotonic function of α_p when averaging over one or more revolutions.

2.2 Deriving the wind speed from pitot-tube measurements of modern wind turbines

For modern wind turbines with variable pitch and rotor speed, α_p cannot be used directly as a measure of the axial wind speed. In this case the following procedure is used:

- determine the angle of attack and relative velocity from the flow angle and velocity measured by the pitot tube
- map the angle of attack, relative velocity and pitot-tube side-slip angle from spherical coordinates to a 3-D Cartesian flow vector
- determine and subtract the velocity due to the movement of the pitot tube
- map the wind speed vector onto global coordinates and extract the horizontal component.

2.2.1 Estimating the angle of attack

At the pitot-tube tip, i.e. near the airfoil, the flow angle, α_p, and the relative speed, $|v_{relp}|$, are different due to local circulation around the blade section and deceleration of the flow; see Fig. 5. The first step is therefore to find the angle of attack, α, and the relative speed, $|v_{rel}|$.

For the simulations, this step is not necessary, as HAWC2 directly computes α and $|v_{rel}|$ based on the blade element momentum (BEM) model.

For the measurements, 2-D computational fluid dynamics (CFD) simulations have been used to compute the velocity, v_{relp}, for different angles of attack. From these velocities two functions are generated. The first function, F_α, maps α_p to α (see Fig. 6a), while the second, F_{vrel}, gives the flow speed at the pitot tube, $|v_{relp}|$, relative to the flow speed some distance upstream, $|v_{rel}|$:

$$|\boldsymbol{v}_{rel}| = \frac{|\boldsymbol{v}_{relp}|}{F_{vrel}(\alpha)}; \tag{3}$$

see Fig. 6b.

2.2.2 Map onto 3-D flow vector

In Fig. 7 the relations between the wind speed in polar coordinates, $(\alpha, \beta, |v_{rel}|)$, and Cartesian coordinates, $(v_{rel,x}, v_{rel,y}, v_{rel,z})$, are seen.

These relations can be formulated as

$$\tan\alpha = \frac{v_{rel,y}}{v_{rel,x}}, \tag{4}$$

$$\tan\beta = \frac{-v_{rel,z}}{v_{rel,x}}, \tag{5}$$

$$|\boldsymbol{v}_{rel}| = \sqrt{v_{rel,x}^2 + v_{rel,y}^2 + v_{rel,z}^2}, \tag{6}$$

and, now, $\boldsymbol{v}_{rel} = \begin{bmatrix} v_{rel,x} & v_{rel,y} & v_{rel,z} \end{bmatrix}^T$ can be derived:

$$v_{rel,x} = \begin{Bmatrix} -\sqrt{\dfrac{|\boldsymbol{v}_{rel}|^2}{1+(\tan\alpha)^2+(\tan\beta)^2}} & , \text{for } |\beta| \le 90^\circ \\ \sqrt{\dfrac{|\boldsymbol{v}_{rel}|^2}{1+(\tan\alpha)^2+(\tan\beta)^2}} & , \text{for } |\beta| > 90^\circ \end{Bmatrix}, \tag{7}$$

$$v_{rel,y} = \begin{Bmatrix} -\sqrt{\dfrac{|\boldsymbol{v}_{rel}|^2}{\left(\frac{1}{\tan\alpha}\right)^2+1+\left(\frac{\tan\beta}{\tan\alpha}\right)^2}} & , \text{for } \alpha > 0 \\ 0 & , \text{for } \alpha = 0 \\ \sqrt{\dfrac{|\boldsymbol{v}_{rel}|^2}{\left(\frac{1}{\tan\alpha}\right)^2+1+\left(\frac{\tan\beta}{\tan\alpha}\right)^2}} & , \text{for } \alpha < 0 \end{Bmatrix}, \tag{8}$$

$$v_{rel,z} = \begin{Bmatrix} \sqrt{\dfrac{|\boldsymbol{v}_{rel}|^2}{\left(\frac{1}{\tan\beta}\right)^2+\left(\frac{\tan\alpha}{\tan\beta}\right)^2+1}} & , \text{for } \beta > 0 \\ 0 & , \text{for } \beta = 0 \\ -\sqrt{\dfrac{|\boldsymbol{v}_{rel}|^2}{\left(\frac{1}{\tan\beta}\right)^2+\left(\frac{\tan\alpha}{\tan\beta}\right)^2+1}} & , \text{for } \beta < 0 \end{Bmatrix}. \tag{9}$$

2.2.3 Estimate and subtract the movement of the pitot tube

The pitot-tube movement derives from three factors: the rotor speed, pitch motions and the speed due to blade deflection.

The rotor speed contributes with a tangential speed, v_{rot}, which is the product of the rotor speed, ω_{rot}, and the radius of the pitot-tube tip; see Fig. 8a. Note that the radius changes during pitch motion.

Similarly, pitch motions also result in a velocity, v_{pitch}, tangential to the pitch axis; see Fig. 8b.

As the speed due to blade deflection cannot be extracted from the current measurement database, this contribution is not included in the present study. The error introduced by this simplification is, however, analysed in Sect. 4.3.

The measured relative flow velocity, rotational velocity and pitch velocity are now mapped to a common blade co-

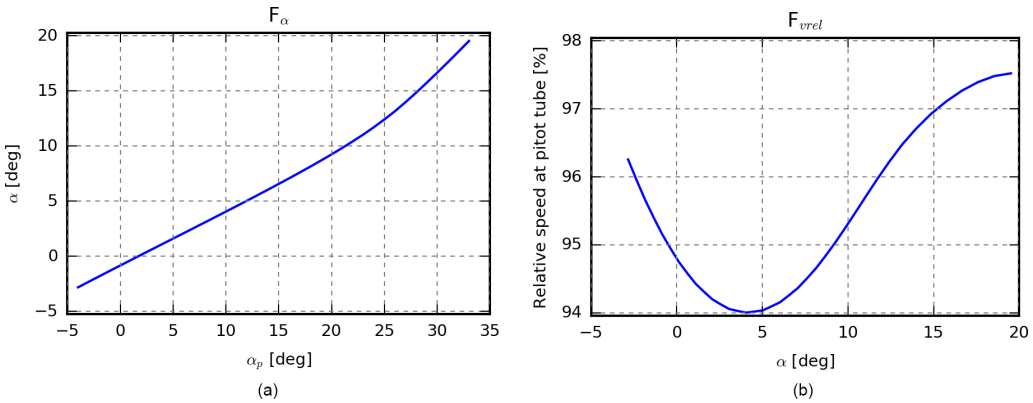

Figure 6. **(a)** Angle of attack, α, as a function of flow angle measured by pitot tube, α_p. **(b)** Relative speed at position of pitot tube as a function of the angle of attack.

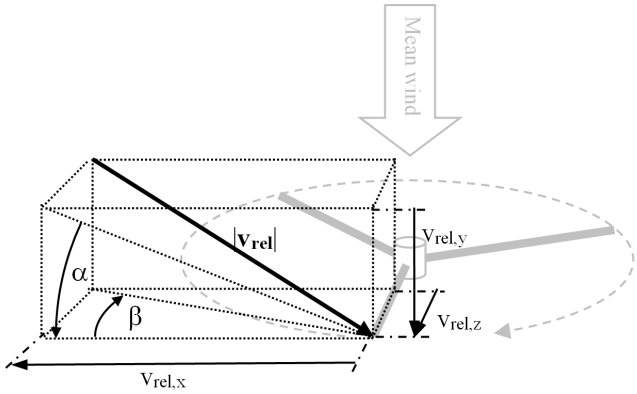

Figure 7. Relation between $(\alpha, \beta, |v_{\mathrm{rel}}|)$ and $[v_{\mathrm{rel},x}, v_{\mathrm{rel},y}, v_{\mathrm{rel},z}]^T$.

ordinate system (indexed B) and subtracted.

$$\boldsymbol{v}^{\mathrm{B}} = V_{\mathrm{rel}}^{\mathrm{B}} - \boldsymbol{v}_{\mathrm{rot}}^{\mathrm{B}} - \boldsymbol{v}_{\mathrm{pitch}}^{\mathrm{B}} \tag{10}$$

2.2.4 Map to global coordinates

Finally the flow velocity is mapped to a global coordinate system using rotation from pitch, coning (downwind angle of blades relative to a line perpendicular to the shaft) , rotor position and tilt, and the horizontal wind speed component parallel to the main shaft, v_y, is extracted.

2.3 Power of variable-speed wind turbines

Wind turbines convert aerodynamic power to electrical power, but some energy is "stored" as angular momentum in the rotor. When dealing with small timescales on modern variable-speed wind turbines, the fraction of the aerodynamic power used to accelerate or decelerate the rotor may be significant. To include this energy buffer, the power observations used in this study are compensated for rotor speed variations when the power is below rated power by

$$\overline{\mathrm{Power}} = \overline{\mathrm{Power}_{\mathrm{electric}}} + \frac{\frac{1}{2} I \left(\omega_{\mathrm{rot},t1}^2 - \omega_{\mathrm{rot},t2}^2\right)}{t2 - t1}, \tag{11}$$

where I is the inertia of the rotor, ω_{rot} is the rotational speed, and $t1$ and $t2$ are the start and end time of the observation period, e.g. one revolution.

2.4 Performance curves

First the observations are binned based on their wind speed values. In this study bins of $0.5\,\mathrm{m\,s^{-1}}$ ranging from 3 to $18\,\mathrm{m\,s^{-1}}$ are used. For each bin the mean wind speed is calculated as well as the mean power/flap load, and then the power and flap load performance curves are generated by linear interpolation between these mean values.

2.5 Error measure

The accuracy of the pitot-based power and load curves cannot be evaluated in its present form as the curves cannot be compared to reference curves of existing methods that are based on free-flow wind speed. We will therefore focus on variability between periods or cases instead of accuracy.

If the curves obtained in similar conditions are equivalent, then it will be possible to make a small adjustment on the rotor, e.g. changing the tip shape or vortex generator configuration, and to determine whether the change affects the power production or load levels.

For this purpose the variation in terms of the mean standard deviation will be used.

For each set of observations, a power or flap load performance curve, PC, is generated. For M different wind speeds, the standard deviation of all PCs is then calculated, and the mean standard deviation in percent of maximum power or

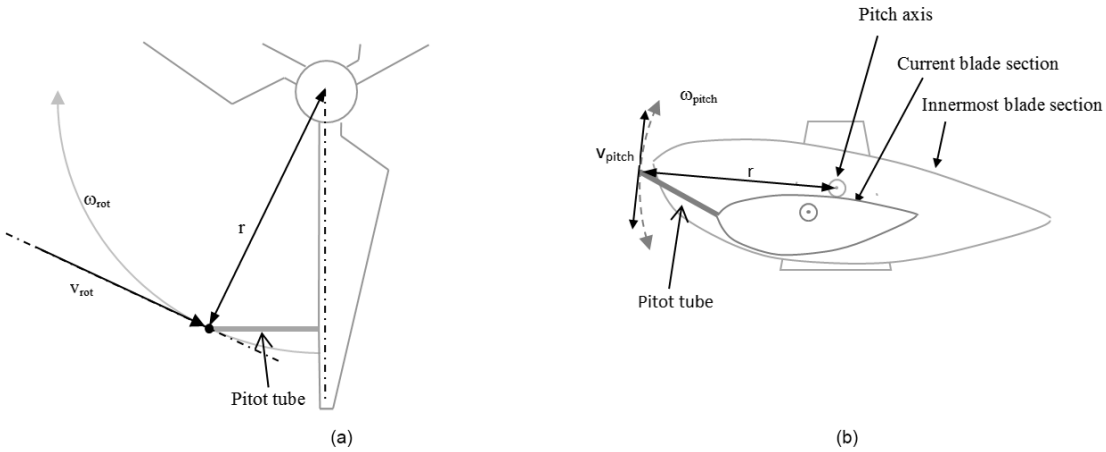

Figure 8. Rotor rotation **(a)** and pitch motion **(b)** moves the pitot tube and contributes to the flow speed measured by the pitot tube.

load is used as an error measure:

$$\text{Variation} = \frac{\frac{1}{M}\sum_{j=1..M}\sqrt{\frac{1}{N}\sum_{i=1..N}\left(\text{PC}_i\left(\text{wsp}_j\right)-\overline{\text{PC}\left(\text{wsp}_j\right)}\right)^2}}{\max(\text{PC})}. \quad (12)$$

In the parameter study referred to in Sect. 5.2, the effects of different inflow conditions are investigated by changing an inflow parameter, e.g. the turbulence intensity, and comparing the resulting power and load curves to a reference curve. In this case the error measure is modified, such that the curves are compared to the reference curve:

$$\text{Variation} = \frac{\frac{1}{M}\sum_{j=1..M}\sqrt{\left(\text{PC}\left(\text{wsp}_j\right)-\text{PC}_{\text{ref}}\left(\text{wsp}_j\right)\right)^2}}{\max(\text{PC})}. \quad (13)$$

3 Numerical study

In this section, simulation results are used to investigate the optimal averaging time, the uncertainties introduced by blade deflection and torsion and the optimal radial position of the blade-mounted flow sensor. Finally, a numerically based estimation of the achievable assessment time reduction is presented.

The simulations are performed using HAWC2, which is a nonlinear aeroelastic code intended for computing wind turbine response in the time domain (Aagaard Madsen et al., 2010b, 2012; Kim et al., 2013; Larsen et al., 2015).

The turbine model used for the simulations is based on the structural and aerodynamic configuration of the Siemens 3.6 MW turbine, which was tested at Høvsøre in 2009 during the DANAERO project (Aagaard Madsen et al., 2010a), i.e. a model of the turbine in the full-scale measurement study in Sect. 5.

3.1 Simulation overview

For the analysis, different simulation sets have been created; see Table 1. All simulation sets contain 30 min of simulation for each wind speed ranging from 3 to 18 m s^{-1} in 0.5 m s^{-1} steps, i.e. 15.5 h of simulation per set.

3.2 Averaging time

For IEC standard power curves, 10 min mean values are required (IEC 61400-12-1, 2005), but in this study shorter average times are also used.

Reducing the averaging time results in more observations with more variation. If the correlation between wind speed and power/load is high, this variation adds usable information, and the uncertainty of the power/load curve decreases. If, on the other hand, the correlation is low, the variation mainly results in more scatter, and nothing is achieved.

To investigate the optimal averaging time, the mean standard deviation of 16 power/load curves has been calculated for different averaging times, ranging from 1 to 600 s. The 16 curves are based on the 16 simulation sets in SIM1; see Table 1. Figure 9 shows an example of the 16 power curves generated from 15 s mean values. The mean variation in the met-mast-based power curves is 0.21 % of rated power, while it is 0.09 % for the pitot-based curves.

The variation is plotted in Fig. 10 as a function of averaging time for power curves based on met-mast wind speeds, free-flow wind speeds at the hub centre and wind speeds from a pitot tube at 36 m.

It is seen that the variation is increased with the distance; i.e. the power curves based on met-mast wind speed have more variation than those based on the wind speed at the hub centre and the pitot wind speed curves have even less variation. Note that in this case the free-flow wind speed at the hub centre is extracted directly from the simulations. This wind speed can be derived from a spinner anemometer or from a nacelle-mounted cup anemometer, but in practice additional

Table 1. Overview of simulations and parameters.

Id	No. sets	No. seeds	Turb. intensity (%)	Shear (power coefficient)	Yaw misalign. (deg)	Air density (kg m^{-3})
SIM1	16	16	Meas.*	Meas.*	0	1.225
Ref	5	5	7.5	0.1	0	1.225
Shear	6	1	7.5	0.01, 0.2, 0.3, 0.4, 0.5, 0.6	0	1.225
Ti	7	1	2.5, 5,. . . , 20	0.1	0	1.225
Yaw	5	1	7.5	0.1	2.5, 5, 7.5, 10	1.225
Dens	4	1	7.5	0.1	0	1.175, 1.2, 1.25, 1.275

* For each wind speed, the mean turbulence intensity and power shear coefficient are extracted from the measurements.

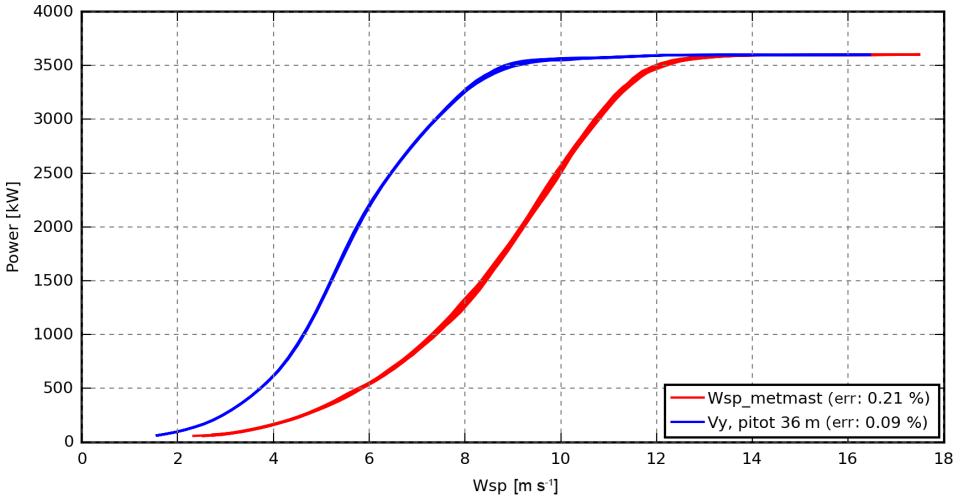

Figure 9. Example of simulated power curve variation based on 15 s mean values. The variation in the 16 met-mast-based curves is twice the variation in the 16 pitot-based curves.

variation is expected to be introduced by tower deflections and the disturbed-to-free-flow transfer function.

The variation in the hub centre and pitot-based curves decreases with shorter averaging times, while the variation in the met-mast-based curves is almost constant due to the lower correlation. In simulations, where the inflow is stationary, the met-mast and hub-centre variations will coincide for longer average times, but in practice long average times are not appropriate due to the non-stationary nature of real inflow.

For average times below one revolution, the variation in the pitot-based curves increases significantly as shear- and turbulence-induced local wind speed variations within the rotor are not averaged out.

Figure 11 shows similar results for the flap moment curves.

3.3 Uncertainty due to blade and tower deflection

During operation, the structure of a modern wind turbine moves and the blades deflect and twist considerably. The motion contributes to the movement of the blade-mounted flow sensor and thereby the measured flow velocity. When calculating the wind speed, the velocity of the sensor should be subtracted from the measured flow velocity, but in this case the velocity deriving from blade deflection is unknown and consequently cannot be subtracted. In addition, blade deflection changes the orientation of the sensor such that the measured flow speed cannot be mapped onto the true global coordinates, as the true orientation is unknown.

The error that these effects introduce to the estimated wind speed has been investigated using numerical simulations. From the first simulation set in SIM1 (see Table 1), pitot-tube data, i.e. α, β, v_{rel}, were output at 11 different radial positions on the blade ranging from the root to the tip. Based on the pitot-tube data, the estimated global wind speed including velocity due to blade deflection was calculated and compared to simulated "real" wind speed.

Figure 12 shows the maximum (a) and mean (b) difference of the axial wind speed component as a function of wind speed and radial position during 30 min of operation. As expected the error increases towards the tip, especially in high wind.

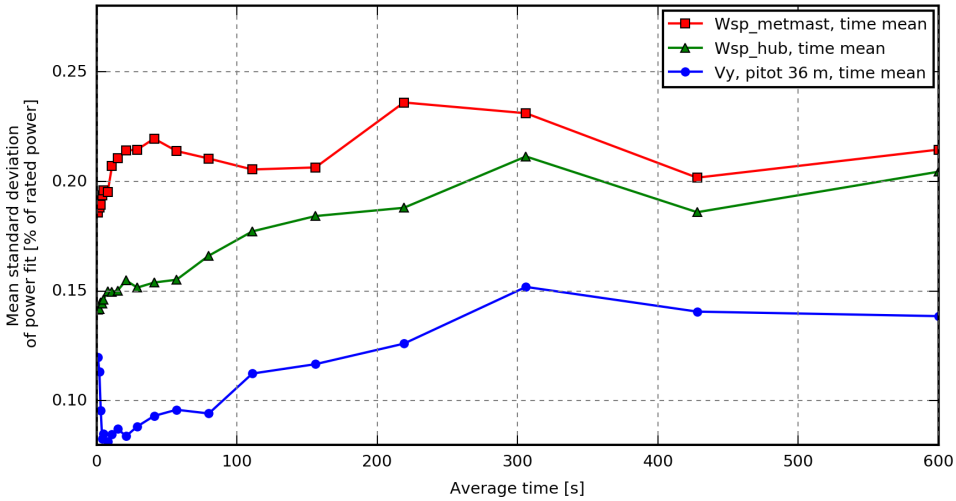

Figure 10. Mean standard deviation of simulated power curves based on met-mast wind speed, free wind speed at the hub centre and wind speed from pitot tube at 36 m. The variation is shown for observation average times ranging from 1 to 600 s.

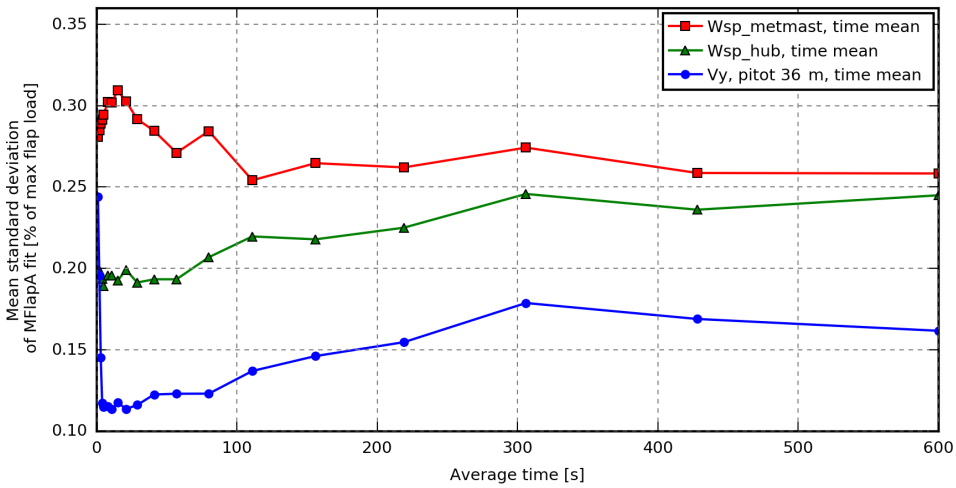

Figure 11. Mean standard deviation of simulated blade flap moment based on met-mast wind speed, free wind speed at the hub centre and wind speed from pitot tube at 36 m. The variation is shown for observation average times ranging from 1 to 600 s.

At 70 %, i.e. close to the position of the pitot tube in the measurements, the maximum error is around 2 m s^{-1}, while the mean error is up to 0.5 m s^{-1}. This means that the instantaneous wind speed estimated from the pitot-tube data is inappropriate for power and load assessment. In this study however, we use the mean of one revolution as the lowest observation average time, and during one revolution the velocity caused by small-scale turbulence-induced deflections as well as 1P (one-per-revolution) periodic deflections, e.g. due to shear, is almost averaged out, as seen in Fig. 13, where the errors of the one-revolution means are shown.

The major part of the remaining error is caused by a static deflection of the blade, which changes the orientation of the sensor. This error is related to the thrust on the rotor and peaks around rated wind speed. For a flow sensor mounted at 70 % in 12 m s^{-1}, Fig. 14a reveals an almost constant offset between the simulated "real" wind speed and the wind speed estimated from the virtual pitot-tube data, which is confirmed by the error distribution plot in Fig. 14b.

The constant part of the error will shift the x axis of the power and load assessment curves in a nonlinear way, but it will not introduce additional variation when comparing power and load curves of different periods, and it can therefore be neglected in this study.

Figure 15 shows the maximum and mean error of the one-revolution mean wind speed after subtracting the mean offset. At 70 % radial position the maximum and mean error are less than 0.2 and 0.05 m s^{-1}, respectively.

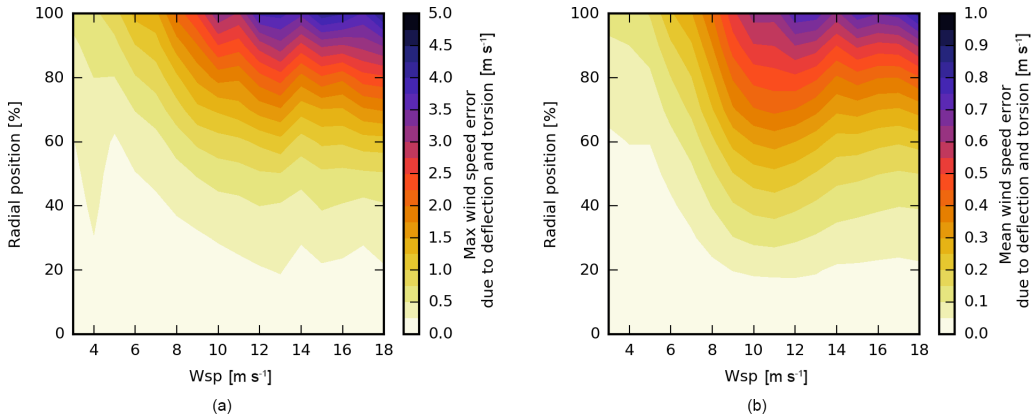

Figure 12. Maximum **(a)** and mean **(b)** simulated wind speed error in the axial direction due to deflection and torsion.

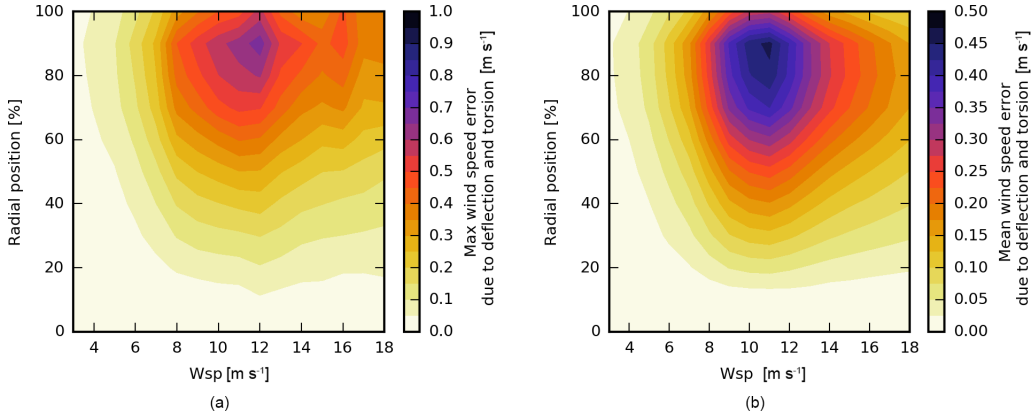

Figure 13. Maximum **(a)** and mean **(b)** simulated error of the wind speed (one-revolution mean) in the axial direction due to deflection and torsion.

3.4 Optimal radial position of blade-mounted flow sensors

A flow sensor mounted near the root will only sweep a small area of the rotor plane, while a flow sensor mounted near the tip will suffer from large deflections, torsion and tip loss effects. From the 16 simulation sets in SIM 1 (see Table 1), power curves are generated based on one-revolution mean values from pitot tubes at different radial positions. The mean standard deviation of these curves is seen in Fig. 16a as a function of radial position. It is seen that a pitot tube at 70 % results in the lowest variation. This means that the position of the pitot tube in the measurements is close to optimal. Using the mean of the wind speeds measured by the pitot tubes at 20, 50 and 80 % gives power curves with only slightly lower variation.

For the flap moment curves, the optimal sensor position is around 50 %; Fig. 16b. In this case a slightly lower variation is also seen when using the mean wind speed measured by three pitot tubes.

3.5 Potential assessment time reduction

In this section we want to quantify the potential assessment time reduction that can be achieved – based on simulations. Due to the higher correlation between the blade-mounted flow sensor wind speed and the power/flap loads, it is expected that fewer observations are required to reach a certain variation level. To quantify the reduction, the variance in power curves generated from 1 to 36 h of one-revolution mean observations is calculated; see Fig. 17. The observations used for the power curves are uniformly distributed; i.e. each of the 1 h power curves is based on approximately 2 min of each simulated wind speed from 3 to 18 m s^{-1}.

It is seen that it requires 36 h of observations based on met-mast wind speed and 15 h of observations based on nacelle wind speed to reach the error level obtained from 4 h of observations using the pitot tube at 36 m. In general the speed-up achieved by using pitot-tube-based observations instead of met-mast-based observations is around 7.

Obviously, the wind speed in real measurement observations is not uniformly distributed – it is not even likely that

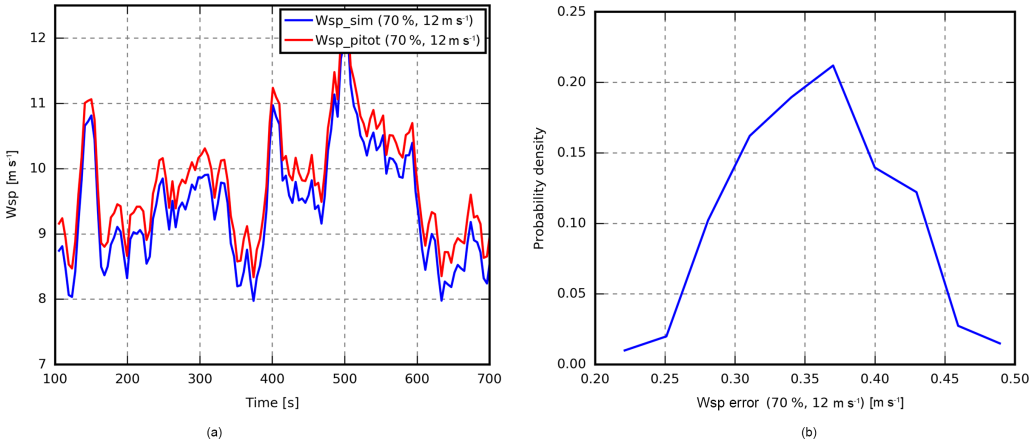

Figure 14. **(a)** Time series of simulated "real" wind speed and simulated wind speed estimated from pitot-tube data. **(b)** Distribution of the simulated error.

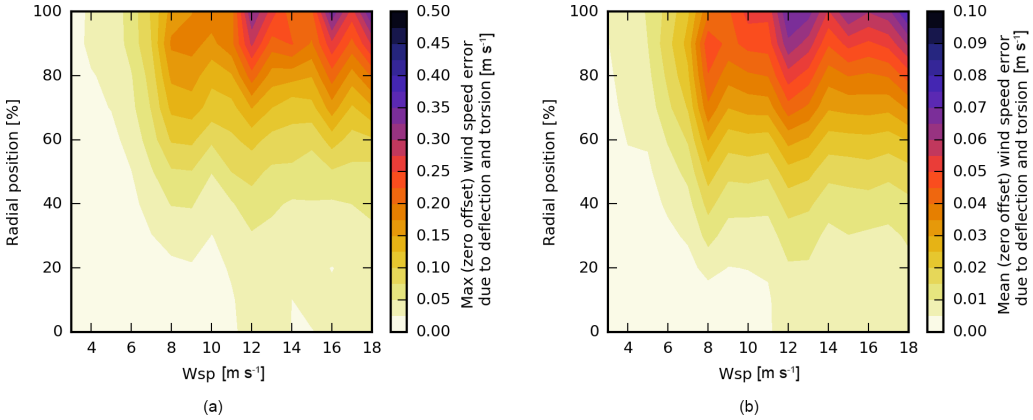

Figure 15. Maximum **(a)** and mean **(b)** simulated error of the wind speed (one-revolution mean neglecting the average offset) in the axial direction due to deflection and torsion.

all wind speeds are observed in the same hour – and therefore a similar speed-up cannot be expected in reality.

4 Full-scale measurement study

In this section, we investigate whether the wind speeds that can be derived from the pitot tube are also highly correlated with the power and flap loads in practice. The results are based on measurements of a full-scale modern wind turbine with a blade-mounted five-hole pitot tube. Furthermore, we address whether more power and flap moment curves with less variation can be obtained by using pitot-tube wind speed instead of met-mast-recorded wind speeds.

4.1 Turbine and site

The measurement data of the 3.6 MW Siemens turbine stems from the DANAERO project 2007–2009 (Aagaard Madsen et al., 2010a). The turbine was located at the Høvsøre test site for large wind turbines in Denmark and equipped with a five-hole CPSPY5 Aeroprobe pitot tube at the 36 m radius of one of its 53.5 m blades.

The turbine is located in the middle of a row of five large turbines, and around 3 months of measurement data are available on the turbine and the nearby met masts; see Fig. 18.

4.2 Effects of shear and turbulence intensity, yaw error, and air density on power and flap load curves

Different turbulence intensity, shear level, yaw misalignment and air density result in different power and load curves (Elliott and Cadogan, 1990; Eggers et al., 2003; Antoniou et al., 2007; Wagner et al., 2011; Fleming et al., 2014; St. Martin et al., 2016). Ideally, all observations should therefore have the same turbulence intensity, shear level, yaw misalignment and air density when calculating the variance in different power and load curves. This is not the case in the measurement dataset and therefore limits must be defined which include observations within a range of turbulence intensities,

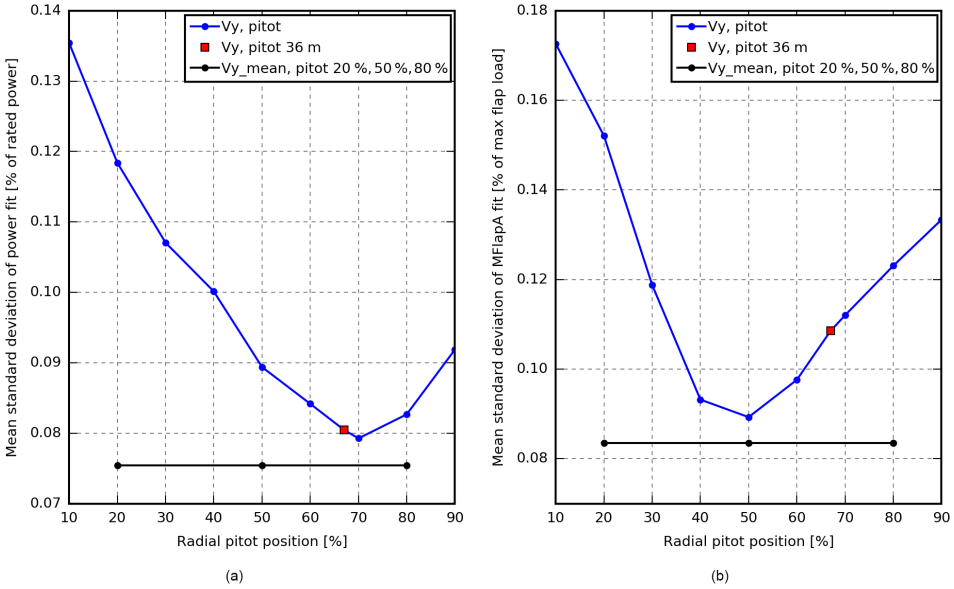

Figure 16. Mean relative standard deviation of simulated power **(a)** and flap load **(b)** fits based on wind speed from pitot tubes at different radial positions. The pitot tube at 36 m, which corresponds to the position of the pitot tube in the measurements, is close to optimal for the power curves, while the mean of three pitot tubes at 20, 50 and 80 % provides slightly less variation.

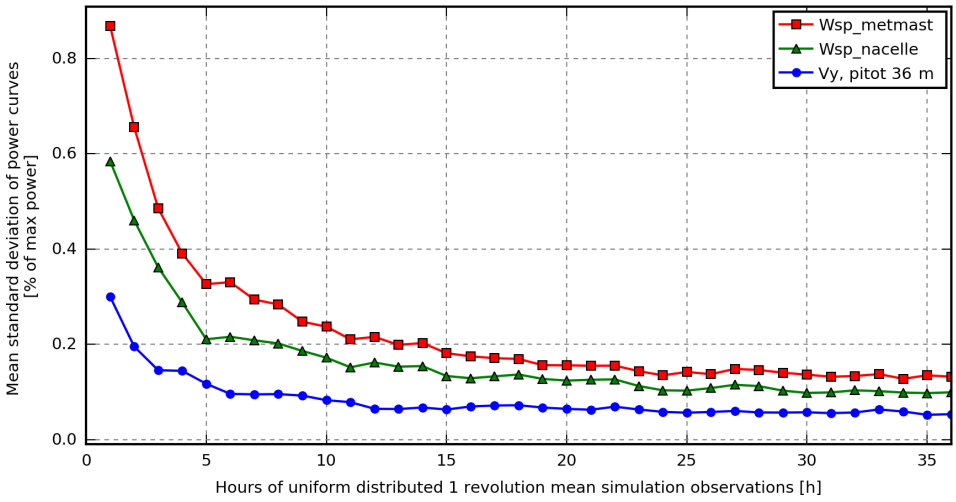

Figure 17. Mean relative standard deviation of simulated power curves based on uniformly distributed observations. Using the pitot-tube instead of the met-mast wind speed as the basis for the power curves, the same error level can be achieved approximately 7 times faster.

shear levels, yaw errors and air densities, without changing the power and load curves too much.

These limits have been found by comparing the reference simulation sets with the sets where different turbulence intensities, shear levels, yaw misalignment angles and air densities have been simulated (see Table 1) in terms of the mean absolute difference between the power and load curves in percent of maximum power and load; cf. Eq. (13).

The power and load curves are highly dependent on the turbulence intensity, which must be in the range of 3–12 % to keep the mean absolute difference below 0.5 %.

For every 10 min of measurements, a shear profile coefficient is calculated by fitting a power shear profile to the one hour mean wind speed measured by the main met mast at 10, 40, 60, 80, 100 and 116.5 m height. Most observations have a power shear coefficient below 0.3, which has been found to keep the mean absolute difference below 0.5 %, and the rest is discarded.

There is no indication that the yaw misalignment exceeds $\pm 10°$, and in this region the mean absolute difference of the power and flap moments curves is below 0.5 %.

Figure 18. Overview of the Høvsøre test site for large turbines in Denmark. The Siemens turbine is located in the middle of a row of five turbines.

The aerodynamic power and loads are proportional to the density of air for constant power and load coefficient, and therefore the normalization

$$\text{Power}_{\text{normalised}} = \text{Power}_{10\,\text{min}} \frac{\rho_0}{\rho_{10\,\text{min}}} \tag{14}$$

must be used for power curves of stall-regulated turbines (IEC 61400-12-1, 2005). Pitch-regulated turbines on the other hand reduce the power coefficient at high wind speeds to maintain rated power. Therefore, another normalization, which normalizes the free-flow wind speed, is used for pitch-regulated turbines. However, in this context we are using the pitot wind speed, and therefore the above normalization is applied up to rated wind speed from where it is faded out. When using this normalization, no limits are required on the air density to keep the mean absolute difference below 0.5 %.

4.3 Selecting measurement observations

A huge effort has been invested in selecting a proper set of observations from the measurement database as well as in correcting or discarding error-prone sensor observations.

The measurement database consists of 1600 h of measurement, but only a few hundred hours are usable for this analysis; see the summary of the selection process in Table 2. The wake filter discards more met-mast observations than pitot observations as the met mast, i.e. Mast 3 in Fig. 18, is in the wake of the turbines in easterly wind directions, but many of these cases are discarded anyway as the turbulence intensity or shear coefficient is outside the accepted range. The final filter that rejects datasets containing corrupted or suspicious pitot observations reduces the amount of observations for the pitot-based analysis far below the amount of observations usable for met-mast-based analysis.

4.4 Pitot inclusion criteria

The current pitot-tube system is very sensitive to rain, especially the P1–P6 sensor, which records the pressure difference between the centre hole and the static ring. Figure 19 shows the typical behaviour of the P1–P6 sensor, before, during and after rainfall. Before the rain starts, the P1–P6 sensor output is independent of rotor position (Fig. 19a), and the first droplets are clearly seen as spikes and sinusoidal patterns; Fig. 19b and c. During the rainfall, water gets inside the tubes and the output becomes continuous sinusoidal; Fig. 19d. During the next couple of hours different more or less abnormal patterns are recorded until the water suddenly disappears and a signal independent of rotor position is restored; Fig. 19e–h. These effects of rainfall have not been detected in the measurements from a previous experiment (Aagaard Madsen et al., 2003), where a Rosemount M858 pitot tube (Schmidt Paulsen, 1990) was used.

Many of these patterns are clearly abnormal and easy to detect, while others are similar to patterns occurring in special inflow conditions, e.g. shear, veer and/or yaw misalignment. It is therefore difficult to make an algorithm that isolates the rain-disturbed observations only, and consequently

Table 2. Measurement selection filters.

Filter	Pitot observations (h)	Met mast observations (h)	Comments
Total	1599	1599	
Normal operation	926	926	Filter on turbine status signal, rpm > 2 and power > 100 kW
Variable rpm	858	858	In the discarded period the turbine was operated with constant rotor speed
No wake	629	528	Avoid wake situations
Turbulence intensity	537	414	Discard observations with turbulence intensity outside the range 0.03–0.12
Shear	481	414	Discard observations with power shear coefficient outside the range 0–0.3
Pitot ok	242	407	Discard observations where pitot-tube data are uncertain; see Sect. 5.4

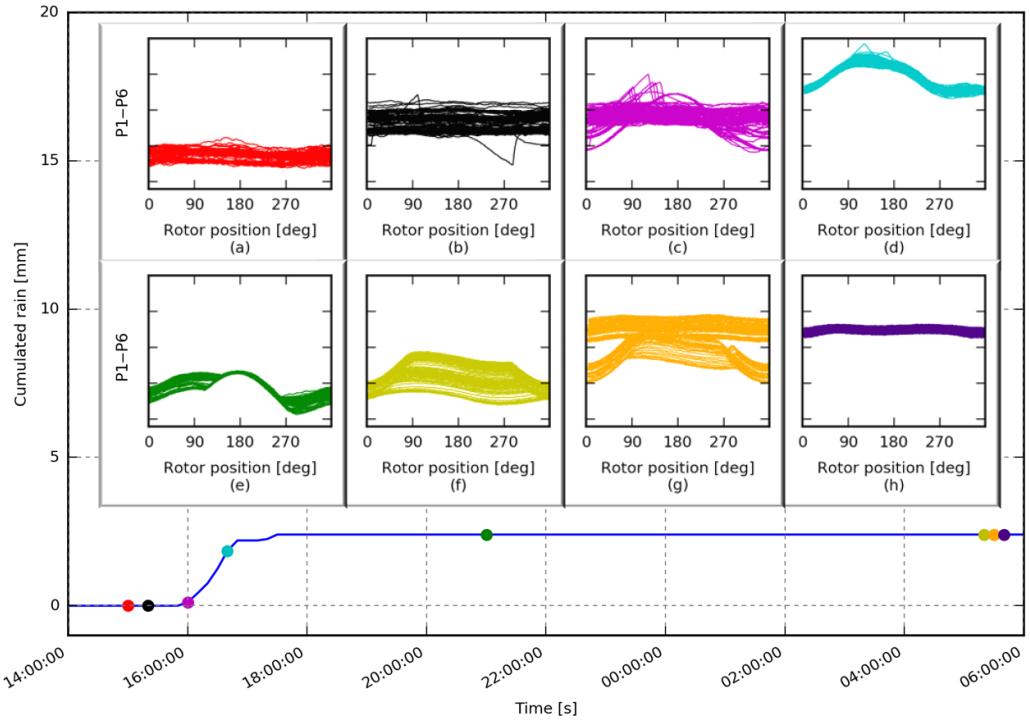

Figure 19. The background plot shows the cumulated rain from 27 to 28 April 2009. Approximately 2.5 mm rain fell between 16:00 and 17:30 LT (UTC+2). The coloured points indicate the temporal position of the corresponding graphs on the timeline. These graphs show the P1–P6 sensor (pressure difference between centre hole and static ring) as a function of rotor position (0°: blade down; 180°: blade up) over a period of 10 min. **(a)** Before the rain, P1–P6 is almost constant. Panels **(b)** and **(c)**: first droplets cause spikes and sinusoidal patterns. **(c)** Water in the tubes is now constantly causing sinusoidal output. **(e)** Sinusoidal output when the blade is in the upper part only. **(f–h)** Transition from disturbed to normal recording.

a rough filter that discards observations made between 1 h prior to rainfall and 12 h after rainfall is applied in this study.

Over an interval of approximately 1 month in the middle of the measurement period, spikes are often seen in the output of the P1–P6 sensor; see Fig. 20a. Often the spikes occur at a fixed rotor position for some time, as seen in Fig. 20b, but the position moves from time to time. In many cases the duration of the spike is only a few degrees as in Fig. 20b, while in other cases the sensor output level seems to be increased for half a revolution.

A rough filter that discards datasets where the maximum absolute instant change of the P1–P6 sensor output exceeds 50 Pa has been applied.

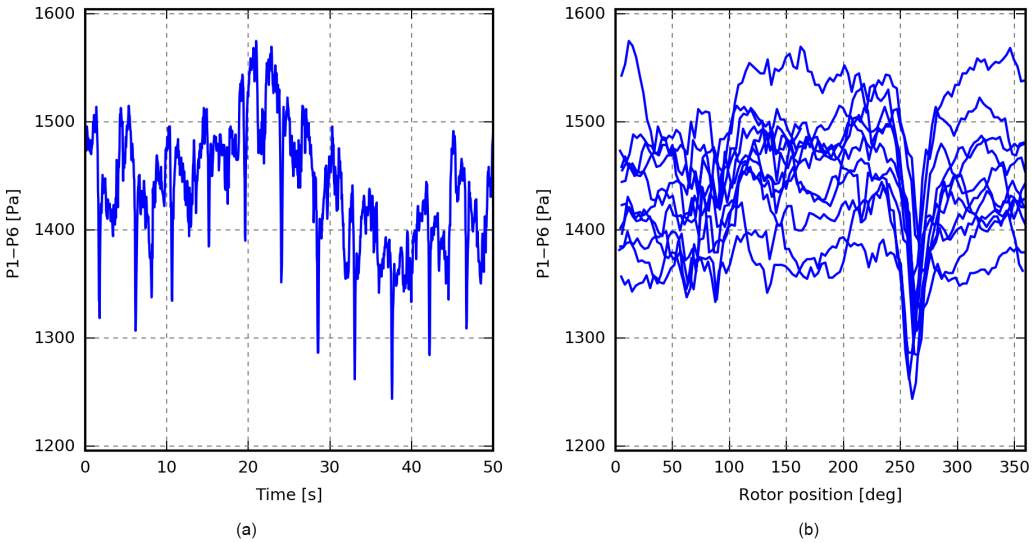

Figure 20. Output of the P1–P6 sensor (pressure difference between centre hole and static ring) as a function of time **(a)** and rotor position **(b)**. Spikes are clearly seen around 260°.

The sensors P2–P3 and P4–P5, which record the inflow and side-slip angle, respectively, also have periods with abnormal sinusoidal patterns. These periods are more distinct but not related to rainfall, and in this study they are identified based on their 1P (one-per-revolution) Fourier coefficients values.

4.5 Pitot wind speed correlation with power and flap load

Figure 21 shows the power (a and c) and flap load (b and d) observations measured on the 9 and 10 May as a function of pitot and met-mast wind speeds. In (c) and (d) the met-mast observations represent 600 s mean values, while all other observations are 120 s mean values. The pitot-based observations have less scatter than the 120 s met-mast observations (a and b), while they are comparable to the 600 s met-mast observations which comprise far fewer observations (c and d).

These results are similar to the results from the Tellus experiment (see Figs. 2 and 3) and indicate that it is possible to reduce the scatter of the power and load observations or increase the number of observations by using pitot-tube instead of met-mast recordings – also on modern wind turbines.

In Fig. 21, the pitot observations are based on 120 s mean values. The simulation results in Fig. 10, however, indicate that the best results are obtained from averaging times between one revolution and 30 s. Figure 22a shows the power observations from a 10 min period based on 600 s, 120 s and one-revolution mean values. The five 120 s mean values provide information about the slope of the curve in contrast to the single 600 s observation, while the one-revolution mean observations provide information about an even wider range of wind speeds. The scatter of the one-revolution mean observations, however, is remarkable. The scatter is mainly caused by a pitch motion procedure, which changes the pitch angle by 1° every minute to exercise the pitch bearings. These pitch steps result in two levels and increased scatter in both horizontal and vertical directions as both power and pitot wind speeds are affected (Hansen et al., 2005). In Fig. 22b, the one-revolution mean observations are coloured according to the current pitch state, which is seen to split the observations in two less scattered groups. Unfortunately this means that the averaging time must be at least 120 s to average out the scatter caused by the pitch motion procedure.

In Fig. 21, the pitot-based power and flap load observations over a 2-day period were located on a relatively thin line. Plotting all observations, however, results in a thick belt instead of a thin line; see Figs. 23 and 24. Colouring the observations according to the time of recording reveals that in many periods the observations are describing a relatively thin line, but the line shifts from time to time.

The reason for these shifts has been investigated by comparing time series with similar pitot-tube wind speed and different power levels. In most of these cases the met-mast wind speeds are different, but the pitot-tube wind speeds become equal due to higher loading and thereby different induction. In other cases a combination of fluctuating wind speeds and the pitch motion procedure results in a different response to similar mean wind speeds. Finally, the rated power level clearly changes over the period; see Fig. 23. This indicates that the control settings are not fixed, and it is therefore likely that the behaviour at lower wind speeds also changes during the measurement period.

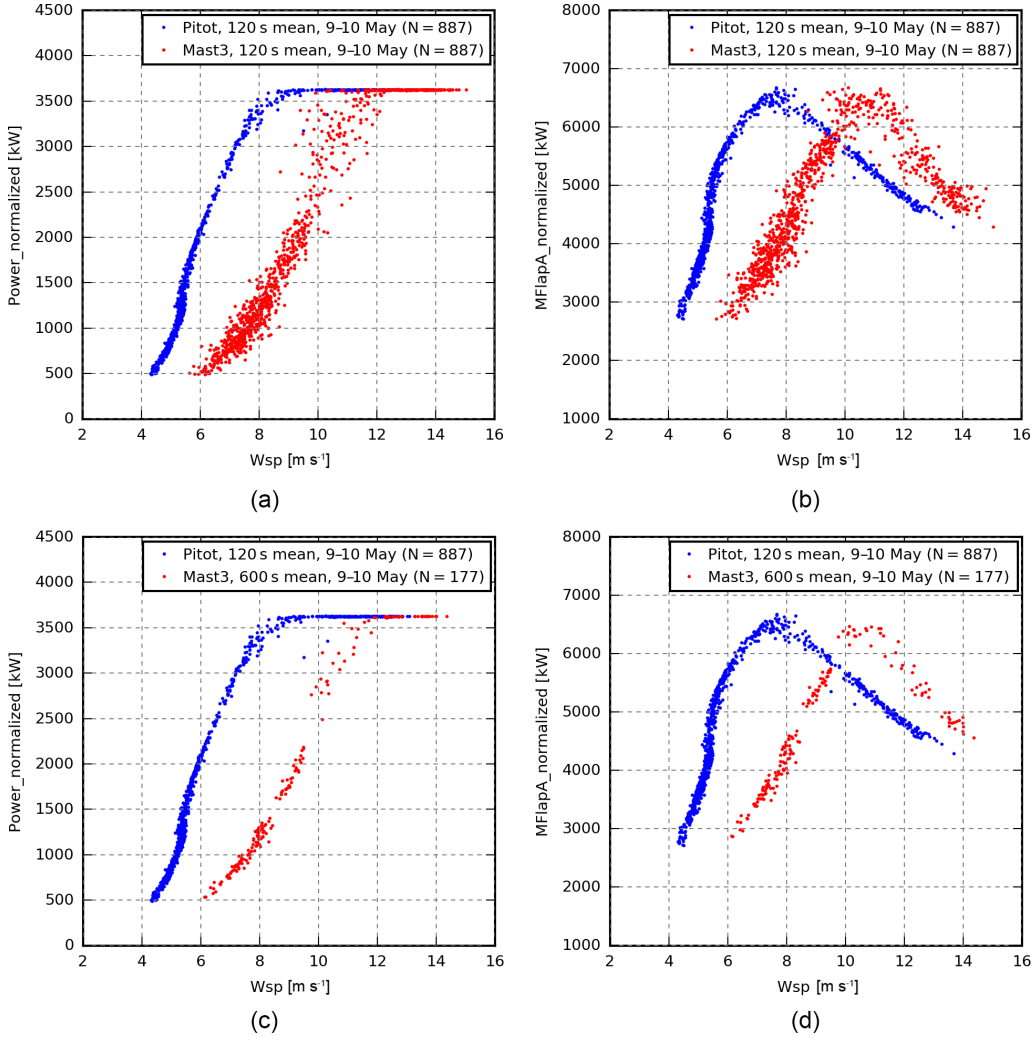

Figure 21. Measured power **(a, c)** and flap load **(b, d)** observations as a function of pitot and met-mast wind speed. In **(a, b)** all observations are 120 s mean values, while the met-mast observations in **(c, d)** are 600 s mean values. Using pitot instead of met-mast wind speed, the amount of scatter can be reduced **(a, b)** or more observations can be obtained **(c, d)**.

4.6 Number and variation in performance curves

In Sect. 4, the comparison of uniformly distributed simulation observations showed that the number of hours required to obtain power curves with a variation level below a certain threshold can be reduced around 7 times by using pitot-based instead of met-mast-based wind speeds. This result was based on one-revolution mean values, which in Sect. 4.2 were found to give the lowest variation. However, this is not feasible for the measurements, due to the scatter introduced by the pitch motion procedure.

In practice it is not possible to obtain a full power curve, e.g. every 4 h, as both low- and high-wind situations must occur, and from the current measurement database only a few power curves can be obtained. The exact number of curves depends on the wind speed range and resolution of interest. In the following analysis, the range from 4 to 13 m s^{-1} (met-mast wind speed) is divided into bins of 0.5 m s^{-1}. Observations are then collected for the first power curve until all bins contain at least three observations, then for the next power curve, etc.

Figure 25 shows the resulting power curves and the underlying observations. In this case the pitot-based approach provides three curves with 1.1 % variation (percent of maximum power), while four curves with slightly higher variation are obtained from the met-mast-based observations. This means that from the current measurement database, an assessment time reduction cannot be achieved by using pitot-tube wind speed instead of met-mast wind speed.

This result is highly constrained by the pitch motion procedure that introduces scatter for averaging times below 120 s as well as by the amount of discarded observations due to abnormal pitot sensor values. These constraints may be different for another turbine and pitot-tube instrument. An in-

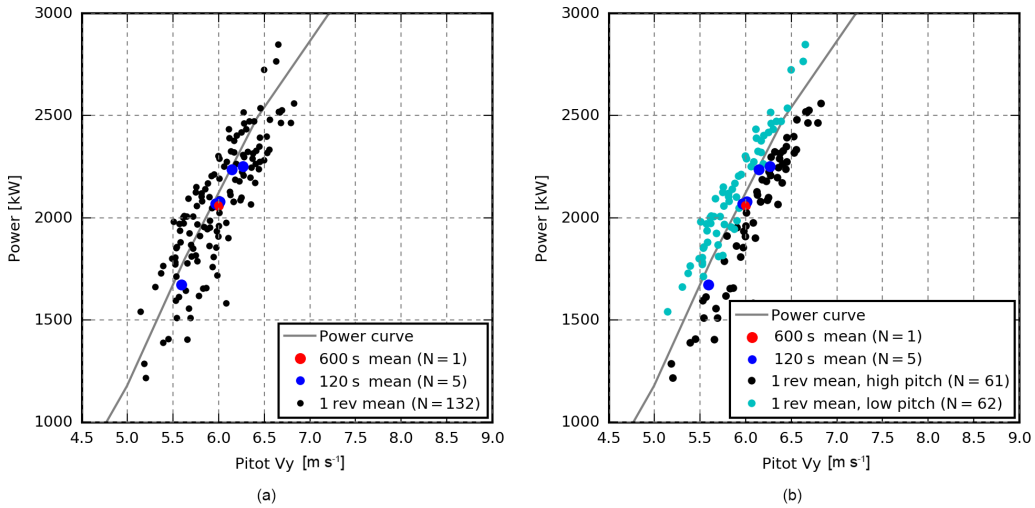

Figure 22. **(a)** Reducing the averaging time increases the number of observations and gives information about a wider wind speed range. Averaging times below 120 s, however, results in a remarkable amount of scatter, which is mainly caused by a pitch motion procedure. **(b)** The one-revolution mean values are coloured according to the pitch state; i.e. black points are observations where the pitch angle is increased by 0.5° and cyan points are observations where the pitch angle is decreased by 0.5°. The pitch state splits the observations into two less scattered groups.

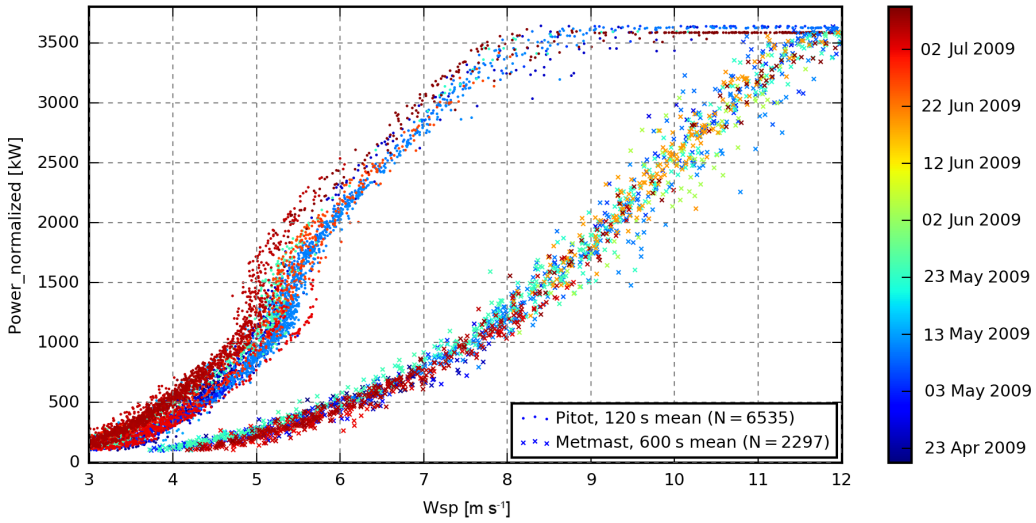

Figure 23. Measured power observations from the entire database. In many periods, the pitot observations describe a relatively thin line, but the line shifts from period to period.

dication of the optimal potential has been achieved by relaxing the constraints, i.e. suppressing the pitot ok filter and using one-revolution mean values. In this optimal case, the pitot-based approach results in 20 power curves, and the 19 June produces four power curves in a single day, i.e. the same number as obtained from the whole period using the met-mast-based approach. Note, however, that the variation in these curves may be significant due to shorter averaging times and the line shifting seen in Figs. 23 and 24.

5 Conclusions

In the numerical part of this paper it is shown that the wind speed derived from a blade-mounted flow sensor of a modern pitch-regulated, variable-speed wind turbine correlates more highly with the power and flap loads than the wind speed measured 2.5 diameters upstream. The correlation is also higher than the wind speed that can be obtained from a fixed-point instrument, e.g. a nacelle-mounted cup anemometer.

When using wind speed from a blade-mounted flow sensor as the basis for power and flap load curves, shorter ob-

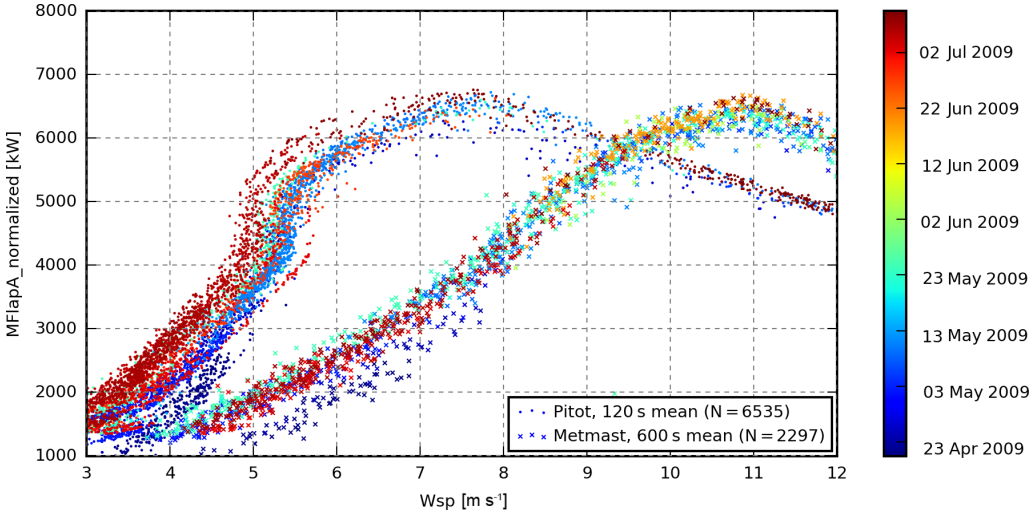

Figure 24. Measured flap load observations from the entire database. In many periods, the pitot observations describe a relatively thin line, but the line shifts from period to period.

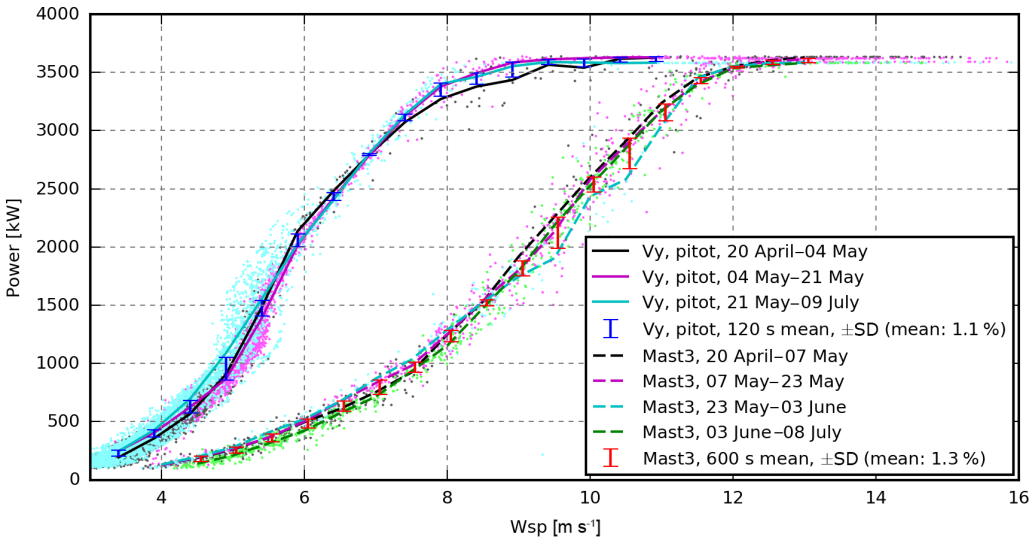

Figure 25. Only two or three full-range power curves can be obtained from the current measurement database.

servation average times, in the range of 5–90 s, reduce the variation in the curves.

Deflection and torsion of the blades introduce an error into the wind speed derived from a blade-mounted flow sensor. When averaging over one or more revolutions, the error is significantly reduced and the major part of the remaining error is a constant offset, which can be ignored when power and flap load curves of different periods are compared. For the current turbine the radial flow sensor position that results in the lowest variation in power curves was found to be 70 %, while a sensor in 50 % is optimal for flap load curves.

Finally, the analysis showed that the length of the assessment period, which is required to achieve a certain power or flap load curve variation can be reduced around 7 times by using uniformly distributed wind speed observations from a blade-mounted flow sensor instead of a met mast.

The measurement part of the paper concludes that the current pitot-tube system is highly sensitive to rain, and a proper algorithm must be applied to discard error-prone observations.

During shorter periods the pitot-tube wind speed often correlates more highly with power and flap loads than the metmast wind speed, such that the scatter can be reduced or the number of observations increased by reducing the observation average time. During longer periods, however, the scatter of the pitot-tube-based power and flap load observations becomes significant and often the observations seem to group around relatively thin lines that shift from period to period.

From the current measurement database, an assessment time reduction cannot be achieved using pitot-tube wind speeds instead of met-mast wind speeds. A limiting factor for the present dataset is the pitch motion of 1° every minute that introduces severe scatter when applying averaging times below 120 s and the high number of observations that are discarded to avoid error-prone pitot observations. Relaxing these constraints reveals that the method may have a high potential for turbines without the pitch motion procedure and equipped with a more robust flow sensor system.

The wind speeds measured by a blade-mounted flow sensor have advantages over the wind speeds measured at the met mast, as the blade-mounted flow sensor can be used offshore, in wind farms and in complex terrain, where it may not be possible to put a met mast. It can be used to investigate aerodynamic modifications or detect performance issues, e.g. due to leading-edge roughness, by comparing the relative pitot-based power and load curve between different periods or turbines. In addition it follows the yaw direction; i.e. it is never in the wake of the current turbine in contrast to a traditional met mast. Moreover additional information about the angle of attack, wind speed variations within the rotor plane (e.g. shear, veer, height-dependent turbulence intensity) and wake effects can be extracted. This information can be used as input for the control of individual pitch or active trailing-edge flap to optimize power and/or reduce loads or noise (Larsen et al., 2005; Barlas et al., 2012; Kragh and Hansen, 2012; Kragh et al., 2012; Aagaard Madsen, 2014).

The measured wind speeds are, however, affected by the wind turbine induction. This means that it cannot be used for IEC standard power curves, and changing the induction, e.g. by another control strategy, yaw misalignment or by the pitch step procedure seen in the present study, will shift the resulting wind speed. Another problem is that the induced wind speeds increase up to rated power; i.e. in this region the flow-sensor-based power curve has a higher slope, which for the present turbine was found to be almost vertical around rated rotor speed, such that small wind speed uncertainties result in large power variations.

It is possible to compensate for the presence of the turbine using an aerodynamic model (Pedersen et al., 2015), but it requires detailed knowledge about the aerodynamic properties of the blades, several assumptions and compromises, and it adds additional uncertainty.

Finally the wind speeds derived from pitot-tube measurements are more vulnerable to uncertainties and errors in the measurement system, as they are derived from 10 sensors instead of 1. Therefore, a robust measurement system is required and the pitot-tube instrument and pressure transducers must be designed to prevent rain, moisture and dust from entering the tubes by using a heater or a draining and/or a pneumatic cleaning system, etc.

It is therefore concluded that the wind speed measured by a blade-mounted flow sensor is highly correlated with the power and flap loads, especially during shorter periods, but the potential assessment time speed-up that was obtainable in the simulation could not be confirmed from the current measurements.

Blade-mounted flow sensors are, however, able to provide additional valuable information about the inflow variations within the rotor plane, but a robust instrument and measurement system is required to extract reliable wind speed measurements.

Data availability. Measurement and simulation data not available due to confidentiality.

Appendix A: List of symbols

α	Angle of attack
α_p	Inflow angle measured by pitot tube
β	Side-slip angle; see Fig. 7
F_α	Function mapping α_p onto α
F_vrel	Function mapping vrel_p onto vrel
I	Inertia of rotor
ω_pitch	Angular pitch speed of blade with pitot tube
ω_rot	Angular rotational speed
$\boldsymbol{v}_\mathrm{rel} = \begin{bmatrix} v_{\mathrm{rel},x} & v_{\mathrm{rel},y} & v_{\mathrm{rel},z} \end{bmatrix}$	Flow velocity at pitot tube relative to the sensor adjusted for reduced flow velocity and deflection near the airfoil due to bound circulation
$\boldsymbol{v}_\mathrm{relp} = \begin{bmatrix} v_{\mathrm{relp},x} & v_{\mathrm{relp},y} & v_{\mathrm{relp},z} \end{bmatrix}$	Relative flow velocity measured by the pitot tube including effects of bound circulation
v_rot	Velocity caused by blade rotation
v_pitch	Velocity of pitot tube due to pitch motion
$\boldsymbol{v} = \begin{bmatrix} v_x & v_y & v_z \end{bmatrix}$	Wind velocity at position of pitot tube including induction effects (v_y is horizontal in direction of main shaft)
θ_tilt	Tilt angle
$\theta_\mathrm{rotorposition}$	Azimuthal angle of blade with pitot tube
θ_pitot	Angle of pitot tube relative to the centre line of the blade
θ_pitch	Pitch angle of blade with pitot tube
v_rel	Relative flow speed at pitot tube, compensated reduced flow velocity near the airfoil

Competing interests. The authors declare that they have no conflict of interest.

Acknowledgements. The authors would like to acknowledge Siemens Wind Power for providing data for the simulation model, and the funding from the Danish Energy Agency EUDP programme of the DANAERO MW projects, contracts ENS no. 33033-0074 and 64009-0258, is acknowledged for providing important data for the present study.

Edited by: Julie Lundquist
Reviewed by: Vasilis A. Riziotis and one anonymous referee

References

Aagaard Madsen, H.: Aerodynamics and Structural Dynamics of a Horizontal Axis WindTurbine – Raw Data Overview, Technical Report Risø-M-2902, Risø National Laboratory, Roskilde, Denmark., 1991.

Aagaard Madsen, H.: Correlation of amplitude modulation to inflow characteristics, Proc. 43rd Int. Congr. Noise Control Eng., available at: http://www.acoustics.asn.au/conference_proceedings/INTERNOISE2014/papers/p171.pdf (last access: 13 November 2017), 2014.

Aagaard Madsen, H., Thomsen, K., and Petersen, S. M.: Wind Turbine Wake Data from Inflow Measurements using a Five hole Pitot Tube on a NM80 Wind Turbine Rotor in the Tjæreborg Wind Farm, Technical Report Risø-I-2108, Risø National Laboratory, Roskilde, Denmark, 2003.

Aagaard Madsen, H., Bak, C., Schmidt Paulsen, U., Gaunaa, M., Fuglsang, P., Romblad, J., Olesen, N. A., Enevoldsen, P., Laursen, J., and Jensen, L.: The DAN-AERO MW Experiments: Final report, Danmarks Tekniske Universitet, Risø Nationallaboratoriet for Bæredygtig Energi, available at: orbit.dtu.dk (last access: 13 November 2017), 2010a.

Aagaard Madsen, H., Bak, C., Døssing, M., Mikkelsen, R. F., and Øye, S.: Validation and modification of the Blade Element Momentum theory based on comparisons with actuator disc simulations, Wind Energy, 13, 373–389, https://doi.org/10.1002/we.359, 2010b.

Aagaard Madsen, H., Riziotis, V., Zahle, F., Hansen, M. O. L., Snel, H., Grasso, F., Larsen, T. J., Politis, E., and Rasmussen, F.: Blade element momentum modeling of inflow with shear in comparison with advanced model results, Wind Energy, 15, 63–81, https://doi.org/10.1002/we.493, 2012.

Antoniou, I., Wagner, R., Markkilde Petersen, S., Schmidt Paulsen, U., Madsen Aagaard, H., Ejsing Jørgensen, H., Thomsen, K., Enevoldsen, P., and Thesbjerg, L.: Influence of wind characteristics on turbine performance, in: Conference proceedings, European Wind Energy Association (EWEA), 2007.

Barlas, T. K., van der Veen, G. J., and van Kuik, G. A. M.: Model predictive control for wind turbines with distributed active flaps: incorporating inflow signals and actuator constraints, Wind Energy, 15, 757–771, https://doi.org/10.1002/we.503, 2012.

Eggers A. J., J., Digumarthi, R., and Chaney, K.: Wind Shear and Turbulence Effects on Rotor Fatigue and Loads Control, 75944, 225–234, https://doi.org/10.1115/WIND2003-863, 2003.

Elliott, D. L. and Cadogan, J. B.: Effects of wind shear and turbulence on wind turbine power curves, Presented at the European Community Wind Energy Conference and Exhibition, Madrid, Spain, 10–14 September 1990, available at: http://www.osti.gov/scitech/servlets/purl/6348447, 1990.

Fleming, P. A., Scholbrock, A. K., Jehu, A., Davoust, S., Osler, E., Wright, A. D., and Clifton, A.: Field-test results using a nacelle-mounted lidar for improving wind turbine power capture by reducing yaw misalignment, J. Phys. Conf. Ser., 524, 12002, available at: http://stacks.iop.org/1742-6596/524/i=1/a=012002, 2014.

Hansen, M. H., Hansen, A. D., Larsen, T. J., Øye, S., Sørensen, P., and Fuglsang, P.: Control design for a pitch-regulated, variable speed wind turbine, Technical Report Risø-R-1500, Risø National Laboratory, Roskilde, Denmark, available at: www.orbit.dtu.dk (last access: 13 November 2017), 2005.

IEC 61400-12-1: Power performance measurements of electricity producing wind turbines, International Electrotechnical Commission, Geneva, Switzerland, available at: www.iec.ch, 2005.

Kim, T., Hansen, A. M., and Branner, K.: Development of an anisotropic beam finite element for composite wind turbine blades in multibody system, Renew. Energ., 59, 172–183, https://doi.org/10.1016/j.renene.2013.03.033, 2013.

Kragh, K. and Hansen, M.: Individual Pitch Control Based on Local and Upstream Inflow Measurements, in: 50th AIAA Aerospace Sciences Meeting including the New Horizons Forum and Aerospace Exposition, Reston, Virigina, American Institute of Aeronautics and Astronautics, https://doi.org/10.2514/6.2012-1021, 2012.

Kragh, K. A., Henriksen, L. C., and Hansen, M. H.: On the Potential of Pitch Control for Increased Power Capture and Load Alleviation, Presented at The Science of Making Torque from Wind 2012, 9–11 October 2012, Oldenburg, Germany, available at: orbit.dtu.dk (last access: 13 November 2017), 2012.

Larsen, T. J. and Hansen, A. M.: How 2 HAWC2, the user's manual, Technical Report, Risø National Laboratory, Roskilde, Denmark, available at: orbit.dtu.dk (last access: 13 November 2017), 2007.

Larsen, T. J., Aagaard Madsen, H., and Thomsen, K.: Active load reduction using individual pitch, based on local blade flow measurements, Wind Energy, 8, 67–80, https://doi.org/10.1002/we.141, 2005.

Larsen, T. J., Larsen, G., Aagaard Madsen, H., and Petersen, S. M.: Wake effects above rated wind speed . An overlooked contributor to high loads in wind farms, in: Scientific Proceedings, EWEA Annual Conference and Exhibition, Paris, France, 95–99, European Wind Energy Association (EWEA), 2015.

Pedersen, M. M., Larsen, T. J., Larsen, G. C., and Madsen, H. A.: Turbulent wind field characterization and regeneration based on pitot tube measurements mounted on a wind turbine, in 33rd Wind Energy Symposium, Kissimmee, Florida, American Institute of Aeronautics and Astronautics, https://doi.org/10.2514/6.2015-1467, 2015.

Petersen, J. T. and Aagaard Madsen, H.: Risø-R-993(EN): Local Inflow and Dynamics – Measured and Simulated on a Rotating Wind Turbine Blade, Risø National Laboratory, Roskilde, Denmark, 1997.

Schmidt Paulsen, U.: Risø-M-2878: Calibration of Rosemount M858 Pitot tube sensor, Risø National Laboratory, Roskilde, Denmark, 1990.

St. Martin, C. M., Lundquist, J. K., Clifton, A., Poulos, G. S., and Schreck, S. J.: Wind turbine power production and annual energy production depend on atmospheric stability and turbulence, Wind Energ. Sci., 1, 221–236, https://doi.org/10.5194/wes-1-221-2016, 2016.

Wagner, R., Courtney, M., Gottschall, J., and Lindelöw-Marsden, P.: Accounting for the speed shear in wind turbine power performance measurement, Wind Energy, 14, 993–1004, https://doi.org/10.1002/we.509, 2011.

APPENDIX C

Free flow wind speed from a blade-mounted flow sensor

Wind Energ. Sci. Discuss., https://doi.org/10.5194/wes-2017-57
Manuscript under review for journal Wind Energ. Sci.
Discussion started: 2 January 2018

eawe european academy of wind energy
Open Access WIND ENERGY SCIENCE DISCUSSIONS

Free flow wind speed from a blade-mounted flow sensor

Mads Mølgaard Pedersen[1], Torben Juul Larsen[1], Helge Aagaard Madsen[1], and Søren Juhl Andersen[2]

[1]Wind Energy Department, Technical University of Denmark, Frederiksborgvej 399, 4000 Roskilde, Denmark
[2]Wind Energy Department, Technical University of Denmark, Nils Koppels Alle, Building 403, 2800 Kgs. Lyngby, Denmark

Correspondence to: Mads M. Pedersen (mmpe@dtu.dk)

Abstract. This paper presents a method for obtaining the free inflow velocities from a 3D flow sensor mounted on the blade of a wind turbine.

From its position on the rotating blade, e.g. one third from the tip, a blade mounted flow sensor (BMFS) is able to provide valuable information about the turbulent sheared inflow in different regions of the rotor. At the rotor, however, the inflow is affected by the wind turbine, and in most cases the wind of interest is the inflow that the wind turbine is exposed to; i.e. the free inflow velocities.

The current method applies a combination of aerodynamic models and procedures to estimate the induced velocities, i.e. the disturbance of the flow field caused by the wind turbine. These velocities are subtracted from the flow velocities measured by the BMFS to obtain the free inflow velocities. Aeroelastic codes, like HAWC2, typically use a similar approach to calculate the induction, but they use it for the reversed process, i.e. they add the induction to the free inflow to get the flow velocities at the blades which are required to calculate the resulting aerodynamic forces.

The aerodynamic models included in the current method comprise blade-element-momentum (BEM) based models for axial and tangential induction, a radial induction model and tip loss correction as well as models for skew and dynamic inflow.

It is shown that the method is able to calculate the free inflow velocities with high accuracy when applied to aeroelastic HAWC2 simulations with a stiff structural model while some deviations are seen in simulations with a flexible structure.

Furthermore, the method is tested on simulations performed by a flexible structural model coupled with a large eddy simulation (LES) flow solver. The results of this higher fidelity verification confirm the HAWC2-based conclusion.

Wind Energ. Sci. Discuss., https://doi.org/10.5194/wes-2017-57
Manuscript under review for journal Wind Energ. Sci.
Discussion started: 2 January 2018

eawe european academy of wind energy
Open Access WIND ENERGY SCIENCE DISCUSSIONS

1 List of symbols

a	Axial induction factor
a'	Tangential induction factor
a_r	Radial induction factor
c	Chord length
C_T	Trust coefficient
$C_{T,avg}$	Average trust coefficient
C_x	Lift and drag coefficient projected into x^R
C_y	Lift and drag coefficient projected into y^R
D	Aerodynamic drag force
F_a	Thrust reduction factor in skew inflow model
F_{azi}	Azimuthal dependent reduction factor in skew inflow model
F_{tip}	Prandtl's tip loss factor
$\mathrm{f_W}$	Function calculating induced velocities
$k_i, i = 0..3$	Constants
k_x, k_y	Factors in skew inflow model
L	Aerodynamic lift force
$\mathrm{LP}(\tau, X)$	Low pass filter with filter characteristics, τ
N_B	Number of blades
r	Sensor radius
R	Blade tip radius
$\boldsymbol{T_{ab}}$	Transformation matrix from coordinate system a to coordinate system b
$\boldsymbol{V_r}$	Measured flow velocity at rotor plane
$\boldsymbol{V_{rel}}$	Measured velocity relative to the sensor
V_{relxy}	Relative wind speed in the (x^R, y^R)-plane
$\boldsymbol{V_{rot}}$	Velocity of sensor due to rotor rotation
$\boldsymbol{V_s}$	Velocity of the sensor
$\boldsymbol{V_0}$	Free flow wind speed
$\boldsymbol{V_{0,est}}$	Estimated free flow wind speed
$\boldsymbol{W}$	Induced velocity
$\boldsymbol{W_{est}}$	Estimated induced velocity
$\boldsymbol{W_{avg}}$	Average induced velocity
$\boldsymbol{W_{dyn}}$	Induced velocity, estimated using dynamic inflow model
$\boldsymbol{W_{dyn,azi}}$	Induced velocity, estimated using dynamic inflow model applied to fixed azimuthal positions

Wind Energ. Sci. Discuss., https://doi.org/10.5194/wes-2017-57
Manuscript under review for journal Wind Energ. Sci.
Discussion started: 2 January 2018

eawe european academy of wind energy
Open Access WIND ENERGY SCIENCE DISCUSSIONS

α	Angle of attack
χ	Angle between $\boldsymbol{V_r}$ and rotor plane
χ_{hor}	Horizontal angle between $\boldsymbol{V_r}$ and rotor plane
χ_{ver}	Vertical angle between $\boldsymbol{V_r}$ and rotor plane
ω	Angular rotor velocity
ϕ	Angle between rotor plane and V_{relxy}
Φ_r	Angle between rotor plane and $\boldsymbol{V_0}$
θ_{pitch}	Pitch angle
θ_{rotor}	Rotor azimuthal position
θ_{tt}	Tower top deflection angle
θ_{twist}	Twist angle

Coordinate systems, see section 3.1

G	Ground coordinate system
R	Rotating rotor coordinate system
S	Blade section coordinate system

Modifiers

*	Actual velocity or deflected direction (opposed to the assumed velocity or undeflected direction)

2 Introduction

Detailed knowledge about the atmospheric turbulent wind and its variation is essential for understanding and analysing many aspects regarding wind turbines, e.g. load conditions, power generation, noise aspects, and fatigue and extreme loads (Elliott and Cadogan, 1990; Larsen et al., 2005; Barlas et al., 2012; Madsen, 2014; St. Martin et al., 2016)

The wind of interest is the free undisturbed turbulent inflow, but at the location of the wind turbine rotor. The problem is that this free wind is immeasurable, as the inflow is influenced by the presence of the rotor itself: near the turbine, the flow is disturbed by the turbine, and further away, the wind is different. The ideal measure, therefore, is the free flow wind speed at the position of the turbine, i.e. the wind speed as it would have been at the same location and time without the turbine.

A cup or sonic anemometer at a nearby met mast, e.g., 2-3 diameters away, measures the free flow wind when not in the wake of the turbine or the mast, but smaller turbulence structures will be different due to the distance. As these structures have only limited influence on e.g. 10 min statistics, the wind speeds measured by met masts are still valuable and extensively used.

The wind speed measured by a nacelle- or spinner-mounted anemometer is influenced by the turbine. This influence is measurable more than one diameter upstream (Meyer Forsting et al., 2017) and continues until the wake is recovered far downstream. This means that a model or calibration function is required to estimate the free flow wind speed from a nacelle- or spinner-mounted anemometer.

Wind Energ. Sci. Discuss., https://doi.org/10.5194/wes-2017-57
Manuscript under review for journal Wind Energ. Sci.
Discussion started: 2 January 2018

eawe european academy of wind energy
Open Access WIND ENERGY SCIENCE DISCUSSIONS

The turbine is, however, not only exposed to the wind at the hub centre, and with the long blades of modern wind turbines, the wind-speed variations within the rotor may be considerable. This variation can be measured using lidars which are typically ground or nacelle based. From the nacelle, a lidar is able to measure the inflow field some distance upstream while the inflow field at the rotor plane can be measured using a set of ground-based scanning lidars (Mikkelsen et al., 2008, 2010; Scholbrock et al., 2015; Wagner et al., 2015). Nevertheless, the problem is the same; the lidars must either measure outside the induction zone to measure the free inflow or use a model to compensate for the presence of the turbine. Troldborg and Meyer Forsting (2017) describe a simple analytical model that is able to estimate the free wind speed, appropriate for power curves, from lidar measurements. The model is applicable for any rotor down to one rotor radius upstream.

Another option is to mount a flow sensor directly on the blade, e.g. one third from the tip. From this location, the sensor sweeps the rotor area and is thereby able to measure a lot of the variation that takes place within the rotor area.
Blade-mounted five-hole pitot tubes have been used in several research projects (Madsen, 1991; Brand et al., 1996; Petersen and Aagaard Madsen, 1997; Simms et al., 1999; Schepers et al., 2002; Madsen et al., 2003, 2010b; Medina et al., 2011), but other types of sensors could be used as well. In the current context, a blade-mounted flow sensor (BMFS) is assumed to measure the 3D inflow velocity at its position, i.e. the temporal resolution of a point fixed in space is limited to once per revolution, and multiple sensors are required for measuring in both the inner and outer part of the rotor. From the 3D inflow velocities measured by a BMFS, information about the angle of attack, relative velocity and the instant wind speed at the rotor plane can be extracted. This information can be used as input for the control of individual pitch or active trailing edge flaps to optimise power and reduce loads and noise (Larsen et al., 2005; Barlas et al., 2012; Kragh and Hansen, 2012; Kragh et al., 2012; Madsen, 2014). Another application is the generation of relative power or load curves that can be compared between similar periods or turbines. These relative curves can be used to investigate e.g. aerodynamic modifications or detect performance issues (Pedersen et al., 2017).

As a BMFS is inside the induction zone, a model is required to estimate the free flow wind speed. In this case, however, well-defined models already exist as they are used in aeroelastic codes, e.g. HAWC2, to simulate the flow that generates the aerodynamic forces at the blades (Larsen and Hansen, 2007; Madsen et al., 2018). These models calculate the disturbance of the flow caused by the turbine in terms of the induced velocities, which are then added to the free flow velocity to get the disturbed wind speed at the blades. Reversing this process, the free flow wind speed can be obtained by subtracting the induced velocities from the measured velocities.

This paper describes the necessary aerodynamic models as well as a procedure to obtain the free flow wind speed from a BMFS. A preliminary implementation of the method has previously been applied to measurements of a full-scale wind turbine with a blade-mounted five-hole pitot tube to estimate the free inflow in different wake conditions (Pedersen et al., 2015).

To test the method, both the disturbed and the immeasurable free flow wind speeds are required. A real validation against measurements is therefore infeasible. Instead, the method is tested in two independent simulated environments.
The first environment is simulated by HAWC2, a nonlinear aeroelastic code intended for computing wind turbine response in the time domain (Larsen and Hansen, 2007). HAWC2 uses Taylor's well-known frozen turbulence hypothesis (Taylor, 1938) and a combination of aerodynamic models, which are similar to the models of the current method, to calculate the disturbed

Wind Energ. Sci. Discuss., https://doi.org/10.5194/wes-2017-57
Manuscript under review for journal Wind Energ. Sci.
Discussion started: 2 January 2018

eawe european academy of wind energy
Open Access WIND ENERGY SCIENCE DISCUSSIONS

flow velocity at the rotor plane. Both the free inflow and the disturbed flow at the rotor plane are therefore directly available for verification of the method.

In the second environment, the simulations are performed by the structural model of FLEX5 (Øye, 1996) coupled with the large eddy simulation (LES) flow solver, EllipSys3D (Michelsen, 1992; Sørensen, 1995). This environment is completely independent of the aerodynamic models of the current method as well as Taylor's frozen turbulence hypothesis and is therefore valuable as a high fidelity verification. In this case, the free undisturbed inflow is obtained from a separate equivalent simulation where the effects of the aerodynamic forces on the flow are disabled.

3 Method

This section presents the aerodynamic models and the procedure used to obtain the free inflow velocities from a BMFS.

3.1 Coordinate systems

The coordinate systems used in this paper are listed in table 1.

Table 1. Coordinate systems used in this paper

Coordinate system	Abbreviation	Definition
Blade section coordinates	S	x^S: Along chord line from centre towards leading edge y^S: Perpendicular to chord line centre to suction side z^S: Aligned blade center line from root to tip
Rotating rotor coordinates	R	x^R: Tangential in rotational direction y^R: Aligned with main shaft in direction of the wind z^R: Aligned with the blade on which the BMFS is mounted
Ground coordinates	G	x^G: Horizontal left, perpendicular to the main shaft when seen from the front y^G: Horizontal in direction of main shaft z^G: Vertical, down

Transformation matrices are used to map velocities between the coordinate systems. As an example, the transformation matrix, $\boldsymbol{T_{RG}}$, describes the rotating-rotor coordinate-system axes in ground coordinates. $\boldsymbol{T_{RG}}$ can be used to map velocities in rotor coordinates, $\boldsymbol{V^R}$, to velocities in ground coordinates, $\boldsymbol{V^G}$:

$$\boldsymbol{V^G} = \boldsymbol{T_{RG}} \boldsymbol{V^R} \tag{1}$$

Wind Energ. Sci. Discuss., https://doi.org/10.5194/wes-2017-57
Manuscript under review for journal Wind Energ. Sci.
Discussion started: 2 January 2018

eawe european academy of wind energy
Open Access WIND ENERGY SCIENCE DISCUSSIONS

3.2 Wind speed from a BMFS

The method described in this paper take as input the effective 3D inflow velocities measured relative to the blade, locally at the rotor plane, i.e. including the effects caused by the presence of the turbine.

Near the airfoil, the local flow field is deflected and the speed is also influenced by the bound circulation on the surface of the airfoil; see the example in Fig. 1. As seen, this effect has a huge impact on the flow velocity measured near the airfoil and must therefore be compensated for before applying the current method. In the current study, however, it is neglected as the two verification environments, HAWC2 and EllipSys3D/Flex5, do not model the surface of the airfoils.

Shen et al. (2006, 2009), Guntur and Sørensen (2014) and Rahimi et al. (2017) present several methods to calculate the flow near the airfoil that also take 3D effects into account, but the methods require information that cannot be obtained directly from a BMFS. Pedersen et al. (2017) describes how to obtain the effective 3D inflow from the relative wind speed and two perpendicular angles measured by a blade-mounted five-hole pitot, including compensation for bound circulation. The compensation method uses a look-up table generated by 2D computational fluid dynamic (CFD) simulations, thus neglecting 3D effects, and tip- and root vortices.

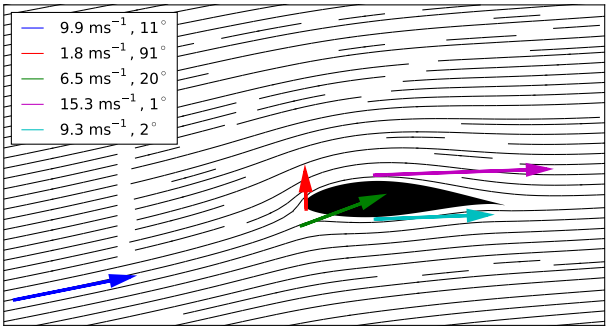

Figure 1. Near the airfoil, the flow is disturbed by upwash and stagnation. This effect is not included in the current method

From the relative velocity, $\boldsymbol{V_{rel}}$, the wind speed at the rotor plane, $\boldsymbol{V_r}$, is found by subtracting the velocity of the sensor, $\boldsymbol{V_s}$:

$$\boldsymbol{V_r} = \boldsymbol{V_{rel}} - \boldsymbol{V_s} \tag{2}$$

In this study, the sensor velocity, $\boldsymbol{V_s}$, includes movement due to rotor rotation and pitch motion. Structural dynamics, e.g. blade deflection, will therefore result in a mismatch between the assumed and the actual sensor velocity.

3.3 Aerodynamic models

The wind speed measured in the rotor plane of an operating wind turbine is different from the free flow wind speed that would have been present at the same time and location if the wind turbine was absent. The difference is induced by the wind turbine

Wind Energ. Sci. Discuss., https://doi.org/10.5194/wes-2017-57
Manuscript under review for journal Wind Energ. Sci.
Discussion started: 2 January 2018

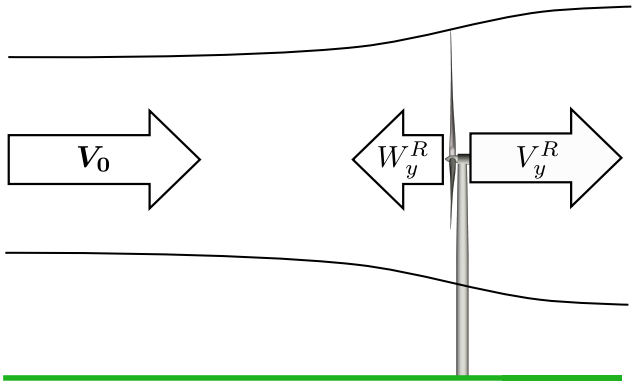

Figure 2. At the rotor plane, the free inflow wind velocity, $\boldsymbol{V_0}$, is reduced by the axial induction, W_y^R. A sensor at the rotor plan will therefore measure the reduced velocity, $V_{r,y}^R$, in the axial direction

induction and is rather complex. In this section, a set of simplified engineering aerodynamic models that each explains elements of the induction are presented. One can argue that the models are too simple compared to the physical processes. In general, however, the loads simulated by aeroelastic codes that use these models are found to agree well with measured loads; see e.g. Larsen et al. (2013). The models are therefore expected to be appropriate for the reverse process too.

The aerodynamic models in aeroelastic codes like FAST, Flex5, Bladed and HAWC2 is based on the Blade Element Momentum (BEM) model first presented by Glauert (1935). The original formulation, however, was derived for one-dimensional, steady and uniform inflow, which is far from the conditions that a real turbine operates in. The BEM model is therefore typically modified and combined with additional sub models, e.g. for tip loss and for skew and dynamic inflow. In this study, the aerodynamic model is based on the HAWC2 implementation (Madsen et al., 2018).

3.3.1 Axial induction

When operating, a wind turbine extracts kinetic energy from the wind by reducing the axial wind speed. This reduction is called the axial induction, W_y^R; see Fig. 2.

The axial induced wind speed is defined in terms of the axial induction factor, a:

$$W_y^R = a|\boldsymbol{V_0}| \tag{3}$$

where $\boldsymbol{V_0}$ is the free inflow velocity.

For laminar flow through the rotor, the axial induction factor is related to the thrust coefficient, C_T, by

$$C_T = 4a(1-a) \tag{4}$$

Wind Energ. Sci. Discuss., https://doi.org/10.5194/wes-2017-57
Manuscript under review for journal Wind Energ. Sci.
Discussion started: 2 January 2018

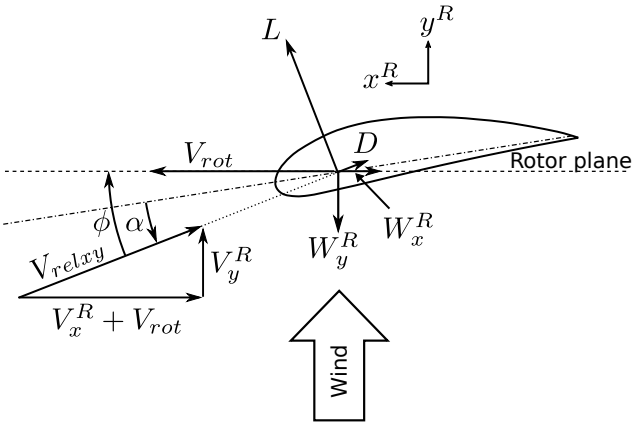

Figure 3. Cross-sectional airfoil element

while empirical results show higher values of C_T for induction factors above 0.3 - 0.5 (Eggleston and Stoddard, 1987). The current method uses a third order polynomial, as described by Madsen et al. (2018),

$$a = k_3 C_T^3 + k_2 C_T^2 + k_1 C_T \tag{5}$$

with coefficients $k_3 = 0.0883, k_2 = 0.0586, k_1 = 0.2460$ that fits to (4) for lower values of a and to empirical results and actuator disc simulations for higher loading (Madsen et al., 2010a).

For an annular ring element at radius r, the thrust coefficient is calculated by the formula presented by Madsen et al. (2018):

$$C_T = \frac{V_{relxy}^2 c C_y(\alpha) N_B}{2\pi r |\boldsymbol{V_0}|^2} \tag{6}$$

where V_{relxy} is the relative wind speed in the (x^R, y^R)-plane (see Fig. 3), c is the chord length, α is the angle of attack, N_B is the number of blades and C_y is the projection of the lift and drag coefficient into y^R:

$$C_y = cos(\phi) C_L(\alpha) + sin(\phi) C_D(\alpha) \tag{7}$$

where $\phi = \alpha + \theta_{twist} + \theta_{pitch}$ is the angle between V_{relxy} and the rotor plane.

From the measurements of a BMFS, V_{relxy} and α can be obtained directly, and the number of blades, the pitch angle, the radius, the chord length and the blade twist angle are assumed to be known. Hence, if the angle-of-attack dependent lift and drag coefficients are accessible from a look-up table, then the only unknown term on the right-hand side of (6) is $\boldsymbol{V_0}$.

In aeroelastic simulations, $\boldsymbol{V_0}$ is obtained from the wind input model, but in this case, $\boldsymbol{V_0}$ is the wind speed that we want to find. It can, however, be found using the iterative approach described in section 3.4, such that the induced axial velocity can be calculated via equation 6, 5 and 3.

Wind Energ. Sci. Discuss., https://doi.org/10.5194/wes-2017-57
Manuscript under review for journal Wind Energ. Sci.
Discussion started: 2 January 2018

eawe european academy of wind energy
Open Access WIND ENERGY SCIENCE DISCUSSIONS

3.3.2 Tip correction

The relationship between the thrust coefficient and the axial induction factor stated in (4) is based on the assumption that the induced velocities are constant within an annular element. This is not the case for turbines with a finite number of blades and therefore Prandtl's tip loss factor, presented by Glauert (1935),

$$F_{tip} = \frac{2}{\pi}\cos^{-1}\left(\exp\left(-\frac{N_B}{2}\frac{R-r}{r\sin(\phi)}\right)\right) \tag{8}$$

where R is the blade tip radius, is applied in the current method by replacing C_T with $\frac{C_T}{F_{tip}}$ in (5) as described by Madsen et al. (2018). Calculating and applying the tip loss factor is straightforward as the only variable on the right-hand side, ϕ, can be calculated from the BMFS output.

3.3.3 Tangential induction

The tangential induction is a reaction to the torque force and results in a rotation of the wake downstream. The tangential velocity of the wake is defined in terms of the tangential induction factor, a':

$$W_x^R = a'\omega r \tag{9}$$

where ω is the angular velocity of the rotor. Unlike the axial induction, this effect does not affect the flow upstream. The amount of tangential induction at the position of a BMFS is therefore dependent on the sensor position relative to the blade, the pitch angle and the blade-deflection state. The current implementation of the method assumes full tangential induction, but for some applications, it may be more appropriate to switch it off.

The tangential induction factor is obtained by the formula presented by Madsen et al. (2018):

$$a' = \frac{V_{relxy}^2 c C_x(\alpha) N_B}{8\pi r^2 (1-a)|\boldsymbol{V_0}|\omega} \tag{10}$$

where $C_x = sin(\phi)C_L(\alpha) + cos(\phi)C_D(\alpha)$ is the projection of the lift and drag coefficient into x^R; see Fig. 3.

In (10), the only unknown term on the right-hand side is also $\boldsymbol{V_0}$, which can be found via the iterative approach described in section 3.4. To help this iterative procedure in finding the right solution, the value of a used in (10) is limited to the range $[0; 0.5]$.

3.3.4 Radial induction

The radial induction results in an expansion of the flow, as illustrated in Fig. 2. Introducing the radial induction factor, a_r, the radial induced velocity is:

$$W_z^R = |\boldsymbol{V_0}|a_r \tag{11}$$

Wind Energ. Sci. Discuss., https://doi.org/10.5194/wes-2017-57
Manuscript under review for journal Wind Energ. Sci.
Discussion started: 2 January 2018

eawe european academy of wind energy
Open Access WIND ENERGY SCIENCE DISCUSSIONS

The standard one-dimensional BEM theory does not handle radial induction and therefore the analytical equation derived by Madsen et al. (2010a) is used in the current method:

$$a_r = \frac{1}{2.24}\frac{C_{T,avg}}{4\pi}\ln\left(\frac{0.04^2+\left(\frac{r}{R}+1\right)^2}{0.04^2+\left(\frac{r}{R}-1\right)^2}\right) \tag{12}$$

where $C_{T,avg}$ is the average thrust coefficient of the whole rotor. In the current model, the revolution averaged local thrust coefficient of the BMFS is used. This is obviously not the same, and the approximation is therefore only appropriate if the thrust coefficient of the radial position corresponds to the average thrust coefficient of the whole rotor. This is typically not the case near the root and the tip, and even for a sensor that is one third from the tip, some discrepancies must be expected.

3.3.5 Dynamic inflow

The induced velocities are parts of an equilibrium which is gradually established between the load on the blades, the rotor wake and the induced velocity at the rotor plane (Sørensen and Aagaard Madsen, 2006).

Small and high frequent turbulence is assumed to pass unaffected though the rotor and can therefore be measured directly, while the effect of large stationary turbulence eddies can be described by the BEM models in section 3.3.1 and section 3.3.3. In between, the modification of the wind flow depends on the wake recovery velocity. Snel and Schepers (1995) present different engineering approaches to model the wind turbine response in dynamic inflow.

In the current method, the model used in HAWC2 (Madsen et al., 2018) has been implemented with two modifications. This implementation applies two first-order low-pass filters to the induced velocities to model the slow and gradually changing induction,

$$\boldsymbol{W}^{\boldsymbol{R}}_{\boldsymbol{dyn}} = 0.6\mathrm{LP}(\tau_{NW}, \boldsymbol{W}^{\boldsymbol{R}}) + 0.4\mathrm{LP}(\tau_{FW}, \boldsymbol{W}^{\boldsymbol{R}}) \tag{13}$$

where $\mathrm{LP}(\tau, X)$ is a first-order low-pass filter. The two filters model the near- and far-wake effects respectively, and their filter characteristics are given by:

$$\tau_{NW} = \tau^*_{NW}\frac{1.8R}{|\boldsymbol{V_0}|\min\left[1-3\frac{W^R_{y,avg}}{|\boldsymbol{V_0}|}, 2.0\right]} \tag{14}$$

$$\tau_{FW} = \tau^*_{FW}\frac{R}{|\boldsymbol{V_0}|\max\left[1+3\frac{W^R_{y,avg}}{|\boldsymbol{V_0}|}, 0.2\right]} \tag{15}$$

where

$$\tau^*_{NW} = -0.4783(r/R)^2 + 0.1025(r/R) + 0.6125 \tag{16}$$

$$\tau^*_{FW} = -0.4751(r/R)^2 + 0.4101(r/R) + 1.9210 \tag{17}$$

Equation (16) and (17) can be calculated straight away, while $\boldsymbol{V_0}$ and $W^R_{y,avg}$ are required for (14) and (15). $\boldsymbol{V_0}$ can be estimated as described in section 3.4, while the instant average axial induction of the whole rotor, $W^R_{y,avg}$, requires information from the

Wind Energ. Sci. Discuss., https://doi.org/10.5194/wes-2017-57
Manuscript under review for journal Wind Energ. Sci.
Discussion started: 2 January 2018

eawe european academy of wind energy
Open Access WIND ENERGY SCIENCE DISCUSSIONS

whole rotor which cannot be obtained from a BMFS.

In the current implementation, the revolution averaged local induction is used as an approximation. This means that the filter characteristics may be inaccurate if the induction at the radial position of the BMFS is not representative for the whole blade. The sensitivity to $W^R_{y,avg}$ is, however, limited and even extreme values have only a minor impact on the final estimated free wind speed.

The other modification is more severe. In HAWC2, the rotor is discretised in grid points and the dynamic inflow model is applied to the local induced velocities of each of these grid points. This is possible because the local induction is calculated for each grid point in every time step, and this means that the induction of a certain grid point reflects the current circumstances as well as the history of that particular grid point.

In the current method, only the local induction at the position of the BMFS is obtainable as no information is available from other parts of the rotor. Applying the dynamic inflow model to the induced velocities at the position of the BMFS means that the estimated induction reflects the history of the moving BMFS instead of a fixed position. In a situation with wind shear, the estimated induction will therefore be too high in the lower part of the rotor and too low in the upper part, resulting in too much variation in the estimated free wind speed.

Instead, the low pass filters are applied to the induced wind speeds of fixed azimuthal positions. As the BMFS only passes a certain azimuthal position once per revolution, the sample frequencies of these signals are very low and some discrepancies must be expected.

Figure 4 shows the induced velocities in a simulation with turbulent inflow and shear. The quasi steady induced velocities estimated without the dynamic inflow model, W^R_y, are seen to vary much more than the HAWC2 reference, while applying the low-pass filters to the rotating measurements, $W^R_{y,dyn}$, smoothens the induction too much. Applying the low-pass filters to the low-frequency signals of fixed azimuthal positions, $W^R_{y,dyn,azi}$, results in an estimate closer to the HAWC2 reference even though there is still some mismatch.

3.3.6 Skew inflow

In skewed inflow, where the mean wind is not perpendicular to the rotor plane, the axial induction is not directed exactly towards the wind. Hence the speed of the inflow is reduced less, and the thrust is increased. Furthermore, variation in the wake vorticity concentration results in an azimuthal dependent variation of the axial induction; see Fig. 5.

The first effect is modelled by the method described in Madsen et al. (2018) where the axial induction factor is multiplied by a reduction factor, F_a, that is calculated from the average thrust coefficient, $C_{T,avg}$ and the skew inflow angle, Φ_r.

$$F_a = k_3 C^3_{T,avg} + k_2 C^2_{T,avg} + k_1 C_{T,avg} + k_0 \tag{18}$$

Wind Energ. Sci. Discuss., https://doi.org/10.5194/wes-2017-57
Manuscript under review for journal Wind Energ. Sci.
Discussion started: 2 January 2018

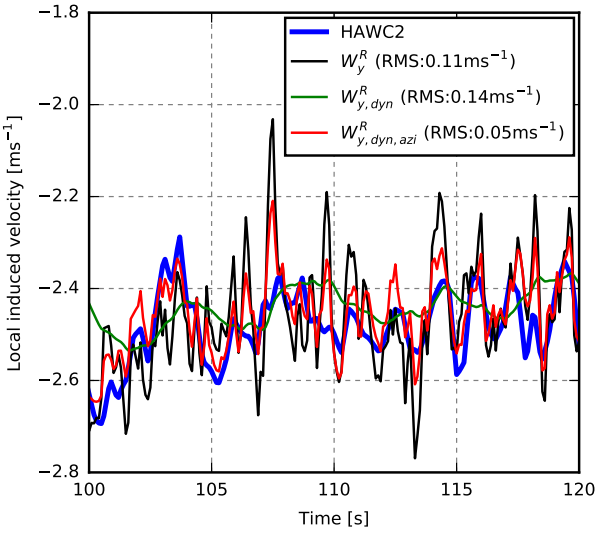

Figure 4. Local induced axial velocity calculated by HAWC2 and the current method in three configurations: W without the dynamic inflow model (W_y^R), with the dynamic inflow model applied to the rotating measurements ($W_{y,dyn}^R$), and with the dynamic inflow model applied to the low-frequency signals of fixed azimuthal positions ($W_{y,dyn,azi}^R$)

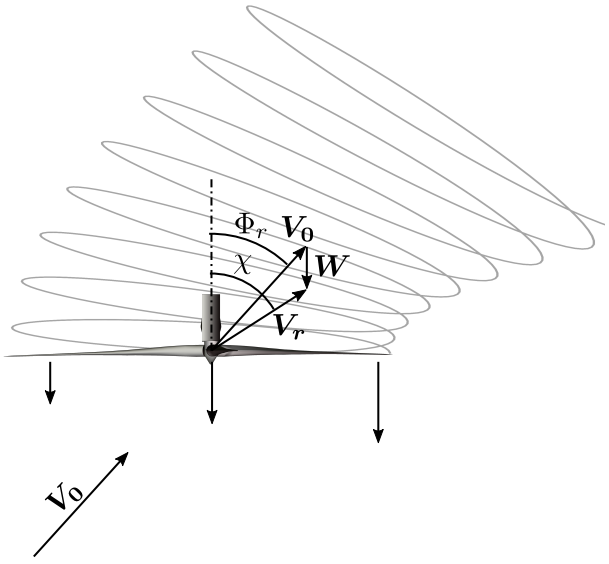

Figure 5. Wind turbine in skew inflow. The axial induction varies due to different wake vorticity concentration, and it is not directed exactly towards the wind

Wind Energ. Sci. Discuss., https://doi.org/10.5194/wes-2017-57
Manuscript under review for journal Wind Energ. Sci.
Discussion started: 2 January 2018

eawe european academy of wind energy
Open Access WIND ENERGY SCIENCE DISCUSSIONS

where

$$k_0 = 1 \tag{19}$$

$$k_1 = -0.164\Phi_r^3 + 0.4438\Phi_r^2 - 0.5136\Phi_r \tag{20}$$

$$k_2 = 0.8646\Phi_r^3 - 2.6145\Phi_r^2 + 2.1735\Phi_r \tag{21}$$

$$k_3 = -0.6481\Phi_r^3 + 2.1667\Phi_r^2 - 2.0705\Phi_r \tag{22}$$

The average thrust coefficient is estimated by the revolution averaged local thrust coefficient as described in section 3.3.4, and in this case the approximation is also expected to introduce discrepancies. The inflow angle, Φ_r, is calculated by

$$\Phi_r = \arctan\left(\frac{\sqrt{{V_{0,x}^R}^2 + {V_{0,z}^R}^2}}{V_{0,y}^R}\right) \tag{23}$$

Note that the $C_{T,avg}$ used in (18) must be limited to the range $[0;1]$ as the model is invalid outside this range.

The azimuthal variation is calculated by a model presented by Madsen et al. (2018). In this model, the axial induction factor is multiplied with a rotor-position dependent factor, F_{azi}:

$$F_{azi} = 1 - k_x \frac{r}{R}\sin(\theta_{rotor}) - k_y \frac{r}{R}\cos(\theta_{rotor}) \tag{24}$$

where θ_{rotor} is the rotor-azimuth position. The factors, k_x and k_y, depend on the inflow angle, χ, in the horizontal and vertical plane (see Fig. 5):

$$k_x = \tan(0.4\chi_{hor}) \tag{25}$$

$$k_y = \tan(0.4\chi_{ver}) \tag{26}$$

3.3.7 Combining models

The presented aerodynamic models are now combined into a function, f_W, that comprises the following steps:

1. Calculate C_T using (6)
2. Calculate tip loss factor by (8)
3. Calculate a by (5) replacing C_T with $\frac{C_T}{F_{tip}}$
4. Apply skew inflow model
   (a) Calculate reduction factor F_a using (18)
   (b) Calculate azimuthal variation factor F_{azi} using (24)
   (c) Apply correction by multiplying a with F_a and F_{azi}

Wind Energ. Sci. Discuss., https://doi.org/10.5194/wes-2017-57
Manuscript under review for journal Wind Energ. Sci.
Discussion started: 2 January 2018

5. Calculate tangential induction factor using (10)
6. Calculate radial induction factor using (12)
7. Calculate the quasi-steady induced velocities $\boldsymbol{W^R} = \begin{pmatrix} a'\omega r & a|\boldsymbol{V_0}| & |\boldsymbol{V_0}|a_r \end{pmatrix}^T$
8. Apply dynamic inflow model
   (a) Extract the induced velocities of each azimuthal position
   (b) calculate filter characteristics using (14) - (17)
   (c) Apply the dynamic inflow model (13) to the induced velocities of each azimuthal position to obtain $\boldsymbol{W^R_{dyn,azi}}$

Using this function, the estimated induced velocities can be calculated for a given $\boldsymbol{V_0}$,

$$\boldsymbol{W_{est}} = \mathrm{f_W}(|\boldsymbol{V_0}|) \tag{27}$$

3.4 Estimating $\boldsymbol{V_0}$

The flow velocity measured by the BMFS is the sum of the free flow and the induced velocities, hence:

$$\boldsymbol{V_0} = \boldsymbol{V_r} - \boldsymbol{W} \tag{28}$$

Using $\mathrm{f_W}$, defined in section 3.3.7, an estimate of the free flow velocity can be obtained

$$\boldsymbol{V_{0,est}} = \boldsymbol{V_r} - \mathrm{f_W}(|\boldsymbol{V_0}|) \tag{29}$$

Figure 6 shows the estimated free wind speed, $|\boldsymbol{V_{0,est}}|$, as a function of $|\boldsymbol{V_0}|$ in an example where the measured wind speed,

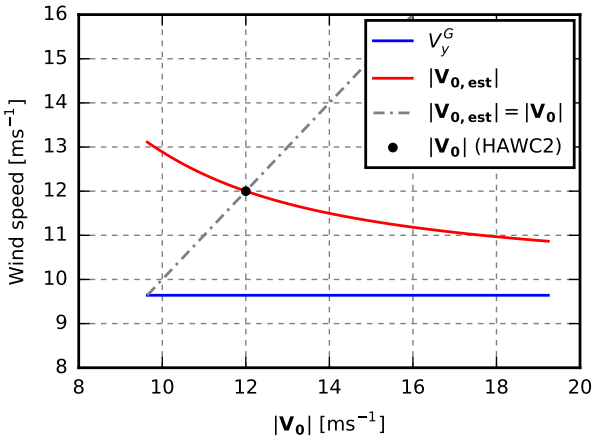

Figure 6. Example of free wind speed estimation. For $|V_0| = 12$, the estimated free wind speed, $|\boldsymbol{V_{0,est}}|$, calculated by (29) equals $|\boldsymbol{V_0}|$

Wind Energ. Sci. Discuss., https://doi.org/10.5194/wes-2017-57
Manuscript under review for journal Wind Energ. Sci.
Discussion started: 2 January 2018

eawe european academy of wind energy
Open Access WIND ENERGY SCIENCE DISCUSSIONS

$V_{r,y}^N$ is around 9.6 $\mathrm{m\,s^{-1}}$.

We now want to find the correct free wind speed, i.e. the $\boldsymbol{V_0}$ that, when inserted into (29), results in $\boldsymbol{V_{0,est}}$ being equal to $\boldsymbol{V_0}$ (12 $\mathrm{m\,s^{-1}}$ in Figure 6). In other words, we solve

$$|\boldsymbol{V_0}| - |(\boldsymbol{V_r} - \mathrm{f_W}(\boldsymbol{V_0}))| = 0 \tag{30}$$

with respect to $\boldsymbol{V_0}$ iteratively using the Newton-Raphson method and $\boldsymbol{V_r}$ as the initial guess for $\boldsymbol{V_0}$.

3.5 Verification

3.5.1 HAWC2

The method is verified using HAWC2 simulations of a Siemens 3.6 MW turbine with a 107 m rotor. The turbine has a 6° tilt and 3.5° coning angle, and is controlled by the basic DTU Wind Energy controller (Hansen and Henriksen, 2013). The inflow turbulence for the turbulence cases is generated using the Mann model (Mann, 1994).

From the simulations, the relative wind speed is extracted at a point on the blade at radius 36 m, i.e. around one third from the tip. From this wind speed the estimated free wind speed is calculated and compared to the free wind speed used as the input to HAWC2. Note that the current version of HAWC2 (version 12.5) does not include radial induction, and therefore this model is disabled when testing against HAWC2.

As the current method is based on the same aerodynamic models as HAWC2, one may argue that this verification just adds and subtracts the same value, which obviously results in the original velocity. There are, however, differences that are important to investigate, e.g. the effect of the differences and approximation in the aerodynamic models of the current method, the effect of a flexible structure and the $\boldsymbol{V_0}$-estimation procedure.

3.5.2 EllipSys3D/Flex5

The method is furthermore verified using EllipSys3D/Flex5 simulations of a 2.3 MW Siemens turbine with a 93 m rotor. In these simulations, the flow field is obtained from large eddy simulations (LES) performed by the finite-volume and incompressible Navier-Stokes solver, EllipSys3D (Michelsen, 1992; Sørensen, 1995). The turbine is modelled using the actuator line method as developed by Sørensen and Shen (2002), where the individual blades are modelled by imposing body forces into the flow solver. The actuator lines are fully coupled to the aeroelastic tool, Flex5 (Øye, 1996), which models the structural dynamics according to the incoming flow; see (Sorensen et al., 2015) for details on the coupling. The inflow turbulence, which is similar to the turbulence of the HAWC2 simulations, is imposed 8.25 radius upstream from the rotor.

From these simulations, the flow speed is extracted at radius 32 m, i.e. also around one third from the tip. All EllipSys3D/Flex5 simulations use a flexible structural model. Flex5 is based on modal shape functions as opposed to the multibody formulation of HAWC2, and hence does not include torsional rotation of the blades.

Wind Energ. Sci. Discuss., https://doi.org/10.5194/wes-2017-57
Manuscript under review for journal Wind Energ. Sci.
Discussion started: 2 January 2018

eawe european academy of wind energy
Open Access WIND ENERGY SCIENCE DISCUSSIONS

To obtain the free inflow velocities, a separate identical flow simulation is performed, in which the effect of the aerodynamic forces on the flow is disabled such that the flow is not unaffected by the turbine. From this simulation the flow field in the vertical plane through the rotor centre is obtained for each time step.

3.5.3 Free flow reference

The estimated free flow velocities are based on the velocities measured at the sensor position (red dot in Fig. 7). In the current verification, however, the reference free flow velocity is extracted at the assumed (undeflected) sensor position (green dot in Fig. 7). This mismatch is expected to introduce some deviation as the turbulence is different at the two positions.

In the HAWC2 simulations, which are based on Taylor's frozen turbulence hypothesis, the turbulence is transported unaffected by the mean wind, i.e. with constant (free flow) speed along the y^G axis. This means that time can be mapped into space and the free flow velocities can be extracted from the 3D turbulence field that is generated prior to the simulation.

The EllipSys flow, on the other hand, includes properties of real flow, e.g. that turbulence structures change and break up over time. The 3D turbulence field will therefore change in every time step and only the velocities at the rotor-centre flow plane are available for this study. The assumed sensor position, however, does not exactly intersect this plane, due to the rotor tilt angle. We are therefore compelled to rely on Taylor's frozen turbulence hypothesis to obtain the free flow reference velocity at the assumed sensor position, but only from the rotor-centre plane to the sensor position (blue arrow in Fig. 7), i.e. at most 3.3 m.

Furthermore, the EllipSys flow is affected by the turbine. Near the rotor, the axial induction reduces the turbulence transport speed, while the radial induction results in an expansion of the flow that moves the turbulence structure outwards.

This means that the BMFS is exposed to "delayed" turbulence structures that originate from a smaller radial position (white dot in Fig. 7), and even more deviation is therefore expected.

Wind Energ. Sci. Discuss., https://doi.org/10.5194/wes-2017-57
Manuscript under review for journal Wind Energ. Sci.
Discussion started: 2 January 2018

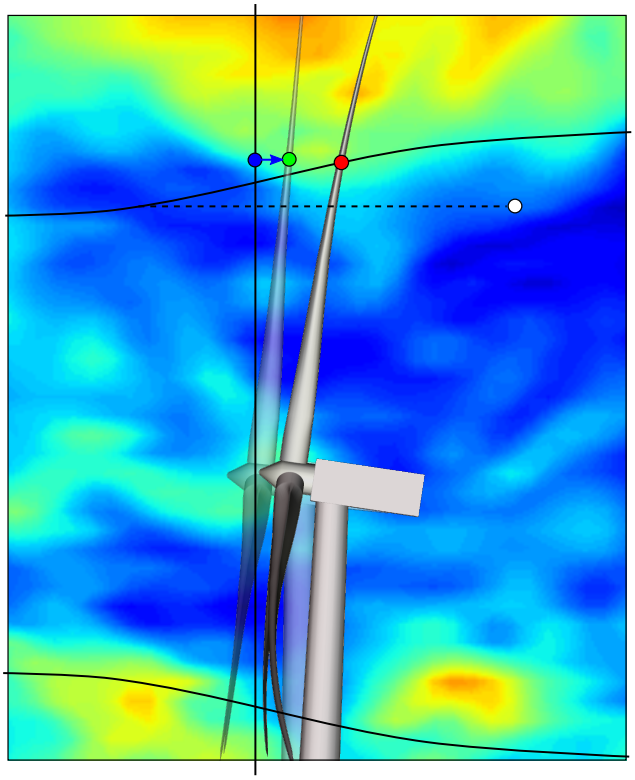

Figure 7. The estimated free flow at the sensor position (red dot) is compared to the free flow at the assumed position (green dot). In the EllipSys3D/Flex5 simulations, the nearest available free flow velocity is at the rotor-centre plane (blue dot). The sensor is, however, exposed to "delayed" turbulence structures that originate from a smaller radial position (white dot).

Wind Energ. Sci. Discuss., https://doi.org/10.5194/wes-2017-57
Manuscript under review for journal Wind Energ. Sci.
Discussion started: 2 January 2018

eawe european academy of wind energy
Open Access WIND ENERGY SCIENCE DISCUSSIONS

4 Results

4.1 HAWC2 verification

The root-mean-squared error, RMS, of the estimated instantaneous free wind speed, $\boldsymbol{V_{0,est}}$, is shown for 7 $\mathrm{m\,s^{-1}}$ in Fig. 8 for HAWC2 simulations of increasing complexity and the EllipSys3D/Flex5 simulations.

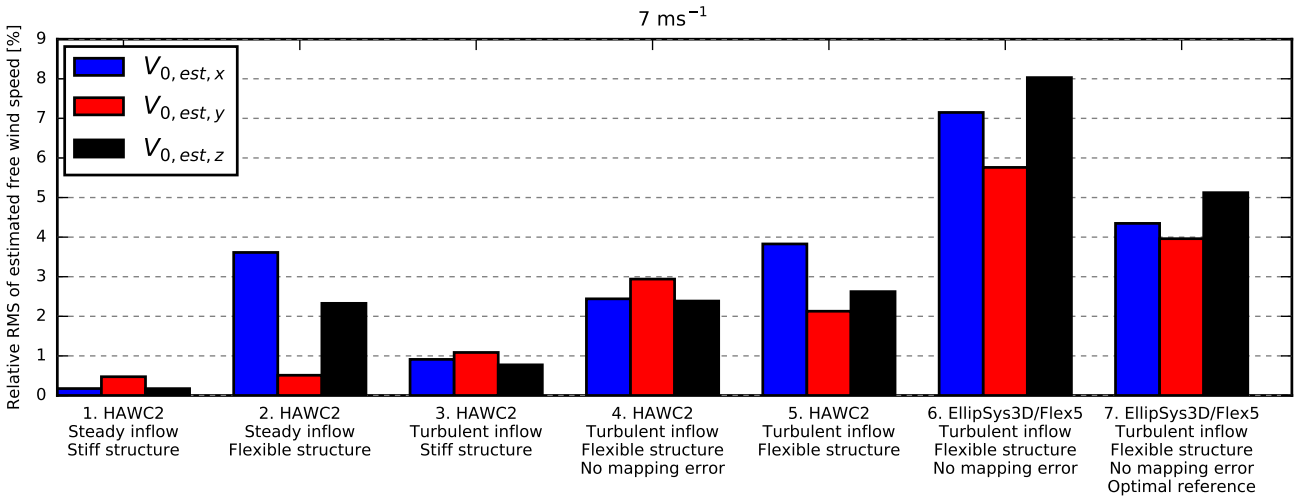

Figure 8. Relative RMS of the estimated free wind speed at 7 $\mathrm{m\,s^{-1}}$. For Case 4, 6 and 7, "No mapping error" means that deviations introduced in the transformation from the deflected blade-section coordinates to the fixed ground coordinates are not included

Starting with steady, uniform inflow and a stiff structural model, **Case 1**, the RMS error is very small and the minor deviations between the estimated free velocities and the HAWC2 references in Fig. 9 are caused by the effects of rotor tilt that are not exactly compensated by the skew inflow model.

In **Case 2**, the structural model is flexible. The rotation of the sensor due to the deflection and torsion of the tower and blade results in increased error levels that are clearly seen in the x- and z-velocity components in Fig. 9.

The most significant error is the 90° phase-shifted sinusoidal oscillation of the estimated velocities. This error is caused by thrust dependent flap-wise deflection of the blade that results in a part of $V_{r,y}^{R}$ being inaccurately projected onto the z^{R}-direction; see Fig. 10. This constant error leads to oscillations of the x and z components in the non-rotating ground coordinate system.

This error is reduced by a counteracting effect, namely the torque pushing the blade forward in the edge-wise direction. At this forward-pushed position, the direction of the actual velocity due to rotor rotation, $\boldsymbol{V_{rot}}^{*}$, is slightly changed, but the blade-section coordinate system is rotated even more as seen in the right-hand side of Fig. 11. A small part of $\boldsymbol{V_{rot}}^{*}$ is thereby measured in the radial $-z^{R}$ direction, while the current model assumes the rotational velocity, $\boldsymbol{V_{rot}}$, to be tangential. This

Wind Energ. Sci. Discuss., https://doi.org/10.5194/wes-2017-57
Manuscript under review for journal Wind Energ. Sci.
Discussion started: 2 January 2018

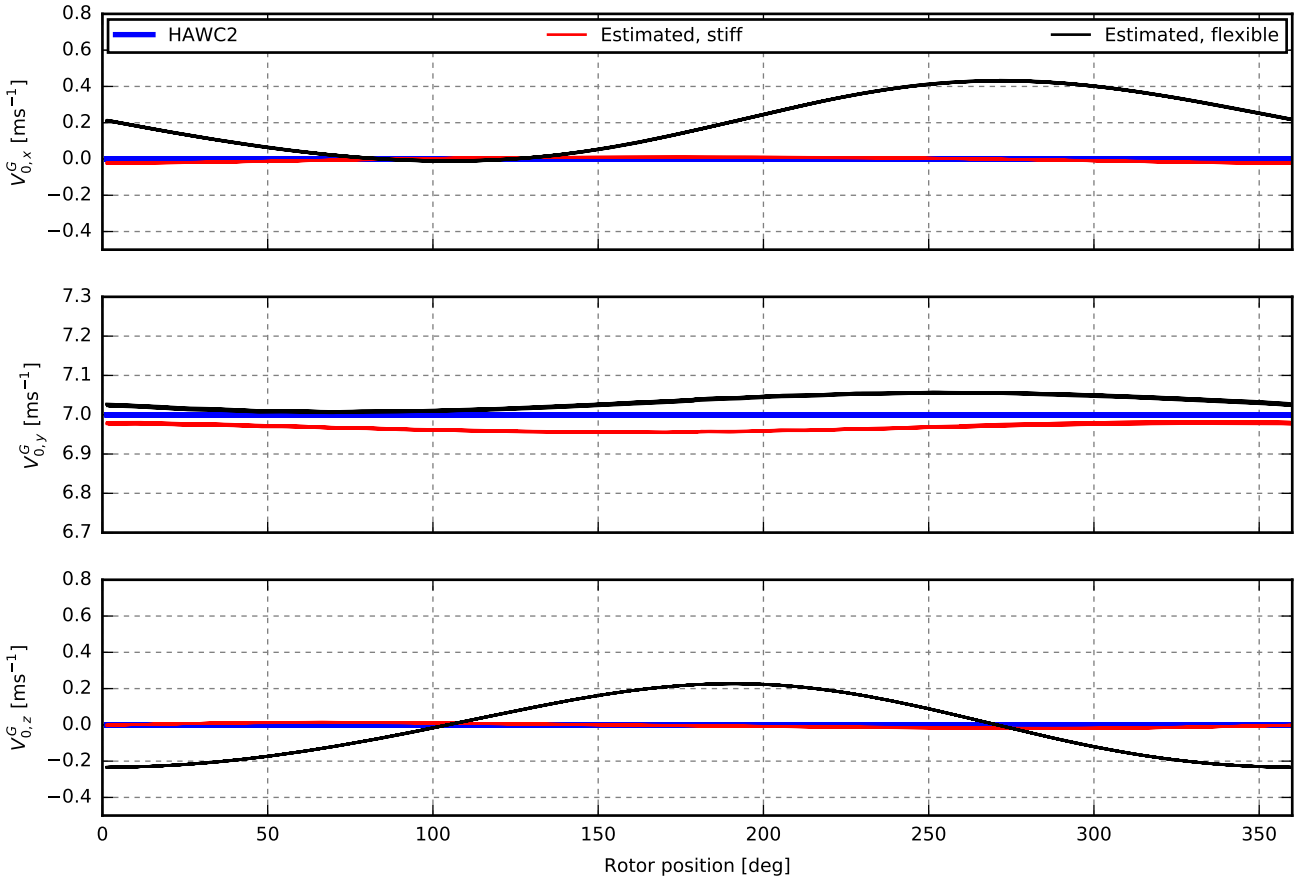

Figure 9. HAWC2 result: The free wind speed estimated in 13 $\mathrm{m\,s^{-1}}$ steady uniform inflow for stiff (Case 1) and flexible (Case 2) structural models.

mismatch leads to a torque-dependent error in the $-z^R$-direction that reduces the thrust-dependent contribution from flap-wise deflection.

A closer look at Fig. 9 reveals a positive offset in the estimated x-component. The reason for this offset, which corresponds to a spurious side wind, is a combination of two effects, both caused by gravity-induced edge-wise deflections of the blade. When the blades are horizontal, the gravity pulls the blades down towards the earth; see the left- and right-hand side of Fig. 11. This asymmetric edge-wise deflection leads to a small part of $\boldsymbol{V_{rot}}^*$ being measured in the radial $-z^R$ direction on the right-hand side of the rotor and in the $+z^R$-direction on the left-hand side, i.e. in the $+x^G$-direction on both sides. Furthermore, the transition from backward to forward deflection results in the blade moving faster in the upper part of the rotor and vice versa in the lower part. In the current method, however, the assumed rotational speed, $\boldsymbol{V_{rot}}$, is uniform. The mismatch results in deviations that also map to $+x^G$ in both vertical positions; see Fig. 11.

In combination, these two effects result in the almost constant positive offset of the $V^G_{0,est,x}$-velocity seen in Fig. 9.

Wind Energ. Sci. Discuss., https://doi.org/10.5194/wes-2017-57
Manuscript under review for journal Wind Energ. Sci.
Discussion started: 2 January 2018

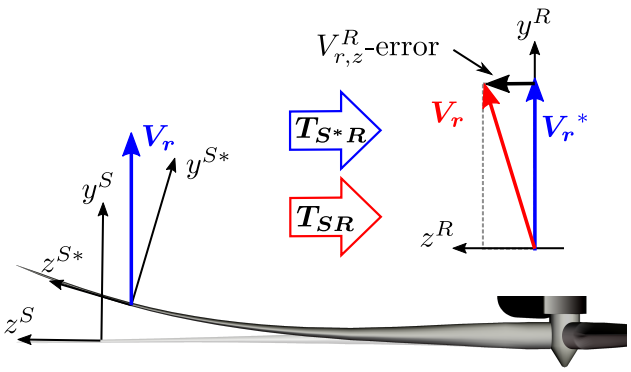

Figure 10. The rotation angle of the deflected blade section is unknown in the current method. An error is thereby introduced when mapping the measured wind speed, $\boldsymbol{V_r}$, from the blade section to the rotating rotor coordinates using the transformation matrix, $\boldsymbol{T_{SR}}$. The result is a constant error in the z^R-direction that leads to sinusoidal oscillations of the x- and z-component of the estimated free wind speed seen in Fig. 9

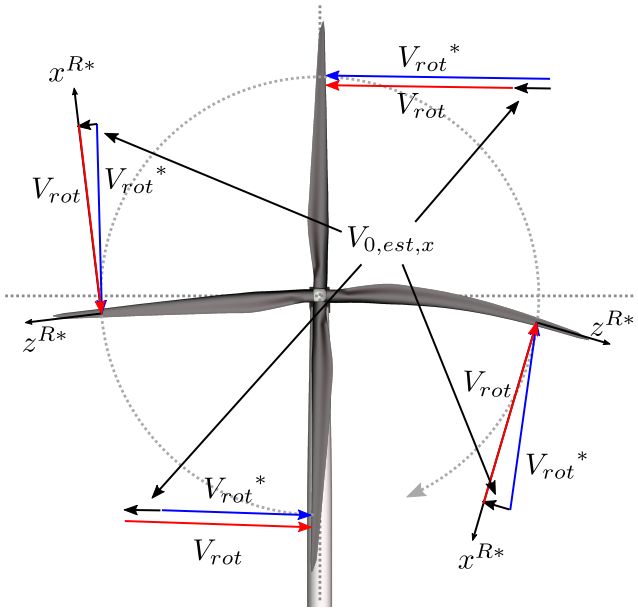

Figure 11. When the blades are horizontal, a small part of $\boldsymbol{V_{rot}}^*$ is measured in the $-z^{R*}$-direction on the right-hand side of the rotor and in the $+z^{R*}$-direction on the left-hand side due to the gravity induced deflection of the blade section. Furthermore, the blade is moving faster in the upper part of the rotor due to the transition from backward to forward deflection, and slower in the lower part. In the current method, however, the rotational speed, $\boldsymbol{V_{rot}}$, is assumed to be tangential and uniform. The mismatch results in a spurious side wind, seen as a mean offset in the x-component of Fig. 9.

Wind Energ. Sci. Discuss., https://doi.org/10.5194/wes-2017-57
Manuscript under review for journal Wind Energ. Sci.
Discussion started: 2 January 2018

eawe european academy of wind energy
Open Access WIND ENERGY SCIENCE DISCUSSIONS

For higher wind speeds, the estimated free wind speed in the y^G direction is overestimated due to the rotation of the elastic blade section. As the rotation angles are unknown in the current method, an error is introduced in the transformation from blade-section to ground coordinates; see Fig. 12. Blade torsion is an obvious source of the rotation, but for the current turbine model flap-wise bending also contributes considerably. This effect is highly dependent on the wind speed and blade design, and for the DTU 10MW reference wind turbine (Bak et al., 2013), an underestimation was seen instead.

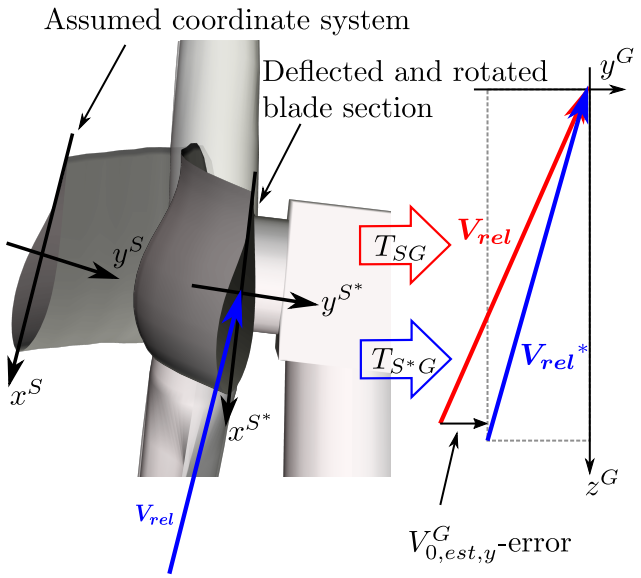

Figure 12. The torsion angle of the deflected blade section is unknown in the current method. An error is thereby introduced when mapping the relative velocity, $\boldsymbol{V_{rel}}$, from the blade section to the ground coordinates using the transformation matrix, $\boldsymbol{T_{SG}}$. The result is the overestimation of the y-component of the estimated free wind speed, $V^G_{0,est,y}$

Another effect that is seen in higher wind speeds is a negative mean offset in the z component due to tower deflection. In the transformation from rotating-rotor to ground coordinates, the angle between y^R and y^G is assumed to equal the tilt angle, but due to tower deflection the real angle is slightly larger, as it also includes the tower-top deflection angle, θ_{tt}; see Fig. 13. A small part of $\boldsymbol{V_r}$ is therefore inaccurately projected onto z^G, resulting in a small error in $V_{0,est,z}$.

This error can easily be compensated for by including the tower-top deflection angle, measured by an inclinometer, in the transformation from rotating rotor to ground coordinates. Similarly, the blade deflection and torsion angles can be included in the transformation from blade-section to rotor coordinates. These angles are, however, more challenging to measure, due to the large centrifugal force.

In **Case 3**, a stiff structural model is simulated in turbulent inflow. As seen in Fig. 8 and 14, the discrepancies are very limited despite the differences in the dynamic inflow model.

Case 4 combines the flexible structure with turbulent inflow, but the BMFS-measured flow velocities are extracted in the ground coordinates such that errors introduced in the transformation from deflected blade-section coordinates are avoided. The

Wind Energ. Sci. Discuss., https://doi.org/10.5194/wes-2017-57
Manuscript under review for journal Wind Energ. Sci.
Discussion started: 2 January 2018

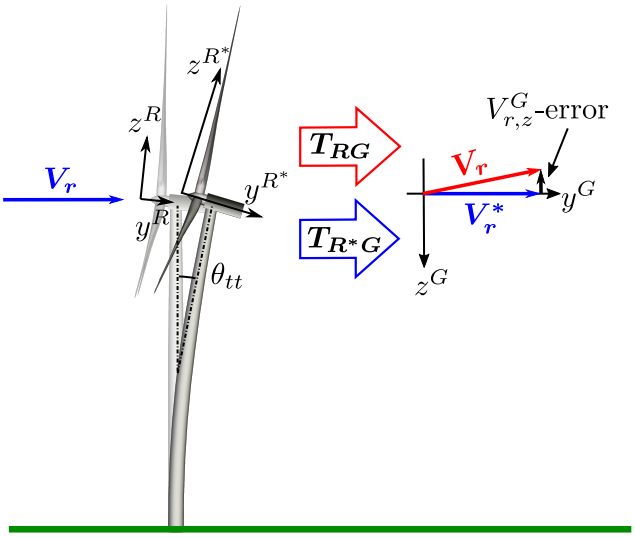

Figure 13. The tower top deflection angle, θ_{tt}, is unknown in the current method, and therefore the applied transformation matrix, $\boldsymbol{T_{RG}}$, inaccurately projects a small part of $\boldsymbol{V_r}$ onto $V_{r,z}^G$. The result is the small negative offset in the z-component in Fig. 9.

errors are significantly increased in all components; see Fig. 8. The reason is the mismatch between the assumed sensor velocity, i.e. the velocity due to rotor rotation and pitch motion, and the real velocity, which also includes velocity due to dynamic deflections of the structure. Furthermore, deviations are introduced because the free flow reference velocity is extracted at the assumed (undeflected) sensor position, while the model estimates the velocity at the deflected sensor position; see Fig. 7. This mismatch can be reduced, assuming that the real sensor position can be measured, e.g. using a GPS, or estimated by a method that includes tower and blade deflection.

Wind Energ. Sci. Discuss., https://doi.org/10.5194/wes-2017-57
Manuscript under review for journal Wind Energ. Sci.
Discussion started: 2 January 2018

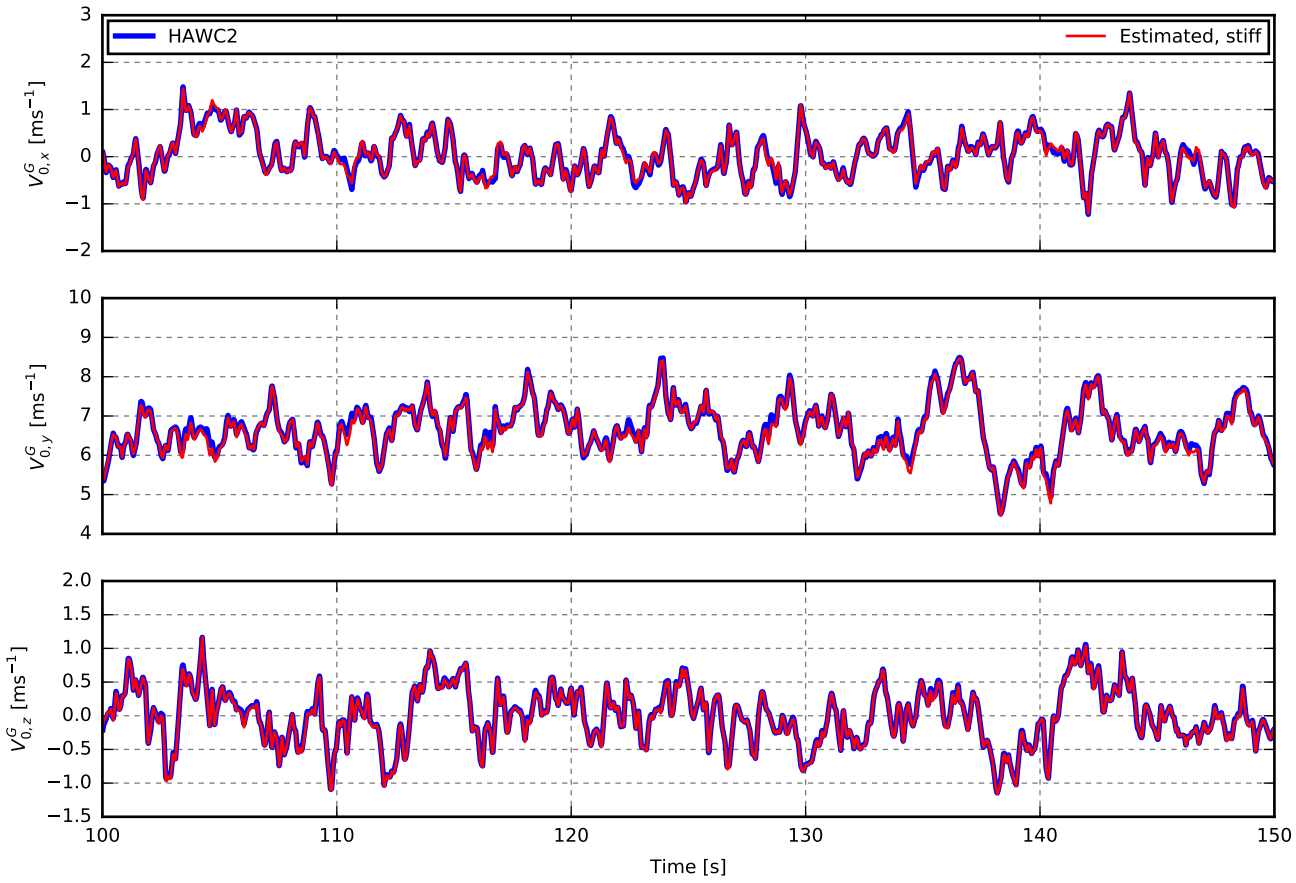

Figure 14. HAWC2 result: The free wind speed estimated in turbulent inflow for a stiff structural model (Case 3).

Wind Energ. Sci. Discuss., https://doi.org/10.5194/wes-2017-57
Manuscript under review for journal Wind Energ. Sci.
Discussion started: 2 January 2018

In **Case 5**, the BMFS-measured flow velocities are extracted in deflected blade-section coordinates and error is introduced due to the unknown orientation of this coordinate system; see Fig. 8 and 15. Higher RMS errors are therefore expected, but in this case, the error of the y component is reduced because the error due to coordinate transformation counteracts the error introduced by dynamic deflections.

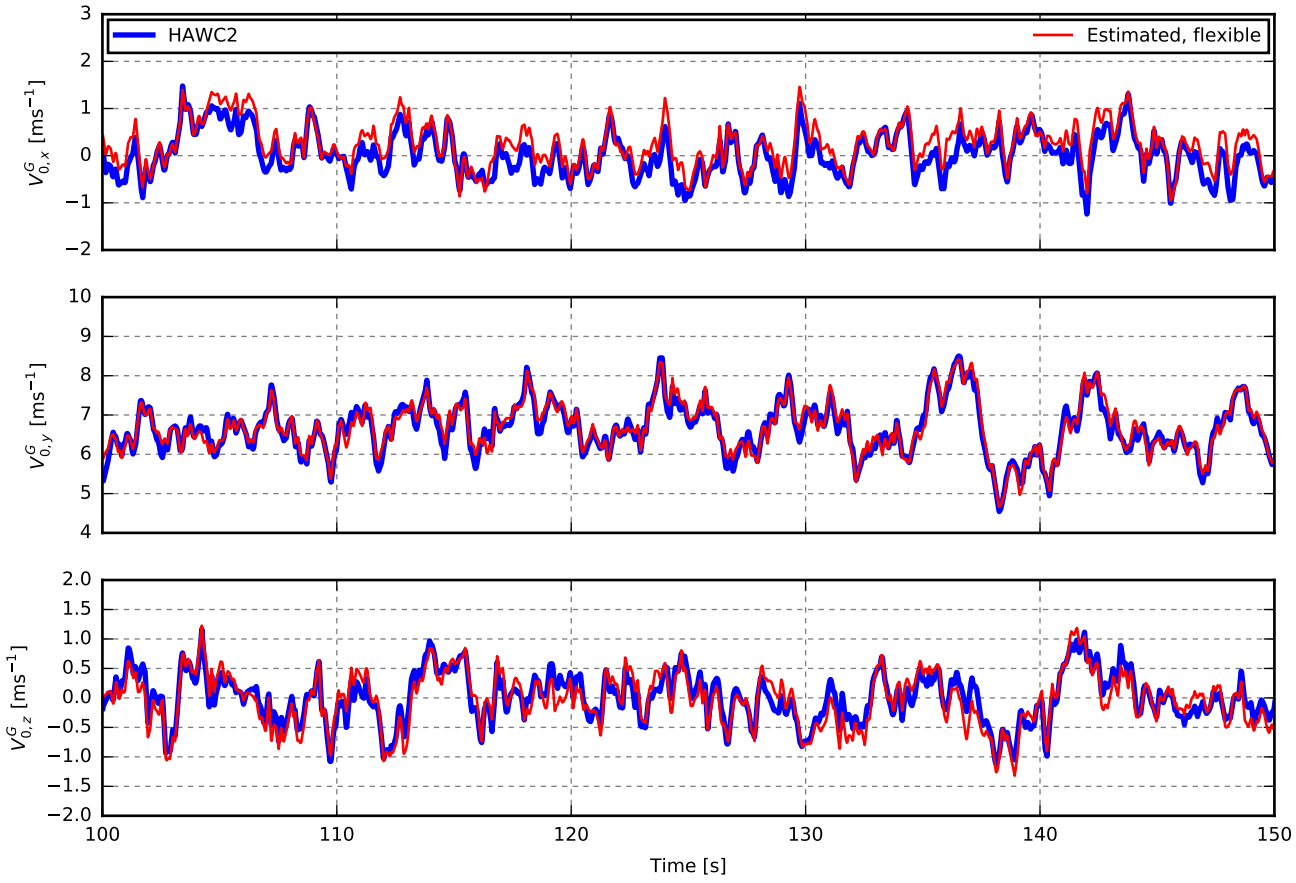

Figure 15. HAWC2 result: The free wind speed estimated in turbulent inflow for a flexible structural model (Case 5).

Figure 16 shows the power spectrum density of Case 5. The 1P (once per revolution) oscillating errors seen in the x and z component in Fig. 9 are seen around 0.2 Hz, while the deviations caused by dynamic deflections are seen in the y component above 0.4 Hz. At first it seems strange that the energy of the y component of the estimated free wind speed is lower than the HAWC2 reference, as the additional velocity due to the movement of the BMFS is expected to increase the energy. In reality, however, the deflection of the structure is correlated with the turbulence, as a blade exposed to a gust will deflect. This means that a BMFS that measures the gust relative to the deflecting blade will measure a less severe gust with less energy.

Wind Energ. Sci. Discuss., https://doi.org/10.5194/wes-2017-57
Manuscript under review for journal Wind Energ. Sci.
Discussion started: 2 January 2018

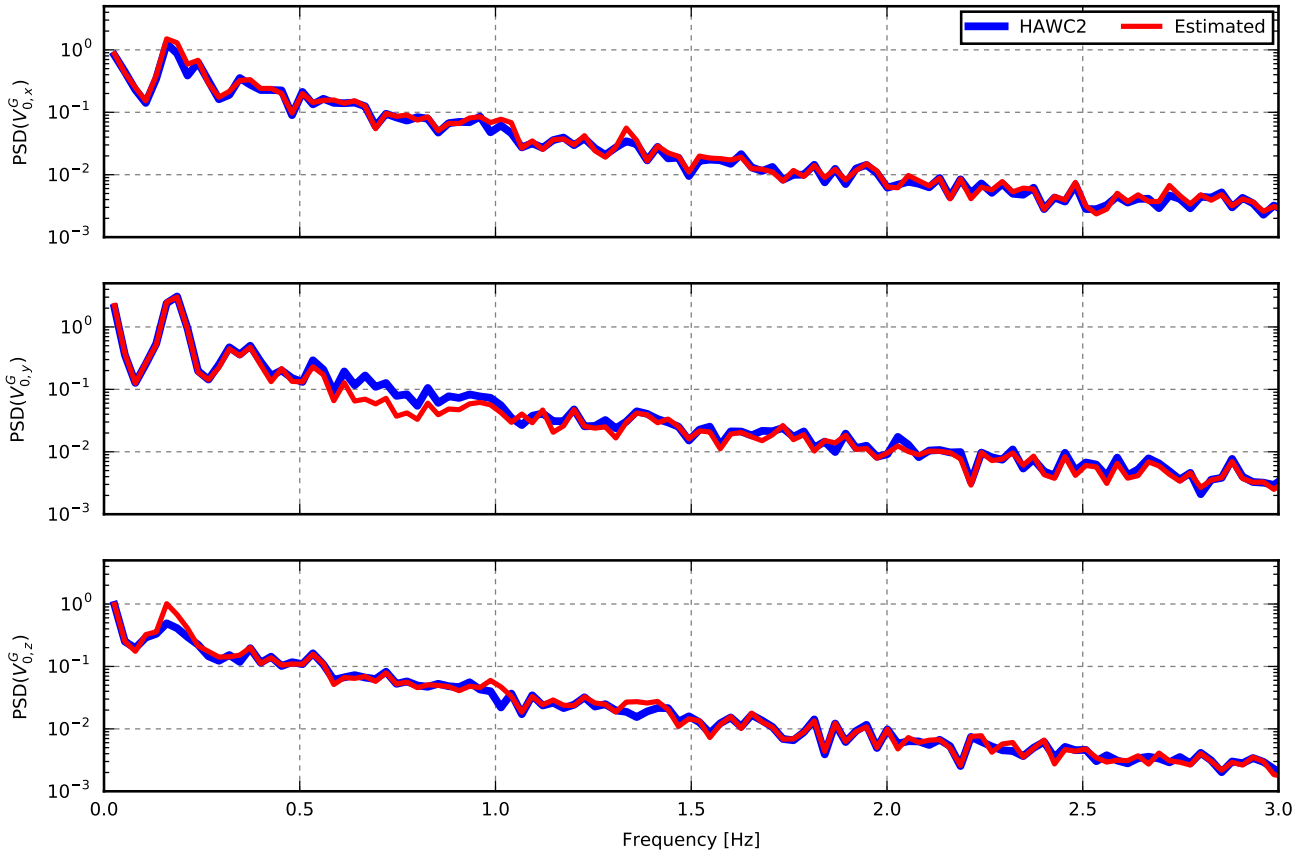

Figure 16. HAWC2 result:The power spectrum density of the free wind speed estimated in turbulent inflow for a flexible structural model.

Figure 17 shows the instant and revolution-averaged wind direction in a simulation with 20° yaw misalignment. The estimated wind direction is seen to follow the HAWC2 reference with a few degrees offset due to the spurious side wind caused by gravity induced edge-wise blade deflections.

Wind Energ. Sci. Discuss., https://doi.org/10.5194/wes-2017-57
Manuscript under review for journal Wind Energ. Sci.
Discussion started: 2 January 2018

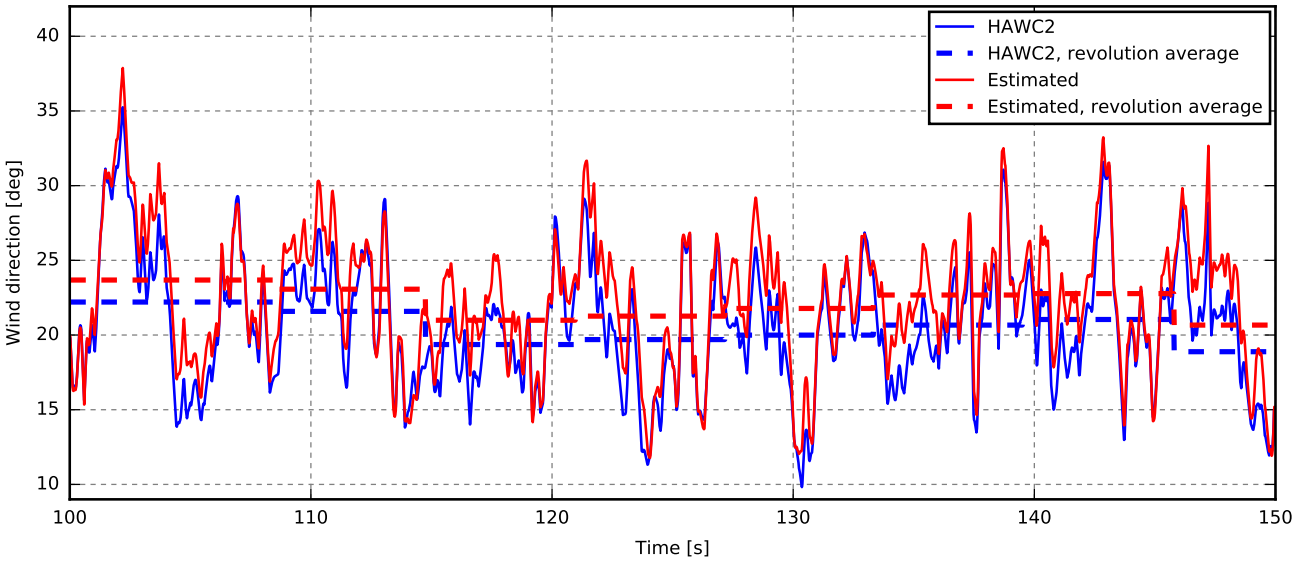

Figure 17. HAWC2 result: The wind direction derived from estimated free wind speed and HAWC2 reference in a simulation with 20° yaw misalignment.

Wind Energ. Sci. Discuss., https://doi.org/10.5194/wes-2017-57
Manuscript under review for journal Wind Energ. Sci.
Discussion started: 2 January 2018

Case 6 is based on the EllipSys3D/Flex5 simulations. The RMS errors are higher than in Case 4, which is the most equivalent HAWC2 case. Note, however, that the numbers are not directly comparable due to the different turbine sizes. The time series are compared in Fig. 18.

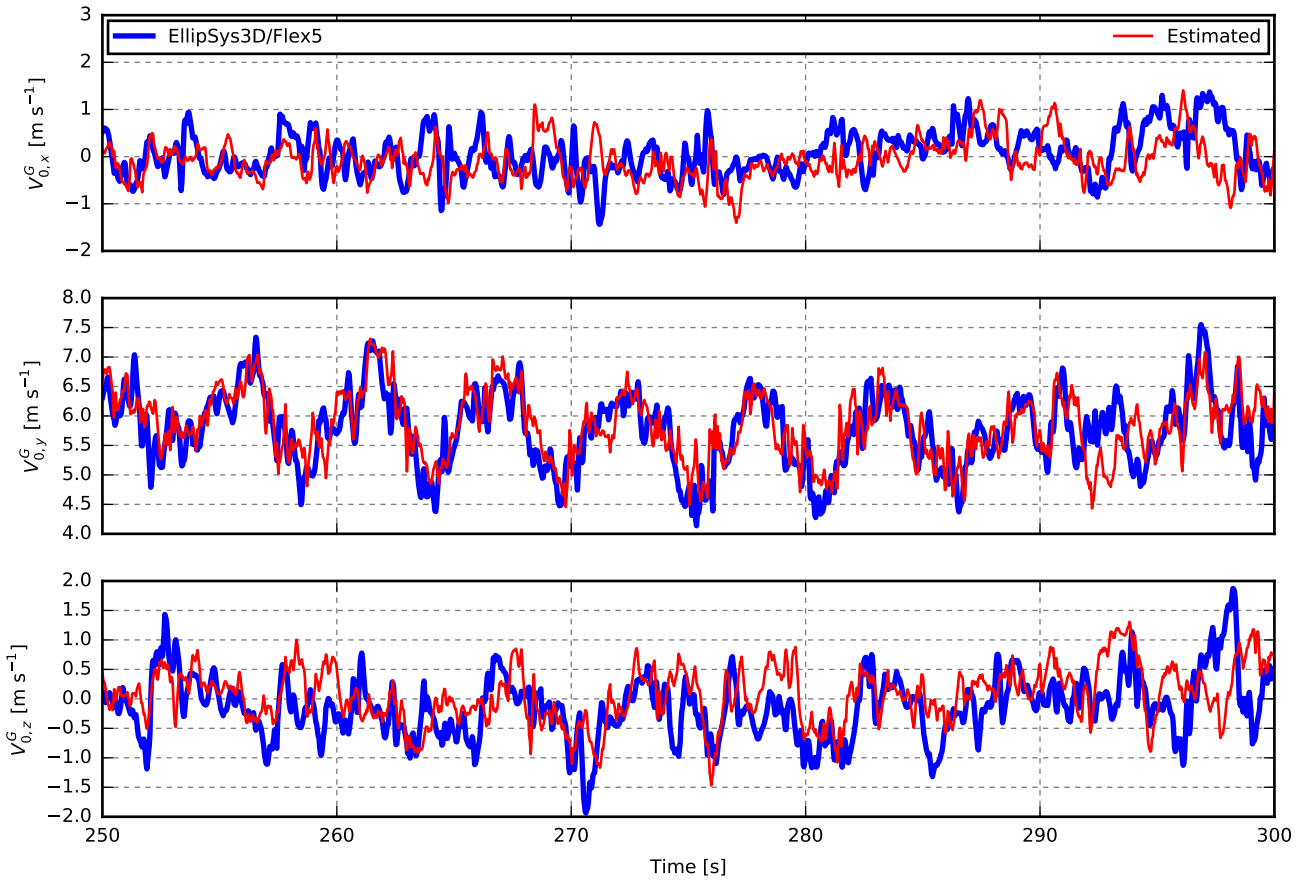

Figure 18. EllipSys3D/Flex5 result: The free wind speed estimated in turbulent inflow ($7\ \mathrm{m\,s^{-1}}$) based velocity in blade section coordinates (Case 6)

For the last case, **Case 7**, an optimisation routine was used to find the optimal reference position. For the $7\ \mathrm{m\,s^{-1}}$ the lowest RMS error was found when the estimated free velocities were compared to the free flow that hits the rotor-centre plane $2.2\ \mathrm{s}$ before and $4.2\ \mathrm{m}$ closer to the rotor centre. As seen in Fig. 8, the error is significantly reduced in all components. It is therefore concluded that the relatively high error of Case 6 is more related to the difference between the turbulence at the sensor and the reference position than to deviations introduced in the aerodynamic models and free flow estimation procedure.

Finally, Fig. 19 shows the difference between the free mean wind speed and estimated free mean wind speed at the position of the sensor, and similarly for the standard deviation. The HAWC2 results are based on 10 minutes of simulations of the Siemens $3.6\ \mathrm{MW}$ turbine. The deviations are mainly introduced in the mapping of velocities from the deflected blade-section

Wind Energ. Sci. Discuss., https://doi.org/10.5194/wes-2017-57
Manuscript under review for journal Wind Energ. Sci.
Discussion started: 2 January 2018

eawe european academy of wind energy
Open Access WIND ENERGY SCIENCE DISCUSSIONS

coordinate system to the ground coordinate system. The EllipSys3D/Flex5 results are based on 200 s of simulations of the Siemens 2.3 MW turbine. These velocities are extracted in ground coordinates; i.e. deviations due to mapping are not included. In Fig. 18, instantaneous deviations are seen, mainly because the turbulence at the sensor position is different from the free flow turbulence at the reference position due to expansion, delay and evolvement of the flow. In this case, however, most of these deviations are averaged out, and the error in Fig. 19 is mainly introduced by differences in the induction modelling approach.

The error introduced in the transformation from deflected blade-section coordinates to ground coordinates are clearly seen in all components of the HAWC2 results. In the x component, the rotor speed and torque dependent spurious side wind increases the error of the mean wind speed up to rated rotor speed (around 9 $\mathrm{m\,s^{-1}}$). In the y component, the overestimation due to blade torsion is seen. The error in the mean wind speed in the z direction, due to tower deflection, increases with the thrust up to rated wind speed (around 11 $\mathrm{m\,s^{-1}}$). Above rated wind speed, the error is rather constant as increased drag on the tower counterbalances the decrease in thrust. Finally, the error, due to flap-wise deflection of the blades, that results in the 1P oscillating deviations of the x and z components are clearly seen in the error of the standard deviation, which peaks with the thrust around rated wind speed.

Wind Energ. Sci. Discuss., https://doi.org/10.5194/wes-2017-57
Manuscript under review for journal Wind Energ. Sci.
Discussion started: 2 January 2018

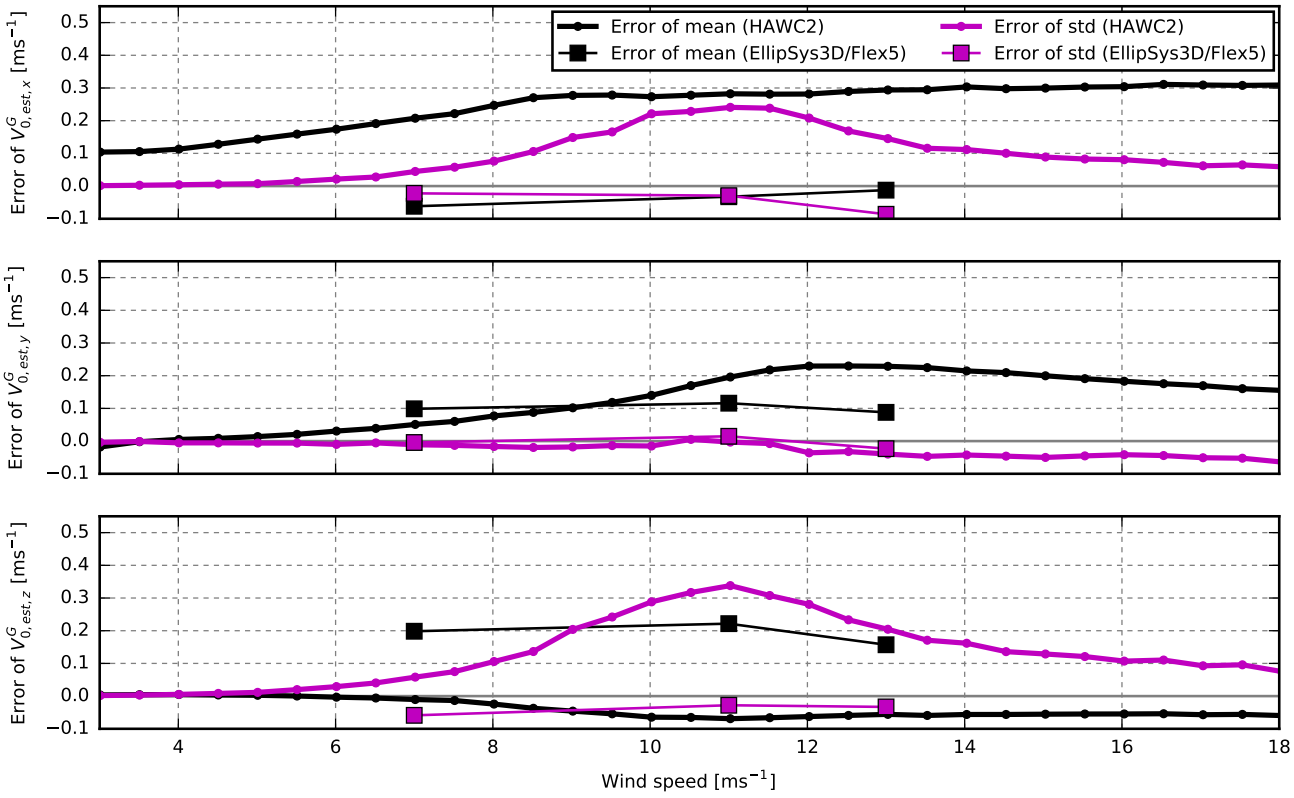

Figure 19. The difference between the mean/std of the free wind speed at the position of the sensor and the mean/std of the estimated free wind speed. The HAWC2 results are based on 10 minutes of simulations of the Siemens 3.6 MW turbine. The deviations are mainly introduced in the mapping of velocities from the deflected blade-section coordinate system to the ground coordinate system. The EllipSys3D/Flex5 results are based on 200 s of simulations of the Siemens 2.3 MW turbine. In this case, the deviations are mainly introduced by differences in the induction modelling approach. Both results are obtained from simulations of a flexible structure in turbulent inflow without shear.

Wind Energ. Sci. Discuss., https://doi.org/10.5194/wes-2017-57
Manuscript under review for journal Wind Energ. Sci.
Discussion started: 2 January 2018

eawe european academy of wind energy
Open Access WIND ENERGY SCIENCE DISCUSSIONS

5 Conclusions

In this paper, a method to estimate the undisturbed free inflow velocities from the flow velocities measured by a blade-mounted flow sensor, BMFS, has been presented and verified. The method includes a combination of aerodynamic models and procedures to estimate the free flow velocities from the measurements of a BMFS. The aerodynamic models comprise BEM-based models for axial and tangential induction, a radial induction model and tip loss correction as well as models for skew and dynamic inflow. Some of these models require information, e.g. the average thrust coefficient of the whole rotor, that cannot be obtained from a BMFS. In these cases, approximations are used even though they are expected to introduce errors. Most of the models also take as input the free wind speed which is the final output of the current method. An iterative procedure is therefore used to find the estimated free wind speed.

The method has been verified on HAWC2 simulations. This verification reveals that the method works well and provides accurate results when using a stiff structural model. Using a flexible structural model, larger deviations are seen. These deviations are caused by the rotation of the sensor due to the deflection and torsion of the tower and blade, movement of the sensor due to turbulence induced dynamic deflections of the structure, and the mismatch between the turbulence at the real deflected sensor position and the reference position, i.e. the assumed (undeflected) sensor position. These effects are highly dependent on the wind speed and the structural design.

Furthermore, the method has been verified by simulations performed using EllipSys3D/Flex5; a flexible structural model coupled with a large eddy simulation (LES) flow solver. In these results, the free velocities estimated by the current method deviate more from the simulated free velocities, but it is concluded that the error is more related to the difference between the turbulence at the sensor and the reference position than to errors introduced in the aerodynamic models and free flow estimation procedure.

Data availability. Simulation results are not available due to confidentiality.

Competing interests. The authors declare that they have no conflict of interest.

Acknowledgements. The authors would like to acknowledge Siemens Wind Power for providing data for the simulation model.

Wind Energ. Sci. Discuss., https://doi.org/10.5194/wes-2017-57
Manuscript under review for journal Wind Energ. Sci.
Discussion started: 2 January 2018

eawe european academy of wind energy
Open Access WIND ENERGY SCIENCE DISCUSSIONS

References

Bak, C., Zahle, F., Bitsche, R., Kim, T., Yde, A., Henriksen, L. C., Hansen, M. H., Blasques, J. P. A. A., Gaunaa, M., and Natarajan, A.: The DTU 10-MW Reference Wind Turbine, Tech. rep., Presented at Danish Wind Power Research 2013, Fredericia, Denmark, 27/05/2013, www.orbit.dtu.dk, 2013.

Barlas, T., van der Veen, G., and van Kuik, G.: Model predictive control for wind turbines with distributed active flaps: incorporating inflow signals and actuator constraints, Wind Energy, 15, 757–771, https://doi.org/10.1002/we.503, http://doi.wiley.com/10.1002/we.503, 2012.

Brand, A., Dekker, J., de Groot, C., and Späth, M.: Overview of aerodynamic measurements on an Aerpac 25 WPX wind turbine blade at the HAT 25 experimental wind turbie, ECN-DE-Memo-96-014, ECN, 1996.

Eggleston, D. M. and Stoddard, F. S.: Wind turbine engineering design, Van Nostrand Reinhold,, 1987.

Elliott, D. L. and Cadogan, J. B.: Effects of wind shear and turbulence on wind turbine power curves, in: Wind Energy, pp. 10–14, Pacific Northwest Lab., Richland, WA (USA), Presented at the European Community Wind Energy Conference and Exhibition, Madrid, Spain, 10-14 Sep. 1990, http://www.osti.gov/scitech/servlets/purl/6348447, 1990.

Glauert, H.: Airplane Propellers, pp. 169–360, Springer Berlin Heidelberg, Berlin, Heidelberg, https://doi.org/10.1007/978-3-642-91487-4_3, 1935.

Guntur, S. and Sørensen, N. N.: An evaluation of several methods of determining the local angle of attack on wind turbine blades, Journal of Physics: Conference Series, 555, 12 045, http://stacks.iop.org/1742-6596/555/i=1/a=012045, 2014.

Hansen, M. H. and Henriksen, L. C.: Basic DTU Wind Energy controller, Tech. rep., DTU Wind Energy, www.orbit.dtu.dk, 2013.

Kragh, K. and Hansen, M.: Individual Pitch Control Based on Local and Upstream Inflow Measurements, in: 50th AIAA Aerospace Sciences Meeting including the New Horizons Forum and Aerospace Exposition, Reston, Virigina, Aerospace Sciences Meetings, American Institute of Aeronautics and Astronautics, https://doi.org/10.2514/6.2012-1021, 2012.

Kragh, K. A., Henriksen, L. C., and Hansen, M. H.: On the Potential of Pitch Control for Increased Power Capture and Load Alleviation, in: Torque, the science of making torque from wind., Presented at The Science of Making Torque from Wind 2012, 9–11 October 2012, Oldenburg, Germany, www.orbit.dtu.dk, 2012.

Larsen, T. J. and Hansen, A. M.: How 2 HAWC2, the user's manual, no. December in Denmark. Forskningscenter Risoe. Risoe-R, Technical Report, Risø National Laboratory, Roskilde, Denmark, www.orbit.dtu.dk, 2007.

Larsen, T. J., Aagaard Madsen, H., and Thomsen, K.: Active load reduction using individual pitch, based on local blade flow measurements, Wind Energy, 8, 67–80, https://doi.org/10.1002/we.141, 2005.

Larsen, T. J., Aagaard Madsen, H., Larsen, G. C., and Hansen, K. S.: Validation of the dynamic wake meander model for loads and power production in the Egmond aan Zee wind farm, Wind Energy, 16, 605–624, https://doi.org/10.1002/we.1563, 2013.

Madsen, H. A.: Risø-M-2902: Aerodynamics and Structural Dynamics of a Horizontal Axis WindTurbine - Raw Data Overview, Technical Report Risø-M-2902, Risø National Laboratory, Roskilde, Denmark, 1991.

Madsen, H. A.: Correlation of amplitude modulation to inflow characteristics, Proceedings of 43rd International Congress on Noise Control Engineering, http://www.acoustics.asn.au/conference{_}proceedings/INTERNOISE2014/papers/p171.pdf, 2014.

Madsen, H. A., Thomsen, K., and Petersen, S. M.: Risø-I-210: Wind Turbine Wake Data from Inflow Measurements using a Five hole Pitot Tube on a NM80 Wind Turbine Rotor in the Tjæreborg Wind Farm, Tech. Rep. December, be, 2003.

Madsen, H. A., Bak, C., Døssing, M., Mikkelsen, R. F., and Øye, S.: Validation and modification of the Blade Element Momentum theory based on comparisons with actuator disc simulations, Wind Energy, 13, 373–389, https://doi.org/10.1002/we.359, 2010a.

Madsen, H. A., Bak, C., Schmidt Paulsen, U., Gaunaa, M., Fuglsang, P., Romblad, J., Olesen, N. A., Enevoldsen, P., Laursen, J., and Jensen, L.: The DAN-AERO MW Experiments: Final report, Denmark. Forskningscenter Risoe. Risoe-R, Danmarks Tekniske Universitet, Risø Nationallaboratoriet for Bæredygtig Energi, www.orbit.dtu.dk, 2010b.

Madsen, H. A., Larsen, T. J., Pirrung, G., Verelst, D., and Zahle, F.: An implementation of the BEM model for simulation of non-uniform loading and inflow, To be published, 2018.

Mann, J.: The spatial structure of neutral atmospheric surface-layer turbulence, Journal of Fluid Mechanics, 273, 141, https://doi.org/10.1017/S0022112094001886, 1994.

Medina, P., Singh, M., Johansen, J., Jove, A. R., Machefaux, E., Fingersh, L. J., and Schreck, S.: Aerodynamic and performance measurements on a SWT-2.3-101 wind turbine, Tech. rep., National Renewable Energy Laboratory (NREL), Golden, CO., 2011.

Meyer Forsting, A. R., Troldborg, N., Murcia Leon, J. P., Sathe, A., Angelou, N., and Vignaroli, A.: Validation of a CFD model with a synchronized triple-lidar system in the wind turbine induction zone, Wind Energy, 20, 1481–1498, https://doi.org/10.1002/we.2103, 2017.

Michelsen, J. A.: Basis3D – a Platform for Development of Multiblock PDE Solvers, Tech. rep., Danmarks Tekniske Universitet, 1992.

Mikkelsen, T., Mann, J., Courtney, M., Sjöholm, M. M., Mann, J., Courtney, M., and M: Windscanner: 3-D wind and turbulence measurements from three steerable doppler lidars, IOP Conference Series: Earth and Environmental Science, 1, 12 018, http://stacks.iop.org/1755-1315/1/i=1/a=012018, 2008.

Mikkelsen, T., Hansen, K. H., Angelou, N., Sjöholm, M., Harris, M., Hadley, P., Scullion, R., Ellis, G., and Vives, G.: Lidar wind speed measurements from a rotating spinner, in: European Wind Energy Conference and Exhibition, www.orbit.dtu.dk, 2010.

Øye, S.: FLEX4 simulation of wind turbine dynamics, in: Proceedings of 28th IEA Meeting of Experts Concerning State of the Art of Aeroelastic Codes for Wind Turbine Calculations. Available through International Energy Agency., pp. 71–76, Danmarks Tekniske Universitet, Lyngby, Denmark, 1996.

Pedersen, M. M., Larsen, T. J., Larsen, G. C., Madsen, H. A., and Toldborg, N.: Turbulent wind field characterization and re-generation based on pitot tube measurements mounted on a wind turbine, in: 33rd Wind Energy Symposium, AIAA SciTech, American Institute of Aeronautics and Astronautics, Kissimmee, Florida, https://doi.org/10.2514/6.2015-1467, 2015.

Pedersen, M. M., Larsen, T. J., Madsen, H. A., and Larsen, G. C.: Using wind speed from a blade-mounted flow sensor for power and load assessment on modern wind turbines, Wind Energy Science, 2, 547–567, https://doi.org/10.5194/wes-2-547-2017, 2017.

Petersen, J. T. and Aagaard Madsen, H.: Risø-R-993(EN): Local Inflow and Dynamics – Measured and Simulated on a Rotating Wind Turbine Blade, Risø National Laboratory, Roskilde, Denmark, 1997.

Rahimi, H., Schepers, G., Shen, W. Z., García, N. R., Schneider, M., Micallef, D., Ferreira, C. S., Jost, E., Klein, L., and Herráez, I.: Evaluation of different methods for determining the angle of attack on wind turbine blades with CFD results under axial inflow conditions, arXiv preprint arXiv:1709.04298, 2017.

Schepers, J. G., Brand, A. J., Bruining, A., Hand, M., Infield, D., Madsen, H., Maeda, T., Paynter, J., van Rooij, R., and Shimizu, Y.: Final report of IEA Annex XVIII: enhanced field rotor aerodynamics database, Energy Research Center of the Netherlands, ECN-C-02-016, February, ftp://ftp.ecn.nl/pub/www/library/report/2002/c02016.pdf, 2002.

Scholbrock, A. K., Fleming, P. A., Wright, A., Slinger, C., Medley, J., and Harris, M.: Field Test Results from Lidar Measured Yaw Control for Improved Power Capture with the NREL Controls Advanced Research Turbine, in: 33rd Wind Energy Symposium, AIAA SciTech Forum, American Institute of Aeronautics and Astronautics, Reston, Virginia, https://doi.org/10.2514/6.2015-1209, 2015.

Shen, W. Z., Hansen, M. O. L., and Sørensen, J. N.: Determination of Angle of Attack (AOA) for Rotating Blades, www.orbit.dtu.dk, 2006.

Shen, W. Z., Hansen, M. O. L., and Sørensen, J. N.: Determination of the angle of attack on rotor blades, Wind Energy, 12, 91–98, https://doi.org/10.1002/we.277, 2009.

Simms, D. A., Hand, M. M., Fingersh, L. J., and Jager, D. W.: Unsteady aerodynamics experiment phases II-IV test configurations and available data campaigns, Tech. rep., National Renewable Energy Lab, https://www.nrel.gov/docs/fy99osti/25950.pdf, 1999.

Snel, H. and Schepers, J. G.: Joint investigation of dynamic inflow effects and implementation of an engineering method, Netherlands Energy Research Foundation ECN, https://www.ecn.nl/publications/E/1995/ECN-C--94-107, 1995.

Sørensen, J. N. and Shen, W. Z.: Numerical modelling of Wind Turbine Wakes, J. Fluids Eng., 124, 393–399, https://doi.org/10.1115/1.1471361, 2002.

Sorensen, J. N., Mikkelsen, R. F., Henningson, D. S., Ivanell, S., Sarmast, S., and Andersen, S. J.: Simulation of wind turbine wakes using the actuator line technique, Philosophical Transactions of the Royal Society A: Mathematical, Physical and Engineering Sciences, 373, 20140 071–20140 071, https://doi.org/10.1098/rsta.2014.0071, 2015.

Sørensen, N. N.: General Purpose Flow Solver Applied to Flow over Hills, Ph.D. thesis, Technical University of Denmark, www.orbit.dtu.dk, 1995.

Sørensen, N. N. and Aagaard Madsen, H.: Modelling of transient wind turbine loads during pitch motion, in: paper and poster). In: Proceedings (online). 2006 European Wind Energy Conference and Exhibition, Athens (GR), vol. 27, 2006.

St. Martin, C. M., Lundquist, J. K., Clifton, A., Poulos, G. S., and Schreck, S. J.: Wind turbine power production and annual energy production depend on atmospheric stability and turbulence, Wind Energ. Sci., 1, 221–236, https://doi.org/10.5194/wes-1-221-2016, 2016.

Taylor, G. I.: The Spectrum of Turbulence, Proceedings of the Royal Society A: Mathematical, Physical and Engineering Sciences, 164, 476–490, https://doi.org/10.1098/rspa.1938.0032, 1938.

Troldborg, N. and Meyer Forsting, A. R.: A simple model of the wind turbine induction zone derived from numerical simulations, Wind Energy, https://doi.org/10.1002/we.2137, http://doi.wiley.com/10.1002/we.2137, 2017.

Wagner, R., Vignaroli, A., Angelou, N., Sathe, A., Meyer Forsting, A. R., Sjöholm, M., and Mikkelsen, T. K.: Measurement of turbine inflow with a 3D windscanner system and a spinnerlidar, www.orbit.dtu.dk, 2015.

APPENDIX D

More accurate aeroelastic wind-turbine load simulations using detailed inflow information

Wind Energ. Sci. Discuss., https://doi.org/10.5194/wes-2018-4
Manuscript under review for journal Wind Energ. Sci.
Discussion started: 3 April 2018

eawe european academy of wind energy
Open Access WIND ENERGY SCIENCE DISCUSSIONS

More accurate aeroelastic wind-turbine load simulations using detailed inflow information

Mads Mølgaard Pedersen[1], Torben Juul Larsen[1], Helge Aagaard Madsen[1], and Gunner Christian Larsen[1]
[1]Wind Energy Department, Technical University of Denmark, Frederiksborgvej 399, DK-4000 Roskilde, Denmark
Correspondence to: Mads M. Pedersen (mmpe@dtu.dk)

Abstract.

In this paper, inflow information is extracted from a measurement database and used for aeroelastic simulations to investigate if using more accurate inflow descriptions improves the accuracy of the simulated fatigue loads.

The inflow information is extracted from the nearby met masts and a blade-mounted five-hole pitot tube. The met masts provide measurements of the inflow at fixed positions some distance away, whereas the pitot tube measures the inflow while rotating with the rotor.

The met mast measures the free-inflow velocity, but the measured turbulence may evolve on its way to the turbine, pass besides the turbine, or the mast may be in the wake of the turbine. The inflow measured by the pitot tube, on the other hand, is very representative of the wind that acts on the turbine as it is measured close to the blades and includes variations within the rotor plane. This inflow is, however, affected by the presence of the turbine, and therefore an aerodynamic model is used to estimate the free-inflow velocities that would have been at the same time and position without the presence of the turbine.

The inflow information used for the simulations includes the mean wind speed and trend, the turbulence intensity, wind shear profile, atmospheric stability dependent turbulence parameters, and azimuthal variations within the rotor plane. In addition, the instantly measured wind speed is used to constrain the turbulence.

It is concluded that the period-specific turbulence intensity must be included in the aeroelastic simulations to make the range of the simulated fatigue loads representative for the range of the measured fatigue loads. Furthermore, it is found that the one-to-one correspondence between the measured and simulated fatigue loads is improved considerably by using inflow characteristics extracted from the pitot tube instead of the met-mast-based sensors as input for the simulations. Finally, the use of pitot-tube wind speed to constrain the turbulence is found to decrease the variation of the simulated loads due to different turbulence realisations (seeds), such that the need for multiple simulations is reduced.

1 Introduction

Aeroelastic simulations are extensively used in the development of modern wind turbines. These simulations are used to estimate the dynamic response of the wind turbine structure in both the research, the design and the certification phase; they are used to investigate new concepts, evaluate different designs, and to prove that the life-time fatigue and extreme loads are below the capability limits of the components.

Wind Energ. Sci. Discuss., https://doi.org/10.5194/wes-2018-4
Manuscript under review for journal Wind Energ. Sci.
Discussion started: 3 April 2018

eawe european academy of wind energy
Open Access WIND ENERGY SCIENCE DISCUSSIONS

Aeroelastic simulations are typically based on simplified models of the wind-turbine structure, its aerodynamic properties and the inflow conditions. Often, standard or the site-average turbulence parameters and shear profile are used for the inflow modelling. This approach makes it possible to compare the simulation results with the average load level of the measurements despite the often massive measurement scatter, which is mainly caused by different inflow conditions; see the example in Fig. 1 (left).

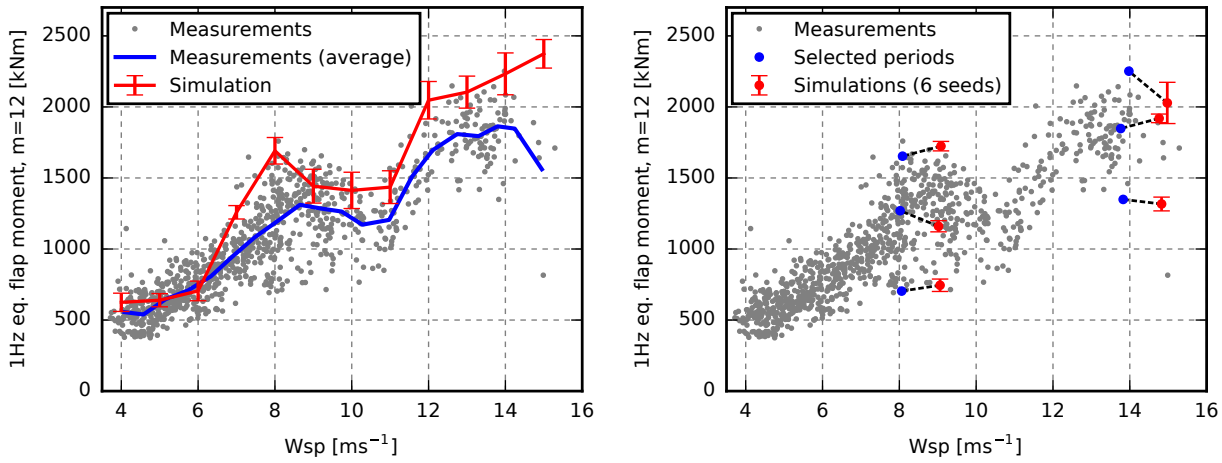

Figure 1. Two approaches for comparing the measured and simulated loads. Left: The traditional approach where the site-average turbulence characteristics and shear profile are used as input for the aeroelastic simulations. The results are compared to the measured average load levels. Right: The suggested one-to-one approach where measured inflow characteristics are extracted from selected time series. The simulation results are compared to the corresponding measurement observation. Note that the simulation error bars are offset 1 ms^{-1} to the right to increase clarity.

In this paper, the effects of using more specific inflow characteristics for aeroelastic simulations are investigated. The idea is to select single measurement time series and extract information for more accurate inflow fields, i.e. descriptions of the mean inflow velocities, as well as the turbulent fluctuations. These inflow fields are subsequently used as input for numerical load simulations, and the simulated loads are compared to the original measured loads; see Fig. 1 (right).

As seen in Fig. 2, the measured blade-root fatigue load increases with the wind speed. The scatter is, however, massive. Different levels of turbulence intensity can explain some of the variation, especially for low wind speeds, but a lot of the variation is caused by a combination of other factors, e.g. variability in wind shear profile, atmospheric stability, etc. The hope is, therefore, that it will be possible to select a period of interest, extract the inflow characteristics, and thus reproduce the period in an aeroelastic simulation giving similar loads. In this way, the reason for the high loads can be investigated and subsequently used to predict future loads with higher accuracy. In addition, the measurement period required for load validation can potentially be reduced by using a reduced set of single time series instead of the average of a large measurement dataset.

Wind Energ. Sci. Discuss., https://doi.org/10.5194/wes-2018-4
Manuscript under review for journal Wind Energ. Sci.
Discussion started: 3 April 2018

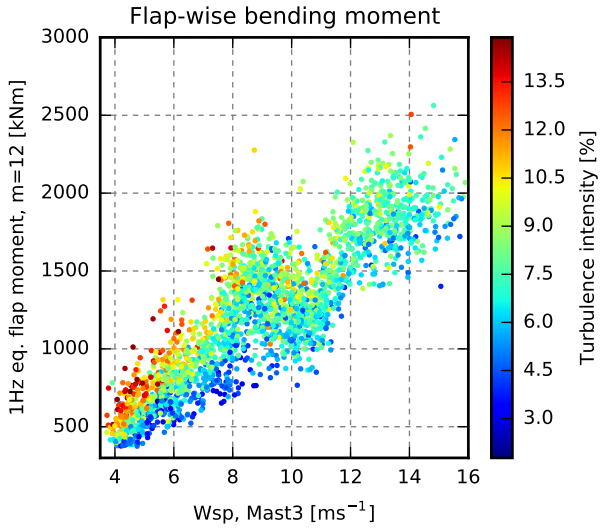

Figure 2. The blade-root flap-wise fatigue load plotted as a function of wind speed and coloured by turbulence intensity. The turbulence intensity affects the blade-root fatigue loads. Much of the scatter is, however, caused by other factors.

The inflow characteristics required for the description of the more accurate inflow fields can be extracted from cup or sonic anemometers at a nearby met mast, if the anemometers are exposed to similar inflow conditions. This means that the mast must be close to the turbine, but out of the rotor induction zone. Furthermore, wind directions where the anemometers are in the wake of turbines or the mast itself must be discarded, as well as situations where the turbine is in the wake of other turbines. In addition, anemometers at different heights are required to measure the shear profile.

The inflow parameters can, alternatively, be obtained from a blade-mounted flow sensor, BMFS. Mounted at the blade, a BMFS is exposed to exactly the same inflow conditions as the turbine, and that goes for all wind directions. In addition, a BMFS also provides valuable information about the variation within the rotor area.

A BMFS is, however, located inside the rotor induction zone, and therefore a method to compensate for the presence of the turbine is required; i.e. a method that takes the flow velocities measured relative to the BMFS and calculates the free-stream inflow velocities that would have been observed at the same time and location without the presence of the wind turbine. In this study, the method presented by Pedersen et al. (2018) is used. This method uses a combination of aerodynamic models to estimate the disturbance that the turbine induces on the free-stream inflow.

In the right setup, lidars are able to provide information similar to a BMFS – in fact, the BMFS could be a lidar as in the experiment by Pedersen et al. (2013). Typically, however, lidars are mounted on the nacelle or on the ground, and set up to measure the inflow some distance up- or downstream, in which case they have other advantages and drawbacks.

The current study is based on the measurement database established during the DAN-AERO project (Madsen et al., 2010b), where a 3.6MW Siemens wind turbine at Høvsøre Test Centre for Large Wind Turbines was equipped with a blade-mounted

Wind Energ. Sci. Discuss., https://doi.org/10.5194/wes-2018-4
Manuscript under review for journal Wind Energ. Sci.
Discussion started: 3 April 2018

eawe european academy of wind energy
Open Access WIND ENERGY SCIENCE DISCUSSIONS

five-hole pitot tube. The aeroelastic simulations in this study are performed using HAWC2, which is a non-linear aeroelastic code intended for computing wind turbine response in time domain (Larsen and Hansen, 2007).

2 Method

From the measurement database (see Section 2.1), 20 different 10-min periods, denoted P1 - P20, are extracted. These periods are selected to be no-wake situations representing a wide range of load levels at 8 and 14 ms^{-1}; i.e. below and above the rated wind speed. From each period, inflow characteristics are extracted for the simulation cases, Cases 1 - 5, which utilise different details about the inflow, e.g. wind speed trend, turbulence intensity, shear etc.

For each of the selected periods, these inflow characteristics are used as input for a set of six simulations with different turbulence realisations (seeds). Finally, the simulated loads are compared to their measured counterparts.

2.1 Site, turbine, sensor and data overview

The measurement database used in this study was recorded from April to July 2009 as part of the DAN-AERO project (Madsen et al., 2010b; Troldborg et al., 2013). It contains 9600 data files with 10-minute measurements from a Siemens 3.6 MW wind turbine located at Høvsøre Test Site for Large Wind Turbines in Denmark, as well as measurements from the nearby met masts; see Fig. 3. The rotor diameter is 107 m and the hub height is 89.5 m. The turbine was equipped with blade-root bending-moment sensors and a blade-mounted five-hole pitot tube.

As seen in Fig. 3, the turbine was located in the middle of a row of five megawatt wind turbines. Mast3, which is located around 2.5 diameters west of the turbine, provides hub-height wind-speed observations, while the main met mast, 820 m south of the turbine, measures the wind speed at six different heights ranging from 10 to 116.5 m.

2.2 Blade-mounted five-hole pitot tube

During the measurement period, an Aeroprobe CPSPY5 five-hole pitot tube was mounted on one of the blades in radius 36 m, i.e. around one third from the tip. A five-hole pitot tube measures the relative flow speed as well as the flow angle at two perpendicular planes. From this information, the relative 3D flow velocity can be calculated, and subtracting the velocity due to sensor movement yields the flow velocity in the rotor plane; see Pedersen et al. (2017) for more details. In this study, the velocity due to sensor movement is calculated based on the rotor rotation and the pitch motion. This means that movement due to dynamic tower and blade deflection is not included, and some discrepancy is therefore expected.

The flow velocity is mapped from the rotating blade section coordinate system to fixed global coordinates. In this process, additional uncertainty is introduced, as the exact orientation of the blade section is unknown due to the deflection and torsion of the structure.

Finally, the wind turbine induction, i.e. the disturbance of the inflow field caused by the presence of the rotor, is estimated using a combination of aerodynamic models. In this study, the aerodynamic models comprise blade-element-momentum (BEM)

Wind Energ. Sci. Discuss., https://doi.org/10.5194/wes-2018-4
Manuscript under review for journal Wind Energ. Sci.
Discussion started: 3 April 2018

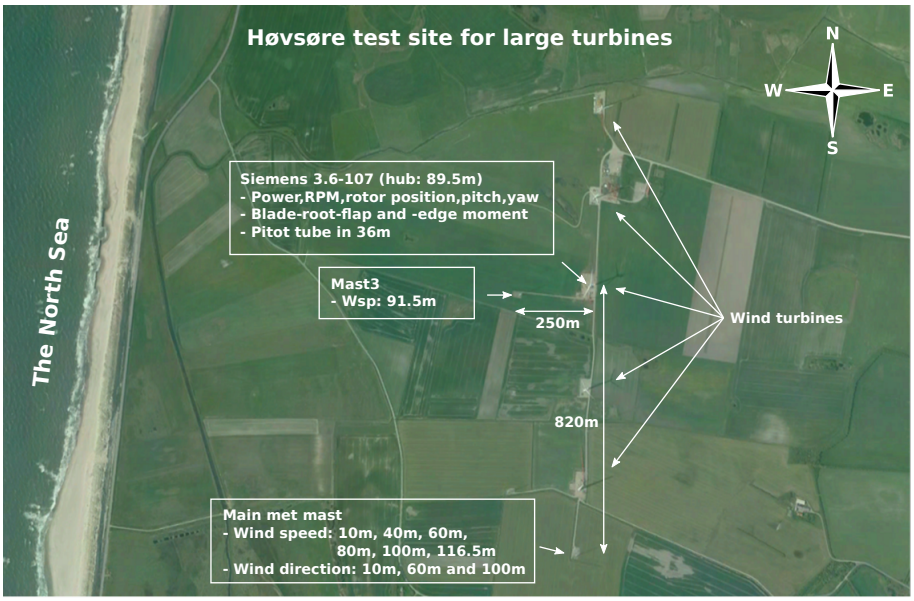

Figure 3. Overview of the Høvsøre Test Site for Large Wind Turbines in Denmark. The Siemens turbine is located in the middle of a row of five megawatt turbines.

based models for axial and tangential induction, a radial induction model and tip loss correction as well as models for skew and dynamic inflow.

Subtracting the estimated induction from the measured flow velocity results in an estimate of the free-stream inflow velocity that would have been observed at the same time and location without the presence of the turbine. In this step, uncertainty is also introduced due to the mismatch between the applied simple engineering models and the complex real world. The process and the introduced uncertainty are described in detail by Pedersen et al. (2018) that also, based on numerical simulations, conclude that the estimated free wind speed obtained from a BMFS is relatively accurate. Whether the introduced uncertainties outweigh the advantage of measuring at the blade will be investigated in this study.

2.3 Calibration of load sensors

The blade-root load sensors comprise flap- and edge-wise bending-moment sensors on all three blades. They are located 3.2 m from the hub centre.

A subset of the sensors is found to drift considerably with the temperature. A linear temperature correction is therefore applied before the calibration.

The edge-wise bending-moment sensors are calibrated using a set of time series measured at low wind speed and with pitch angles around 0°. In these cases, the edge-wise loads are dominated by the gravity loading, and the loads are therefore fitted to

Wind Energ. Sci. Discuss., https://doi.org/10.5194/wes-2018-4
Manuscript under review for journal Wind Energ. Sci.
Discussion started: 3 April 2018

a sinusoidal signal with magnitude equal to the own-weight moment of the blade:

$$\underset{a,b}{\text{Minimise}} \left(\sum_{\theta_{rotor}} |aMy(\theta_{rotor}) + b - M_{ow} \sin(\theta_{rotor})| \right) \tag{1}$$

where a and b are calibration factors, My is the measured edge-wise bending moment, θ_{rotor} is the rotor position and M_{ow} is the moment when the blade is in horizontal position due to the weight of the blade from the load sensor to the tip.

Similarly, the flap-wise bending-moment sensors can be calibrated using time series measured at a low wind and 90° pitch angle. The measurement database, however, contains no time series with 90° pitch and low wind, and it was therefore necessary to use time series with lower pitch angles for the calibration. Hence, the pitch angle must be included in the calibration formula:

$$\underset{a,b}{\text{Minimise}} \left(\sum_{\theta_{rotor}} |aMx(\theta_{rotor}) + b - M_{ow} \sin(\theta_{pitch}) \sin(\theta_{rotor})| \right) \tag{2}$$

where Mx is the measured flap-wise bending moment, and θ_{pitch} is the pitch angle.

The mean flap-wise bending moments of the three blades are not equal after this calibration. This is, however, justified as the measured pitch angles of blade 2 and 3 are offset by around -0.4 and +1° respectively, compared to blade 1. These pitch offsets are included in the simulations.

2.4 Derived tower load sensors

The current measurement database contains no tower-load sensors. The dynamic tower loads are, however, mainly induced by the aerodynamic blade loads, and it is therefore possible to derive tower-load estimations from the blade-root loads sensors.

The tower-bottom fore-aft bending moment is dominated by the constant weight of the rotor and the dynamic thrust on the rotor. The thrust is related to the rotor-plane projection of the blade-root bending moments (i.e. mainly the flap-wise bending moments) and using a linear calibration a good approximation can be achieved for a certain wind speed:

$$MTB_{foreaft,est} = a_{tb} \sum_{i=1..3} MBR_i + b_{tb} \tag{3}$$

where $MTB_{foreaft,est}$ is the estimated tower-bottom fore-aft bending moment, MBR_i is the rotor-plane projection of the blade-root bending moment of blade i, and a_{tb} and b_{tb} are calibration constants.

Similarly, approximations of the tower-top tilt and yaw moments can be formulated:

$$MTT_{tilt,est} = a_{tilt} \sum_{i=1..3} MBR_i \cos\left(\theta_{rotor} - \frac{2i}{3}\pi\right) + b_{tilt} \tag{4}$$

$$MTT_{yaw,est} = a_{yaw} \sum_{i=1..3} MBR_i \cos\left(\theta_{rotor} - \frac{2i}{3}\pi + \frac{\pi}{2}\right) + b_{yaw} \tag{5}$$

The derived tower-load sensors have been calibrated based on HAWC2 simulations. Applied to other HAWC2 simulations with similar wind conditions, the tower loads derived from the blade-root sensors fit quite well with the actual simulated tower loads; see the example of 8 ms^{-1} in Fig. 4.

Wind Energ. Sci. Discuss., https://doi.org/10.5194/wes-2018-4
Manuscript under review for journal Wind Energ. Sci.
Discussion started: 3 April 2018

The calibration constants are, however, dependent on the wind speed. Hence, the fine agreement seen in Fig. 4 is only obtainable when using the correct wind-speed-specific calibration constants.

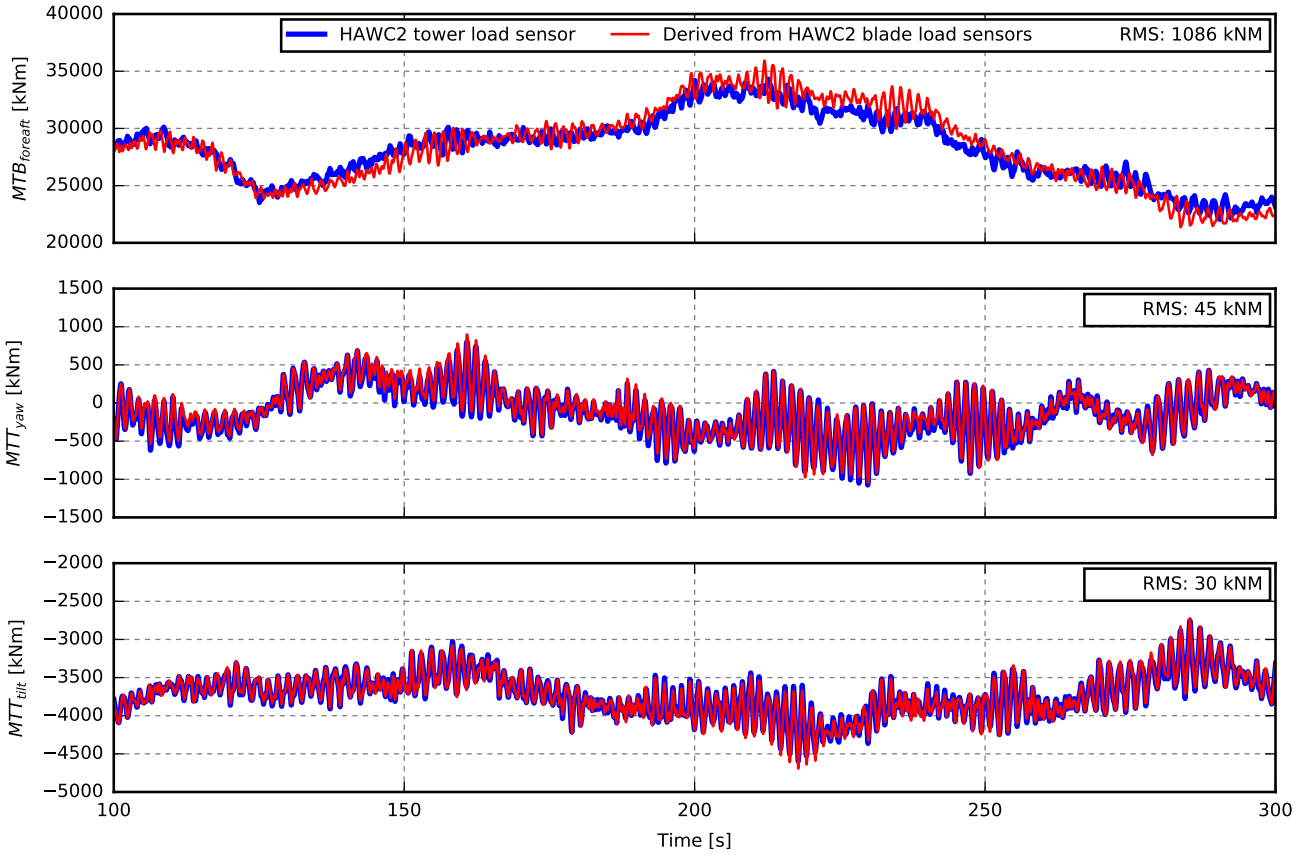

Figure 4. Comparison of the HAWC2 simulated tower loads and the derived tower loads, which is derived from the HAWC2 simulated blade-root load sensors and calibrated for 8 ms^{-1}.

The calibration constants are therefore determined for wind speeds ranging from 4 to 15 ms^{-1} and interpolated based on the revolution-averaged pitot-tube mean wind speed. To test the calibration, the equivalent fatigue load of the derived tower-load sensors have been calculated for five independent simulation sets. The estimated loads are then compared to the HAWC2-simulated "real" tower loads. The relative error is shown in Fig. 5.

At low wind speeds, the tower-bottom bending moment is dominated by structural loads while the impact of the aerodynamic blade loads is limited. Hence, the derived tower-bottom sensor deviates considerably from the simulated tower-bottom signal, and the fatigue load error is relatively high; see Fig. 5. The derived tower-bottom fore-aft loads will therefore be discarded for wind speeds below 6 ms^{-1}. In all other cases, the mean error is less than 5 %. Note that this deviation will not affect the

Wind Energ. Sci. Discuss., https://doi.org/10.5194/wes-2018-4
Manuscript under review for journal Wind Energ. Sci.
Discussion started: 3 April 2018

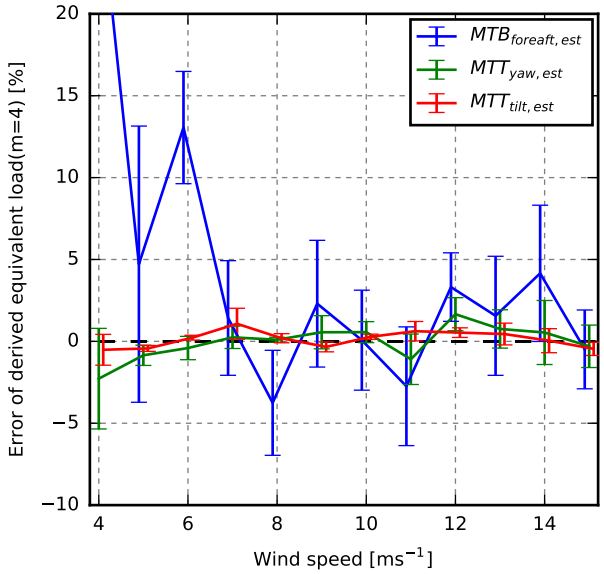

Figure 5. Relative fatigue load error of the derived tower load sensors compared to the HAWC2 simulated tower loads. The derived tower load sensors are obtained from the HAWC2 simulated blade-root load sensors and calibrated using wind-speed-dependent calibration constants.

discrepancies between the measurements and simulations in the results section directly, as the presented tower loads in both cases will be derived from the blade-root loads even though the "real" tower loads are also simulated directly by HAWC2.

2.5 Simulation model

The simulations used in this study are performed using HAWC2 - a non-linear aeroelastic code intended for computing wind turbine response in the time domain (Madsen et al., 2010a, 2012; Kim et al., 2013; Larsen et al., 2015).

The turbine model used for the simulations is based on the structural and aerodynamic data of the Siemens 3.6 MW turbine, which was tested at Høvsøre in 2009 during the DAN-AERO project; see Section 2.1. Within the HAWC2 framework, the turbine is controlled by the Basic DTU controller (Hansen and Henriksen, 2013), and the blades are modelled with slightly different pitch angles to match the offsets seen in the measurements; see Sect. 2.4.

2.6 Inflow characteristics

In this section, the inflow characteristics used for the different cases are described; see an overview of the 5 cases in Table 1. Cases 1 - 3 are based on met-mast sensors, while Cases 4 and 5 are based on the estimated free-stream pitot-tube wind speed; see Sect. 2.2. Table 2 gives an overview of the actual inflow parameters extracted from the 20 periods.

Wind Energ. Sci. Discuss., https://doi.org/10.5194/wes-2018-4
Manuscript under review for journal Wind Energ. Sci.
Discussion started: 3 April 2018

Table 1. Case overview.

Case	Wsp	Wsp trend	Tint	Shear	L, Γ	$\alpha\epsilon$ fitted to	Constrained to
Case 1	Mast3	-	Site avg.	Site avg.	Standard	-	-
Case 2	Mast3	Mast3	-	Main met mast	Stability dependent	Mast3 variance	-
Case 3	Mast3	Mast3	-	Main met mast	Stability dependent	Mast3 variance	Mast3 wsp
Case 4	Pitot	Pitot	-	Pitot (power-law)	Standard	Pitot variance	-
Case 5	Pitot	Pitot	-	Pitot (grid)	Standard	Pitot variance	Pitot wsp

Table 2. Inflow characteristics of P1 - P20.

		Wsp [ms^{-1}]		Trend $\left[\frac{\text{ms}^{-1}}{10\text{min}}\right]$		Turb. int. [%]			Power shear exp. [-]			Stability
Obtained from		M [1]	P[2]	M[1]	P[2]	S[3]	M[1]	P[2]	S[3]	M[1]	P[2]	M[1]
P1	2009-07-02 05:30	8.1	7.9	-0.2	-0.2	7.8	3.5	2.8	0.09	0.21	0.15	Stable
P2	2009-07-05 17:10	8.0	7.5	-0.2	0.2	7.8	3.1	3.4	0.09	0.08	0.03	Very unstable
P3	2009-05-10 19:00	8.0	8.2	-0.2	0.1	7.8	5.3	3.0	0.09	0.09	-0.01	Unstable
P4	2009-07-05 08:50	8.1	7.5	-0.3	-0.4	7.8	7.1	5.9	0.09	0.09	0.00	Very unstable
P5	2009-07-05 14:30	7.9	7.5	0.1	0.5	7.8	9.2	7.0	0.09	0.06	0.01	Very unstable
P6	2009-07-05 09:10	8.0	7.6	-0.6	-0.7	7.8	5.2	6.1	0.09	0.06	-0.00	Very unstable
P7	2009-07-05 02:10	8.1	7.8	-2.9	-1.6	7.8	7.0	6.1	0.09	0.13	0.02	Neutral
P8	2009-05-10 10:30	7.9	8.1	0.9	1.3	7.8	8.1	6.0	0.09	0.07	-0.01	Very unstable
P9	2009-07-05 00:10	8.1	7.5	1.3	2.0	7.8	7.0	7.3	0.09	0.12	0.01	Unstable
P10	2009-05-24 20:50	8.1	7.9	-1.7	-1.9	7.8	6.9	7.7	0.09	0.10	-0.00	Very unstable
P11	2009-07-09 04:50	13.8	13.7	0.6	0.4	7.2	5.6	4.6	0.13	0.13	0.03	Very unstable
P12	2009-07-09 02:20	13.9	13.6	-0.6	-0.5	7.2	5.8	4.8	0.13	0.12	0.04	Near unstable
P13	2009-05-23 03:30	14.3	14.4	1.6	2.2	7.2	8.0	6.5	0.13	0.13	0.09	Unstable
P14	2009-05-23 00:40	13.8	13.5	-1.0	0.2	7.2	7.2	6.9	0.13	0.13	0.07	Near unstable
P15	2009-05-09 01:30	13.8	13.6	0.6	0.5	7.2	6.9	6.3	0.13	0.15	0.07	Neutral
P16	2009-05-23 02:00	14.1	13.4	-1.2	-0.7	7.2	5.7	6.6	0.13	0.13	0.11	Near unstable
P17	2009-05-09 01:10	14.0	13.4	0.0	0.1	7.2	6.9	6.6	0.13	0.15	0.06	Neutral
P18	2009-05-09 01:40	14.0	13.6	-0.4	1.0	7.2	6.3	5.2	0.13	0.15	0.07	Neutral
P19	2009-07-09 03:50	14.2	13.8	1.2	1.5	7.2	5.8	7.0	0.13	0.12	0.03	Unstable
P20	2009-05-23 02:40	14.0	13.8	1.4	0.2	7.2	8.3	7.6	0.13	0.13	0.12	Near unstable

[1] Mast 3 / main met mast

[2] Pitot tube

[3] Mast 3 / main met mast (Site average)

Wind Energ. Sci. Discuss., https://doi.org/10.5194/wes-2018-4
Manuscript under review for journal Wind Energ. Sci.
Discussion started: 3 April 2018

eawe european academy of wind energy
Open Access WIND ENERGY SCIENCE DISCUSSIONS

2.6.1 Wind speed

In Cases 1 - 3, the 10-min-mean wind speed measured at Mast3 is used. Mast3 is located around 2.5 diameters to the west of the turbine; see Fig. 3. Its 10-min-mean wind speed is therefore expected to match the mean wind speed at the rotor quite well in the selected periods.

In Cases 4 and 5, the mean wind speed is extracted from the estimated free-stream pitot-tube wind speed. To avoid the problem that the mean wind speed is influenced by non-linear shear, only observations recorded in 85 - 95 m are included (i.e. the hub height ± 5 m at both sides of the rotor).

2.6.2 Wind speed trend

In some of the selected periods, the mean wind speed changes considerably during the period. A linear wind-speed trend is therefore calculated for all periods and included in the simulations in all cases except Case 1.

Wind speed trends may result in increased loads, e.g. tower-bottom fatigue loads, as the trend will contribute with one (large) cycle. Furthermore, the target turbulence intensity will be too high if calculated from the standard deviation of the raw wind speed signal. Note, however, that periods with wind speed trends may be problematic as it means that the turbulence conditions are not stationary, and the theory behind the applied turbulence model assumes stationary conditions.

2.6.3 Shear and mean wind speed variation

The wind shear profile has a high impact on the flap loads as well as on the tower-top tilt and yaw loads. The 10-min-mean wind speed is not known in all parts of the rotor, and therefore a shear model is necessary. In this study, the power-law shear profile is used, and it is fitted to one hour of measurements. As the wind may change during one hour, we would like to base the shear profile on the selected 10-min observations. The 10-min-mean vertical profile, however, can have almost any shape, and therefore a longer time period is usually required to make a proper power-profile fit.

In Case 1, the site-average wind-speed-dependent shear profile is used while the mean wind speeds at different heights, measured at the main met mast 850 m away, are used to estimate the vertical shear profile for Cases 2 and 3. Note that the main met mast has sensors up to 116.5 m, and the upper part of the rotor is therefore not represented.

It is possible to use the measured 10-min pitot-tube shear profile directly inside the pitot tube altitude range, but another approach is required outside this range. A power-law shear profile is therefore fitted to one hour of the estimated free-stream pitot-tube wind speed and used for Cases 4 and 5.

Ideally the 10-min-mean wind speed is known everywhere at the rotor. This is obviously not the case, but from the pitot tube measurements, the 10-min-mean wind speed at the path of the pitot tube can be extracted and used to specify the mean wind speed in a grid covering the rotor; see Fig. 6 (left). This information is used in combination with the one-hour power-shear profile (Fig. 6 (middle)) to specify a grid-based mean wind speed for Case 5; see Fig. 6 (right).

Wind Energ. Sci. Discuss., https://doi.org/10.5194/wes-2018-4
Manuscript under review for journal Wind Energ. Sci.
Discussion started: 3 April 2018

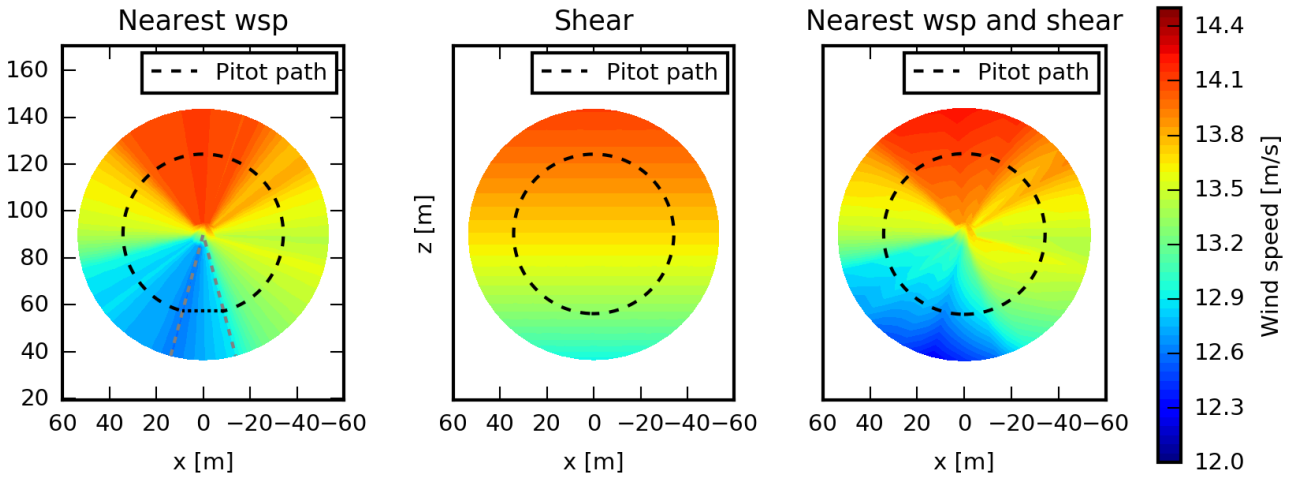

Figure 6. Left: wind speed based on nearest pitot-tube wind speed (interpolated values are used in a 30° sector around the tower to the exclude effects of tower shadow). Middle: wind speed based on the one-hour power-shear profile. Right: wind speed based on the nearest pitot-tube wind speed and power shear profile.

The aerodynamic models that are used to estimate the free-stream pitot-tube wind speed do not include a model of the tower shadow. The wind speed drop due to tower shadow should not, however, be included in the inflow input to the simulations. The mean wind speed is therefore linearly interpolated in a 30° sector around the tower as indicated in Fig. 6 (left).

2.6.4 Turbulence

The turbulence used in the simulations is generated using the Mann turbulence model (Mann, 1994, 1998). This model requires three parameters as input: a length scale of the spectral velocity tensor, L, an energy dissipation factor, $\alpha\epsilon$, and a shear distortion parameter, Γ. Standard parameters can be used, or they can be fitted to the turbulence spectra calculated from a long period of e.g. 3D sonic measurements.

For Cases 1, 4 and 5, standard values are used for L and Γ as specified in IEC 61400-1 (2005) while fitted values are used for Cases 2 and 3.

The Mann turbulence model assumes neutral atmospheric stability conditions. The parameters can, however, be fitted to spectra non-neutral stability classes where slightly different parameters are obtained. The stability-dependent parameters used for Cases 2 and 3 (see Table 3) are extracted from Peña et al. (2010) who investigated the turbulence at the current site.

Standard- or long-term-average values may be appropriate for L and Γ, but as we want to simulate the current situation and not a monthly or yearly average, another approach is required for the $\alpha\epsilon$-parameter that for fixed L and Γ is closely related to the turbulence intensity and, thus, the fatigue loads.

Wind Energ. Sci. Discuss., https://doi.org/10.5194/wes-2018-4
Manuscript under review for journal Wind Energ. Sci.
Discussion started: 3 April 2018

eawe european academy of wind energy
Open Access WIND ENERGY SCIENCE DISCUSSIONS

Table 3. Standard and stability dependent turbulence parameters.

	Length scale, L	Shear distortion, Γ
Standard (IEC)	33.6	3.9
Very stable	7.7	2.88
Stable	11.6	2.79
Near stable	24.6	2.68
Neutral	33.1	2.57
Near unstable	50.8	3.32
Unstable	69.2	2.09
Very unstable	79.1	1.54

In Case 1, the turbulence is scaled after generation, such that the turbulence intensity in the centre of the turbulence field matches the turbulence intensity measured by Mast3 in the selected period. This approach is convenient as it ensures agreement between the measured and simulated hub-height turbulence intensity. It may, however, result in energy from scales that are not represented in the turbulence model being distributed on other frequencies. Furthermore, the approach is inappropriate if the centre of the turbulence field is not representative for the whole field.

In Cases 2 - 5, the $\alpha\epsilon$ parameter is defined, such that the integral of the uu-Mann-model spectrum equals the integral of the measured uu spectrum. For Cases 2 and 3, the measured uu spectrum is obtained from the detrended wind speed measured by Mast3, while the pitot-tube-based wind speed is used for Cases 4 and 5.

Due to the low fixed-position resolution of the pitot-tube wind speed, only the low frequency part of the uu spectrum can be obtained from the pitot tube, and this part is not suitable for fitting. Assuming that the turbulence field is homogeneous, the uu spectra are therefore calculated from all of the pitot tube observations after subtracting the position-dependent mean wind speed and trend. The resulting spectra are very different from the normal fixed-position spectra because the pitot tube moves in and out of turbulence structures, as also reported by Hardesty et al. (1981) and Verholek (1978), and theoretically described by Kristensen and Frandsen (1982). The variance of the turbulence, i.e. the integral of the spectrum, is, however, independent of the frame of reference.

In Cases 3 and 5, the measured wind speeds are used as the input to a constraint turbulence simulator that modifies existing turbulence fields, e.g. stochastic realizations of the Mann turbulence model, to reproduce the specified wind speeds at the corresponding positions while preserving the statistics. The applied constraint turbulence simulation approach is described by Nielsen et al. (2003). In Case 3, the wind speed measured by Mast3 is used to constrain the turbulence at the position of Mast3, while the pitot-tube wind speed is used to constrain the turbulence in Case 5 at the instantaneous position of the rotating pitot tube.

Wind Energ. Sci. Discuss., https://doi.org/10.5194/wes-2018-4
Manuscript under review for journal Wind Energ. Sci.
Discussion started: 3 April 2018

eawe european academy of wind energy
Open Access WIND ENERGY SCIENCE DISCUSSIONS

3 Results

Figures 7, 8 and 9 show the equivalent loads coloured by turbulence intensity, shear and atmospheric stability, respectively. The strongest dependence on these three single parameters is seen by the tendency to stratification in the flap and tower-bottom loads for low wind speeds, where the lowest loads are seen to occur in stable conditions with low turbulence intensity and high shear. The colours are, however, rather mixed, and wide areas have similar colours. It is therefore concluded that the scatter is somewhat independent of these three single parameters, and a more sophisticated approach, which considers the actual combination of inflow parameters, is required to predict the loads of specific periods.

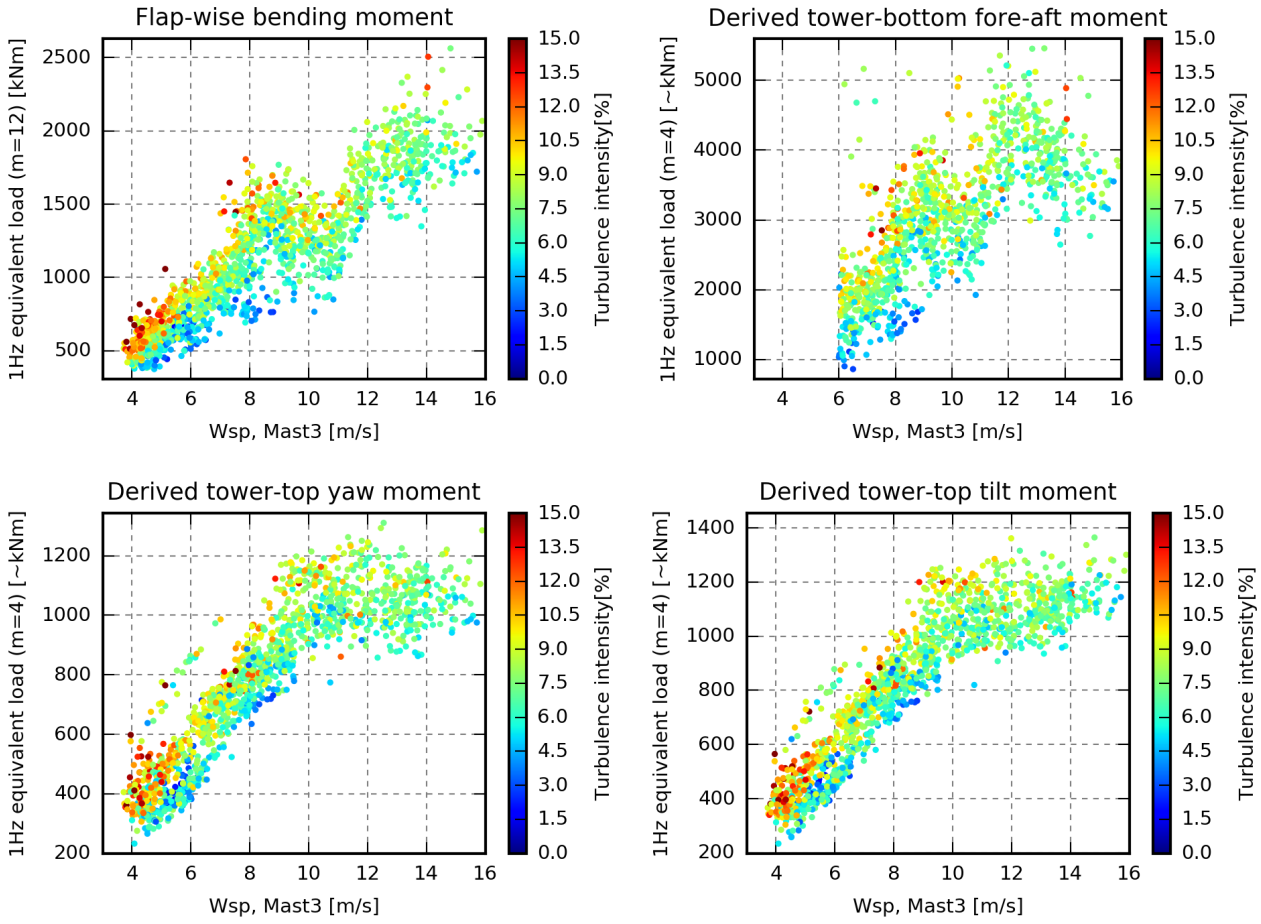

Figure 7. 1 Hz equivalent loads coloured by the turbulence intensity measured at Mast3.

Wind Energ. Sci. Discuss., https://doi.org/10.5194/wes-2018-4
Manuscript under review for journal Wind Energ. Sci.
Discussion started: 3 April 2018

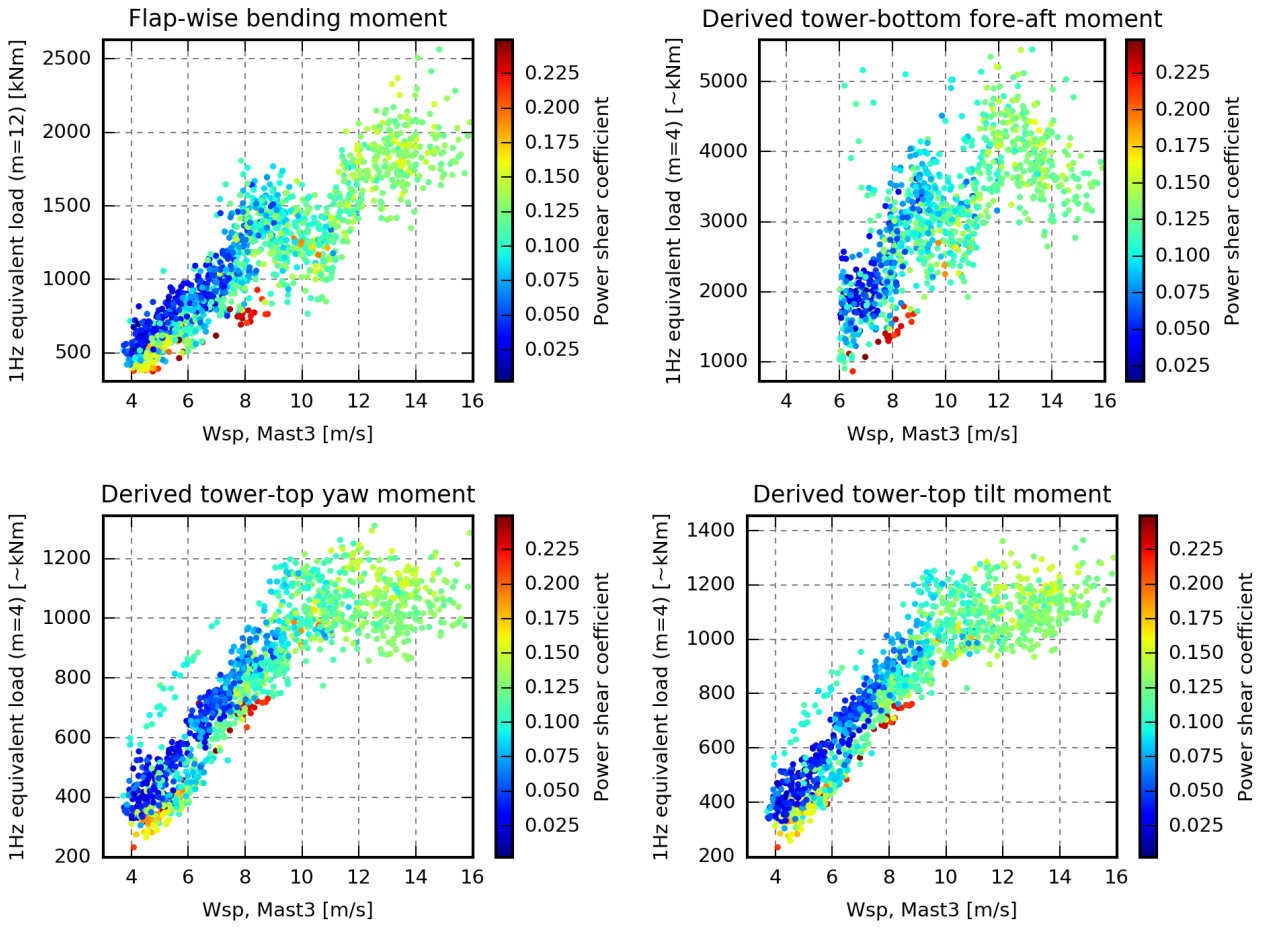

Figure 8. 1 Hz equivalent loads coloured by the power shear coefficent extracted from the main met mast.

Wind Energ. Sci. Discuss., https://doi.org/10.5194/wes-2018-4
Manuscript under review for journal Wind Energ. Sci.
Discussion started: 3 April 2018

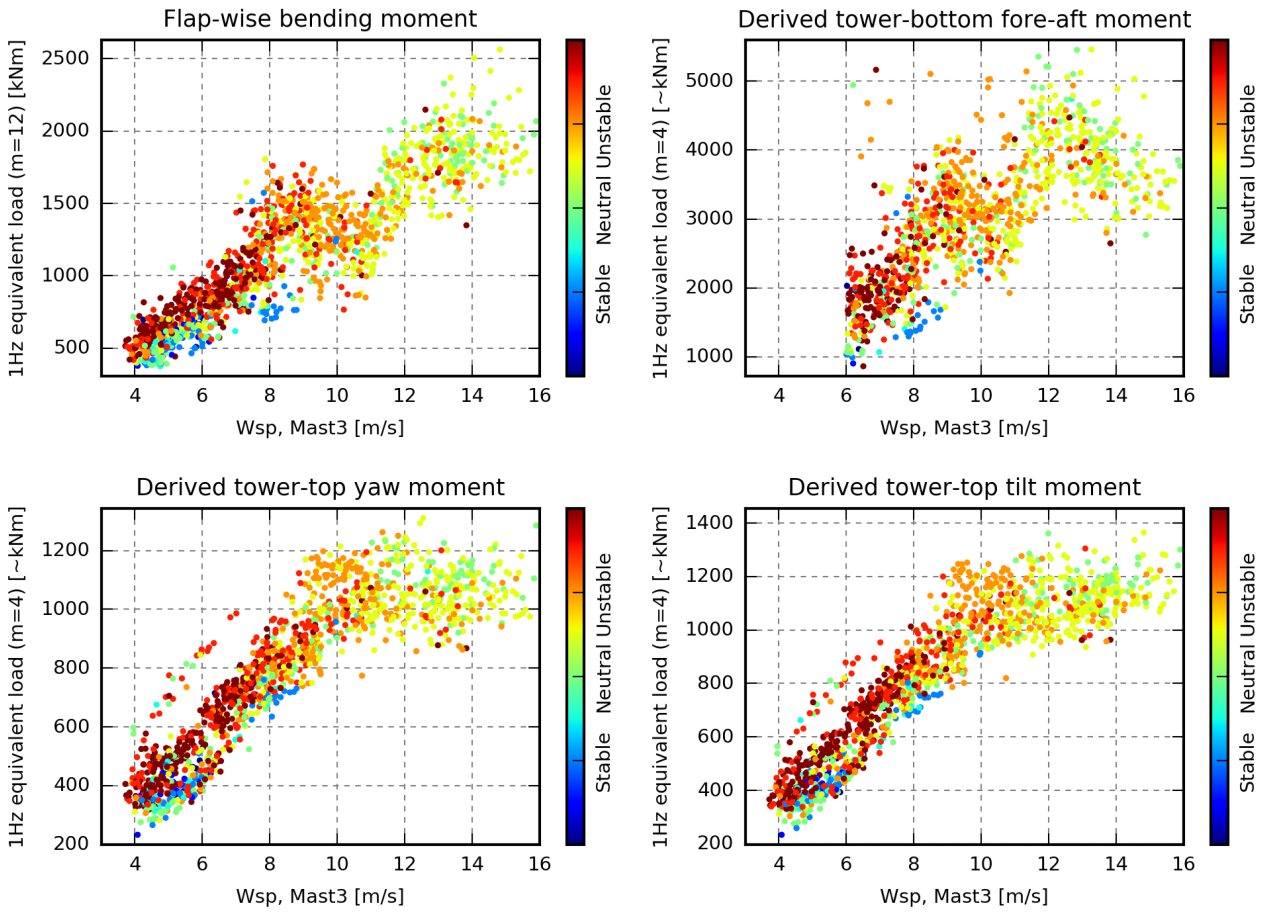

Figure 9. 1 Hz equivalent loads coloured by atmospheric stability extracted from the main met mast.

Wind Energ. Sci. Discuss., https://doi.org/10.5194/wes-2018-4
Manuscript under review for journal Wind Energ. Sci.
Discussion started: 3 April 2018

eawe european academy of wind energy
Open Access WIND ENERGY SCIENCE DISCUSSIONS

An overview of the mean absolute relative error of the different cases can be found in Fig. 10, while Fig. 11 shows the distribution of the relative simulation errors. Figure 12 shows how to interpret Fig. 13 - 16, which offer more details of the cases by showing the measured and simulated loads of P1 - P20.

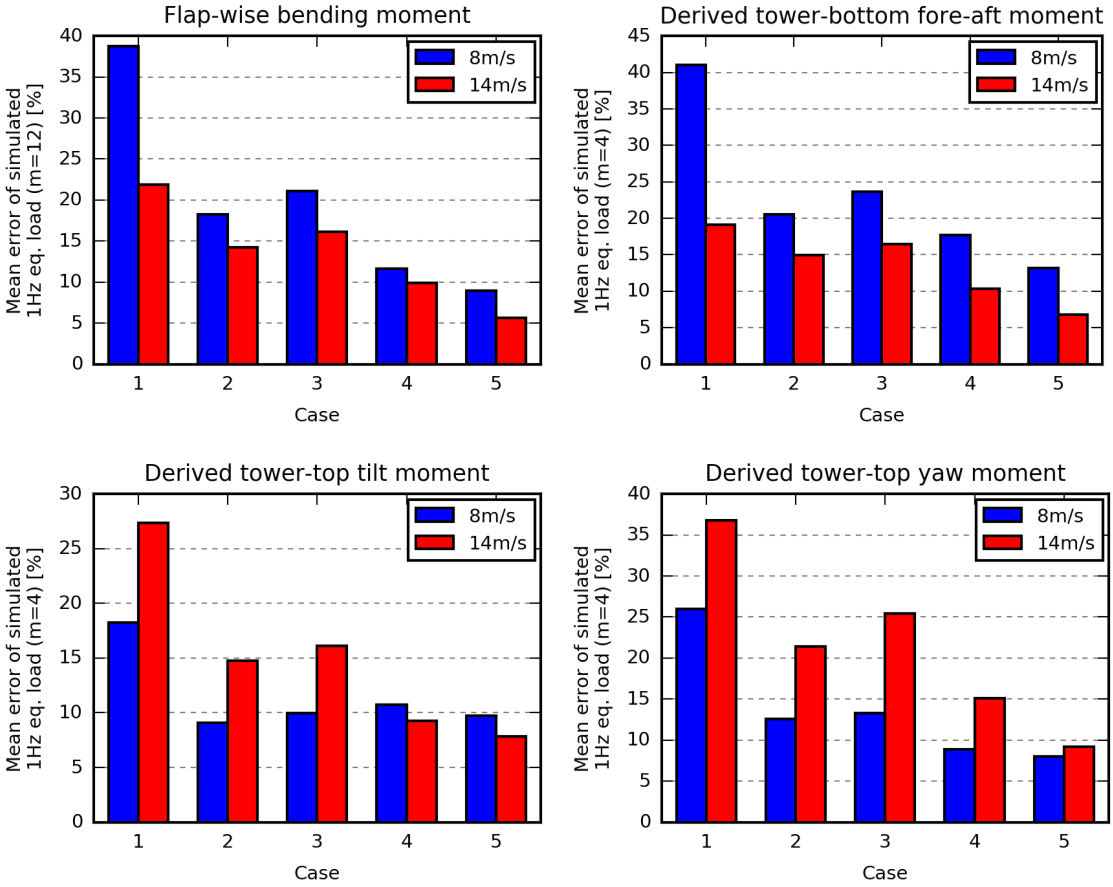

Figure 10. Mean absolute error of the simulated equivalent loads.

Wind Energ. Sci. Discuss., https://doi.org/10.5194/wes-2018-4
Manuscript under review for journal Wind Energ. Sci.
Discussion started: 3 April 2018

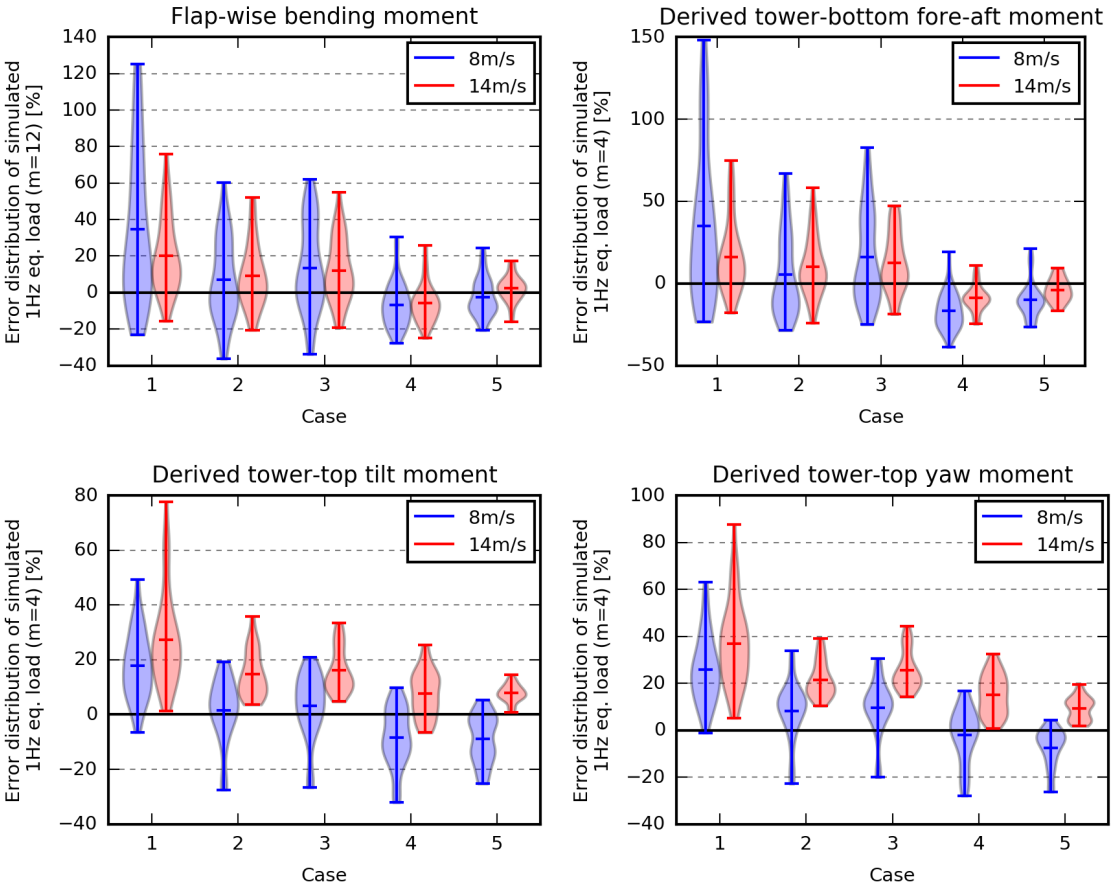

Figure 11. Error distribution of the simulated equivalent loads.

Wind Energ. Sci. Discuss., https://doi.org/10.5194/wes-2018-4
Manuscript under review for journal Wind Energ. Sci.
Discussion started: 3 April 2018

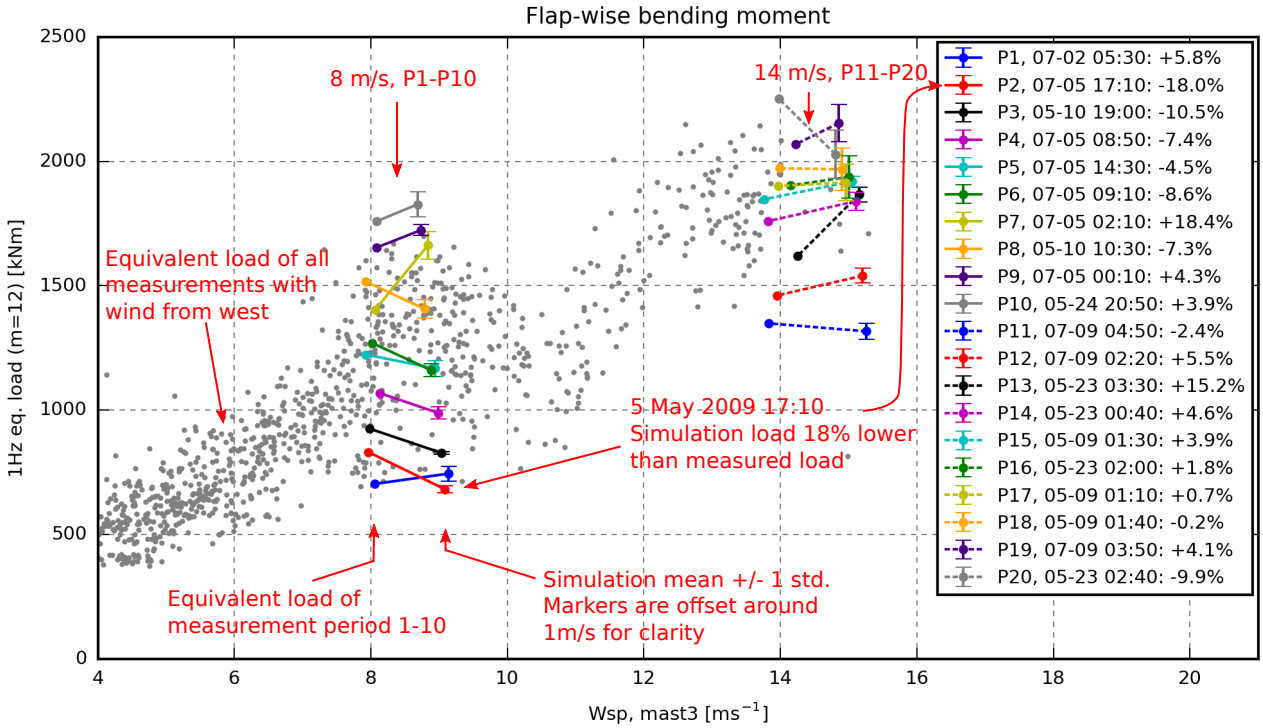

Figure 12. Example showing how to interpret Fig. 13 - 16. The title states that the figure shows the equivalent flap-wise bending moment of blade A. The grey background dots represent the equivalent loads of all measurements with wind from the west; i.e. no-wake situations. The 20 selected periods, P1 - P10 at 8 $\mathrm{ms}^{-1}$and P11-P20 at 14 $\mathrm{m/s}$, are illustrated by dots connected to error bars. The dots show the measured equivalent load and wind speed while the error bars illustrate the simulated mean loads $\pm 1\sigma$. Note that the error bars are offset around 1 $\mathrm{ms}^{-1}$to the right for clarity. The red dot and error bar, for instance, represent P2; i.e. 7th May, 17:10 - 17:20. The equivalent load measured in this period was around 830 kNm, while the six corresponding simulations have a mean load level around 682 kNm and a standard deviation of 16 kNm.

Wind Energ. Sci. Discuss., https://doi.org/10.5194/wes-2018-4
Manuscript under review for journal Wind Energ. Sci.
Discussion started: 3 April 2018

eawe european academy of wind energy
Open Access WIND ENERGY SCIENCE DISCUSSIONS

In **Case 1**, only the wind speeds are different between the periods. The load levels within the two wind-speed groups are therefore very similar as seen in Fig. 13. In this case, the simulated loads do not reflect the measured load variation, and the mean absolute relative error seen in Fig. 10 is therefore high, especially for the flap and tower-bottom loads at 8 ms^{-1} where the relative variation is huge, but also in the tilt and yaw moments at 14 ms^{-1} where the simulated loads are too high. It should also be noted that the variation of the simulations due to different turbulence realisations (seeds) does not reflect the measured variation, except for the yaw and tilt moment in the high-wind situations.

Wind Energ. Sci. Discuss., https://doi.org/10.5194/wes-2018-4
Manuscript under review for journal Wind Energ. Sci.
Discussion started: 3 April 2018

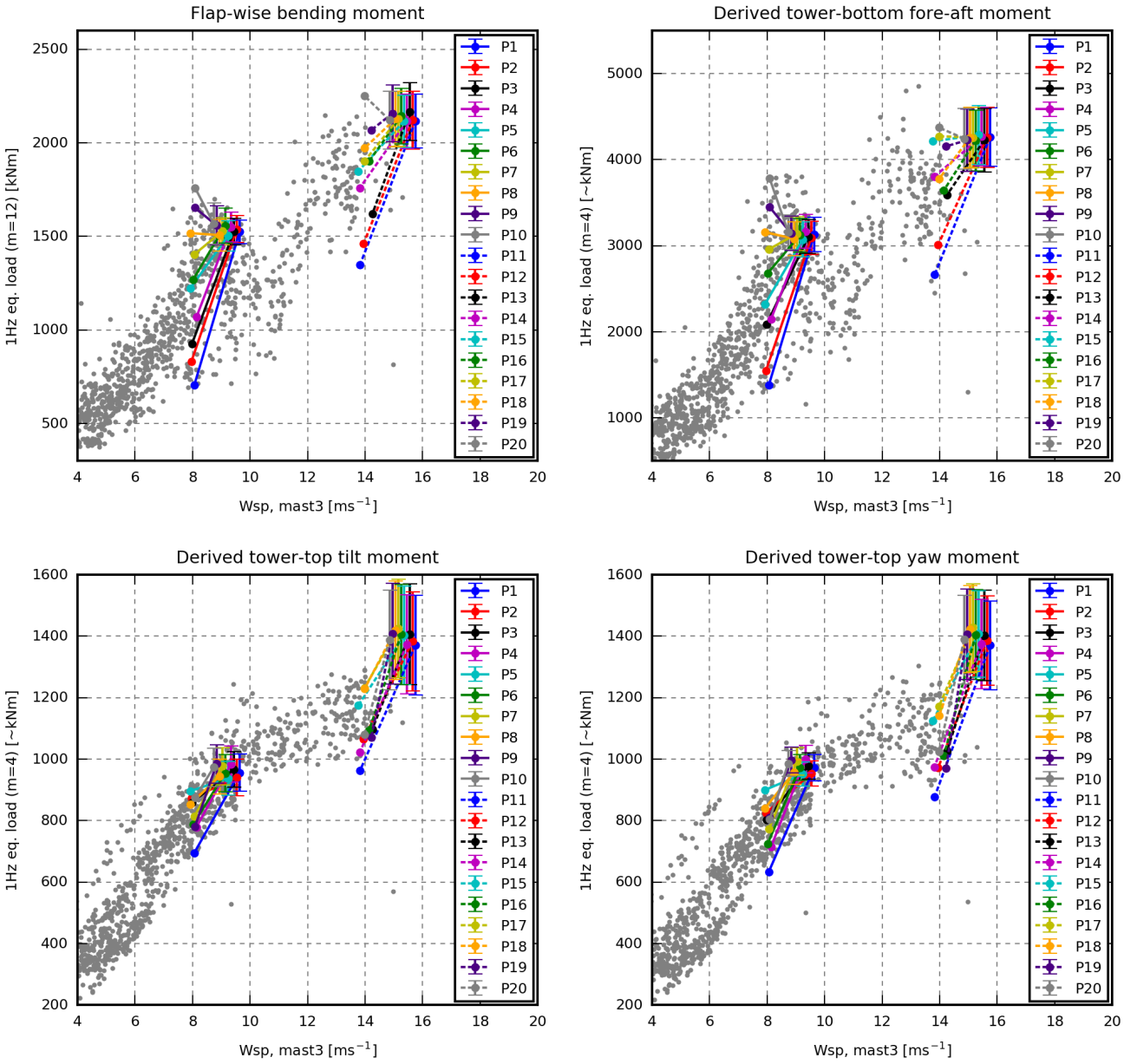

Figure 13. Case 1. Site average turbulence intensity and shear (wind speed trend neglected). For interpretation see Fig. 12.

Wind Energ. Sci. Discuss., https://doi.org/10.5194/wes-2018-4
Manuscript under review for journal Wind Energ. Sci.
Discussion started: 3 April 2018

eawe european academy of wind energy
Open Access WIND ENERGY SCIENCE DISCUSSIONS

In **Case 2**, information about the wind speed trend, the measured turbulence level and shear profile is included in the simulations.

Including the wind speed trend increases the loads considerably in some periods. In P7, for example, the mean wind speed decreases 2.9 ms^{-1} (linear fit) during the 10 minutes; see Table 2. Including this trend increases the flap and tower-bottom fatigue loads by around 30 $\%$. It indicates that wind-speed trends are important to include in simulations for load validations.

In the selected periods, the turbulence intensity varies from 3.1 to 9.2 $\%$. Including this information makes the range of the simulated loads reflects the range of the measured loads. The turbulence scaling approach, which is used for Case 1, is found to introduce substantial variation due to different turbulence realisations (seeds). This variation is considerably reduced in this and the succeeding cases by fitting the $\alpha\epsilon$ turbulence parameter. Seen in isolation, the $\alpha\epsilon$-fitting method reduces the average seed-induced variation of yaw loads at 14 ms^{-1} from 450 kNm to 90 kNm, while the maximum error of the tilt and yaw moments at 14 ms^{-1} is approximately reduced from 80 $\%$ to 40 $\%$.

The terrain is rather flat towards the west, and the power-shear exponents are therefore modest (0.06 to 0.21), and in general similar to the site-average values (0.09 for 8 ms^{-1} and 0.13 for 14 ms^{-1}). The largest difference is found in P1, where the shear coefficient is increased from 0.09 to 0.21, which seen in isolation increases the simulated flap loads of this period by 9-18 $\%$. In general, however, the effect of including the measured shear profile is limited, but the situation may be different if periods with wind from other directions were also considered.

Furthermore, the stability dependent L and Γ parameters are used for the turbulence generation. Using these non-standard parameters, affects the flap and tower-bottom loads significantly in some periods. In P1 (stable conditions), the tower-bottom load decreases by 22 $\%$, while it increases by 20 $\%$ in P11 (very unstable conditions). In these periods, however, the error of the simulated loads is not reduced.

Figure 10 reveals that the mean error of all loads is significantly reduced by utilising these inflow characteristics. The correlation between the measured and simulated load levels is, however, still poor. The simulated tower-bottom load of P5, for instance, is up to 67 $\%$ too high, and the measured tilt-moment fatigue loads of P2 and P5 are almost equal, but they account for the minimum and maximum simulated loads, respectively; see Fig. 14

Wind Energ. Sci. Discuss., https://doi.org/10.5194/wes-2018-4
Manuscript under review for journal Wind Energ. Sci.
Discussion started: 3 April 2018

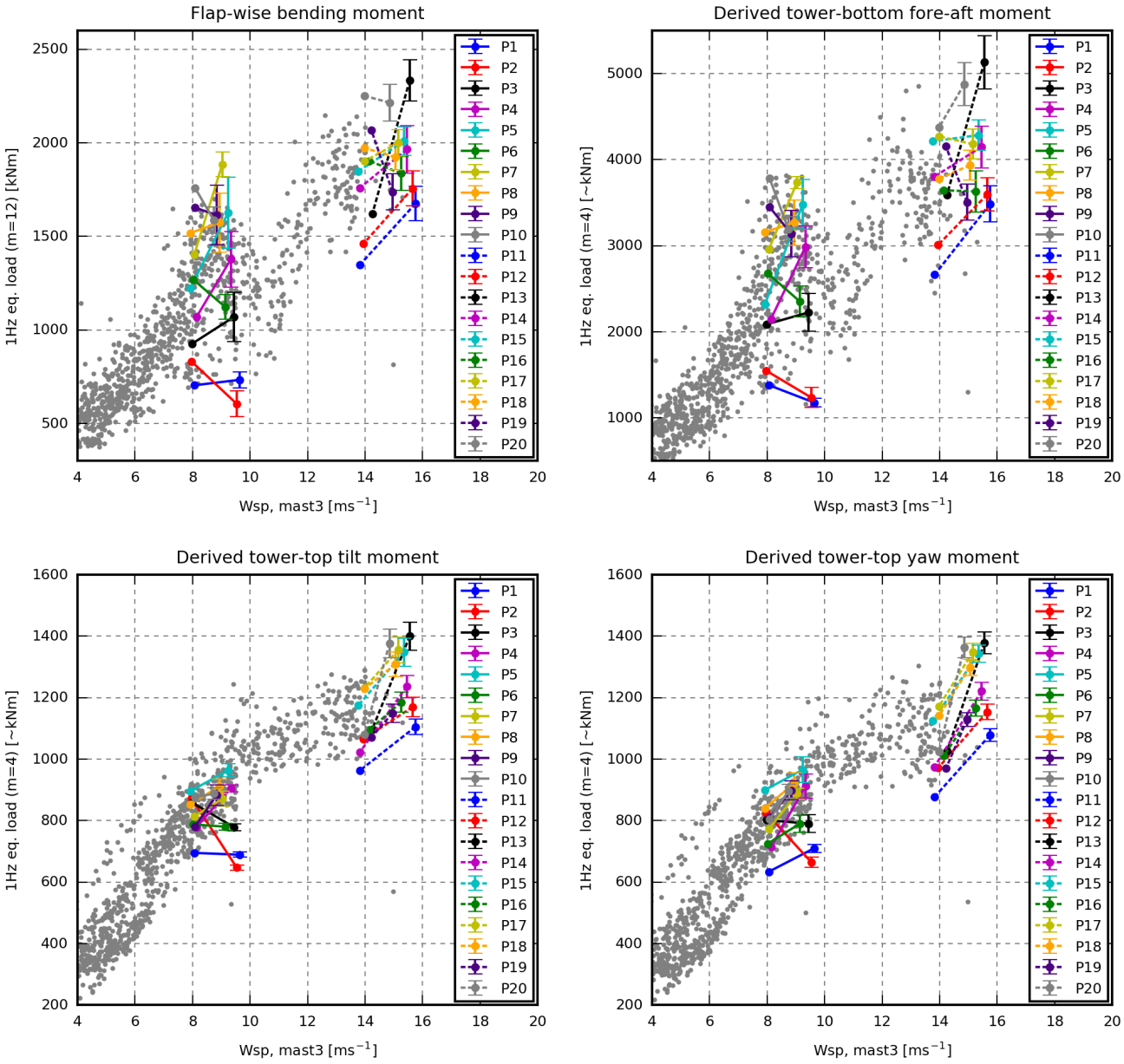

Figure 14. Case 2. Best case based on met mast inflow information. For interpretation see Fig. 12.

Wind Energ. Sci. Discuss., https://doi.org/10.5194/wes-2018-4
Manuscript under review for journal Wind Energ. Sci.
Discussion started: 3 April 2018

eawe european academy of wind energy
Open Access WIND ENERGY SCIENCE DISCUSSIONS

In **Case 3**, constraint turbulence simulation has been applied to constrain the turbulence to match the Mast3 wind speed at the position of Mast3, i.e. 250 m upstream. It has an effect on most of the simulated loads, but it slightly increases the mean error of all load sensors; see Fig. 10.

The biggest error increase is seen for P5, which has a distinct drop in the wind speed measured by Mast3 in the middle of the period. In the simulations, a similar drop, introduced by the constraint turbulence simulator, is transported unaffected with the steady mean wind to the turbine in agreement with Taylor's frozen turbulence hypothesis (Taylor, 1938). Around 30 s later, the same wind speed drop therefore hits the turbine and induces significant fatigue loads. In the real world, however, the turbulence structures changes, the mean wind is not always steady, and the wind-speed drop may even pass beside the turbine. In P5, a small drop is measured in the flap-wise bending moment, but it is only half the size of the simulated drop.

Case 4 uses inflow characteristics extracted from the estimated free-stream pitot tube wind speed. As seen in Table 2, these characteristics are different from the met mast characteristics; the mean wind speed deviates up to 0.77 ms^{-1}, the wind speed trend up to 1.45 ms^{-1}, the turbulence intensity up to 2.3 $\%$ and the power shear coefficient up to 0.11.

The mismatches are caused by the spatial distance between the locations of measurements, fundamental differences in the sensor technology and measurement method, and the uncertainties introduced in the conversion from pitot-tube measurement to free-stream wind speed in the fixed global coordinates; see section 2.2.

Compared to Case 2 (the most equivalent met-mast case), all mean errors decrease by 5 $\%$ or more except the mean error of the tilt moment at 8 ms^{-1}; see Fig. 10. The error ranges also decrease considerably for the flap and tower-bottom loads (see Fig. 11), while they are similar for the tilt- and yaw-moment error.

Wind Energ. Sci. Discuss., https://doi.org/10.5194/wes-2018-4
Manuscript under review for journal Wind Energ. Sci.
Discussion started: 3 April 2018

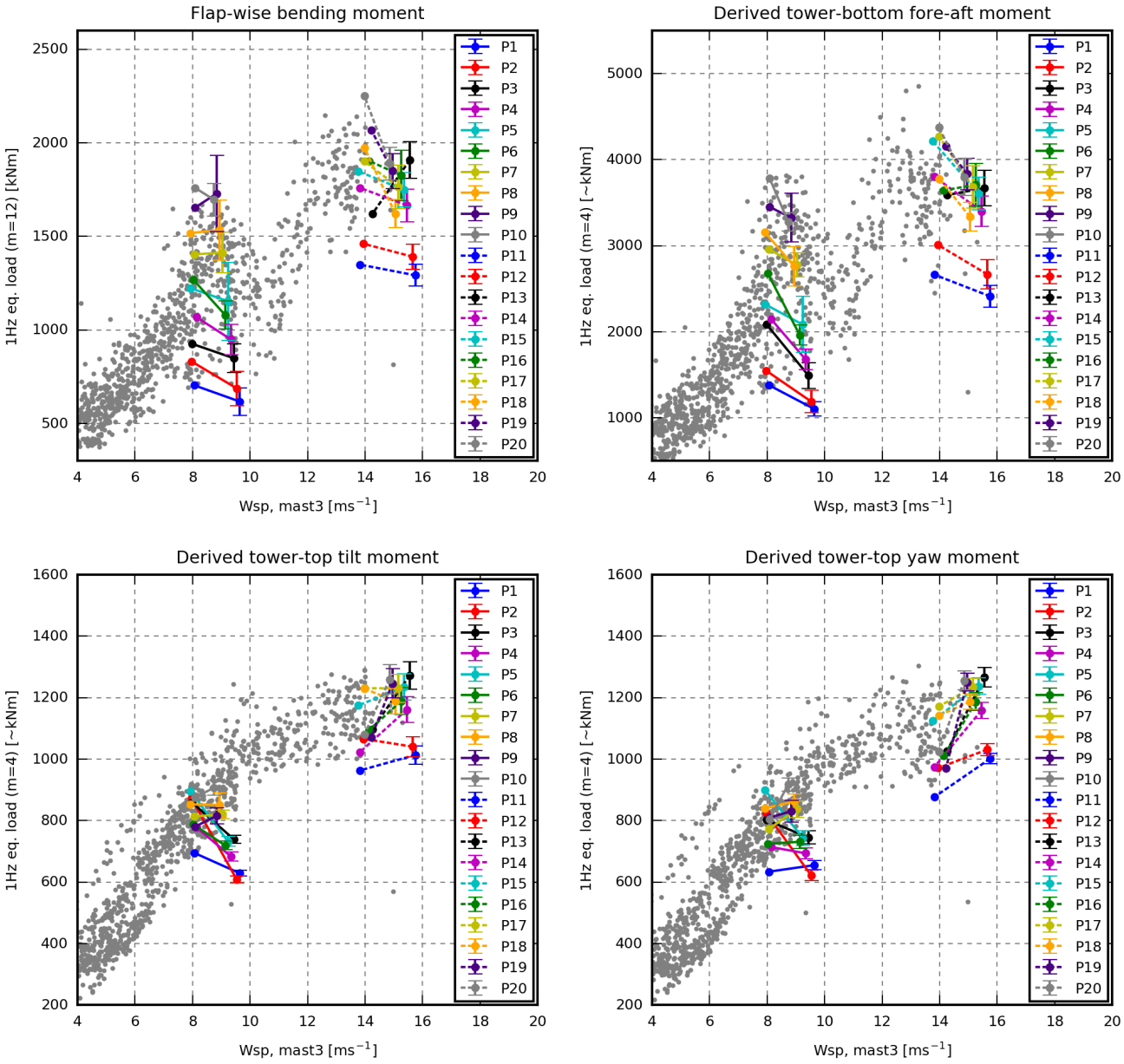

Figure 15. Case 4. Best case based on pitot tube inflow information. For interpretation see Fig. 12.

Wind Energ. Sci. Discuss., https://doi.org/10.5194/wes-2018-4
Manuscript under review for journal Wind Energ. Sci.
Discussion started: 3 April 2018

eawe european academy of wind energy
Open Access WIND ENERGY SCIENCE DISCUSSIONS

In **Case 5**, the measured mean-wind-speed variations within the rotor is modelled, and furthermore, the instant measured pitot tube wind speed is used to constrain the turbulence model.

Modelling the measured mean-wind-speed variations via the grid-based approach (exemplified in Fig. 6) increases all loads, except the yaw moments. In some periods, the flap load increases up to 15 $\%$, and seen in isolation, the use of this approach slightly decreases the error of most of the simulated loads. It may be that the mismatch introduced by extrapolating the wind speed measured on the pitot tube path to the whole rotor area almost neutralises the positive effects, in which case more pitot tubes would be beneficial.

In this case, the turbulence field is generated using standard L and Γ parameters and constraint turbulence simulation. In theory, this approach is problematic as the statistics of the applied constraints may be different from the standard parameters, such that the constraint turbulence simulator needs to compensate in other parts of the turbulence field to obtain the requested statistics. Using the stability-dependent L and Γ parameters instead has been tried. It was found to have a small positive effect on the errors at 8 ms^{-1} and a similar small, but negative, effect on the errors at 14 ms^{-1}. We have therefore chosen to use the standard parameters in this case, to avoid the need for met-mast measurements to determine the stability conditions.

In the selected periods, the use of constraint turbulence simulation reduces the mean error for all load sensors. Furthermore, the range of the simulated loads due to different turbulence realisations decreases considerably, such that the need for multiple simulations with different seeds is reduced; see Fig. 16.

In Cases 5, the range of the simulated loads reflects the range of the measured loads. They are therefore assumed to be much more suitable for load extrapolation than the loads of Case 1.

The derived tower loads are slightly underestimated at 8 $\mathrm{ms}^{-1}$and overestimated at 14 ms^{-1}. These deviations may be introduced by the tower-load derivation and calibration procedure, uncertainties in the measured pitch angle offsets, and by different control behaviour due to differences between the Siemens controller and the Basic DTU controller.

Only a few of the lines that connect the measured and simulated flap and tower-bottom observations intersect, meaning that the inflow conditions that result in high load levels in the measurements also result in high load levels in the simulations and vice versa. The same tendency is seen for the tilt and yaw moment at 14 ms^{-1}.

Wind Energ. Sci. Discuss., https://doi.org/10.5194/wes-2018-4
Manuscript under review for journal Wind Energ. Sci.
Discussion started: 3 April 2018

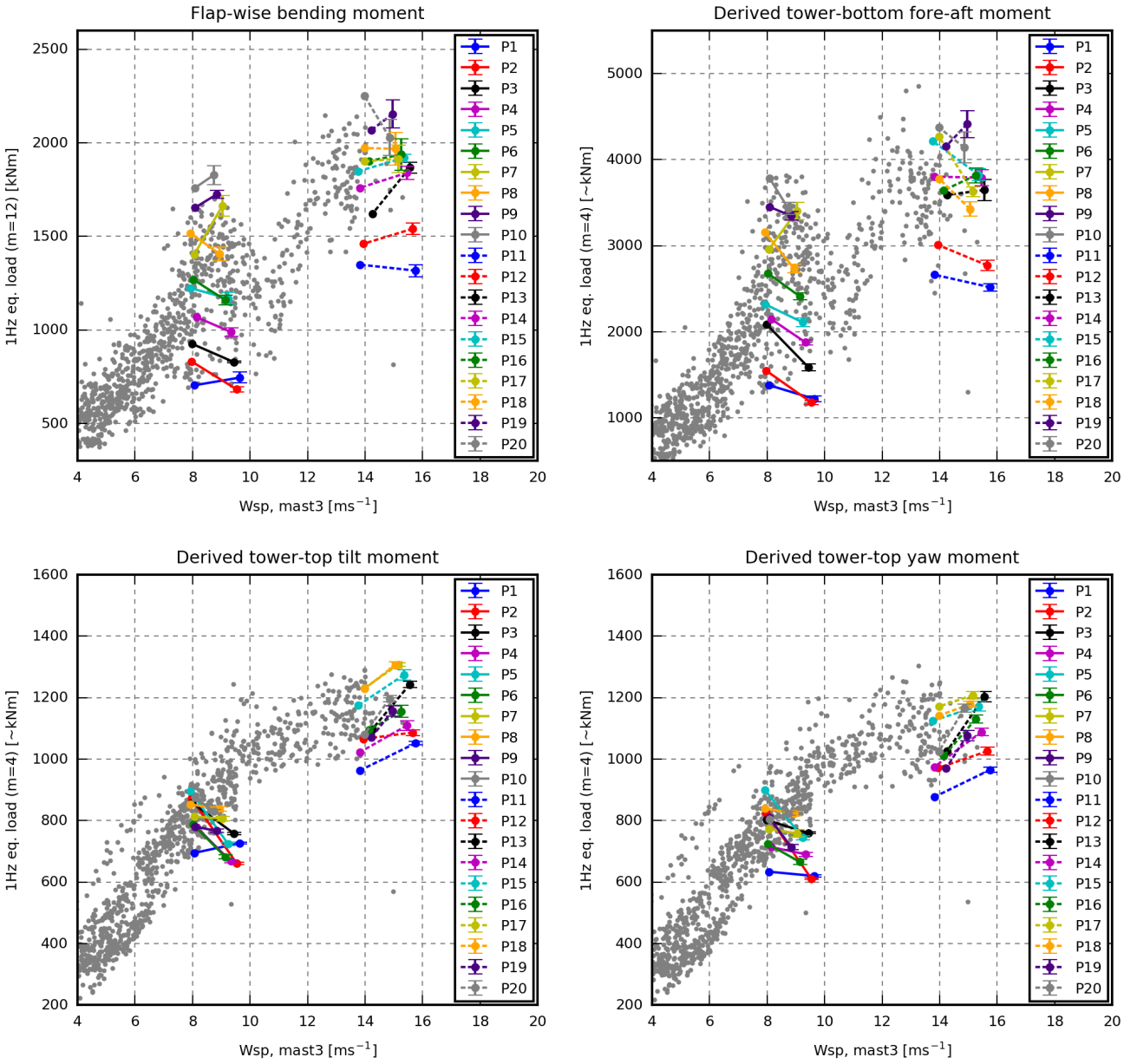

Figure 16. Case 5. Best case based on pitot tube inflow information. For interpretation see Fig. 12.

Wind Energ. Sci. Discuss., https://doi.org/10.5194/wes-2018-4
Manuscript under review for journal Wind Energ. Sci.
Discussion started: 3 April 2018

eawe european academy of wind energy
Open Access WIND ENERGY SCIENCE DISCUSSIONS

At the beginning of this section, it was concluded that an advanced approach that considers combinations of inflow parameters would be required to predict the loads of specific periods. Aeroelastic simulations can be considered to be such an approach, and to compare to the single parameter approach in Fig. 7, 8 and 9, two additional simulation sets were performed. Both sets comprise 970 simulations representing all suitable periods in the measurement database (one seed per period). In the first set, inflow information is extracted from the met masts (similar to Case 2) while the second set is based on information from the pitot tube (similar to Case 5). Figure 17 and 18 show the equivalent loads, coloured by the HAWC2-simulated load relative to the wind-speed-dependent measured load range. This means that the red dots represent periods where the simulated load equals the maximum measured load at that wind speed, while the blue dots represent periods where the simulated load equals the minimum measured load. In other words, unmixed rainbow-coloured scatter means that the measured and simulated loads are similar and that the measured scatter can be predicted.

The most promising result is seen in the flap and tower-bottom loads coloured by the pitot-tube-based simulations (top row of Fig. 18) where the scatter is almost rainbow-coloured. This means that HAWC2 simulations with inflow characteristics extracted from the pitot tube are able to explain most of the measured flap and tower-bottom load scatter. The met-mast-based counterparts (top row of Fig. 17) are more mixed, even though most of the red observations are in the upper part of the scatter and most of the blue observations are in the lower part.

The tilt and yaw moment scatter, on the other hand, cannot be explained using these approaches. In both cases, most high-load observations are underestimated from 4 to 8 ms^{-1} and from 10 to 12 ms^{-1}, while low-load observations are overestimated from 8 to 10 ms^{-1} and above 12 ms^{-1}.

Wind Energ. Sci. Discuss., https://doi.org/10.5194/wes-2018-4
Manuscript under review for journal Wind Energ. Sci.
Discussion started: 3 April 2018

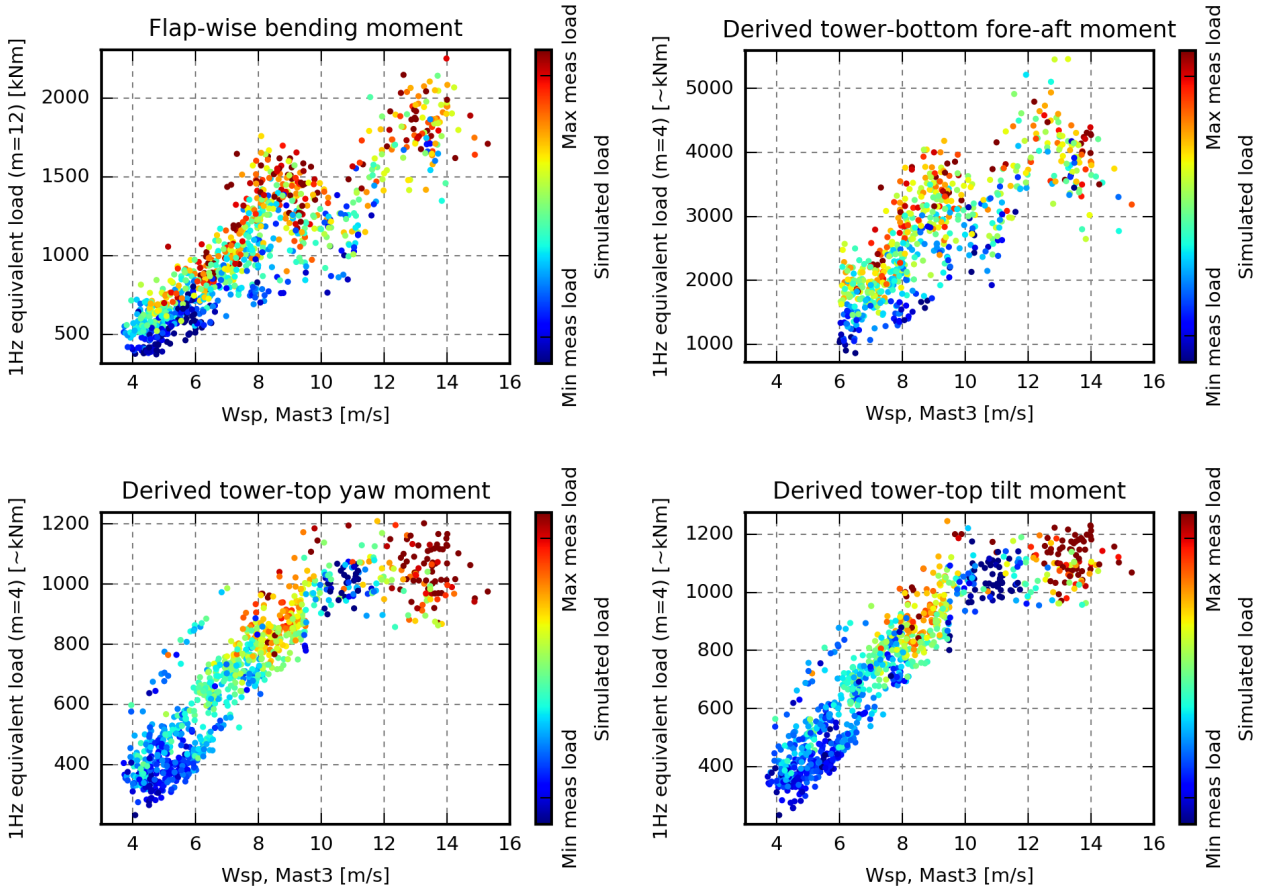

Figure 17. Equivalent measured loads, coloured by the corresponding simulation result. The simulations are performed using inflow information from the met masts, similar to Case 6 (but only one seed per period). If the simulated load equals the maximum measured load at the current wind speed, then the observation is red, while observations where the simulated load equals the minimum load measured at the current wind speed are blue.

Wind Energ. Sci. Discuss., https://doi.org/10.5194/wes-2018-4
Manuscript under review for journal Wind Energ. Sci.
Discussion started: 3 April 2018

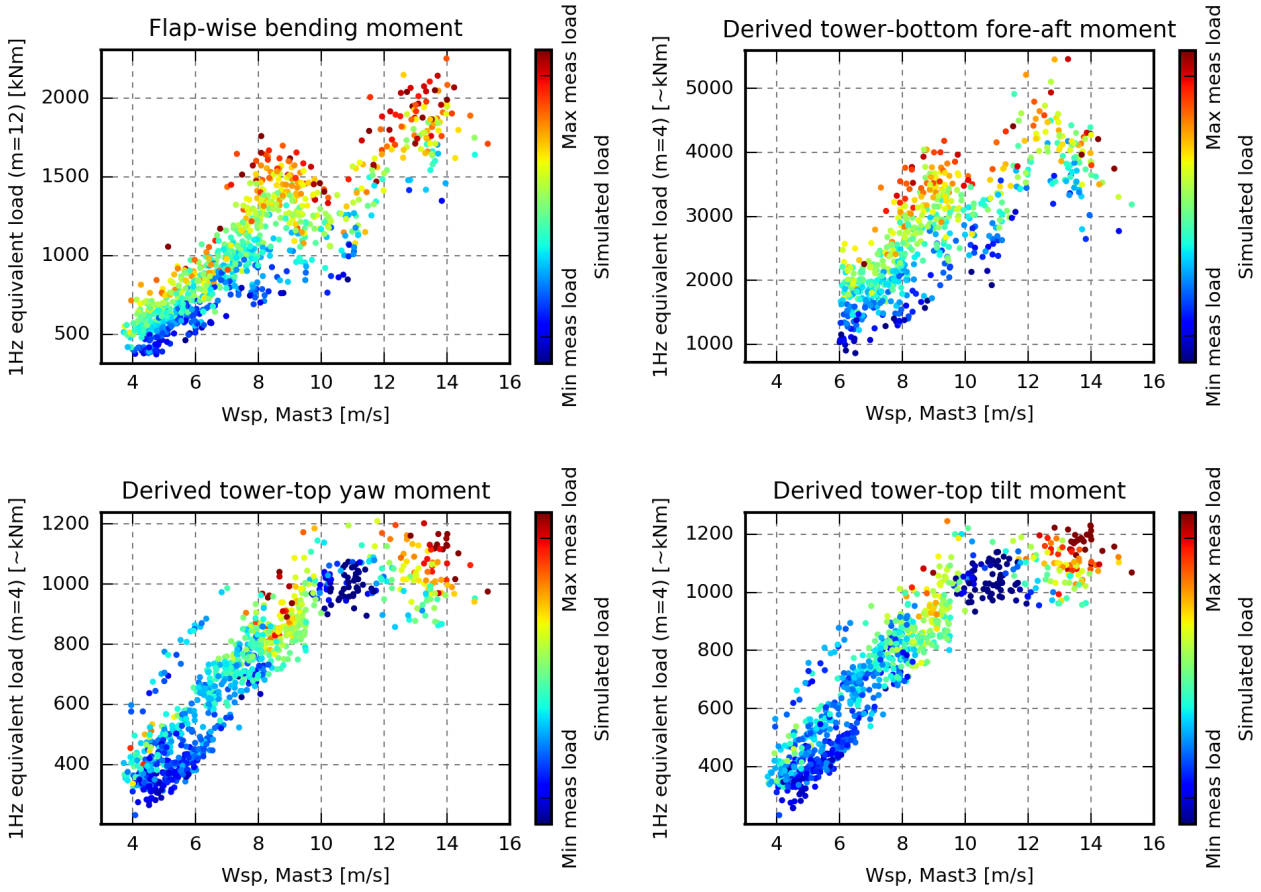

Figure 18. Equivalent measured loads, coloured by the corresponding simulation result. The simulations are performed using inflow information from the pitot tube, similar to Case 11 (but only one seed per period). If the simulated load equals the maximum measured load at the current wind speed, then the observation is red, while observations where the simulated load equals the minimum load measured at the current wind speed are blue.

Wind Energ. Sci. Discuss., https://doi.org/10.5194/wes-2018-4
Manuscript under review for journal Wind Energ. Sci.
Discussion started: 3 April 2018

4 Conclusions

In this paper, different inflow information is extracted from a measurement database and used for aeroelastic simulations to investigate if using more detailed inflow descriptions improves the accuracy of the simulated loads.

The inflow information is extracted from nearby met masts and a blade-mounted five-hole pitot tube. The pitot tube is located inside the induction zone, i.e. the measured flow velocity is influenced by the presence of the turbine. An aerodynamic model is therefore used to estimate the free-stream inflow velocity that would have been observed at the position of the pitot tube without the presence of the turbine.

In the case study, 20 periods, which represent a wide range of loads at 8 and 14 ms^{-1}, were selected. From these periods, inflow information was extracted for simulations.

The case study revealed that the loads in simulations based on site-average turbulence intensity and shear profile (the typical load validation approach) did not reflect the measured loads, and most of the simulated load ranges were considerably smaller than the ranges of measured loads. Load extrapolation based on this approach may therefore be misleading.

Including the met-mast measured turbulence intensity increases the variation of the simulated loads, and makes the simulated load range reflect the measured range. The one-to-one correspondences were, however, poor, with deviations up to 67 $\%$.

The turbulence scaling approach, where the turbulence is scaled such that the turbulence intensity in the centre of the field matches the target intensity, was found to introduce a considerable variation in the simulated loads. Therefore, the scaling the turbulence such that the integral of the target uu-spectrum matches the target variance is highly recommended.

In most periods, the inflow characteristics extracted from the pitot tube deviate from the inflow characteristics extracted from the met masts. The mismatches are caused by the spatial distance between the locations of met masts and the pitot tube, fundamental differences in the sensor technology and measurement method, and uncertainties introduced in the conversion from pitot tube measurement to estimated free-stream inflow wind speed in fixed global coordinates.

Using the wind speed, turbulence intensity and shear measured by the blade-mounted pitot tube reduces the errors of the flap and tower-bottom loads in this study, while the errors of the tilt and yaw moments are similar. This indicates that it is beneficial to measure the inflow with a BMFS even though errors are introduced due to the dynamic and static deflection and torsion of the blade, as well as in the aerodynamic model that corrects for the turbine induction.

Including the measured wind speed trend, shear profile, rotor-position-dependent variations in the mean wind, and stability-dependent turbulence parameters were all found to change the loads significantly in some simulations, while the mean errors were only slightly affected. This information may, however, be important to include in other situations, e.g. half-wake situations and periods with high shear.

Constraint turbulence simulation was used to constrain the turbulence to match the instantaneously measured wind speeds. Constraining the turbulence to the wind speed measured by the met mast (250 m upstream) increased the errors of the simulated loads. In the simulations, a turbulence event introduced by the constraint turbulence simulator at the met mast is transported unaffected with the steady mean wind to the turbine, in agreement with Taylor's frozen turbulence hypothesis. In the real world, however, the turbulence structures change, and an upstream turbulence event may even pass beside the turbine. The event that

hits the turbine in the simulation is thereby different from the event that hits the real turbine. It is therefore not recommended to use constraint turbulence simulation based on the wind speed measured far away.

Based on pitot-tube wind speed, however, constraint turbulence simulation reduces the mean error of all load sensors in this study. The final case is based on pitot tube mean wind speed, turbulence intensity and shear, and constraint turbulence simulation based on the pitot-tube-recorded wind speed. In this case, the range of the simulated loads reflects the range of the measured loads. It is therefore assumed to be more suitable for load extrapolation. Moreover, the sequences of the simulated and measured flap and tower-bottom loads are almost similar, meaning that the inflow conditions that result in high load levels in the measurements in most cases also result in high load levels in the simulations and vice versa. The same tendency is seen for the tilt and yaw moment at 14 ms^{-1}. In the final case, the range of the simulated loads due to different turbulence realisations (seeds) decreases considerably, meaning that the need for multiple simulations is reduced.

It was investigated whether the enormous scatter that is seen, especially in the flap and tower-bottom loads, can be predicted by the turbulence intensity, shear profile or atmospheric stability alone. The turbulence intensity explains some of the scatter and the lowest loads are seen in stable conditions with low turbulence intensity and high shear. It is, however, concluded that a more sophisticated approach, which considers the actual combination of inflow parameters, is required to predict the loads of specific periods

Aeroelastic simulations can be considered to be such an approach. Simulations representing all suitable periods have therefore been performed based on inflow information from the met masts (wind speed, wind-speed trend, turbulence intensity and shear) and the pitot tube (wind speed, wind-speed trend, turbulence intensity, rotor-position-dependent shear and the instantaneously measured wind speed for constraint turbulence simulation). Based on these simulations, it is concluded that HAWC2 simulations based on inflow information from the pitot tube are able to predict the measured flap and tower-bottom load scatter very well in most periods. The met-mast-based simulations yield high loads for most periods in the upper half of the load scatter and vice versa, but the result is less striking.

In both cases, the simulations cannot explain the tilt and yaw moment scatter, as most high-load observations are underestimated at some wind-speed ranges, and low-load observations are overestimated at other wind-speed ranges.

Data availability. Simulation results are not available due to confidentiality

Competing interests. The authors declare that they have no conflict of interest.

Acknowledgements. The authors would like to acknowledge Siemens Wind Power for providing the data for the simulation model, and the funding from the Danish Energy Agency EUDP programme of the DAN-AERO MW projects, contracts ENS no. 33033-0074 and 64009-0258, for providing important data for the present study.

Wind Energ. Sci. Discuss., https://doi.org/10.5194/wes-2018-4
Manuscript under review for journal Wind Energ. Sci.
Discussion started: 3 April 2018

eawe european academy of wind energy
Open Access WIND ENERGY SCIENCE DISCUSSIONS

References

Hansen, M. H. and Henriksen, L. C.: Basic DTU Wind Energy controller, Tech. rep., DTU Wind Energy, www.orbit.dtu.dk, 2013.

Hardesty, R. M., Korrel, J. A., and Hall, F. F.: Lidar measurement of wind velocity spectra encountered by a rotating turbine blade, Tech. rep., NOAA Technical Memorandum Washington DC, https://www.osti.gov/scitech/servlets/purl/7101820, 1981.

IEC 61400-1: Wind turbines - Part 1: Design requirements, Tech. rep., International Electrotechnical Commission, Geneva, Switzerland, www.iec.ch, 2005.

Kim, T., Hansen, A. M., and Branner, K.: Development of an anisotropic beam finite element for composite wind turbine blades in multibody system, Renewable Energy, 59, 172–183, https://doi.org/10.1016/j.renene.2013.03.033, 2013.

Kristensen, L. and Frandsen, S.: Model for power spectra of the blade of a wind turbine measured from the moving frame of reference, Journal of Wind Engineering and Industrial Aerodynamics, 10, 249–262, https://doi.org/https://doi.org/10.1016/0167-6105(82)90067-8, 1982.

Larsen, T. J. and Hansen, A. M.: How 2 HAWC2, the user's manual, no. December in Denmark. Forskningscenter Risoe. Risoe-R, Technical Report, Risø National Laboratory, Roskilde, Denmark, www.orbit.dtu.dk, 2007.

Larsen, T. J., Larsen, G., Aagaard Madsen, H., and Petersen, S. M.: Wake effects above rated wind speed . An overlooked contributor to high loads in wind farms, in: Scientific Proceedings, EWEA Annual Conference and Exhibition, Paris, France, pp. 95–99, European Wind Energy Association (EWEA), 2015.

Madsen, H. A., Bak, C., Døssing, M., Mikkelsen, R. F., and Øye, S.: Validation and modification of the Blade Element Momentum theory based on comparisons with actuator disc simulations, Wind Energy, 13, 373–389, https://doi.org/10.1002/we.359, 2010a.

Madsen, H. A., Bak, C., Schmidt Paulsen, U., Gaunaa, M., Fuglsang, P., Romblad, J., Olesen, N. A., Enevoldsen, P., Laursen, J., and Jensen, L.: The DAN-AERO MW Experiments: Final report, Denmark. Forskningscenter Risoe. Risoe-R, Danmarks Tekniske Universitet, Risø Nationallaboratoriet for Bæredygtig Energi, www.orbit.dtu.dk, 2010b.

Madsen, H. A., Riziotis, V., Zahle, F., Hansen, M. O. L., Snel, H., Grasso, F., Larsen, T. J., Politis, E., and Rasmussen, F.: Blade element momentum modeling of inflow with shear in comparison with advanced model results, Wind Energy, 15, 63–81, https://doi.org/10.1002/we.493, 2012.

Mann, J.: The spatial structure of neutral atmospheric surface-layer turbulence, Journal of Fluid Mechanics, 273, 141, https://doi.org/10.1017/S0022112094001886, 1994.

Mann, J.: Wind field simulation, Probabilistic Engineering Mechanics, 13, 269–282, https://doi.org/10.1016/S0266-8920(97)00036-2, http://www.sciencedirect.com/science/article/pii/S0266892097000362http://linkinghub.elsevier.com/retrieve/pii/S0266892097000362, 1998.

Nielsen, M., Larsen, G. C., Mann, J., Ott, S., Hansen, K. S., and Pedersen, B. J.: Wind simulation for extreme and fatigue loads, Technical report, Risø-R-1437 (EN), 104, www.orbit.dtu.dk, 2003.

Pedersen, A. T., Sjöholm, M., Angelou, N., Mikkelsen, T., Montes, B. F., Engholm Pedersen, J., Slinger, C., and Harris, M.: Full-Scale Field Test of a Blade-Integrated Dual-Telescope Wind Lidar, http://orbit.dtu.dk/files/52390492/Full_Scale_Field_Test_poster.pdf, 2013.

Pedersen, M. M., Larsen, T. J., Madsen, H. A., and Larsen, G. C.: Using wind speed from a blade-mounted flow sensor for power and load assessment on modern wind turbines, Wind Energy Science, 2, 547–567, https://doi.org/10.5194/wes-2-547-2017, 2017.

Pedersen, M. M., Larsen, T. J., Madsen, H. A., Andersen, S. J., and Aagard Madsen, H.: Free flow wind speed from a blade-mounted flow sensor, Wind Energ. Sci. Discuss., 2018, 1–33, https://doi.org/10.5194/wes-2017-57, 2018.

Wind Energ. Sci. Discuss., https://doi.org/10.5194/wes-2018-4
Manuscript under review for journal Wind Energ. Sci.
Discussion started: 3 April 2018

Peña, A., Gryning, S.-E., and Mann, J.: On the length-scale of the wind profile, Quarterly Journal of the Royal Meteorological Society, 136, 2119–2131, https://doi.org/10.1002/qj.714, http://doi.wiley.com/10.1002/qj.714, 2010.

Taylor, G. I.: The Spectrum of Turbulence, Proceedings of the Royal Society A: Mathematical, Physical and Engineering Sciences, 164, 476–490, https://doi.org/10.1098/rspa.1938.0032, 1938.

Troldborg, N., Bak, C., Aagaard Madsen, H., and Skrzypinski, W. R.: DANAERO MW: Final Report, DTU Wind Energy, Denmark, http://orbit.dtu.dk/files/80542014/DanaeroFinalReport.pdf, 2013.

Verholek, M.: Preliminary results of a field experiment to characterize wind flow through a vertical plane, Tech. rep., Pacific Northwest National Laboratory (PNNL), Richland, WA (United States), https://doi.org/10.2172/6722047, 1978.

{2.7182818284}ϑωερτυθιοπσδφγηξκλ